# Nonequilibrium electron-lattice dynamics

Dissertation zur Erlangung des Doktorgrades
an der Fakultät für Mathematik, Informatik und Naturwissenschaften,
der Universiät Hamburg,
Fachbereich Physik

vorgelegt von

**Sharareh Sayyad**

Hamburg, 2016

Tag der Disputation: 06.12.2016

Folgende Gutachter empfehlen die Annahme der Dissertation:

Erstgutachter: Prof. Dr. Martin Eckstein

Zweitgutachter: Prof. Dr. Alexander Lichtenstein

# Eidesstattliche Versicherung
# Declaration on Oath

Hermit erkläre ich an Eides statt, dass ich die vorliegende Dissertationsschrift selbst verfasst und keine anderen als die angegebenen Quellen und Hilfsmittel benutzt habe.

I hereby declare, on oath, that I have written the present dissertation by my own and have not used other than the acknowledged resources.

Hamburg, den ..... Unterschrift.....

**Abstract**

Optimizing various properties of materials have been under intensive focus for many decades. In recent years, the exposure of ultrafast techniques enhance the possibility of seizing this goal. As by employing these techniques, one can expose the system under strong short fields, and investigate the transient response of various low-lying excitations. Such studies will strengthen our understanding of interplays among various degrees of freedom in correlated materials, and thereby facilitate the chance to manipulate different properties of these systems. Of our particular attention is the electron-lattice dynamics, where modulating a particular vibrational mode of the crystal lattice, will lead to the emergence of new "quasi stable" lattice structures as well as novel transient phenomena. Aside from these experimental prospects, the above mentioned goals were also the subject of an extensive theoretical studies.

In this thesis, we investigated the in and out of equilibrium dynamics of electronic systems which are interacting with lattice degrees of freedom. We employed the two-time Keldysh Green's function within the framework of the dynamical mean field theory to conduct our researches on this subject. In our first attempt, we studied the dynamical response of a one-electron system under a linear electron-lattice interaction. We explored the real-time formation of a bound quasiparticle, known as a polaron, under various parameter regimes of the model. We presented that when the carrier is suddenly coupled to the lattice degrees of freedom, the long-time response of the system in the strong coupling limit exhibits both bound, polaronic, and unbound, delocalized, states. We characterized the nature of such a mixed state using the adiabatic picture of the model. We also showed that the formed polaron is dressed by excited phononic states, in contrast to its equilibrium counterpart, where the ground-state phononic states are bounding the electron.

We also addressed the response of a many-body electronic system, weakly coupled to a bosonic bath, under various time dependent excitations, which brings the system to a bad-metallic phase. We employed a model which treated the Coulomb repulsive interaction locally. We presented that the relaxation of this excited state varies by the strength of the electron-electron interaction. We demonstrated that, for both insulating and metallic regimes of the system, a slow relaxation dynamics can be observed close to the phase transition from the metallic to insulating regimes of the system. Our analysis revealed that in the metallic side, this slow evolution is rooted in the spin-related physics of the problem. However, in the insulating regimes of the model, our results showed that presence of a gap in the spectral density of the insulating system prohibits the relaxation of the excited particles. We also studied the associated timescale for the adiabatic dynamics near the Mott transition. Our results exhibited that there is a "nonadiabatic window" in the

metallic side of the phase transition, in which the adiabatic timescale is extremely long. We pointed out that the presence of such a window is intertwined with the slow relaxation timescale of the spin-related dynamics close to the Mott transition.

We also captured an induced metallic phase near metal-to-insulator transition out of equilibrium. We initiated this study using the slave-rotor impurity solver, which is been coupled to the self-energies obtained from the first-order Luttinger-Ward functional for the Phonon degrees of freedom. We presented the emergence of the larger spectral density at small frequencies both in metallic and insulating phases close to the phase transition, which is surrounded by pseudo gaps. We explored the physics of such spectral densities as well as their dependencies on the phononic parameters. We postulated that this response of the system is due to the evolution of the system, in a non-thermal mechanism, towards a temperature which is less than the initial temperature of the system, before coupling to the bath. We also pointed out that the associated very slow relaxation dynamics is the result of the formation of psuedo-gaps around the quasiparticle peak.

## Zusammenfassung

Die Optimierung verschiedener Materialeigenschaften ist seit Jahrzehnten ein Ziel der Festkrperphysik. In den letzten Jahren hat die Entwicklung von ultraschnellen Techniken neue Mglichkeiten erffnet, dieses Ziel zu verfolgen. So kann man die transiente Antwort der verschiedenen Anregungen des Festkrpers auf starke und extrem kurze Laserpulse untersuchen. Solche Studien strken unser Verstndnis der Wechselwirkungen zwischen verschiedenen Freiheitsgraden in korrelierten Materialien und ermglichen es, Eigenschaften dieser Systeme kontrolliert zu manipulieren. Zum Beispiel kann die Modulation einer bestimmten Schwingungsmode des Kristallgitters zum Entstehen von neuen quasistabilen Gitterstrukturen oder neuen transienten Phnomenen fhren.

In dieser Arbeit untersuchen wir insbesondere die Dynamik von elektronischen Systemen, die mit Freiheitsgraden des Kristallgitters wechselwirken. Wir verwendeten dazu den Keldysh-Formalismus im Rahmen der dynamischen Molekularfeldtheorie. Im ersten Teil der Arbeit untersuchen wir die dynamische Reaktion eines einzelnen photo-angeregten Elektrons unter Einfluss einer linearen Elektron-Gitter-Wechselwirkung (Holstein-Modell). Wir knnen so in verschiedenen Parameterbereichen des Holstein-Modells die Bildung eines gebundenen Quasiteilchens (ein Polaron) explizit als Funktion der Zeit analysieren. Im adiabatischen Limes, d.h., wenn die Dynamik des Elektrons schnell gegenber der des Gitters ist, findet man eine Energiebarriere fr die Bildung des polaronischen Zustands. Das System bleibt auf langes Zeiten in einem Zustand gefangen, der sich als eine Superposition von lokalisierten und delokalisierten Anteilen verstehen lsst, obwohl der Grundzustand dem Polaron entspricht.

Weiterhin haben wir die Reaktion des elektronischen Systems nahe am Mott-bergang untersucht, nachdem dieses auf verschiedene Weise angeregt wird und danach durch schwache Kopplung an Gitterfreiheitsgrade wieder in den Ausgangszustand relaxiert. Die Relaxation des angeregten Zustands hngt hier stark von der Elektron-Elektron-Wechselwirkung und dem Abstand zum Mott-bergang ab. Sowohl fr isolierende als auch fr metallische Phase des Systems finden wir eine langsame Relaxationsdynamik in der Nhe des Phasenbergangs, d.h., der photo-angeregte Zustand behlt auf langen Zeitskalen die Eigenschaften eines schlechten Metalls ohne wohldefinierte Quasi-Teilchen. Auf der metallischen Seite ist diese langsame Entwicklung in der langsamen Dynamik der lokalen Spin-Momente begrndet.

Diese Untersuchungen wurden mit Hilfe einer Slave-Rotor Darstellung der Strstellenproblems der dynamischen Molekularfeld-Theorie durchgefhrt, das im Rahmen dieser Arbeit fr Nichtgleichgewichtsprozesse verallgemeinert wurde. Im letzten Teil der Arbeit wurde

diese Methodik weiterhin verallgemeinert, um Strstellen-Probleme zu lsen, in der sowohl die Elektron-Phonon als auch die Elektron-Elektron Kopplung eine Rolle spielt (Hubbard-Holstein Modell).

**Acknowledgements**

The adventurous journey of my doctoral study with all of its highs and lows is approaching towards its end. The highs where I was thrilled by "the pleasure of finding things out", and lows where tough challenges had to be overcome. During these moments, there were people whose presence were always a true privilege for me. Here, I would like to convey my sincere appreciation to them.

First of all, I would like to express my deepest gratitude to my advisor, Prof. Martin Eckstein, who gave me the opportunity to become familiar with the field of nonequilibrium strong correlated systems. I am indebted for his tremendous support, continuous encouragement, and never-ending trust since the time that I have joined his group. His extensive knowledge, and inspiring enthusiasm for physics were constant motivations for me to work harder and learn more.

Immersing in a scientific atmosphere was not possible without great group members. I am extremely grateful for getting to know Dr. Karsten Balzer, Dr. Johan Mentink, and Dr. Elena Canovi. I would like to sincerely thank them for their faithful attitude, for sharing their scientific perspectives, and for various constructive pieces of advice that they have gave me since we have met. I also would like to thank Dr. Nagamalleswara Rao Dasari, Yusuf Mohammed, Ilias Seifie, and Melf Johannsen as the friendly environment of the group owes to them.

I would like to express my gratitude to Prof. Alexander Lichtenstein for kindly reviewing this thesis. My sincere thank will also go to Prof. Oriol Vendrell for accepting to be one of the members of the advisory panel, and for his time on reviewing the progress of my doctoral work.

During my doctoral studies, I have benefited from the International Max Planck Research School for Ultrafast Imaging and Structural Dynamics (IMPRS-UFAST). I specially would like to thank the coordinators Anja Bleidorn, Dr. Sonia Utermann, and Dr. Julia Quante for their support throughout the time that I was part of the school. I would like to acknowledge the joyful companionship and beneficial discussions with Dr. Alexandra Zampetaki during the doctoral journey, especially when we were preparing for our joint presentations.

I also would like to sincerely thank Vera V. Vyborova for her warm heart help on proofreading one of the chapters of this thesis, and lots of insightful discussions that we had during her short stay in Hamburg.

The sincere help of librarians at the Deutsches Elektronen-Synchrotron (DESY) is appreciated. In particular, I would like to truly thank Ms. Outi Wulff for her very quick and

effective responses in providing books, which were not available in Hamburg. Through her help, I was able to have access to all of the book that I was pondering about, and pass many encountering challenges in the shortest amount of time.

My wholeheartedly gratitude goes to my very first teachers, who I have owed a lot to them, my parents. From the deepest part of my heart, I would like to thank my parents for their unconditional love, endless support, infinite patience, and firm guidance. They are without any doubt the best parent that I can ever imagine.

My special appreciations and profusely thanks are for the man, who I shared a lot of moments of my whole life with, my brother. His companionship to create brilliant moments of my life was a true privilege, which can not be forgotten.

Finally, I would like to thank all of my teachers who either were, or are going to be, in my life. Those who gave me the opportunity to learn how to stand on my own feet and left an undeniable imprint on my life. This thesis is dedicated to them.

# List of publications

- **Coexistence of excited polarons and metastable delocalized states in photoinduced metals**
  Sharareh Sayyad, Martin Eckstein
  Phys. Rev. B **91**, 104301 (2015).

- **Slowdown of the Electronic Relaxation Close to the Mott Transition**
  Sharareh Sayyad, Martin Eckstein
  Phys. Rev. Lett. **117**, 096403 (2016).

*To my teachers since my birth till my death*

# Table of Contents

# List of Figures

# Chapter 1

# Introduction

Since the beginning of the quantum mechanics, scientists have been expressing a deep concern about the underlying physics of systems which are assemblages of many particles. In solid state physics, the main constituents of these assemblies are atoms, which are composed of other elementary particles such as electrons. As a result of quantum correlation, understanding the properties of these systems meets lots of challenges. One of the most interesting classes of such systems are those, where correlations play a significant role, known as strongly correlated systems. Construing the many-body physics in these systems is accompanied by lots of fascinations and difficulties. While the former is originated from the affluent and, usually, nontrivial phases of matter, the latter is rooted in the strong interplay among various degrees of freedom. Over decades, lots of prosperous theoretical proposals have been introduced to detangle the complexity of observed physics in strongly correlated materials, and to disclose the nature of various responses in these materials. These theoretical predictions have been followed by, or were following, numbers of experimental measurements, which were mainly restricted by the technological limitations.

The advent of technological instruments, in recent years, capacitates researchers to push the boundaries of this field even further by employing novel probing techniques. Although most of these techniques are made to perform experiments in equilibrium or slightly perturbed from the equilibrium (near-equilibrium) conditions, exposure of ultrafast techniques opens a new and fairly enchanting path to explore strong correlated systems in nonequilibrium conditions. Ultrafast spectroscopic techniques are characterized by their very large pulse energy, in the range of meV to eV, and their very short pulse duration, usually a few-cycle pulse with the duration of about few decades to hundreds femtosecond (fs). Employing such pulses will enable researchers to dynamically engineer various

excitations of correlated materials. Such experiments provide remarkable milestones to get the full control over the properties of materials.

These experimental successes were also motivating the development of nonequilibrium theories. In the extreme energy and time limits of these experiments, well-studied equilibrium physics barely can produce comparable results. Hence, nonequilibrium theories, such as nonequilibrium Green's function techniques [76, 74, 7], and quantum kinetic equations [95], have been developed to provide relevant interpretations for experimental measurements. Nevertheless, due to the scarce nonequilibrium analytical solutions and expensive numerical calculations of many-body problems out of equilibrium, theoretical researches are constantly pondering about possible ways of overcoming these challenges.

In this thesis, we share some of these theoretical challenges as well as our conquering strategies. In the forthcoming chapters, we will focus on employing the nonequilibrium Green's function technique within the dynamical mean field theory. We will concentrate on investigating the interaction between electrons and their coupling to the lattice, which provides the ground for the emergence of novel phenomena such as insulator-to-metal transitions, and temporal formation of quasiparticles.

To develop the foundation of our favorable problems, we will first review the related theoretical and experimental researches. In the following, we will present a general review on the experimental progress of the nonequilibrium dynamics with a particular attention on the electron-lattice physics, and then continue the chapter by focusing on the precise questions which we will cover in the rest of this doctoral thesis. We will close this chapter by providing the outline of this thesis.

## 1.1 Nonequilibrium electron-lattice dynamics

Manipulation and control of different properties of matter have been tantalizing ambitions for many years. Approaches like the chemical doping or controlling thermodynamical parameters, such as pressure [131] or temperature [3], were classical proposals for achieving this goal. Along with the technological development of ultrafast lasers, new suggestions for fulfilling this aspiration have been adopted. These suggestions are based on tunning the properties of the strong optical pulse, i.e. frequency, polarization, energy, and fluence, with respect to a target excitation of the relevant material. When the material is impinged by these optical pulses, the selected target excitation will be modified, and as a consequence the system can present behaviors which were not observable, or stable, under equilibrium conditions.

In general, low-lying excitations of correlated materials are manipulated by three different pulses [109], which are

1. **Near-infrared and visible** pulses with the frequencies of $10^2 - 10^3$ THz, wavelength of about $0.4 - 1$ $\mu m$, and energies of $2500 - 12500$ meV.

   Pulses with near-infrared and visible frequencies can stimulate electronic degrees of freedom. Such stimulations can lead to various photo-induced phase transitions, i.e. insulator-to-metal [14, 116, 144], or optical melting of order parameters, like the magnetic one [34]. In multi-band system, depending on the gap size, the interband transition as well as transfer of hot carriers above the Fermi energy is also a possible scenario [53]. In addition, the electronic excitations can also lead to the modification of the lattice structure by inducing a new quasi-equilibrium position for the ions of a particular vibrational modes [102]. This response is also associated with the modification of the electron-phonon coupling in the material.

2. **Mid-infrared** pulses with the frequencies of $10 - 50$ THz, wavelength of about $5 - 20$ $\mu m$, and energies of $5 - 20$ meV.

   Exploiting these pulses empowers experimentalists to resonantly excite various lattice vibrational modes. This is the core idea behind the *nonlinear phononic* mechanism, where the excitation of the infrared-active phonons results in a net deformation of the lattice structure [39, 97].

   To intuitively understand the idea behind this mechanism, we will provide a semi-classical argument for infrared-active and Raman phonons with frequencies of $\omega_{\mathrm{IR}}$ and $\omega_{\mathrm{R}}$, respectively. For simplicity, we would also set the damping coefficient of the phononic mode to zero and assume a centrosymmetric crystal. We expose such a system under a pulse field of the shape $f(t) = E_0 F(t) \sin(\omega_{\mathrm{IR}} t)$, where $E_0$ is the electric amplitude of the pulse, and $F(t)$ is the time-dependent pulse envelope. By exposing this pump pulse to the sample, the displacement of the infrared-active phonons ($Q_{\mathrm{IR}}$) satisfies

$$\ddot{Q}_{\mathrm{IR}} + \omega_{\mathrm{IR}}^2 Q_{\mathrm{IR}} = \frac{E_0 e^*}{\sqrt{M_{\mathrm{IR}}}} F(t) \sin(\omega_{\mathrm{IR}} t), \tag{1.1}$$

   where $M_{\mathrm{IR}}$ is the effective mass of ions, whose displacement produces the infrared-active phonons, and $e^*$ is the effective electron charge. Solving the above equation will give us [41],

$$Q_{\mathrm{IR}} = \Big[ \int_{-\infty}^{\infty} F(\tau) \mathrm{d}\tau \Big] \frac{E_0 e^*}{\omega_{\mathrm{IR}} \sqrt{M_{\mathrm{IR}}}} \cos(\omega_{\mathrm{IR}} t), \tag{1.2}$$

at times which are much larger than the pulse width. When the anharmonic coupling ($A$) between the infrared-active and Raman phonons is nonzero, the effective potential of the Raman phonons can be written as

$$V_{\mathrm{R}} = \omega_{\mathrm{R}}^2 Q_{\mathrm{R}}^2 - A Q_{\mathrm{IR}}^2 Q_{\mathrm{R}}. \tag{1.3}$$

Employing this potential would lead us to the equation of motion of the form

$$\ddot{Q_{\mathrm{R}}} + \omega_{\mathrm{R}}^2 Q_{\mathrm{R}} = A Q_{\mathrm{IR}}^2, \tag{1.4}$$

with the solution of

$$Q_{\mathrm{R}} = \frac{A}{2\omega_{\mathrm{R}}^2}\Big[\int_{-\infty}^{\infty} F(\tau)\mathrm{d}\tau\Big]^2 \frac{(E_0 e^*)^2}{\omega_{\mathrm{IR}}^2 M_{\mathrm{IR}}}\big(1-\cos(\omega_{\mathrm{IR}} t)\big). \tag{1.5}$$

This result indicates that apart from the oscillating response of the Raman phonon, there is a constant displacement of the associated ions due to the coupling between the infrared-active and Raman phonons.

Investigating the superconducting behavior of copper oxide materials under such mechanisms exhibited a transient light-induced superconductivity [35, 40]. It has been also shown that the nonlinear phonon mechanism, by imposing a new metastable crystal structure, can induce an insulator-to-metal transition, which is the result of a change in the overlap between different orbitals in the new configurations of ions [122, 97]. This response can modify the exchange interaction, and as a result can melt the magnetic orders in the system [41].

3. **Single or sub- terahertz** pulses with frequencies up to 1 THz, wavelength of about $300\mu m$, and energies of $few$ meV.

   It has been shown that exploiting a single terahertz pulses can control the number of cooper pairs in superconducting materials as this intense pulse can selectively break the electrons bound state [100]. Experiments also exhibit that employing the magnetic field of the terahertz pulse, with the magnitude of almost 0.3 T, can transiently control the magnetism through the Zeeman interaction between the pulse magnetic field and the magnetic orders of the system [146].

So far, we have provided a general energy-based classification of optical pulses in terahertz frequencies, where some of them where directly, or indirectly, linked to the lattice responses of the system. As we are intended to put our focus on investigating the electron-lattice dynamics in forthcoming chapters, it would be illustrative to particularly categorize possible experimental proposals for manipulations of electron-lattice parameters. In

general, different dynamics of an interacting electron-lattice systems are subsequences of changes in the electron-lattice coupling, modifications of vibrational frequencies, and deformations of crystal structures [41]. These changes are consequences of the light-matter interaction, which are as follows.

i. The dipole moment of infrared-active phonons can directly couple to the vector potential of pump pulses resulting in the modulating the lattice vibrational frequencies [22].

ii. Inducing various electronic excitations by a pump-pulse can modify the electron-phonon coupling [102].

iii. As a result of anharmonicities of the lattice, the Raman phonons as well as the lattice structure can be modified by resonantly stimulating the infrared-active phonons [97]. This process has a displacive character, which deform the lattice structure.

From the theoretical perspective, manipulating any of these characteristic parameters of the lattice can be either done by considering time-dependent variables, for instance time-dependent electron-phonon coupling or time-dependent hopping amplitude, or by renormalizing the coupling between the lattice and other degrees of freedom, such as phonon softening as a result of time-dependent electron-mediated renormalization of the phonon's frequency.

In the following, we will present an extensive survey on few- and many-electron systems which are coupled to lattice degrees of freedom. We will present evidences regarding the crucial influence of the lattice on the transient dynamics of the electronic systems. We will gather results concerning the localization of the electronic density, and emergence of quasiparticles. We will also review analyzed proposals for the induction of the metallic behavior in Mott insulating systems.

### 1.1.1 Few-electron systems

In condensed matter physics, few-electron systems refers to systems where few number of electrons are placed on the highest occupied bands, with respect to the chemical potential of the system, which are separated from the low-energy bands. The preparation of such situation out of equilibrium can be done by exposing a system with separated conduction and valance bands under the electric field of a pulse. When the pulse duration is short and its energy and polarization are tuned to excite only electrons which were associated to a very small window of the Brillouin zone, few electrons would be transfered to the empty conduction band.

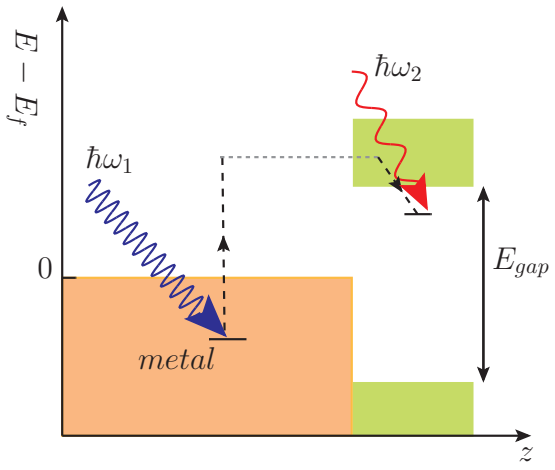


Figure 1.1: Schematic promotion of few electrons by a high-energy pulse with the frequency of $\omega_1$ to the valance band of an adsorbate. Dashed black lines indicate the evolution of the electron density from the metallic substrate to the insulating adsorbate. $z$ is the space axis perpendicular to the surface layer. $E_{\mathrm{f}}$ is the Fermi energy of the metallic substrate. Probing the evolution of this system will be done by a probe pulse with the frequency of $\omega_2 < \omega_1$. The figure shows that at the probing time a state which is inside the gap is going to be observed. This state is a polaronic state which would occupy when the electron-phonon coupling is strong. Adopted from Ref. [46].

Few-electron systems are not restricted to samples which are made of only one material, instead they can also be attained in two-layer samples. These samples usually consists of two layers where the upper layer is a two dimensional surface, with or without translational symmetry, located on a metallic substrate. The adsorbate layer usually has a very large gap, e.g. around 8.9 eV in ice [46]. Incident of a pulse with an energy which is less than the gap size, see Fig. 1.1, will excite some carriers from the metallic substrate to the valance band of the adsorbate surface [46, 49, 50, 1].

These promoted carriers are exhibiting non-thermal distribution immediately after they are transferred to the valance band. This high-energy density will then start dissipating its absorbed energy by reorientating the structure of the adsorbate layer. Theoretical investigations for one-band systems, after neglecting all interband interactions, showed that the initial relaxation of the electronic energy (kinetic energy) is by exciting more phonons in the system, and thus transferring the excess energy to the lattice [55]. In addition, simulation of a one dimensional lattice showed that when the phonon frequency is smaller than the electron hopping (adiabatic regime) the kinetic energy can be described

by an exponential decay rate in the limit of weak electron-lattice couplings. In Chap. 4, we will show that this exponential behavior of the kinetic energy will become a power-law asymptotic response when the system has a semi-elliptical density of state. Theoretical calculations presented that when the coupling between electron and the lattice is strong, the relaxation of the hot excited density is faster [128, 55, 26], which is in agreement with experiments [46, 49, 50, 1].

When this coupling is very strong, the electron-induced phonons, or induction of structural changes in amorphous adsorbate layer, can not only absorb the excess energy of electrons, but also can trap the electronic density as a result of electron-mediated polarization of its surrounding. These electron-induced polarizations would bound the electrons and will form quasiparticles known as *polarons*. The assembly of polarons is a well-known imprint of a strong coupling between the lattice and electrons degrees of freedom, which its equilibrium study dated back to the seminal work of Landau in 1933 [84].

Experimental observations out of equilibrium exhibited the coexistence of delocalized and polaronic bands in strong electron-phonon coupling regimes [46, 49, 50, 1]. Theoretical simulations report similar results in adiabatic regime [55, 82, 128]. Investigation also presented the influence of dimensionality on such observations, and showed that in two and three dimensions also such a mixed state is existing [82]. Analysis disclosed that the nonequilibrium localized, polaronic, band is an exited polaron which is accompanied by larger numbers of phonons in comparison to its counterpart in equilibrium [128]. Regarding the formation timescale of the excited polaron, Ku and Trugman pointed out that at zero-temperature this timescale has dependencies on the spatial dimension, on the initial electron energy, and on parameters of the Hamiltonian [82].

Understanding the properties of the electron localization within a polarizable medium, estimating the relevant timescale for the formation of the self-trapped electron, and assessing the relaxation process of reaching either a thermal or a steady state after bringing the system out of equilibrium, were the main pursuing goals in studying the few-electron problem. In Chap. 4, we will investigate answers of such questions, we will explore the properties of the excited polaron, and we will illustrate an intuitive explanation for the coexistence of the delocalized and localized state in the strong electron-phonon coupling regime.

### 1.1.2 Many-electron systems

In the preceding sections, we have mentioned investigations regarding the emergence or optimization of different phases of matter in nonequilibrium studies. We have also pointed

out that, in correlated many-electron systems, controlling the material properties is accompanied by lots of fascinations as quasi-stable correlation-induced physics may take place. Among lots of phase-controlling proposals, transforming an insulator ( a band [13], a Mott [71], or a topological [145] insulator) into a metal, in a controlled way, captures a widespread attention.

Of our particular interest is the transition in which the metallic state is forming from the Mott insulator. These induced phase-transitions can later be practical for optical switches. In the photo-induced phase, after shedding the pump-pulse to the sample, the same number of electrons and holes will be generated, and the lifetime of the new phase, which is usually metallic, is determined by the recombination processes. Evaluating this relaxation timescale is intertwined to the lattice structure as well as the involved correlations of the system. Thereby, having the control over this class of physics possess a necessity for theorist and experimentalists to investigate such timescales.

The relaxation mechanism of the metal-induced phase has been investigated in Mott-insulator compounds, such as Ni-chain compound [71] and $1\mathrm{T}-\mathrm{TaS}_2$ [119]. Within the pump-probe experiments, the energy of the pump pulse will be tuned such that it can excite carriers from the in-gap band to the upper Hubbard band. Performing this experiment at room temperature, exhibits the fast excitation of a hot electronic density above the Fermi energy which decayed within 500 fs [119]. Low-temperature measurements, around $T = 30K$, show a fast collapse of the insulating gap by the appearance of the Drude-like peak, immediately after the pump-pulse, in the reflectivity of the system, which is retrieved within few hundreds of femtosecond [119, 71]. One can interpret these excited electron as hot carriers which decay back to their thermal state by cooling down. Photo-induced carriers are initially transfered to the upper Hubbard band, when the pulse energy is larger than the gap [31, 154]. These carriers dissipated their excess energy by either electron-electron scattering, or by scattering of the electron with other external degrees of freedom, i.e. magnons [89] or phonons [152]. In systems with short-range spin fluctuation, spin-spin correlation will also assist the relaxation of the photo-doped electrons [32]. In cases where the excitation of other degrees of freedom is suppressed, i.e. by symmetry, energy conservation, or when they are not at all included in model Hamiltonians, hot carriers will rapidly thermalize in the system [129, 30]. When the excitation timescale of other degrees of freedom, i.e. phonons or magnons, is larger than the timescale of this rapid thermalization, the long-time physics of the system will be independent of its initial excitation. In Chap. 5, we will elaborate this response of the system and we will take the advantage of its occurrence to study the relaxation dynamics of the system close to the Mott transition.

In a purely electronic system at either high temperature or under high fluence of the

field, if the interaction strength is much larger than the bandwidth of the Hubbard bands, an exponentially slow relaxation timescale can be observed [134, 132]. Such a gradual relaxation process can be understood by recalling that the decaying channel in the strong coupling limit is either due to the in-band electron-electron scattering, or the doublon-hole recombination across the band. The initial one keeps the particle number fixed, i.e. the number of doublons, while the second mechanism varies the number of doublons. Nevertheless, both relaxation scenarios are presenting a multi-particle scattering mechanism. Hence, a multi-particle scattering process is taking the responsibility to thermalize the system. One of the examples of the multi-particle relaxation mechanism across the Hubbard bands is the *impact ionization* [154]. It is discussed that such a relaxation process is playing a noticeable role, when the frequency of the pump-pulse is larger than twice of the gap between Hubbard bands, in two-band spectral densities. This mechanism does not strongly depend on the pulse fluence. In addition, during the impact ionization the number of doublons will be enhanced, and the occupied spectral density of the upper Hubbard band will be amplified up to the factor of three.

Theoretical studies also presented that when the nonlocal density-density Coulomb repulsion is included in the model, a new relaxation channel for the photo-doped carriers, will be opened [93, 92, 138, 56]. In low-dimensional systems, simulations presented the suppression of the spin density wave as well as the enhancement of the charge density wave after the irradiation of the pump-pulse. Results also reported the shrinking of the gap size [56], and appearance of an in-gap state [91] in systems with nonlocal electron-electron interactions. This nonlocal density fluctuation will screen the on-site repulsive Coulomb interaction, and thereby the system exhibits more metallic tendency at a fixed Hubbard strength in comparison to the Hubbard model. When the interaction with phonons is also considered in the system, the phonon-induced screening will cooperate with the nonlocal electron-induced screening, and as a competition between various relaxation mechanism arises. It has been shown that the initial relaxation process can be associated with large excitations of phonons in these systems [99].

Investigation on the photo-induced insulator-to-metal transitions on the hetrostructures, with nickelate thin films, reveal that when the frequency of the pulse is tuned to the vibrational frequency of the substrate, the conductivity of the thin film will be enhanced by five orders of magnitude and will last for a long time [15]. Hu, *et. al.* explored this response in a large range of temperatures below the equilibrium metal-insulator temperature [68]. They presented that the long-lived induced metallic behavior is neither associated with the structural change of the substrate nor the melting of the magnetic ordering of the thin film. Their result presented that relaxation timescale of the excited carriers would exceed a thousand picosecond around the critical metal-insulator transition temperature.

In Chap. 5, we will present the underlying physics of the electronic problem near the Mott transition. Our results reveal a very slow relaxation timescale of these systems which is due to the emergence of a spin-related correlation timescale.

Performing experiments on heavy fermion materials also exhibit insulator-to-metal transitions [24]. A strong temperature dependence of the electronic relaxation time, below the Kondo temperature, in the magnetic compound has been reported. It has been shown that the relaxation timescale of the the nonmagnetic compound is about few thousands of femtosecond, and is independent of the temperature. For the magnetic heavy fermion, the corresponding timescale extends to hundreds of picoseconds, when the temperature of the system goes below the Nèel's temperature. It has been argued that this response was due to the comparable electron-phonon as well as electron-electron thermalization timescales below the critical temperature. It has been also pointed out that the low-temperature density of state in the magnetic compound has a large density near its Fermi energy, which contributes in suppressing the scattering of electrons by its coupling to phonons. In Chap. 6, we will show how phonons can assist the accumulation of the spectral density near the Fermi energy. We will also present that the induced phase is long-lived and its nature roots in the transient enhancement of the electron-phonon coupling strength [52].

Alternative scenarios for inducing metallic behaviors in insulators out of equilibrium includes static or time-dependent electric fields in the system [31]. Although we will not present any results regarding this type of problems in upcoming chapters, we will provide an overview on the topic for the purpose of completeness.

One of the intriguing questions, is characterizing the field-induced metallic phase in an insulating system, designated as "dielectric breakdown" of the Mott insulator. For large time-dependent [112, 115, 29] or, abruptly switched on, static [114, 113] field, the current approach a quasi-stationary state, after a short field-dependent transient response, which corresponds to a nonzero current in the Mott insulator. It has been shown that at very small temperatures, this current can be deducted from the universal many-body Schwinger-Landau-Zener mechanism, where nonadiabatic quantum-tunneling can describe the observed physics [114]. Moreover, various studies present that this induced current, in one [113] and infinite dimension [29], for the field strength of $E$ is proportional to $\exp(E_{\rm th}/E)$, where $E_{\rm th}$ is the threshold strength of the field for the occurrence of the dielectric breakdown. Results reveal that $E_{\rm th}$ nonlinearly depends on the charge-gap in Mott insulators [88, 112]. The presence of a nonlinear response of the current-field response has been also confirmed experimentally [70, 140, 58, 127]. It has been shown that, at higher temperatures, the thermal current will also start playing a role in the total current of the system. Results indicate that for the stationary state the total current is not the simple sum of the tunneling and thermal contributions [29]. This observation implies that the initial

mobile carriers, which have been thermally excited, will be bounded in the stationary state.

After surveying the many, and few, -body physics in the presence of electron-electron and electron-lattice interactions, it is not unquestionable that investigating various phases of matter out of equilibrium will empower us to enlighten the path to the emergence of novel approaches to create, control, and optimize different phases of matter. As a consequence, achieving vast technological improvements is extremely conceivable, and tremendous exotic properties would find the opportunity to play a role on the stage of nonequilibrium physics.

## 1.2 Outline of this thesis

This thesis is ordered as follows.

In Chap. 2, we present the theoretical framework employed in this thesis. We provide a concise, but rather complete, overview of the two-time Keldysh Green's function formalism. In the light of Kadanoff-Baym equations, we derive the equation of motions for different components of the Keldysh Green's function.

Chap. 3 embraces the numerical framework of our results known as dynamical mean-field theory (DMFT). We explain approximations within this method as well as its applicability domain. We avoid any particular model-based description of the formalism, and provide a general DMFT setup which we take its advantage in the rest of the thesis.

Chap. 4 is initiated by a brief survey over the Holstein model and its parameter regimes. We develop an impurity solver for the low-density carrier limit to be employed in the DMFT self-consistency. We continue this chapter by presenting the results of the low-density limit of carrier in different parameter regimes with special attention on the real-time formation of the polaron.

Chap. 5 comprises the DMFT solutions of the Hubbard model obtained by the slave-rotor impurity solver. We commence the chapter by providing an overview on the Hubbard model, and continue the discussion by developing an impurity solver for DMFT, known as the slave-rotor solver. We expend this solution to investigate the physics of the Hubbard model near its first order phase transition both in metallic and insulating part of the phase diagram.

In Chap. 6, we tackle the Hubbard-Holstein model with the goal to capture the induced metallic state out of equilibrium. The chapter begins by explaining the model Hamiltonian, and is extended to include the adopted slave-rotor solver in the presence of phonons. We

then explain the equilibrium physics of the problem, and carry out the discussion by explaining the electron dynamics under the quench of the electron-phonon coupling.

Chap. 7 is dedicated to the conclusion of this thesis.

# Chapter 2

# Introduction to the Keldysh formalism for nonequilibrium Green's functions

The Green's function technique [47, 79] plays a vital role in investigating systems of many interacting particles. The method can be used to compute many-body quantum and statistical properties of any generic system, i.e. $n$-point correlation functions, in and out of equilibrium. Various versions of this techniques have been proposed which are commonly known as Matsubara, Feynman, and Keldysh ones. These methods are distinguishable by their definition of the density matrix. In the Matsubara Green's function technique, the density matrix corresponds to a thermal state, while in the Feynman and Keldysh methods the density matrix is computed based on the adiabatic theorem [95]. Introducing a complex time contour, enables us to treat these methods on the same footing. In Fig. 2.1, we present three time-contours.

In the following, we will give an overview on the indispensable nonequilibrium Keldysh Green's function technique to establish the notation for the upcoming chapters. Comprehensive reviews on the Keldysh formalism can be found in Refs. [78, 76, 133, 121], and extensive introduction to the physics of many-body theory is given by Refs. [108, 96].

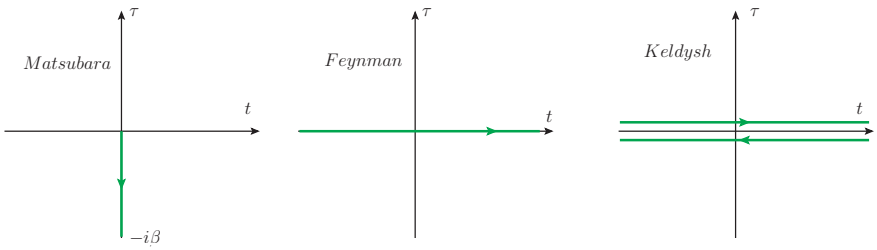


Figure 2.1: Various time contours for the Green's function technique on the complex plane $(t, i\tau)$. The time-evolution on the Matsubara contour goes from $(0, 0)$ to $(0, -i\beta)$, on the Feynman contour runs from $-\infty$ to $\infty$, and on the Keldysh time contour runs back and forth between $(-\infty, 0)$ and $(\infty, 0)$.

## 2.1 Historical remarks

The nonequilibrium Green's function technique is initially credited to Schwinger [130], and Kadanoff and Baym [74], who conducted studies using n-point Green's functions in and out of equilibrium in different contexts. Schwinger demonstrated the concept of two-branch time-contour and studied the motion of a quantum oscillator under an external force in that framework. Kadanoff and Baym introduced two-time Green's functions, derived their equations of motion, and systematically generalized the Boltzmann kinetic theory of transport using one and two-particle Green's functions.

Their work has been followed by the Keldysh [76] who employed a matrix-like Green's function to study generic many-body systems under an external field, switched on adiabatically. In his work, the Green's function is propagated on a time contour consisting of two branches going back and forth between $-\infty$ to $\infty$, and its equation of motion can be solved using the diagrammatic expansion technique. The particular choice of the time-dependent field empowered him to consider his initial interacting state at $t = \pm\infty$ as a noninteracting state, up to a factor due to the Gell-Mann and Low's theorem[36].

The Gell-Mann and Low's theorem is applicable for an interacting system with the generic Hamiltonian of

$$H = H_0 + e^{-\delta|t-t_0|}H_1, \tag{2.1}$$

where $H_0$ is the noninteracting and $H_1$ is the interacting part, with the ground state of $|0\rangle$ and $|\psi\rangle$, respectively. $\delta$ is a positive number, sets such that the interaction is turned on and off extremely slowly (adiabatically). This theorem states that the ground state of

such an interacting system would be

$$|\psi\rangle = \lim_{\delta \to 0} U_\delta(t_0, -\infty)|0\rangle. \tag{2.2}$$

Here, $U_\delta(t_0, -\infty)$ describes the time-evolution of the system from $-\infty$ to $t_0$, where $t_0$ is the time, when the interaction $H_1$ turned on. It is crucial to note that for a Hamiltonian defined as $H = H_0 + e^{-\delta|t-t_0|}gV$, where $g$ is the coupling constant and $V$ is the interaction, Eq. (2.2) will no longer be applicable if the system can not be treated perturbatively in expansions of $g$.

This conveys that the two-branch Keldysh contour requires some modifications since apart from the above mentioned validity range of the Gell-Mann and Low's theorem, no correlation between the initial state and an intermediate interacting state is included in the theory. This inconsideration was amended by including the initial correlation [48] into account. For the initial thermal correlation, concatenating a new branch perpendicular to the two-time Keldysh contour resolved the problem [143, 20]. In the following, we will explain this new shape of the Keldysh contour, as well as the Green's function formalism in this framework.

## 2.2 The three-branch Keldysh contour

The three-branch time-contour, which we will refer to as the Keldysh contour ($\mathcal{C}$) in the rest of this thesis, is shown in Fig. 2.2. The time contour is displayed on the complex plane with two parallel branches along the real-time direction and one perpendicular to those. Real-branches have opposite propagating direction starting from the upper one, $\mathcal{C}^+$, with the evolution along the time-axis from $t_0$ to $t_{\max}$, and continuing to the lower one, $\mathcal{C}^-$, from $t_{\max}$ to $t_0$. $t_0$ is an arbitrary time, which is usually chosen in two manners. Either, one would set $t_0$ to $-\infty$, to evoke the two-branch Keldysh contour formalism, or shift the imaginary axis to $t_0$ and thereby carry out a study in this displaced coordinate where $t_0 = 0$, which is also our choice in this thesis. $t_{\max}$ is fixed to $\infty$, however, due to numerical restrictions, it is not feasible to perform a study till that time. Hence, numerically, $t_{\max}$ will be the largest simulation time.

The third branch, $\mathcal{C}^|$, is connected to the end of $\mathcal{C}^-$ along the negative side of the vertical imaginary axis with the length of inverse temperature ($\beta$). It is worthwhile to mention that due to the Cauchy's integral formula the deformation of the vertical branch would lead to the same physical expectation values if and only if the intersection of any line parallel to the real branches ($\mathcal{C}^\pm$) with $\mathcal{C}^|$ has only one point. With respect to this theorem

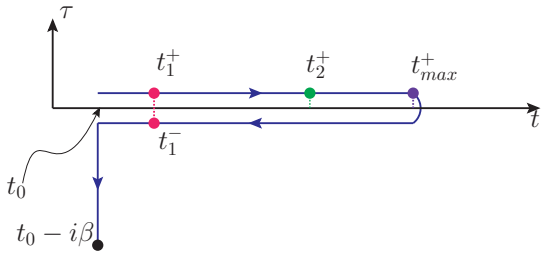


Figure 2.2: The Keldysh contour on the complex plane $(t, \tau)$. Two parallel blue solid lines are real-time branches connected to a vertical branch with the length of $\beta$. The time ordering is performed by following the directions shown by arrows along the whole contour. Due to this contour ordering, the green point $(t_2^+)$ is before the red point $(t_1^-)$ on the lower branch while their physical time-ordering is the other way around. The red-points on upper and lower branches are corresponding to the same physical time. The purple point is the end of real-branch corresponding to the physical time of $t_{\max}$. The black point indicates the end of the contour corresponding to $t = t_0 - i\beta$.

the L-shaped Keldysh contour can deform and have an arbitrary imaginary branch. Time ordering along $\mathcal{C}$ is defined by keeping the evolution direction from $\mathcal{C}^+$ to $\mathcal{C}^-$ and continue to $\mathcal{C}^|$. This implies that for any two times, let's say $t_1$ and $t_2$, one would have $t_1 \succ t_2$ if $t_2$ is closer to $t_0^+$, $t_0^+ \in \mathcal{C}^+$, than $t_1$, where $\succ$ is the contour greater operator. Furthermore, since physical time is the projection of any point on $\mathcal{C}^\pm$ to the real time axis, it is obvious that the contour time-ordering is not the same as the physical time-ordering.

We thereby can express the thermal time-evolution operator,

$$\mathcal{U} = \mathcal{T} e^{-\beta H(0)} \exp(-i \int_0^t H(t_1) \mathrm{dt}_1), \tag{2.3}$$

as a contour ordered exponential,

$$\mathcal{U}_\mathcal{C} = \mathcal{T}_\mathcal{C} \exp(-i \int_\mathcal{C} H(t_1) \mathrm{dt}_1), \tag{2.4}$$

where $\mathcal{T}$ is the physical time-ordering, and $\mathcal{T}_\mathcal{C}$ is the contour time-ordering operator. $\mathcal{U}_\mathcal{C}$ is a unitary operator with the group property of $\mathcal{U}_\mathcal{C}(t_1, t_3) = \mathcal{U}_\mathcal{C}(t_1, t_2)\mathcal{U}_\mathcal{C}(t_2, t_3)$, where $t_1, t_2, t_3 \in \mathcal{C}$.

By employing $\mathcal{U}_\mathcal{C}$, one can express the expectation value of any n-point correlation function as

$$\langle \widehat{\mathcal{O}}_1(t_1) \widehat{\mathcal{O}}_2(t_2) \dots \widehat{\mathcal{O}}_n(t_n) \rangle \equiv \frac{1}{Z} \mathrm{Tr}\big[ \mathcal{T}_\mathcal{C} e^{-i \int_\mathcal{C} \mathrm{dt}' H(t')} \mathcal{O}_1(t_1) \mathcal{O}_2(t_2) \dots \mathcal{O}_n(t_n) \big], \tag{2.5}$$

where $Z = \mathrm{Tr}[\mathcal{T}_{\mathcal{C}} e^{-i\int_{\mathcal{C}} \mathrm{dt}' H(t')}]$ is the partition function, and Tr is taken over all states of a particular ensemble. Unless it is explicitly mentioned, i.e. in Chap. 4, we will describe our systems in grand-canonical ensemble, and the trace is over all states in the Fock space. $\mathcal{O}_i(\widehat{\mathcal{O}}_i)$ is the $i$-th operator occurring at $t_i$ in Schroedinger (Heisenberg) picture. If any two of these operators act at the same contour-time, then the contour time-ordering operator will perform as a normal ordering operator.

Of our particular interest is the two-point correlation function, as

$$\langle \widehat{\mathcal{O}}_1(t_1)\widehat{\mathcal{O}}_2(t_2)\rangle = \frac{1}{Z}\mathrm{Tr}\big[\mathcal{T}_{\mathcal{C}} e^{-i\int_{\mathcal{C}} \mathrm{dt}' H(t')}\mathcal{O}_1(t_1)\mathcal{O}_2(t_2)\big]. \tag{2.6}$$

Whenever $\mathcal{O}_1$ and $\mathcal{O}_2$ are creation or annihilation operators of a particle, this two-point correlation function is the Green's function. Depending on whether $\mathcal{O}_1$ and $\mathcal{O}_2$ follow the fermionic (bosonic) statistics, the two-point correlation function is called the fermionic (bosonic) Green's function.

## 2.3 Nonequilibrium two-time Keldysh Green's functions

The contour Green's function is defined as

$$G_{\alpha\gamma}(t,t') = -i\langle \mathcal{T}_{\mathcal{C}} c_\alpha(t) c^\dagger_\gamma(t')\rangle, \tag{2.7}$$

where $c(t)$ is the annihilation operator at time $t$, $c^\dagger(t')$ creates a particle at $t'$, and $t, t'$ are on the Keldysh contour. $\alpha$ and $\gamma$ denote particles degrees of freedom, for instance, orbital, spin, lattice index, etc. For the simplicity and clarity purposes, we will drop these indices throughout the discussion, unless it induces some confusions. The physical interpretation of this class of correlation functions is describing the propagation of an additional particle or hole in the system. As a result of three-branch time-contour, we can represent $G(t,t')$ as a matrix [4], where each element is associated with a particular location of $t$ and $t'$ on one of the branches of the Keldysh contour as

$$G(t,t') = \begin{pmatrix} G_{++} & G_{+-} & G_{+|} \\ G_{-+} & G_{--} & G-| \\ G_{|+} & G_{|-} & G_{||} \end{pmatrix}, \tag{2.8}$$

where $G_{\iota\varsigma}$ is the Green's function where $c(t)$ is on $\iota \in \mathcal{C}^+, \mathcal{C}^-, \mathcal{C}^|$, and $c^\dagger(t')$ is on $\varsigma \in \mathcal{C}^+, \mathcal{C}^-, \mathcal{C}^|$. Straight forward calculations with the help of the group property of $\mathcal{U}_{\mathcal{C}}$, will

lead us to the conclusion that there are only six independent element out of 9 elements of Eq. (2.8) [143]. This simplification can be done using

$$\widetilde{G}(t,t') = \mathcal{L}\tau_3 G(t,t')\mathcal{L}^\dagger, \tag{2.9}$$

where $\widetilde{G}$ is the transformed Green's function,

$$\mathcal{L} = \frac{1}{\sqrt{2}}\begin{pmatrix} 1 & -1 & 0 \\ 1 & 1 & 0 \\ 0 & 0 & \sqrt{2} \end{pmatrix}, \tag{2.10}$$

and

$$\tau_3 = \begin{pmatrix} 1 & 0 & 0 \\ 0 & -1 & 0 \\ 0 & 0 & 1 \end{pmatrix}. \tag{2.11}$$

The obtained $\widetilde{G}$ is, often, represented as

$$\widetilde{G}(t_\mathcal{C}, t'_\mathcal{C}) = \begin{pmatrix} G^{\rm ret}(t,t') & G^{\rm K}(t,t') & \sqrt{2}G^{\rm tv}(t,\tau') \\ 0 & G^{\rm adv}(t,t') & 0 \\ 0 & \sqrt{2}G^{\rm vt}(\tau,t') & G^{\rm mat}(\tau,\tau') \end{pmatrix}, \tag{2.12}$$

where $t_\mathcal{C}$ is defined on the full Keldysh contour, while $t \in \mathcal{C}^\pm$ and $\tau \in \mathcal{C}^|$. Elements of $\widetilde{G}$ are called as Matsubara ($G^{\rm mat}$), retarded ($G^{\rm ret}$), advanced ($G^{\rm adv}$), left-mixing ($G^{\rm tv}$), right-mixing ($G^{\rm vt}$), and Keldysh ($G^{\rm K}$). These independent elements of $\widetilde{G}$ are then easily given by

$$G^{\rm ret}(t,t') = \frac{1}{2}[G_{++} - G_{+-} + G_{-+} - G_{--}] = -i\Theta(t-t')\langle[c(t), c^\dagger(t')]_\mp\rangle, \tag{2.13}$$

$$G^{\rm adv}(t,t') = \frac{1}{2}[G_{++} + G_{+-} - G_{-+} - G_{--}] = i\Theta(t'-t)\langle[c(t), c^\dagger(t')]_\mp\rangle, \tag{2.14}$$

$$G^{\rm K}(t,t') = \frac{1}{2}[G_{++} + G_{+-} + G_{-+} + G_{--}] = -i\langle[c(t), c^\dagger(t')]_\pm\rangle, \tag{2.15}$$

$$G^{\rm tv}(t,\tau') = \frac{1}{2}[G_{+|} + G_{-|}] = \mp i\langle c^\dagger(\tau')c(t)\rangle, \tag{2.16}$$

$$G^{\rm vt}(\tau,t') = \frac{1}{2}[G_{|+} + G_{|-}] = -i\langle c(\tau)c^\dagger(t')\rangle, \tag{2.17}$$

$$G^{\rm mat}(\tau,\tau') = -iG_{||} = -\langle\mathcal{T}_\tau c(\tau)c^\dagger(\tau')\rangle. \tag{2.18}$$

Here, $\mathcal{T}_\tau$ is the contour-ordering on the imaginary time, $[,]_{+(-)}$ denotes the boson's (fermion's) (anti-)commutation relation, $+(-)$ sign in Eq. (2.16) characterized bosonic (fermionic)

Green's function. $\Theta(t-t')$ is the Heaviside function

$$\Theta(t,t') = \begin{cases} 1 & t \succ t' \\ 0 & \text{else} \end{cases}, \tag{2.19}$$

where $\succ$ is the binary operator on the contour. For further discussion purposes, we will introduce two Green's functions as lesser ($G^<$) and greater ($G^>$), given by

$$G^<(t,t') = \frac{1}{2}[G^{\mathrm{K}}(t,t') - G^{\mathrm{ret}}(t,t') + G^{\mathrm{adv}}(t,t')] = \mp i\langle c^\dagger(t')c(t)\rangle, \tag{2.20}$$

$$G^>(t,t') = \frac{1}{2}[G^{\mathrm{K}}(t,t') + G^{\mathrm{ret}}(t,t') - G^{\mathrm{adv}}(t,t')] = -i\langle c(t)c^\dagger(t')\rangle. \tag{2.21}$$

By exploiting the Hermitian conjugate of above mentioned Green's functions, we find

$$G^{<,>,K}(t,t')^* = -G^{<,>,K}(t',t), \tag{2.22}$$

$$G^{\mathrm{ret}}(t,t')^* = G^{\mathrm{adv}}(t',t), \tag{2.23}$$

$$G^{\mathrm{tv}}(t,\tau')^* = \mp G^{\mathrm{vt}}(\beta-\tau',t), \tag{2.24}$$

where the plus (minus) sign of the last equation is assigned for the fermion (boson). These conditions imply that for Hermitian Hamiltonians, the number of independent Green's functions will decrease to four, with retarded, lesser, left-mixing and Matsubara components. For systems with particle-hole symmetry, the Green's function furthermore satisfy

$$G(t,t') = \pm G(t',t), \tag{2.25}$$

where we take $+$ $(-)$ sign for boson (fermion).

By cyclic permutation of operators under the trace in Eq. (2.6), one can prove the relations

$$G(0^+,t) = \pm G(-i\beta,t), \tag{2.26}$$

$$G(t,0^+) = \pm G(t,-i\beta), \tag{2.27}$$

known as the Kubo-Martin-Schwinger boundary conditions [83, 98], where upper(lower) sign is taken for boson(fermion). Eqs. (2.26, 2.27) is obtained by taking the (anti-) commutation relation inserted by permuting two (fermions) bosons along the contour at $0^+$ and $t$. In addition, for the Matsubara component of the Green's function the above mentioned boundary conditions will simplify to

$$G^{\mathrm{mat}}(\tau) = \pm G^{\mathrm{mat}}(\tau+\beta), \tag{2.28}$$

where we have used the time-translational symmetry of the Matsubara Green's function as $G^{\rm mat}(\tau,\tau') \equiv G^{\rm mat}(\tau-\tau')$, which follows because the Hamiltonian does not depend on imaginary time. In addition, the Matsubara Green's function is real

$$G^{\rm mat}(\tau)^* = G^{\rm mat}(\tau). \tag{2.29}$$

So far, the discussed formalism is applicable for conducting a study in and out of equilibrium. However, in equilibrium, the theory can be simplified since all Green's functions are time-translational invariance, functions of relative time ($t_{\rm rel} = t - t'$). It is also known that any equilibrium Green's function is related to the one-body spectral function by

$$G^{\rm ret}(t,t') = -i\int e^{i\omega(t-t')}A(\omega)\Theta(t-t'){\rm d}\omega, \tag{2.30}$$

$$G^{<}(t,t') = -i\int e^{-i\omega(t-t')}A(\omega)\big(\pm f(\omega)\big){\rm d}\omega, \tag{2.31}$$

$$G^{\rm tv}(\tau,t') = -i\int e^{-\omega\tau}e^{i\omega t'}A(\omega)\big(1\pm f(\omega)\big){\rm d}\omega, \tag{2.32}$$

$$G^{\rm mat}(\tau_{\rm rel}=\tau-\tau') = -\int e^{-\omega\tau_{\rm rel}}A(\omega)\big(1\pm f(\omega)\big){\rm d}\omega, \tag{2.33}$$

with a general relation of

$$G(t,t') = -i\int {\rm d}\omega e^{-i\omega(t-t')}A(\omega)\big(\Theta_{\mathcal{C}}(t,t')\pm f(\omega)\big), \tag{2.34}$$

where $(+)$ is assigned for bosons with Bose-Einstein distribution function $f(\omega) = 1/(e^{\beta\omega}-1)$ and $(-)$ is taken for fermions with Fermi-Dirac distribution function. $A(\omega)$ is the one-body spectral function at energy $\omega$, given by

$$A(\omega) = -\frac{1}{\pi}\Im G^{\rm ret}(\omega+i0), \tag{2.35}$$

which determines all available states for a particle.

The density of occupied (unoccupied) states is then expressed in terms of the lesser (greater) Green's function as

$$G^{<}(\omega) = \mp 2\pi i A(\omega)f(\omega), \tag{2.36}$$

$$G^{>}(\omega) = -2\pi i A(\omega)[1\pm f(\omega)], \tag{2.37}$$

where we set the upper (lower) sign for bosonic (fermionic) system with the respective distribution function ($f(\omega)$). By dividing Eq. (2.36) to Eq. (2.37), we yield the *fluctuation-dissipation* relation as

$$G^{>}(\omega) = \pm e^{\beta\omega} G^{<}(\omega), \tag{2.38}$$

keeping $+(-)$ sign for bosons(fermions).

Out of equilibrium, we usually employ three definitions for the time-dependent spectral function,

$$A(t_{\text{avg}}, \omega) = -\frac{1}{\pi} \Im \int \mathrm{d}s e^{i\omega s} G^{\text{ret}}(t + s/2, t - s/2), \tag{2.39}$$

$$A(t, \omega) = -\frac{1}{\pi} \Im \int \mathrm{d}s e^{i\omega s} G^{\text{ret}}(t, t - s), \tag{2.40}$$

$$A(t, \omega) = -\frac{1}{\pi} \Im \int \mathrm{d}t' e^{i\omega s} G^{\text{ret}}(t + s, t), \tag{2.41}$$

where $s$ is the time difference. We will use Eq. (2.40) to obtain the spectral function of a system at final time, and Eq. (2.41) to capture the initial density of states. The above mentioned nonequilibrium spectral functions satisfy the sum rule of

$$\int \mathrm{d}\omega A(t, \omega) = 1. \tag{2.42}$$

In addition, replacing $G^{\text{ret}}$ by $G^{</>}$ in Eqs. (2.39, 2.40, 2.41) will provide the occupied/unoccupied spectral denisty.

### 2.3.1 Keldysh Contour Calculus

For the completeness purpose, we devote this section to briefly explain the contour notations that we will later encounter. These notations consists of derivation, integration, convolution, product, and delta function on $\mathcal{C}$. The upcoming rules, related to the product and convolution, are also known as Langreth rules.

#### Derivation

For a generic function ($g$), the contour derivative is defined as

$$\partial_t g(t) = \begin{cases} \partial_t g(t^{\pm}) & \text{for } t \text{ on } \mathcal{C}^{\pm} \\ i\partial_\tau g(-i\tau) & \text{for } t = -i\tau \end{cases}. \tag{2.43}$$

### Integration

The contour integration is taken as

$$\int_{\mathcal{C}} \mathrm{dt}\mathcal{G}(t,t') = \int_0^{t_{\max}} \mathrm{dt}^+\mathcal{G}(t^+,t') - \int_0^{t_{\max}} \mathrm{dt}^-\mathcal{G}(t^-,t') - i\int_0^{\beta} d\tau\mathcal{G}(-i\tau,t'), \tag{2.44}$$

with considering $t^{+(-)}$ on $\mathcal{C}^{+(-)}$.

### Convolution

The convolution of two contour correlation functions is

$$\mathcal{C} = [\mathcal{A} * \mathcal{B}](t,t') = \int_{\mathcal{C}} \mathcal{A}(t,t_1)\mathcal{B}(t_1,t')\mathrm{dt}_1. \tag{2.45}$$

This relation for each component of Keldysh Green's function can be explicitly mentioned as

$$\mathcal{C}^{\mathrm{mat}} = \mathcal{A}^{\mathrm{mat}} \ltimes \mathcal{B}^{\mathrm{mat}}, \tag{2.46}$$
$$\mathcal{C}^{\mathrm{ret}} = \mathcal{A}^{\mathrm{ret}} \circ \mathcal{B}^{\mathrm{ret}}, \tag{2.47}$$
$$\mathcal{C}^{\mathrm{adv}} = \mathcal{A}^{\mathrm{adv}} \circ \mathcal{B}^{\mathrm{adv}}, \tag{2.48}$$
$$\mathcal{C}^{\mathrm{tv}} = \mathcal{A}^{\mathrm{tv}} \circ \mathcal{B}^{\mathrm{mat}} + \mathcal{A}^{\mathrm{ret}} \bullet \mathcal{B}^{\mathrm{tv}}, \tag{2.49}$$
$$\mathcal{C}^{\mathrm{vt}} = \mathcal{A}^{\mathrm{vt}} \circ \mathcal{B}^{\mathrm{adv}} + \mathcal{A}^{\mathrm{mat}} \bullet \mathcal{B}^{\mathrm{vt}}, \tag{2.50}$$
$$\mathcal{C}^{<} = \mathcal{A}^{<} \circ \mathcal{B}^{\mathrm{adv}} + \mathcal{A}^{\mathrm{ret}} \circ \mathcal{B}^{<} + \mathcal{A}^{\mathrm{tv}} \bullet \mathcal{B}^{\mathrm{vt}}, \tag{2.51}$$
$$\mathcal{C}^{>} = \mathcal{A}^{>} \circ \mathcal{B}^{\mathrm{adv}} + \mathcal{A}^{\mathrm{ret}} \circ \mathcal{B}^{>} + \mathcal{A}^{\mathrm{tv}} \bullet \mathcal{B}^{\mathrm{vt}}. \tag{2.52}$$

Here,

$$A \bullet B(t,t') = -i\int_0^{\beta} A(t,\tau)B(\tau,t')\mathrm{d}\tau, \tag{2.53}$$

$$A \circ B(t,t') = \int_0^{t_{\max}} A(t,t_1)B(t_1,t')\mathrm{dt}_1, \tag{2.54}$$

and

$$A \ltimes B(\tau) = -i\int_0^{\beta} A(\tau-\tau_1)B(\tau_1)\mathrm{d}\tau_1. \tag{2.55}$$

### Product

The product of two two-point correlation functions is given by

$$\mathcal{C}(t,t') = A(t,t')B(t',t). \tag{2.56}$$

The above equality for each component of Keldysh Green's function will be

$$\mathcal{C}^{\mathrm{mat}} = \mathcal{A}^{\mathrm{mat}}B^{\mathrm{mat}}, \tag{2.57}$$
$$\mathcal{C}^{\mathrm{ret}} = \mathcal{A}^{\mathrm{ret}}\mathcal{B}^{<} + \mathcal{A}^{<}\mathcal{B}^{\mathrm{adv}} = \mathcal{A}^{\mathrm{ret}}\mathcal{B}^{>} + \mathcal{A}^{>}\mathcal{B}^{\mathrm{adv}}, \tag{2.58}$$
$$\mathcal{C}^{\mathrm{adv}} = \mathcal{A}^{\mathrm{adv}}\mathcal{B}^{<} + \mathcal{A}^{<}\mathcal{B}^{\mathrm{ret}} = \mathcal{A}^{\mathrm{adv}}\mathcal{B}^{>} + \mathcal{A}^{>}\mathcal{B}^{\mathrm{ret}}, \tag{2.59}$$
$$\mathcal{C}^{\mathrm{tv}} = \mathcal{A}^{\mathrm{tv}}\mathcal{B}^{\mathrm{vt}}, \tag{2.60}$$
$$\mathcal{C}^{\mathrm{vt}} = \mathcal{A}^{\mathrm{vt}}\mathcal{B}^{\mathrm{tv}}, \tag{2.61}$$
$$\mathcal{C}^{<} = \mathcal{A}^{<}\mathcal{B}^{>}, \tag{2.62}$$
$$\mathcal{C}^{>} = \mathcal{A}^{>}\mathcal{B}^{<}. \tag{2.63}$$

### Delta function

$\delta_{\mathcal{C}}$ is the delta function with a nonzero value when $t = t'$ on the $\mathcal{C}$,

$$\delta_{\mathcal{C}}(t,t') = \partial_t \Theta(t,t'), \tag{2.64}$$
$$\int_{\mathcal{C}} \mathrm{d}t_1 \delta_{\mathcal{C}}(t,t_1)g(t_1) = g(t) \quad \text{for any } g(t), \tag{2.65}$$

where $\Theta$ is the contour step function defined in Eq. (2.19).

## 2.4 Dyson equations of Keldysh Green's functions

Since the Keldysh Green's function formalism had the goal to describe the time-evolution of initial correlations, for instance the evolution of the initial spectral weight, we now put our effort on introducing the equations of motion for each component of two-time Keldysh Green's function.

Let us consider a one-species many-body system which is governed by a Hamiltonian, expressed in second quantization as

$$H = H^{(1)} + H^{(2)}, \tag{2.66}$$
$$H = \sum_{\alpha,\gamma} \langle \alpha | h^{(1)} | \gamma \rangle c_\alpha^\dagger c_\gamma + \frac{1}{2} \sum_{\alpha,\alpha',\gamma,\gamma'} \langle \alpha, \gamma | h^{(2)} | \alpha', \gamma' \rangle c_\alpha^\dagger c_\gamma^\dagger c_{\gamma'} c_{\alpha'}, \tag{2.67}$$

where $H^{(1)}(t)$ includes the time-dependent one-body interactions with the matrix element of $h^{(1)}$ in the basis, which is set by creation ($c^\dagger$) and annihilation ($c$) operators. $H^{(2)}$ is the two-body contribution of the Hamiltonian where its matrix element is obtained in the span space of $|\alpha,\gamma\rangle = |\alpha\rangle \bigotimes |\gamma\rangle$.

On the other hand, the equation of motion for any operator then simply is obtained by the Heisenberg equation

$$-i\frac{\partial}{\partial_t}\mathcal{O}(t) = \big[H(t),\mathcal{O}(t)\big], \tag{2.68}$$

in particular, one can insert Eq. (2.67) in above equation and yield the dynamics of the annihilation operator as

$$-\frac{\partial}{\partial_t}c_\kappa(t) = \big[H(t),c_\kappa(t)\big], \tag{2.69}$$

$$\sum_\gamma \Big( -i\frac{\partial}{\partial_t}\delta_{\kappa,\gamma} - \langle\kappa|h^{(1)}(t)|\gamma\rangle\Big)c_\gamma(t) = \sum_{\gamma,\alpha',\gamma'}\int \mathrm{dt}_1\langle\kappa,\gamma|h^{(2)}(t,t_1)|\alpha',\gamma'\rangle c^\dagger_\gamma(t_1)c_{\gamma'}(t_1)c_{\alpha'}(t). \tag{2.70}$$

Multiplying a creation operator ($c^\dagger_\varsigma(t')$) to the right-hand side of Eq. (2.70) and take the thermal and quantum expectation value of this equation with respect to the Hamiltonian $H$ yields the equation of motion of the Green's function

$$\sum_\gamma \Big( -i\frac{\partial}{\partial_t}\delta_{\kappa,\gamma} - \langle\kappa|h^{(1)}(t)|\gamma\rangle\Big)G_{\gamma,\varsigma}(t,t') = \sum_{\gamma,\alpha',\gamma'}\int_{\mathcal{C}} \mathrm{dt}_1\langle\kappa,\gamma|h^{(2)}(t,t_1)|\alpha',\gamma'\rangle G_{\alpha'\gamma';\gamma\varsigma}(t,t_1;t_1^+,t'), \tag{2.71}$$

where we generalized the time integration into the contour integration. In the right-hand side of Eq. (2.71), the superscript $(+)$ for $t_1$, denotes an infinitesimal time after $t_1$, which is set to ensure the placement of creation operator later than the annihilation one on the contour. The two-body Green's function, which appears in Eq. (2.71), is defined as

$$G_{\alpha'\gamma';\gamma\alpha}(t,t_1;t_1',t') = (-i)^2\langle\mathcal{T}_{\mathcal{C}}c_{\alpha'}(t)c_{\gamma'}(t_1)c^\dagger_\gamma(t_1')c^\dagger_\alpha(t')\rangle. \tag{2.72}$$

Eq. (2.71), known as the Kadanoff-Baym equation [74], implies that the dynamics of the one-body Green's function is related to the two-body Green's function. Similar equation can be cast for the dynamics of the $n$-body Green's function which is related to the higher

orders Green's functions, namely $(n \pm 1)$-body Green's function. This is the Martin-Schwinger hierarchy [98], where Eq. (2.71) is the first of them. Exploiting a contour scattering matrix, as a generalization of the thermal $\mathcal{S}$-matrix [78], enables us to close the Martin-Schwinger hierarchy by introducing

$$\sum_{\gamma,\alpha',\gamma'} \int_{\mathcal{C}} \mathrm{d}t_1 \langle \kappa, \gamma | h^{(2)}(t, t_1) | \alpha', \gamma' \rangle G_{\alpha'\gamma';\gamma\varsigma}(t, t_1; t_1^+, t') \equiv \int_{\mathcal{C}} \mathrm{d}t_1 \Sigma_{\alpha',\gamma}(t, t_1) G_{\gamma',\varsigma}(t_1, t'), \quad (2.73)$$

where $\Sigma$ is the self-energy of the system which is a function of $h^{(2)}$ and one-body Green's function. Kadanoff and Baym [7] investigated the conservation laws within this approximated solutions of Eq. (2.71). Within their work, they expressed a two-body Green's function as a functional of one-body Green's function, with nonzero $h^{(2)}$. They verified that the solution of such an approximate would preserve the conservation laws, i.e. particle number, energy, and momentum, if the approximated two-body Green's function obeys some symmetry conditions, namely

$$G^{\text{approx}}_{\alpha'\gamma';\gamma\alpha}(t, t_1; t_1^+, t') = G^{\text{approx}}_{\gamma'\alpha';\alpha\gamma}(t_1, t; t', t_1^+). \quad (2.74)$$

This is the approximation which is embedded in the self-energy defined in Eq. (2.73). Later, Baym [6] showed that this self-consistent approximation for self-energy is generated by a closed functional by

$$\Sigma = \frac{\delta \Phi}{\delta G^{(1)}}, \quad (2.75)$$

where $\frac{\delta}{\delta G^{(1)}}$ is the functional derivative with respect to the one-body Green's function $G^{(1)}$. This approximation is often called as $\Phi$-derivable approximation. $\Phi$ is the Luttinger-Ward functional [94], whose exact form is typically unknown. In general, one can either obtain the approximate functional in a perturbative [94], shown in Fig. 2.3, or nonperturbative manner [120].

We refrain from further discussion on the construction and verification of the self-energy of the Kadanoff-Baym equation. Instead, we substitute Eq. (2.73) back in Eq. (2.71),

$$\sum_{\gamma} \Big( -\frac{\partial}{\partial_t} \delta_{\kappa,\gamma} - \langle \kappa | h^{(1)}(t) | \gamma \rangle \Big) G_{\gamma,\varsigma}(t, t') = \int_{\mathcal{C}} \mathrm{d}t_1 \Sigma_{\alpha',\gamma}(t, t_1) G_{\gamma',\varsigma}(t_1, t'). \quad (2.76)$$

This equation, with its boundary conditions (2.26, 2.27), is known as the Dyson equation [27].

Figure 2.3: The expansion of the Luttinger-Ward functional up to the two interaction vertices $h^{(2)}$. Solid lines are one-body Green's functions, and wiggly lines are $h^{(2)}$. In principle, one can consider such a functional for a two species system, for instance an interacting fermions and bosons. In that case, the interpretation of the wiggly (solid) lines is a one-body bosonic(fermionic) Green's function.

### 2.4.1 Nonequilibrium Dyson equation

In an abstract way, after dropping the Greek indices of Eq. (2.76), the Dyson equation for an interacting system can be rewritten as

$$G = G_0 + G_0 * \Sigma * G, \tag{2.77}$$
$$= G_0 + G * \Sigma * G_0, \tag{2.78}$$

where $G_0$ is the noninteracting Green's function, $\Sigma$ is the self-energy of the system, and $A*B$ denotes the convolution contour integral. Since $h^{(1)}$ conveys the one-body Hamiltonian, which is usually easy to work with, we would refer to that as a noninteracting Hamiltonian of $H_0(t) = h^{(1)}$. The corresponding noninteracting Green's function satisfies

$$[i\partial_t - h^{(1)}(t)]G_0(t,t') = \delta_{\mathcal{C}}(t,t'), \tag{2.79}$$
$$G_0(t,t')[-i\partial_{t'} - h^{(1)}(t)] = \delta_{\mathcal{C}}(t,t'). \tag{2.80}$$

Here, we obtained Eq. (2.80) by applying the integration by part, in which the right acting $\partial_t$ replace by the left acting $\partial_{t'}$. Solving Eq. (2.79), or equivalently Eq. (2.80), with the boundary conditions, introduced in Eqs. (2.26, 2.26), will give us

$$G_0(t,t') = -i\big[\Theta(t,t') \pm f_{\pm}(h^{(1)}(0))\big]e^{-i\int_{t'}^{t} h^{(1)}(t_1)\mathrm{d}t_1}, \tag{2.81}$$

where plus (minus) sign is considered for fermion (boson), and respectively, $f_{+/-}$ is the Bose-Einstein/Fermi-Dirac distribution function. Eq. (2.79) conveys that $G_0^{-1}$ has a differential form as

$$G_0^{-1}(t,t') = [i\partial_t - h^{(1)}(t)]\delta_{\mathcal{C}}(t,t'). \tag{2.82}$$

Moreover, rearranging Eq. (2.77) will give us

$$G^{-1} = G_0^{-1} - \Sigma. \tag{2.83}$$

Applying an interacting Green's function from the right-hand side of Eq. (2.83) and taking the convolution integral from both sides will present the integral-differential equation of

$$[i\partial_t - h^{(1)}(t)]G(t,t') - \int_{\mathcal{C}} \mathrm{d}t_1 \Sigma(t,t_1)G(t_1,t') = \delta_{\mathcal{C}}(t,t'), \tag{2.84}$$

$$G(t,t')[-i\partial_{t'} - h^{(1)}(t)] - \int_{\mathcal{C}} \mathrm{d}t_1 G(t,t_1)\Sigma(t_1,t') = \delta_{\mathcal{C}}(t,t'), \tag{2.85}$$

where we have substituted $G_0^{-1}$ by Eq. (2.82).

Since the Green's function comprises different components, we can express the general Dyson equation in Eq. (2.84) for each of these components individually as

$$[-\partial_\tau - h^{(1)}(0^-)]G^{\mathrm{mat}}(\tau) - \int_0^\beta \mathrm{d}\tau_1 \Sigma^{\mathrm{mat}}(\tau-\tau_1)G^{\mathrm{mat}}(\tau_1) = \delta(\tau), \tag{2.86}$$

$$[i\partial_t - h^{(1)}(t)]G^{\mathrm{ret}}(t,t') - \int_{t'}^t \mathrm{d}t_1 \Sigma^{\mathrm{ret}}(t,t_1)G^{\mathrm{ret}}(t_1,t') = \delta(t-t'), \tag{2.87}$$

$$[i\partial_t - h^{(1)}(t)]G^{\mathrm{tv}}(t,\tau) - \int_0^t \mathrm{d}t_1 \Sigma^{\mathrm{ret}}(t,t_1)G^{\mathrm{tv}}(t_1,\tau) = \int_0^\beta \mathrm{d}\tau_1 \Sigma^{\mathrm{tv}}(t,\tau_1)G^{\mathrm{mat}}(\tau_1,\tau), \tag{2.88}$$

$$\begin{aligned}[i\partial_t - h^{(1)}(t)]G^{<}(t,t') - \int_0^t \mathrm{d}t_1 \Sigma^{\mathrm{ret}}(t,t_1)G^{<}(t_1,t') = \int_0^{t'} \mathrm{d}t_1 \Sigma^{<}(t,t_1)G^{\mathrm{adv}}(t_1,t') \\ - i\int_0^\beta \mathrm{d}\tau \Sigma^{\mathrm{tv}}(t,\tau_1)G^{\mathrm{vt}}(\tau_1,t').\end{aligned} \tag{2.89}$$

These integral-differential equations are of a general type known as Volterra equations of the second kind

$$\frac{d}{ds}y(s) = q(s) + p(s)y(s) + \int_0^s \mathrm{d}s_1 k(s,s_1)y(s_1), \tag{2.90}$$

where $k$ is the kernel function.

It is worthwhile noting that Eq. (2.77) can be rewritten as

$$[1+F] * G = Q, \tag{2.91}$$

where $F = G_0 * \Sigma$, $Q = G_0$ and the equation is known as the Volterra equation of the first type

$$y(s) + \int_0^s \mathrm{d}s_1 k(s,s_1)y(s_1) = q(s). \tag{2.92}$$

We are frequently encountering this type of equation in bosonic systems, where we have an analytical expression for $G_0$.

The explicit form of Eq. (2.91) for retarded, lesser, left-mixing, and Matsubara would be

$$G^{\mathrm{mat}}(\tau) + \int_0^\beta \mathrm{d}\tau_1 F^{\mathrm{mat}}(\tau - \tau_1) G^{\mathrm{mat}}(\tau_1) = Q^{\mathrm{mat}}(\tau), \tag{2.93}$$

$$G^{\mathrm{tv}}(t,\tau) + \int_0^t \mathrm{d}t_1 F^{\mathrm{ret}}(t,t_1) G^{\mathrm{tv}}(t_1,\tau) = -\int_0^\beta \mathrm{d}\tau_1 F^{\mathrm{tv}}(t,\tau_1) G^{\mathrm{mat}}(\tau_1,\tau) + Q^{\mathrm{tv}}(t,\tau), \tag{2.94}$$

$$G^{\mathrm{ret}}(t,t') + \int_{t'}^t \mathrm{d}t_1 F^{\mathrm{ret}}(t,t_1) G^{\mathrm{ret}}(t_1,t') = Q^{\mathrm{ret}}(t,t') \tag{2.95}$$

$$G^{<}(t,t') + \int_0^t \mathrm{d}t_1 F^{\mathrm{ret}}(t,t_1) G^{<}(t_1,t') = -\int_0^{t'} \mathrm{d}t_1 F^{<}(t,t_1) G^{\mathrm{adv}}(t_1,t') + i\int_0^\beta \mathrm{d}\tau F^{\mathrm{tv}}(t,\tau_1) G^{\mathrm{vt}}(\tau_1,t') + Q^{<}(t,t'). \tag{2.96}$$

In practice, we employ some approximations, i.e. within the dynamical mean filed theory described in the following chapters, to obtain self-energies, and then solve the above mentioned Dyson equations numerically.

# Chapter 3

# Nonequilibrium dynamical mean-field theory

In the preceding chapter, we have briefly reviewed the Keldysh formalism. We have explained how the initial thermal correlation can be included in the temporal evolution using a L-shaped contour. We have also introduced a two-time Green's function and the Kadanoff-Baym equations. We have truncated the hierarchy of equations, where the evolution of a n-body Green's function depends on $(n \pm 1)$-body Green's functions, to the Dyson equation at the cost of introducing a self-energy. Computing the two-time Green's function for a many-body interacting system, with spin, momentum, and orbital degrees of freedom, is indeed a challenge. In this chapter, we will put our effort on introducing an approximation, known as the dynamical mean-field theory (DMFT), which provides a practical strategy for overcoming this challenge.

DMFT is established based on mapping the lattice model onto the one-site impurity problem embedded in a self-consistent bath. In this approach, many lattice degrees of freedom will be reduced to a time-dependent local degrees of freedom, considered on the impurity site, and nonlocal contributions associated with the bath and its hybridization with the impurity site.

In the following, we will review the DMFT formalism and its nonequilibrium generalization within the Keldysh formalism. More detailed reviews on the DMFT can be found in Refs. [4, 51, 123]. We will evade any model-based statement to keep this chapter as general as possible. In the forthcoming chapters, we will explain the DMFT self-consistency loop for particular model systems.

## 3.1 Dynamical mean-field theory

Dynamical mean-field theory [4, 51] is one of the practical methods for investigating many-body systems. The strategy is to map the many-body lattice problem onto a coupled impurity-bath problem. The bath is determined self-consistently and, usually, has a continuous excitation spectrum. This method is also known as the generalization of the Weiss mean-field theory (MFT) [148]. While the latter suppresses the temporal and spatial fluctuations, by employing a static Weiss field, DMFT overcomes some of MFT shortcomings by introducing a time-dependent Weiss field, and thereby only neglects the spatial fluctuations. The method is appliable when the inclusion of the spatial fluctuations is not crucial. The DMFT scheme will become accurate in lattices with large coordination number or with high dimesions [103]. In these cases, let's say on hyper-cubic lattice, it has been shown that by scaling the hopping amplitude ($J_{ij}$), the hopping matrix element from site $i$ to $j$, as

$$J_{ij} \equiv \frac{J^*_{ij}}{\sqrt{d}}, \tag{3.1}$$

where $J^*$ is a fixed constant, one can bring the density of state, defined as

$$D(\epsilon) = \frac{1}{2J\sqrt{\pi d}} \exp\Big(-\frac{\epsilon^2}{4J^2 d}\Big), \tag{3.2}$$

to a finite Gaussian form and thereby obtain a finite kinetic energy [103]. It is worthwhile noting that without rescaling, the kinetic term would be the dominant term of the Hamiltonian and the system would exhibit trivial physics. However, for the rescaled Hamiltonian, one would attain a many-body interacting system with a finite total energy, with no spatial fluctuation. In addition, investigations, conducted by Müller-Hartmann, revealed that the dynamics in $d = \infty$ can be described only by local self-energies [106, 105]. This is indicating that the perturbation expansions of Feynman diagrams can be simplified to only local contributions in higher dimensions. One should note that employing local self-energies do not convey that we map our systems to an effective local model [9], since not only diagrams of Fig. 3.1 b), but also Fig. 3.1 c) are present in the DMFT approach. (One should note that the Fig. 3.1 b) is the local approximation of Fig. 3.1 a).)

In the following, we will elaborate the DMFT set of equations using the two-time Green's function formalism. The notation is applicable in and out of equilibrium, but implication of each situation will be explained when it is needed. We consider a generic Hamiltonian of the type

$$H = H^{\mathrm{1b}}_{\mathrm{loc}} + H^{\mathrm{1b}}_{\mathrm{kin}} + H^{\mathrm{2b}}_{\mathrm{loc}}, \tag{3.3}$$

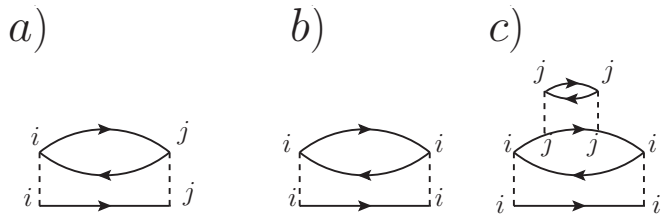


Figure 3.1: Second order perturbation diagram for the Hubbard model [9]. a) The nonlocal self-energy diagram. b) Local self-energy diagram in $d = \infty$, and c) higher order diagram including various lattice site.

where $H^{1b}_{loc}$ contains one-body local contributions, $H^{1b}_{kin}$ describes the hopping term, and $H^{2b}_{loc}$ includes the local two-body interaction. In this thesis, We depict models which do not break the translational and spin symmetry, and thereby, in this chapter, we only present the DMFT scheme that keeps these symmetries unbroken. Generally speaking, for a two-body Hamiltonian, one would also expect the nonlocal two-body interaction which we omit for the simplicity of this discussion. The DMFT strategy starts from mapping the Hamiltonian onto an Anderson impurity model (AIH) consisting of three parts: the impurity, the bath-impurity, and the bath terms.

$$H^{\mathrm{AIM}} = \underbrace{\left[H^{1b}_{loc} + H^{2b}_{loc}\right]_{imp}}_{H^{\mathrm{AIM}}_{imp}} + \underbrace{\left[H^{1b}_{kin}\right]_{imp-bath}}_{H^{\mathrm{AIM}}_{imp-bath}} + \underbrace{\left[H^{1b}_{kin} + H^{1b}_{loc}\right]_{bath}}_{H^{\mathrm{AIM}}_{bath}}. \tag{3.4}$$

Here, $H^{\mathrm{AIM}}_{imp-bath}$ denotes the hopping from the impurity site to the bath, and $\left[H^{1b}_{kin}\right]_{bath}$ governs the kinetic physics inside the bath. Within DMFT the local many-body terms, like $H^{2b}_{loc}$, will only be treated on the impurity site. The evolution of the lattice Green's function under the Hamiltonian of Eq. (3.4) is then captured by solving a Dyson equation, introduced in Eq. (2.84),

$$[i\partial_t - h^{(1)}_k(t)]G_k(t,t') - \int_{\mathcal{C}} \mathrm{d}t_1 \Sigma(t,t_1)G_k(t_1,t') = \delta_{\mathcal{C}}(t,t'), \tag{3.5}$$

where $G_k$ and $h^{(1)}_k$ are reciprocal representation of a nonlocal Green's function ($G_{ij}$) and $H^{\mathrm{AIM}}_{bath}$ at momentum $k$. DMFT considers a local time-dependent self-energy on the lattice and sets that equal to the impurity self-energy [51]. As we mentioned earlier, this statement is exact in infinite dimension but would act as an approximation in finite dimensions. It is crucial to understand that assigning the impurity self-energy to the bath counterpart is a

non-perturbative scheme and thereby, independent of the involved approximations of the the impurity self-energy, DMFT treats the many-body system non-perturbatively [120]. Evaluating the impurity Green's function will be done by first integrating out the bath contribution of the Hamiltonian, which we will explicitly explain in Sec. 3.1.1, resulting in the determination of a two-time hybridization function ($\Delta$). The hybridization function carries the lattice information, and subsequently, the impurity site will also be aware of the density of state. Having this hybridization function, the impurity Green's function satisfies

$$[i\partial_t - H^{\mathrm{1b}}_{\mathrm{loc}}(t)]G_{\mathrm{imp}}(t,t') - \int_{\mathcal{C}} \mathrm{d}t_1 \Big[\Sigma(t,t_1) + \Delta(t,t_1)\Big] G_{\mathrm{imp}}(t_1,t') = \delta_{\mathcal{C}}(t,t'). \tag{3.6}$$

The $H^{\mathrm{2b}}_{\mathrm{loc}}$ is hidden in the self-energy ($\Sigma$) in Eq. (3.6). It is now clear that for having a self-consistent DMFT loop, we should propose a method to evaluate hybridization function and the self-energy. Since determining the self-energy requires more details regarding the involved interactions, we will explain our approaches for tackling Holstein, Hubbard, and Hubbard-Holstein models in Chaps. 4, 5, 6. The only missing part is the hybridization function which we will explain in the following.

### 3.1.1 Evaluation of the hybridization function

In this section we will derive the hybridization function of two class of lattices, namely Bravais and Bethe lattices.

#### Hybridization function of the Bethe lattice

In the previous section, we presented the impurity-bath Hamiltonian by $\Big[H^{\mathrm{1b}}_{\mathrm{kin}}\Big]_{\mathrm{imp-bath}}$. In a more explicit representation, this Hamiltonian can be expressed as

$$\Big[H^{\mathrm{1b}}_{\mathrm{kin}}\Big]_{\mathrm{imp-bath}} = \overbrace{\sum_{ij} |i\rangle t_{ij} \langle j|}^{h_{\mathrm{hop}}} + \overbrace{\sum_{i} |i\rangle \epsilon_i \langle i|}^{h_{\mathrm{loc}}}, \tag{3.7}$$

$$= \sum_{\alpha} |\alpha\rangle E_\alpha \langle \alpha|. \tag{3.8}$$

Here, we consider a kinetic term with the matrix element of $t_{ij}$ and an on-site energy contribution with the energy $\epsilon_i$, which are represented in the span space of the lattice basis, where $i$ and $j$ are site indices (See also Fig. 3.2). (For simplicity we omit other indices

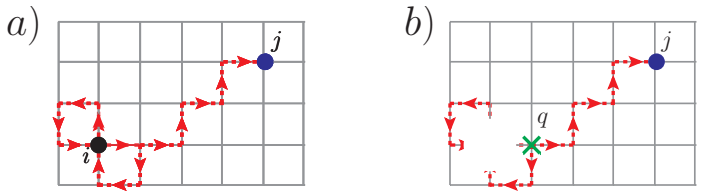


Figure 3.2: a) illustration of a typical path from site $i$ to $j$. b) By removing the site $i$, the connected path shortened to the path from site $q$ to $j$.

such as spin and orbital ones.) $E_\alpha$ is the eigenvalue of the diagonalized Hamiltonian, which corresponds to the eigenstate of $|\alpha\rangle$. It is worthwhile noting that, for simplicity, we have refrained including higher orders in the Hamiltonian, but to present a complete argument, we will make comments on the induced changes on the following argument on deriving the hybridization function.

The Green's function of such Hamiltonian is defined as

$$G_{ij} = \langle i| \frac{1}{z - (h_{\rm hop} + h_{\rm loc})} |j\rangle = \sum_\alpha \frac{\langle i|\alpha\rangle\langle\alpha|j\rangle}{z - E_\alpha}. \tag{3.9}$$

Inserting an identity operator in $G_{ij}$ would lead to

$$G_{ij} = \sum_l \langle i| \frac{1}{z - h_{\rm loc}} |i\rangle\langle i|h_{\rm hop}|l\rangle\langle l| \frac{1}{z - (h_{\rm hop} + h_{\rm loc})} |j\rangle, \tag{3.10}$$

$$= \langle i| \frac{1}{z - h_{\rm loc}} + \frac{1}{z - h_{\rm loc}} h_{\rm hop} \frac{1}{z - h_{\rm loc}} + \frac{1}{z - h_{\rm loc}} h_{\rm hop} \frac{1}{z - h_{\rm loc}} h_{\rm hop} \frac{1}{z - h_{\rm loc}} + \ldots |j\rangle. \tag{3.11}$$

(If the Hamiltonian consists of local higher terms, e.g. $h^{\rm hp}_{\rm loc} = h_{\rm loc} + h^{np}_{\rm loc}$, one should also separate the quadratic terms ($h_{\rm loc}$) from the other terms ($h^{np}_{\rm loc}$), and follow a similar approach as in Eq. (3.10).)

After defining the free Green's function as

$$g_{ii} = \langle i| \frac{1}{z - h_{\rm loc}} |i\rangle, \tag{3.12}$$

and substituting it in Eq. (3.11), we will get

$$G_{ij} = \delta_{ij} g_{ii} + g_{ii} t_{ij} g_{jj} + \sum_l g_{ii} t_{il} g_{ll} t_{lj} g_{jj} + \sum_{kl} g_{ii} t_{il} g_{ll} t_{lk} g_{kk} t_{kj} g_{jj} + \ldots. \tag{3.13}$$

where $\delta_{ij}$ is the Kronecker delta function. The sequence of indices represent a hopping path from site $i$ to $j$. Since these dummy indices, for instance $l$ and $k$, can also be the same as $i$, there are multiple crossing of site $i$ on the path from $i$ to $j$, as shown in Fig. 3.2. (For higher order Hamiltonians, Eq. (3.13) will not only consist of two-point Green's functions, but also will embed higher-point Green's functions.) One thus can rewrite the above equation as

$$G_{ij} = \delta_{ij} g_{ii} + \underbrace{\Big( \sum_{k_1 \ldots k_n} g_{ii} t_{ik_1} g_{k_1 k_1} \ldots t_{k_n i} g_{ii} \Big)}_{G_{ii}} \times \sum_{q \neq i} t_{iq} \underbrace{\Big( \sum_{q_2 \ldots q_n \neq i} g_{qq} t_{q_2 q_3} \ldots g_{q_n q_n} \Big)}_{G^{[i]}_{q_1 q_n}} t_{q_n j} g_{jj}, \tag{3.14}$$

where $G^{[i]}_{qq_n}$ is the Green's function from site $q$ to $q_n$, when site $i$ is removed. We illustrate this type of decomposition in Fig. 3.2, where in a) one of the possible paths from site $i$ to $j$ is drawn , and in b) the site $i$ is removed and the connected path, which terminated at $j$, starts at site $q$.

Applying similar site-removing approach on $G^{[i]}_{q_1 q_n}$, we would obtain

$$G_{ij} = \delta_{ij} g_{ii} + G_{ii} \sum_{q} t_{iq} \sum_{q_2 \ldots q_n} G^{[i]}_{q,q} t_{qq_2} G^{[i,q]}_{q_2 q_2} t_{q_2 q_3} G^{[i,q,q_2]}_{q_3 q_3} \ldots t_{q_n j} g_{jj}. \tag{3.15}$$

Comparing the above equation with conventional lattice Dyson equation of the form

$$G_{ii} = g_{ii} + G_{ii} \Delta g_{ii}, \tag{3.16}$$

will suggest that the hybridization function ($\Delta$) satisfies

$$G_{ii} \Delta g_{ii} = G_{ii} \sum_{q} t_{iq} \sum_{q_2 \ldots q_n} G^{[i]}_{q,q} t_{qq_2} G^{[i,q]}_{q_2 q_2} t_{q_2 q_3} G^{[i,q,q_2]}_{q_3 q_3} \ldots t_{q_n i} g_{ii}. \tag{3.17}$$

Hence, we would obtain a relation for the hybridization function, which is

$$\Delta = \sum_{q q_2} t_{iq} \underbrace{\sum_{q_3 \ldots q_n} G^{[i]}_{q,q} t_{qq_2} G^{[i,q]}_{q_2 q_2} t_{q_2 q_3} G^{[i,q,q_2]}_{q_3 q_3} \ldots G^{[i,q,q_2]}_{q_n q_n}}_{G^{[i]}_{q,q_n}} t_{q_n i}. \tag{3.18}$$

(As we mentioned before, incorporating higher orders in the Hamiltonian includes higher-point Green's functions, which make the above relation even more complicated. In that case, one should note that for a system with the lattice dimension of $d$, the hopping amplitude ($t_{ij}$) and the Green's function ($G^{[o]}_{ij}$) will be scaled by $(1/\sqrt{d})^{|i-j|}$, see Eq. (3.1).

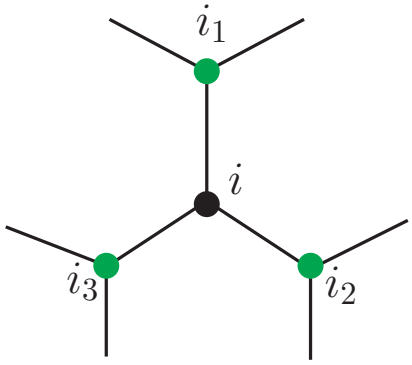


Figure 3.3: The Bethe lattice with coordination number of $Z = 3$.

The scaling order of this term in Eq. (3.18) would be 1, as summing over $i, j$ is of order $d^2$, and $t_{iq}, t_{q_n i}$, and $G_{qq_n}$ has the order of $1/d^2$. For a 2-body Green's function ($G^{[0]}_{ijkl}$), this scaling factor will be of order $(1/\sqrt{d})^{|i-j|}(1/\sqrt{d})^{|i-k|}(1/\sqrt{d})^{|i-l|}$, where $|i-j|, |i-k|, |i-l|$ are at least 2 [51]. As a result, the term which consists of this 4-point Green's function has the order of $1/d^2$, due to the four sums over $i, j, k, l$ and four hopping terms of $t_{ij}, t_{ik}, t_{il}, t_{kl}$. If $i = j$, this total scaling of the term with the 4-point correlation function would become of order $1/d$. Hence, one can notice that if $d \to \infty$, the leading contribution of the hybridization function would be constructed from the two-point correlation function.)

In general, these renormalized path argument is difficult to perform for generic lattices, we will address this issue in Sec. 3.1.1. But, on Bethe lattice, as a result of no loop in this tree-like lattice, Eq. (3.15) can be of help. For clarity purpose, we first consider a tree-like lattice where each site is connected to three neighboring sites ($Z = 3$), as shown in Fig. 3.3.

On this lattice, there is only and only one path connecting site $i$ to $j$ and thereby Eq. (3.15) will be simplified to

$$G_{ii} = g_{ii} + 3G_{ii}tG^{[i]}_{i_i i_1}tg_{ii}, \tag{3.19}$$

where we take the advantage of self-similarity of $i$'s neighboring sites by multiplying the factor of 3 to one of the neighbor's contribution, instead of having the summation over various neighbors. We also take the hopping matrix as a constant value ($t$), and consider the site $i$ as the core of the lattice (See also Fig. 3.3). $G^{[i]}_{i_i i_1}$ describes a lattice where its core is removed. This Green's function also satisfies

$$G^{[i]}_{i_1 i_1} = g_{i_1} + 2G^{[i]}_{i_1 i_1}tG^{[i,i_1]}_{j_1 j_1}tg_{i_1}, \tag{3.20}$$

where the factor of 2 counts the number of $j$-neighbors near site $i_1$ where $i$ is taken out of the lattice.

In the limit of infinite coordination number ($Z \to \infty$), Eqs. (3.19, 3.20) will get the form of

$$G_{ii} = g_{ii} + ZG_{ii}\frac{t^*}{\sqrt{Z}}G^{[i]}_{ii}\frac{t^*}{\sqrt{Z}}g_{ii}, \tag{3.21}$$

$$G^{[i]}_{i_1 i_1} = g_{i_1} + (Z-1)G^{[i]}_{i_1 i_1}\frac{t^*}{\sqrt{Z}}G^{[i,i_1]}_{j_1 j_1}\frac{t^*}{\sqrt{Z}}g_{i_1}, \tag{3.22}$$

where we insert the rescaled hopping as introduced in Eq. (3.1). Since the limit of $[(Z-1)/Z]$ for large $Z$ goes to one, and the lattice is a self-similar one, we can conclude that

$$G^{[i]}_{ii} = G_{ii}, \tag{3.23}$$

and Hence,

$$G_{ii} = g_{ii} + G_{ii}t^*G_{ii}t^*g_{ii}. \tag{3.24}$$

Comparing Eq. (3.16) and Eq. (3.24), will finally offer a closed form of the hybridization function as

$$\Delta = t^*Gt^*. \tag{3.25}$$

### Hybdridization function of a Bravais lattice

Despite the conveyed intuition, the above mentioned results are almost impractical in numerical simulations where the numerical calculations are intended to be done on various lattice structures. We thereby should address the problem in another way. Pursuing this goal, instead of working with the impurity-bath term, we now employ the impurity and bath terms of the Hamiltonian. A generic form of $H^{\text{AIM}}_{\text{bath}}$ and $H^{\text{AIM}}_{\text{imp}}$ are

$$H^{\text{AIM}}_{\text{bath}}(t) = \sum_k (\epsilon_k(t) - \mu(t))n_k(t), \tag{3.26}$$

$$H^{\text{AIM}}_{\text{imp}}(t) = -\mu(t)n(t), \tag{3.27}$$

where $n$ is the particle density, $\mu$ is the chemical potential, and $\epsilon_k$ is the momentum-dependent particle's dispersion relation. For these Hamiltonians, the lattice and impurity Green's function can be captured after solving

$$G_k = g + g * (\epsilon_k + \Sigma) * G_k, \tag{3.28}$$

$$G_{\text{imp}} = g + g * (\Delta + \Sigma) * G_{\text{imp}}, \tag{3.29}$$

respectively, where the noninteracting Green's function is defined as

$$g^{-1}(t,t') = (\partial_t + \mu)\delta_{\mathcal{C}}(t,t'), \tag{3.30}$$

and all Green's functions are two-time Keldysh Green's functions. It is also known that the momentum-sum of the momentum-resolved lattice Green's function is the local Green's function which would be set to the impurity Green's function within the DMFT,

$$G_{\text{loc}} = \sum_k G_k = G_{\text{imp}}. \tag{3.31}$$

With the goal of achieving an equation of motion for the hybridization function, we will now try to establish a connection among $G_k$, $\epsilon_k$, and $\Delta$. We first rewrite Eq. (3.28) and its conjugate as

$$\begin{cases} \mathcal{Z}^{-1} * G_k &= 1 + \epsilon_k * G_k, \\ G_k * \mathcal{Z}^{-1} &= 1 + G_k * \epsilon_k, \end{cases} \tag{3.32}$$

where $\mathcal{Z}^{-1} = g^{-1} - \Sigma$. Multiplying above equations by $\epsilon_k$ from right and left, respectively for upper and lower equalities, has the result of

$$\begin{cases} \mathcal{Z}^{-1} * G_k * \epsilon_k = \epsilon_k + \epsilon_k * G_k * \epsilon_k, \\ \epsilon_k * G_k * \mathcal{Z}^{-1} = \epsilon_k + \epsilon_k * G_k * \epsilon_k. \end{cases} \tag{3.33}$$

On the other hand, Eq. (3.29) and its conjugate after multiplication by $\Delta$ will become

$$\begin{cases} \mathcal{Z}^{-1} * G = 1 + \Delta * G, \\ G_{\text{imp}} * \mathcal{Z}^{-1} = 1 + G_{\text{imp}} * \Delta \end{cases} \Longrightarrow \begin{cases} \mathcal{Z}^{-1} * G * \Delta = \Delta + \Delta * G_{\text{imp}} * \Delta, \\ \Delta * G_{\text{imp}} * \mathcal{Z}^{-1} = \Delta + \Delta * G_{\text{imp}} * \Delta. \end{cases} \tag{3.34}$$

Keeping momentum-sum of the lattice Green's function, as in Eq. (3.31), averaging over momentum indices in Eq. (3.28), and substituting the above equality in that will suggest

$$G_{\text{imp}} = \mathcal{Z} + \sum_k \mathcal{Z} * \epsilon_k * G_k. \tag{3.35}$$

By comparing Eq. (3.35) by Eq. (3.29), we would get

$$\Delta * G_{\text{imp}} = \sum_k \epsilon_k * G_k. \tag{3.36}$$

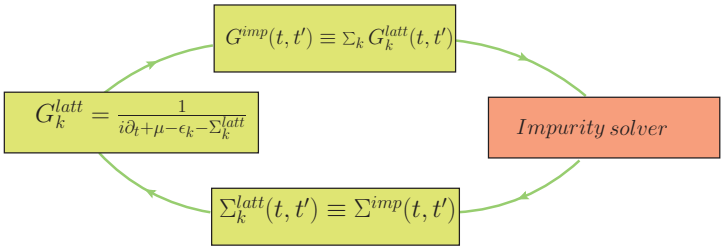


Figure 3.4: The self-consistency loop of the DMFT.

Despite the simple form of the above equation, it is numerically unstable [4], and we thereby should put our effort on bringing this equation to a numerically more stable form. To achieve this aim, we multiply Eq. (3.36) and its conjugate to $\mathcal{Z}^{-1}$ from right and left, respectively, which has the result of

$$\begin{cases} \sum_k \mathcal{Z}^{-1} * G_k * \epsilon_k = \mathcal{Z}^{-1} * G * \Delta, \\ \sum_k \epsilon_k * G_k * \mathcal{Z}^{-1} = \Delta * G * \mathcal{Z}^{-1}. \end{cases} \tag{3.37}$$

Subsequently, after substituting the equivalence of each side, using Eqs. (3.33, 3.34), we will obtain

$$\Delta + \Delta * G * \Delta = \sum_k \epsilon_k + \epsilon_k * G_k * \epsilon_k. \tag{3.38}$$

At last, we will find the hybridization function of any interacting system by solving

$$(1 + \sum_k \epsilon_k * G_k) * \Delta = \sum_k \epsilon_k + \epsilon_k * G_k * \epsilon_k, \tag{3.39}$$

where we have exploited Eq. (3.36) for obtaining the left-hand side of the above equation [30].

### 3.1.2 DMFT self-consistency loop

In previous sections, we derived key equations for the DMFT self-consistency scheme. Here, we will summarize the DMFT loop, see also Fig. 3.4, as the following:

1. We start by a guess for the hybridization function based on the lattice density of state.

2. We will employ an impurity solver and solve the impurity problem to obtain a self-energy and an impurity Green's function. We will elaborately explain this model-dependent part in next chapters.

3. DMFT approximation imposes that the lattice self-energy is the same as the impurity self-energy.

4. Using the obtained self-energy, we will then solve Eq. (3.28) to have the lattice Green's function.

5. DMFT self-consistency is then requires that the momentum-sum of the lattice Green's function be the same as the impurity Green's function.

6. On the Bethe lattice, the hybridization function is then updated by Eq. (3.25), where $G$ is the impurity Green's function. On a Bravais lattice, the hybridization function is acquired after solving Eq. (3.39).

7. The iteration will be continued by going to the second step.

# Chapter 4

# Nonequilibrium DMFT study of the Holstein Model

Understanding of electron-lattice interactions has been the subject of intense works for many years, which range from ab-initio techniques [60, 54] to model-based investigations [2]. The proposed models vary in their level of approximation, or whether ions are treated classically or quantum mechanically. As the most puzzling piece of these treatments is where quantum mechanics sets in the quantization of the ion spectrum is inevitable. This quantization is obtained after approximating the effective ionic potential as a harmonic oscillator associated with quanta known as *phonons*.

In the momentum space, the phonon dispersion is either gapped or gapless. Gapless vibrational modes expose linear dispersion relation for small momenta, designated as *acoustic* phonons, where the name is chosen due to the same low-energy energy-momentum relation in acoustic waves. One the other hand, the gapped modes with a dispersion-less spectrum are named *optical* phonons.

As electron densities are interacting with displacements of ions, one can expand the electron-ion interactions in powers of phonon displacement. With this respect, the most vigorously employed models are related to a linear coupling between the carriers density and the lattice deformation. This type of models, in the absence of electron-electron interaction, is known as the Frölich model [44, 45] for acoustic phonons, and is called as the Holstein model [65, 67] for optical phonons. It has been shown that such models describe particles which are dressed by lattice deformations. When the coupling between electrons and vibrational modes of lattice is very strong, the dressed particle will be self-trapped. Such a self-trapping introduces a composite particle, known as a *polaron*.

To elaborately describe this rich physics, we devote this chapter on understanding the Holstein model for a low density of carriers. We will employ the nonequilibrium DMFT formalism with an analytical impurity solver, which will be developed in the upcoming sections. This will provide an understanding of the dynamical formation of a polaron in various regimes of the model.

## 4.1 Model Hamiltonian

One of the simplest electron-phonon model Hamiltonians assumes a linear interaction between the lattice displacement and the density of electrons. This model, when the electron-electron interaction is neglected, is the intensely studied Holstein model [65, 67]. We will study this model at low carrier doping. This regime is accessible, e.g., in a pump-probe experiment on a two-layer system, where a surface-like layer is grown on top a thick substrate. By irradiation of the pump-pulse, few electrons from the substrate will be excited to the surface layer. In the surface-state, they will start to interact with the vibrational modes of the surface ions [46, 49, 50, 1]. The relaxation process of the electronic density depends very much on its initial energy, and available decay channels determined by surface ions.

Here, we simulate such an experiment by employing a one-band Holstein model, with one electron which is time-dependently coupled to phonons. The Hamiltonian is given by

$$H_{\mathrm{Hol}} = \omega_0 \sum_i b_i^\dagger b_i - \mu \sum_i \sum_\sigma c_{i\sigma}^\dagger c_{i\sigma} - \sum_{\langle ij \rangle} \sum_\sigma \left( J_{ij} c_{i\sigma}^\dagger c_{j\sigma} + \mathrm{H.c.} \right) + g \sum_i c_i^\dagger c_i \left( b_i^\dagger + b_i \right), \quad (4.1)$$

where $c_{i\sigma}^\dagger (c_{i\sigma})$ is the creation (annihilation) operator at site $i$ with spin $\sigma$, $b_i^\dagger (b_i)$ creates (destroys) a phonon at site $i$, $J_{ij}$ is the electron hopping amplitude for jumping from site $i$ to nearest site $j$, $\omega_0$ is the frequency of optical phonons, $g$ is the coupling of the electron density to the displacement of phonons, and $\mu$ is the chemical potential of the system. Here we assume that hopping amplitude is only between nearest neighbors, and it is site-independent $J_{ij} = J$.

The Holstein model is characterized by two independent dimensionless parameters known as adiabatic ($\gamma$) and bare coupling ($\lambda$) constants, which are defined as

$$\lambda = \frac{g^2}{\omega_0 J}, \quad (4.2)$$

$$\gamma = \frac{\omega_0}{J}. \quad (4.3)$$

It is also illustrative to define an additional parameter which measures the strength of the lattice deformation as

$$\alpha = \frac{g}{\omega_0}, \qquad \alpha^2 = \frac{\lambda}{\gamma}. \tag{4.4}$$

Employing $(\alpha, \gamma, \lambda)$ enables us to characterize different regimes of the Holstein model as follows.

- The weak (strong) coupling regime is where $\lambda < 1$ ($\geq 1$).
- The (non-) adiabatic regime occurs when phonon vibrations are slower (faster) than the electron hopping amplitude $\gamma < 1$ ($\geq 1$).
- The multi-phonon regime prevails when $\alpha^2 > 1$.

In the weak coupling regime, the fermionic carriers will be dressed as a result of electron-phonon coupling. This effect will enhance the carrier effective inertial mass and weakly renormalize the spectral function. By increasing $\lambda$, the system will enter a regime where its spectrum is drastically renormalized and the mass of the electron is enlarged significantly. Within this regime, the formation of a so called small polaron, an entity consisting of an electron accompanied by a phonon cloud, will take place if $\gamma$ is small. In the atomic limit, the binding energy of the quasiparticle is $E_{\rm p} = g^2/\omega_0$, and the number of phonons in the cloud is $\langle b^\dagger b \rangle = \alpha^2$. The strong coupling limit is defined as the limit in which the polaron binding energy becomes comparable to the electron bandwidth [2].

In forthcoming sections, we will investigate various parameter regimes of the Holstein model, with particular focus on the formation of the small polaron, in the low density limit of carriers. More precisely, we will briefly explain the underlying physics of the system in the extreme strong-coupling and extreme adiabatic limits.

### 4.1.1 Extreme strong coupling limit

Strong interactions between the electron and its surrounding phonon cloud can trap the electron density and suppress its motion. The extreme case of this strong coupling regime is also known as the "atomic limit", where the lattice problem can be mapped onto an one-site problem. Within this mapping, the local el-ph coupling term in Eq. (4.1) will be removed by shifting the equilibrium positions of ions, equivalently, changing the phonon vacuum. This procedure is known as the Lang-Firsov(LF) transformation [86], which enables us to

decouple an interacting Hamiltonian into two normalized electronic and phononic contributions. In this section, we will study a general time-dependent LF transformation on the impurity site [150].

The atomic Hamiltonian, setting $J_{ij} = 0$ in Eq. (4.1), is given by

$$H_{\text{at}} = g(t)c^\dagger c(b^\dagger + b) + \omega_0 b^\dagger b, \tag{4.5}$$

where we consider the case of a time-dependent el-ph coupling. The transforming unitary operator ($W$) of LF transformation is defined as

$$W(t) = e^{i[PX_0 + XP_0]}, \tag{4.6}$$

where $P = \frac{i(b^\dagger - b)}{\sqrt{2}}$ is the momentum of the oscillator and $X = \frac{b^\dagger + b}{\sqrt{2}}$ is its position, satisfying the commutation relation of the form $[X, P] = i$. By performing the LF transformation, we would get

$$W^\dagger(t) X W(t) = X(t) - X_0(t), \tag{4.7}$$

$$W^\dagger(t) P W(t) = P(t) + P_0(t), \tag{4.8}$$

where $X_0$ ($P_0$) displaces the ions position (momentum). The purpose of introducing $X_0$ and $P_0$ is to remove the electron-phonon interacting term in the Hamiltonian of Eq. (4.5). At $t = 0$, this goal will be achieved by choosing

$$X_0(0) = \sqrt{2}\frac{g(0)}{\omega_0} c^\dagger c, \tag{4.9}$$

$$P_0(0) = 0. \tag{4.10}$$

To obtain $X_0(t)$ and $P_0(t)$ at $t > 0$, we should solve a coupled set of linear differential equations, derived using Heisenberg's equations, of the form

$$X_0'(t) = -\omega_0 P_0(t), \tag{4.11}$$

$$P_0'(t) = \omega_0 X_0(t) - \sqrt{2} g(t) c^\dagger c. \tag{4.12}$$

The solutions of Eqs. (4.11, 4.12) are

$$X_0(t) = \frac{f(0)}{\omega_0}\cos(\omega_0 t) + \int_0^t \mathrm{d}t_1 \sin[\omega_0(t - t_1)] f(t_1), \tag{4.13}$$

$$P_0(t) = \frac{f(0)}{\omega_0}\sin(\omega_0 t) - \int_0^t \mathrm{d}t_1 \cos[\omega_0(t - t_1)] f(t_1), \tag{4.14}$$

where $f(t) = \sqrt{2}g(t)c^\dagger c$.

Apart from displacements of phononic variables, electron operators will also be modified as

$$\widetilde{c}(t) = W^\dagger(t)cW(t) = e^{-i[PX_0(t)+XP_0(t)]}c(t)e^{i[PX_0(t)+XP_0(t)]}, \tag{4.15}$$

$$= e^{-[\gamma(t)b^\dagger - \gamma^*(t)b]}c(t), \tag{4.16}$$

$$\widetilde{c^\dagger}(t) = W^\dagger(t)c^\dagger(t)W(t) = c^\dagger(t)e^{[\gamma(t)b^\dagger - \gamma^*(t)b]}, \tag{4.17}$$

with

$$\gamma(t) = \frac{g(0)}{\omega_0}e^{-i\omega_0 t} + i\int_0^t \mathrm{d}t_1 e^{-i\omega_0(t-t_1)}g(t_1). \tag{4.18}$$

The transformed atomic Hamiltonian will then be written, substituting Eqs. (4.7, 4.8, 4.11) in Eq. (4.5), as

$$H_{\mathrm{LF}} = W^\dagger(t)H_{\mathrm{at}}W(t), \tag{4.19}$$

$$= \frac{\omega_0}{2}\big(X^2+P^2\big) + \frac{\omega_0}{2}\big(X_0^2+P_0^2\big) - \frac{1}{2}\big[X_0(\omega_0 X_0 - f) + \omega_0 P_0^2\big] - fX_0 - \mu c^\dagger c, \tag{4.20}$$

$$= \frac{\omega_0}{2}\big(X^2+P^2\big) - \frac{fX_0}{2} - \mu c^\dagger c, \tag{4.21}$$

$$= \frac{\omega_0}{2}\big(X^2+P^2\big) - c^\dagger c\big(\mu + \lambda(t)\big), \tag{4.22}$$

where

$$\lambda(t) = \frac{g(t)g(0)}{\omega_0}\cos(\omega_0 t) + g(t)\int_0^t \mathrm{d}t_1 \sin[\omega_0(t-t_1)]g(t_1). \tag{4.23}$$

Eq. (4.22) describes a shifted harmonic oscillator with a time-dependent polaron energy, see also Fig. 4.1 for a schematic picture. For the sudden quench of the coupling strength,

$$g(t) = \begin{cases} g_0 & \text{if } t \geq 0 \\ g_1 & \text{if } t < 0 \end{cases}, \tag{4.24}$$

$\lambda$ will be simplified to the form of

$$\lambda(t) = \frac{g_1^2}{\omega_0} + \frac{g_1(g_0-g_1)}{\omega_0}\cos(\omega_0 t). \tag{4.25}$$

In the following, we will use the LF transformation to explore the phonon distribution function and the electron Green's function in the atomic limit. These observables will be used later.

### Phonon distribution function

The quantity which carries some information about the phonon cloud of the polaron is the phonon distribution function, defined as $P(m) = |m\rangle\langle m|$, where $|m\rangle = \frac{1}{\sqrt{m}}(b^\dagger)^m|0\rangle$ is the $m$-phonon state. The expectation value of this correlation under the LF transformation at time $t$, with the help of the Baker-Hausdorff formula,

$$e^{-b^\dagger\gamma(t)+b\gamma^*(t)b} = e^{-b^\dagger\gamma(t)}e^{b\gamma^*(t)}e^{-\frac{|\gamma(t)|^2}{2}}, \tag{4.26}$$

will be

$$\begin{aligned} P(m,t) &= W^\dagger(t)P(m)W(t), && (4.27)\\ &= \frac{1}{\mathcal{Z}_{\rm ph}}\sum_{n=0}^{\infty} e^{-\beta n\omega_0}|\langle n|e^{\gamma^*(t)b-b^\dagger\gamma(t)}|m\rangle|^2, && (4.28)\\ &= \frac{1}{\mathcal{Z}_{\rm ph}}\sum_{n=0}^{\infty} e^{-\beta n\omega_0}e^{-|\gamma(t)|^2}|\langle n|e^{-\gamma(t)b^\dagger}e^{b\gamma^*(t)}|m\rangle|^2. && (4.29) \end{aligned}$$

Here, $\mathcal{Z}_{\rm ph}$ is the zero-electron partition function, given by

$$\mathcal{Z}_{\rm ph} = \sum_{p=0}^{\infty} e^{-\beta\omega_0} = \frac{1}{1-e^{-\beta\omega_0}}. \tag{4.30}$$

At zero temperature, $n = 0$ will be the only contributing state in the phonon distribution function, and thereby Eq. (4.29) will be simplified to

$$\begin{aligned} P_0(m,t) &= e^{-|\gamma(t)|^2}|\langle 0|e^{-b^\dagger\gamma(t)}e^{b\gamma^*(t)}|m\rangle|^2, && (4.31)\\ &= e^{-|\gamma(t)|^2}|\langle 0|e^{b\gamma^*(t)}|m\rangle|^2, && (4.32)\\ &= e^{-|\gamma(t)|^2}|\langle 0|\frac{[b\gamma^*(t)]^m}{m!}|m\rangle|^2 = e^{-|\gamma(t)|^2}|\gamma(t)|^{2m}|\langle 0|\frac{b^m}{m!}|m\rangle|^2, && (4.33)\\ &= e^{-|\gamma(t)|^2}\frac{|\gamma(t)|^{2m}}{m!}, && (4.34) \end{aligned}$$

which is a Poisson distribution with a time-dependent mean of $|\gamma(t)|^2$. For an excited state, let's say a $l$-phonon state, we would get

$$\begin{aligned} P_l(n+l,t) &= e^{-|\gamma(t)|^2}|\langle l|e^{-b^\dagger\gamma(t)}e^{b\gamma^*(t)}|n+l\rangle|^2, && (4.35)\\ &= e^{-|\gamma(t)|^2}|A_{l,n}(\gamma(t))|^2, && (4.36) \end{aligned}$$

Here, the auxiliary function of $A_{l,n}(\gamma(t))$, using Taylor expansions of exponentials, is given by

$$A_{l,n}(\gamma(t)) = \langle n+l|e^{-b^\dagger\gamma(t)}e^{b\gamma^*(t)}|l\rangle, \tag{4.37}$$

$$= \sum_{r=0}^{l} \frac{[\gamma^*(t)]^r[-\gamma(t)]^{l+r}}{r!(l+r)!}\langle n+l|(b^\dagger)^{n+r}b^r|l\rangle, \tag{4.38}$$

$$= \sum_{r=0}^{l} \frac{[\gamma^*(t)]^r[-\gamma(t)]^{l+r}}{r!(l+r)!}\frac{\sqrt{(n+l)!}\sqrt{l!}}{\sqrt{(l-r)!}\sqrt{(l-r)!}}. \tag{4.39}$$

Inserting $A_{l,n}(\gamma(t))$ in $P_l(n+l,t)$, and using the series expansion of the generalized Laguerre polynomial of the form

$$L_n^l(x) = \sum_{r=0}^{n}(-1)^r\frac{x^r}{r!}\binom{l+n}{n-r}, \tag{4.40}$$

will have the result of

$$P_l(l+n,t) = e^{-|\gamma(t)|^2}|\gamma(t)|^{2n}\frac{l!}{(l+n)!}\Big[\sum_{r=0}^{l}\frac{(-1)^r|\gamma(t)|^{2r}}{r!}\binom{l+n}{n-r}\Big]^2, \tag{4.41}$$

$$= P_0(n,t)\frac{n!l!}{(n+l)!}[L_l^{(n)}(|\gamma(t)|^2)]^2. \tag{4.42}$$

**Electron spectral weight**

In the strong coupling regime, the electronic Green's function is

$$G(t,t') = -i\frac{1}{\mathcal{Z}}\mathrm{Tr}\Big[\mathcal{T}_\mathcal{C}e^{-i\int_\mathcal{C}\mathrm{dt}_1 H(t_1)}c(t)c^\dagger(t')\Big], \tag{4.43}$$

$$= -i\frac{1}{\mathcal{Z}}\mathrm{Tr}\Big[\mathcal{T}_\mathcal{C}e^{-i\int_\mathcal{C}\mathrm{dt}_1 H_{\mathrm{LF}}(t_1)}c(t)c^\dagger(t')\Big], \tag{4.44}$$

where $\mathcal{Z}$ is the partition function, determined by $\mathcal{Z} = \mathrm{Tr}\Big[\mathcal{T}_\mathcal{C}e^{-i\int_\mathcal{C}\mathrm{dt}_1 H_{\mathrm{LF}}(t_1)}\Big]$.

Exploiting the transformed electronic operators, introduced in Eqs. (4.16, 4.17), we can

split the Green's function into phononic and fermionic parts as

$$G(t,t') = \mathrm{g}_{\mathrm{el}}(t,t')\mathrm{w}_{\mathrm{ph}}(t,t'), \tag{4.45}$$

$$\mathrm{g}_{\mathrm{el}}(t,t') = \frac{1}{Z_{\mathrm{el}}}\mathrm{Tr}\big[\mathcal{T}_{\mathcal{C}} e^{-i\int_{\mathcal{C}} \mathrm{dt}_1[-\lambda(t)-\mu]c^\dagger c} c(t)c^\dagger(t')\big], \tag{4.46}$$

$$\mathrm{w}_{\mathrm{ph}}(t,t') = \frac{1}{Z_{\mathrm{ph}}}\mathrm{Tr}\big[\mathcal{T}_{\mathcal{C}} e^{-i\int_{\mathcal{C}} \mathrm{dt}\omega_0 b^\dagger b} e^{[\gamma^*(t)b - \gamma(t)b^\dagger]} e^{[\gamma(t')b^\dagger - \gamma^*(t')b]}\big]. \tag{4.47}$$

Here $Z_{\mathrm{ph}}$ and $Z_{\mathrm{el}}$ are phonon and electron partition functions.

The real-time components of the electronic Green's function (g) at finite temperature are

$$\mathrm{g}^<(t,t') = i f_\beta(-\mu-\lambda(0)) e^{\int_{t'}^{t} \mathrm{dt}_1[\mu+\lambda(t)]}, \tag{4.48}$$

$$\mathrm{g}^>(t,t') = -i\big[(i - f_\beta(-\mu-\lambda(0)) e^{i\int_{t}^{t'} \mathrm{dt}_1[\mu+\lambda(t)]}\big], \tag{4.49}$$

where $f_\beta(\epsilon) = 1/(1+e^{\beta\epsilon})$ is the Fermi-Dirac distribution function. For the case of quenching the el-ph coupling, we can evaluate the exponential part as

$$e^{i\int_{t'}^{t} \mathrm{dt}_1[\mu+\gamma(t)]} = e^{i(t-t')[\mu+\mu_1]} \exp\Big(i\frac{g_1(g_0-g_1)}{\omega_0^2}\big[\sin(\omega_0 t) - \sin(\omega_0 t')\big]\Big), \tag{4.50}$$

with $\lambda_1 = \frac{g_1^2}{\omega_0}$

For the phononic contribution ($\mathrm{w}_{\mathrm{ph}}$), utilizing the time-dependancy of bosonic operators,

$$b(t) = be^{-i\omega t}, \tag{4.51}$$

$$b^\dagger(t) = b^\dagger e^{i\omega t}, \tag{4.52}$$

will enable us to determine $\mathrm{w}_{\mathrm{ph}}$, defined as

$$\mathrm{w}_{\mathrm{ph}}(t,t') = \frac{1}{Z_{\mathrm{ph}}}\mathrm{Tr}\big[e^{-\omega_0 b^\dagger b}\mathcal{T}_{\mathcal{C}} e^{[\gamma^*(t)b(t) - \gamma(t)b^\dagger(t)]} e^{[\gamma(t')b^\dagger(t) - \gamma^*(t')b(t)]}\big], \tag{4.53}$$

$$\begin{aligned}\mathrm{w}^>_{\mathrm{ph}}(t,t') = \exp\Big(\frac{1}{2\sinh\left(\frac{\beta\omega_0}{2}\right)}\Big(&\gamma^*(t)\gamma(t')e^{\omega_0[\frac{\beta}{2} - i(t-t')]} \\ &+ \gamma(t)\gamma^*(t')e^{-\omega_0[\frac{\beta}{2} - i(t-t')]} - [|\gamma(t)|^2 + |\gamma(t')|^2]\cosh(\frac{\beta\omega_0}{2})\Big)\Big),\end{aligned} \tag{4.54}$$

$$\mathrm{w}^<_{\mathrm{ph}}(t,t') = \mathrm{w}^>_{\mathrm{ph}}(t',t) = \mathrm{w}^>_{\mathrm{ph}}(t,t')^*. \tag{4.55}$$

For a quench of $g$, introduced in Eq. (4.24), $\mathrm{w}_{\mathrm{ph}}$ will have the form of

$$\mathrm{w}^{>}_{\mathrm{ph,qu}} = \mathrm{w}^{>}_{\mathrm{ph,eq}}(t-t')\exp\Big(i\frac{g_1(g_0-g_1)}{\omega_0^2}[\sin(\omega_0 t')-\sin(\omega_0 t)]\Big), \tag{4.56}$$

where $\mathrm{w}^{>}_{\mathrm{ph,eq}}$ is the phononic factor for the equilibrium state in which the el-ph coupling is $g_1$,

$$\mathrm{w}^{>}_{\mathrm{ph,eq}}(t-t') = \exp\Big(\frac{g_1^2}{\omega_0^2\sinh(\frac{\beta\omega_0}{2})}\Big\{\cosh\big(\frac{\beta\omega_0}{2}-i\omega_0(t-t')\big)-\cosh\big(\frac{\beta\omega_0}{2}\big)\Big\}\Big). \tag{4.57}$$

At last, by inserting Eqs. (4.48, 4.49), as the electronic contributions, and Eqs. (4.56, 4.55), as the phononic part of the Green's function, in Eq. (4.45), the Green's function will become

$$G^{>}(t,t') = G^{>}_{\mathrm{eq}}(t-t'), \tag{4.58}$$
$$G^{<}(t,t') = G^{<}_{\mathrm{eq}}(t-t')Q(t)Q^{*}(t'), \tag{4.59}$$
$$Q(t) = \exp\big(2i\sin(\omega_0 t)\frac{g_1(g_0-g_1)}{\omega_0}\big), \tag{4.60}$$

where $G_{\mathrm{eq}}(t-t')$ is the equilibrium Green's function with the coupling $g_1$ as

$$G^{>}_{\mathrm{eq}}(t) = -i[1-f_\beta(-\mu-\lambda_1)]e^{it(\mu+\lambda_1)}\mathrm{w}^{>}_{\mathrm{ph,eq}}(t), \tag{4.61}$$
$$G^{<}_{\mathrm{eq}}(t) = if_\beta(-\mu-\lambda_1)e^{it(\mu+\lambda_1)}\mathrm{w}^{>}_{\mathrm{ph,eq}}(-t). \tag{4.62}$$

### 4.1.2 Extreme adiabatic limit

When the the hopping of the electron is faster than the ion motion, the system can be studied in a frozen lattice, where the ion deformation is static. This limit is known as the "adiabatic", and sometimes "static", limit. This denomination is related to the validity, and applicability, of the Born-Oppenheimer adiabatic approximation [8] in this parameter regime of the Holstein model.

In this section, we will briefly demonstrate a minimal model to illustrate the physics of the static limit. The discussion is mainly following by the work of Ciuchi, *et. al.* [19]. Since the lattice is frozen, we would have a harmonic oscillator with large mass, described by the Hamiltonian of

$$H_{\mathrm{ph}} = \sum_i \frac{P_i^2}{2M} + \frac{1}{2}M\omega_0^2 X_i^2, \tag{4.63}$$

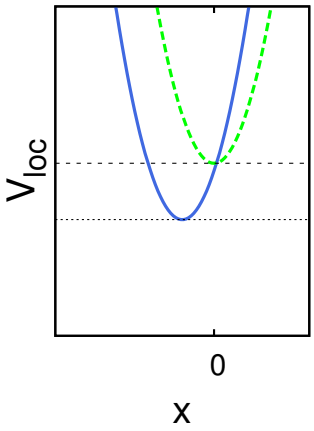


Figure 4.1: The atomic limit potential. The dashed green curve is the noninteracting harmonic potential with a minimum at $x = 0$. The blue curve is the shifted oscillator with the minimum at $x_{\min} = \sqrt{2}g/\omega_0$, and $V_{\rm loc}^{\min} = E_{\rm p}$, where $E_{\rm p}$ is the polaron enrgy.

where $P_i$ ($X_i$) is the momentum (coordinate) of ions at site $i$, associated with a mass $M \to \infty$. To prepare a meaningful Hamiltonian, in large-mass limit, we should also impose the spring-constant condition as

$$k = \lim_{M\to\infty} M\omega_0^2 \equiv \text{constant}, \tag{4.64}$$

indicating that the phonon frequency should be kept small. The el-ph interaction in Eq. (4.1) should also be renormalized as

$$H_{\rm el-ph} = -g' \sum_i n_i X_i, \tag{4.65}$$

where $g' = g\sqrt{2M\omega_0}$, and $\lambda = g'^2/(2kJ)$, where $J$ is the site-independent hopping amplitude. We thus can write the total Hamiltonian of the system as

$$H_{\rm ad} = \sum_i \frac{1}{2} M\omega_0^2 X_i^2 - g' \sum_i n_i X_i + \sum_{\langle ij\rangle} J_{ij} c_i^\dagger c_j. \tag{4.66}$$

Due to the second term of the above equation, in low density limit, the el-ph interaction would be nonzero for the site which is occupied by an electron, let's say at site "0", and be zero at the rest of the lattice sites. In addition, the displacement operator, using the Heisenberg equation, will be a constant,

$$[H_{\rm ad}, X] = 0 \Rightarrow X(t) = X(0). \tag{4.67}$$

$X(0)$ is the frozen ion displacement. We will determine $X_0$, using the Hellmann-Feynman theorem [62, 37] on the ground-state,

$$\langle \frac{\partial H_{\rm ad}}{\partial X} \rangle_0 = M\omega_0^2 \langle X_i \rangle_0 - g' \langle n_i \rangle_0 = 0, \tag{4.68}$$

$$\langle X_i \rangle_0 = \frac{g'}{M\omega_0^2} \langle n_i \rangle_0, \tag{4.69}$$

where $\langle\rangle_0$ set the expectation value with respect to the ground state. When $X_0$ is zero, the system will become a free-electron system, which is totally uncoupled from ions. The Green's function of such a system within DMFT scheme on the Bethe lattice, would be

$$i\partial_t G_{\rm bethe}(t,t') - \big[\Delta * G_{\rm bethe}\big](t,t') = i\delta_{\mathcal{C}}(t,t'), \tag{4.70}$$

where $\Delta(t,t') = J^2 * G_{\rm bethe}(t,t')$. However, for nonzero $X_0$, the electron is localized on distorted site, connected to its neighboring undistorted sites. The Green's function of such a system on the distorted ($G^{0,0}$) and undistorted ($G$) sites are

$$\Big(i\partial_t + g'X_0\Big) G^{0,0}_{\rm bethe}(t,t') + \Big[\Delta * G^{0,0}_{\rm bethe}\Big](t,t') = i\delta_{\mathcal{C}}(t,t'), \tag{4.71}$$

$$i\partial_t G_{\rm bethe} - \Big[\Delta * G_{\rm bethe}\Big](t,t') = i\delta_{\mathcal{C}}(t,t'). \tag{4.72}$$

Employing the same Green's function as for the delocalized state, we can compute the Green's function as a function of $x = g'X_0/J$.

Figure 4.2 a) shows the spectral function, computed by Eq. (2.39), at site zero for various $g'X_0$ values. Results clearly indicate that the larger deformation strongly breaks the symmetricity of the semi-elliptical spectral function ($g'X_0 = 0$). For larger parameter values, the spectral function will be separated into two main features. The larger spectral peak is located out of the initial spectral bandwidth, and a very smaller density accumulated around the uncoupled spectral weight. This conveys that, within this limit, both localized and a delocalized states are coexist.

A more intuitive picture will be achieved, if we figure out the adiabatic potential of the static lattice. Seeking this goal starts from bringing Eq. (4.71) to the real frequency space as

$$G^{0,0}(\omega) = \frac{1}{\omega + g'X_0 - J^2 G_{\rm bethe}(\omega)}, \tag{4.73}$$

where

$$G_{\rm bethe}(\omega) = \begin{cases} \frac{1}{2J^2}\big[\omega - {\rm Sgn}(\omega)\sqrt{-4J^2+\omega^2}\big] & \text{for } 4J^2 \le \omega^2, \\ \frac{1}{2J^2}\big[\omega - i\sqrt{4J^2-\omega^2}\big] & \text{for } 4J^2 \ge \omega^2. \end{cases} \tag{4.74}$$

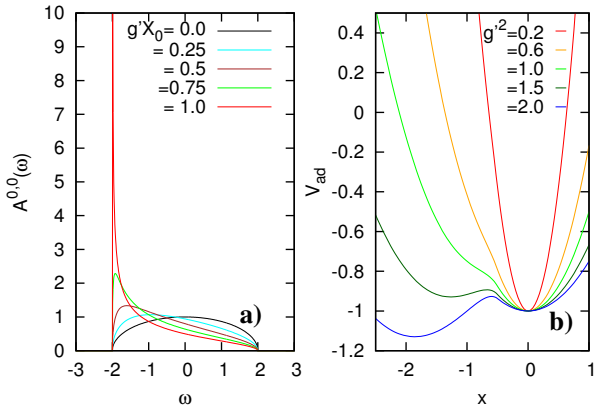


Figure 4.2: a) The spectral function of the site with nonzero electron density. b)The adiabatic potential for various $g'$ values.

Here, the sign function is defined as Sgn(x) = x/|x|. The pole ($E_{\text{el}}$) of this Green's function, which is the ground state energy of the electron, satisfies

$$E_{\text{el}} + g'X_0 - \frac{1}{2}\Re(E_{\text{el}} - \sqrt{E_{\text{el}}^2 - J^2}) = 0, \tag{4.75}$$

with the explicit form of

$$\frac{E_{\text{el}}}{J} = \begin{cases} -1 & \text{for } x < \frac{1}{2} \\ -\frac{1}{4x} - x & \text{for } x > \frac{1}{2} \end{cases}, \tag{4.76}$$

where $x = g'X_0/J$ [19]. The $x < 0.5$ case is a trivial free-electron solution, while $x > 0.5$ describes an electron in a static lattice. We then define the normalized phonon potential as

$$\frac{V_{\text{ad}}(x)}{J} = \frac{1}{J}\Big(\frac{1}{2}kX_0^2 + E_{\text{el}}\Big), \tag{4.77}$$

$$= \frac{1}{4\lambda}x^2 + \frac{E_{\text{el}}}{J}, \tag{4.78}$$

$$= \frac{1}{4\lambda}x^2 + \begin{cases} -1 & \text{for } x \leq -\frac{1}{2} \\ -\frac{1}{4x} - x & \text{for } x > -\frac{1}{2} \end{cases}, \tag{4.79}$$

where $\lambda = g'^2/(2kJ)$. In Fig. 4.2 b), we plot the $V_{\text{ad}}$ for various $g'$, setting $J = k = 1$. Results reveal that for larger el-ph couplings the global minimum of the system would be in a nonzero value, while at smaller couplings the distortion of the harmonic potential

is almost at zero. At larger couplings, there is a small barrier between two minima, determined by $h_{\rm bar} = V_{\rm ad}(-0.5)$. At very large couplings, we would have

$$\lim_{\lambda\to\infty} h_{\rm bar} = \lim_{\lambda\to\infty} \frac{1}{16\lambda} - 1 = -1. \tag{4.80}$$

This is indicating that in extreme strong coupling limit, we would reach an almost flat potential around $x \in [-0.5 : 0.5]$. This means that at this parameter regime, the delocalized state still has an opportunity to play a role in the excited state of the system. Furthermore, we can define two critical parameters based on the global minimum of the adiabatic potential ($V_{\rm ad}$). These critical parameters are

$$\begin{cases} \lambda_{\rm c}^{'} = 0.650, \\ \lambda_{\rm c} = 0.844. \end{cases} \tag{4.81}$$

The physics of systems with $\lambda < \lambda_{\rm c}^{'}$ is mainly related to the delocalized state corresponding to the slightly dressed electron. When $\lambda_{\rm c}^{'} < \lambda < \lambda_{\rm c}$ the localized and delocalized states coexist and the nonzero deformation of the adiabatic potential is comparable to the undistorted potential. The ground state of systems with $\lambda > \lambda_{\rm c}$ is the localized solution of the system which is attained by the nonzero location of the minimum of $V_{\rm ad}$.

## 4.2 DMFT-based method

The local nature of the el-ph interaction, defined in Eq. (4.1), empowers us to propose an accurate DMFT-based solution. To study a dilute system, we adopt the DMFT formalism and propose an analytical impurity solver, which we are going to introduce in the upcoming section. This impurity solver is the generalization of the work which has been conducted by Ciuchi, *et. al.*[19].

### 4.2.1 DMFT Scheme: Single-electron system

The action of the Holstein Hamiltonian in Eq. (4.1), corresponding to the partition function of $\mathcal{Z} = \exp(-i\mathcal{S})$, is

$$\mathcal{S} = \Big\{ \int_{\mathcal{C}} {\rm d}t \sum_{i\sigma} c_{i\sigma}^{\dagger}(t)\big(i\partial_t + \mu\big)c_{i\sigma}(t) + \int_{\mathcal{C}} {\rm d}t \sum_{i} b_i^{\dagger}(t)(i\partial_t - \omega_0)b_i(t) \tag{4.82}$$

$$- \int_{\mathcal{C}} {\rm d}t g(t) \sum_{i} [b_i^{\dagger}(t) + b_i(t)]c_i^{\dagger}(t)c_i(t) + \int_{\mathcal{C}} {\rm d}t J \sum_{\langle ij\rangle\sigma} c_{i\sigma}^{\dagger}(t)c_{j\sigma}(t)\Big\}. \tag{4.83}$$

Within the DMFT, we map our lattice problem on to a momentum-independent impurity problem connected to a self-consistent bath. This will bring the lattice action , Eq. (4.83), to the form of

$$\mathcal{S}_{\rm imp} = \Big\{ \int_{\mathcal{C}} {\rm d}t c^\dagger(t)\big(i\partial_t + \mu\big)c(t) + \int_{\mathcal{C}} {\rm d}t b^\dagger(t)(i\partial_t - \omega_0)b(t) \tag{4.84}$$

$$- \int_{\mathcal{C}} {\rm d}t g(t)[b^\dagger(t) + b(t)]c^\dagger(t)c(t) + \int_{\mathcal{C}} {\rm d}t{\rm d}t' c^\dagger(t)\Delta(t,t')c(t')\Big\}, \tag{4.85}$$

where $\Delta$ is the hybridization function, and we omit spin indices in our spin symmetric case. The impurity Green's function for the action, introduced in Eq. (4.85), is

$$G_{\rm imp}(t,t') = -i\langle c(t)c^\dagger(t')\rangle, \tag{4.86}$$

with the explicit form of

$$G_{\rm imp}(t,t') = -i\frac{{\rm Tr}\Big[\mathcal{T}_{\mathcal{C}} e^{-i\int_{\mathcal{C}} {\rm d}t_1 H_{\rm imp}(t_1)} c(t)c^\dagger(t')\Big]}{{\rm Tr}\Big[\mathcal{T}_{\mathcal{C}} e^{-i\int_{\mathcal{C}} {\rm d}t_1 H_{\rm imp}(t_1)}\Big]}, \tag{4.87}$$

where trace (Tr) is taken over the full span space of the impurity Hamiltonian ($H_{\rm imp}$), defined as

$$H_{\rm imp}(t) = -\mu(t)c^\dagger c + \omega_0(t)b^\dagger b + g(t)(b^\dagger + b)c^\dagger c + c^\dagger \int_{\mathcal{C}} {\rm d}t_1 \Delta(t,t_1)c, \tag{4.88}$$

where the last term of the above equation corresponds to the last term of the DMFT action in Eq. (4.85). One should note that the last term of Eq. (4.88) is originated from integrating bath degrees of freedom from the action, and thereby does not look like a Hamiltonian term.

To study the low-density limit of carriers, we first present electron creation and annihilation operators in the interaction representation with respect to the pure electronic term ($\mu c^\dagger c$) as

$$\begin{cases} c & \to e^{it\mu}c, \\ c^\dagger & \to e^{-it\mu}c^\dagger, \end{cases} \tag{4.89}$$

where $t$ stands on the Keldysh contour. Substituting Eq. (4.89) in Eq. (4.87) will bring us to

$$G_{\rm imp}(t,t') = -i\frac{{\rm Tr}\Big[e^{\beta\mu N}\mathcal{T}_{\mathcal{C}} e^{-i\int_{\mathcal{C}} {\rm d}t_1 H(t_1)} e^{i(t-t')\mu} c(t)c^\dagger(t')\Big]}{{\rm Tr}\Big[\mathcal{T}_{\mathcal{C}} e^{-i\int_{\mathcal{C}} {\rm d}t_1 (H(t_1)-\mu N)}\Big]}, \tag{4.90}$$

where $N = c^\dagger c$ is the electron number operator, $\beta$ is the inverse temperature, and

$$H = \omega_0 b^\dagger b + g(b^\dagger + b)c^\dagger c + c^\dagger \int_{\mathcal{C}} \mathrm{d}t_1 \Delta(t, t_1) c. \tag{4.91}$$

To keep the system in the low-density limit, we take the limit of $\mu \to -\infty$. For further renormalization purpose, we shift the chemical potential by a factor of $\lambda$ as $\mu = \overline{\mu} + \lambda$, where $\overline{\mu} \to -\infty$. We thereby can express the Green's function in a grand-canonical ensemble as

$$G_{\mathrm{imp}}(t, t') = -ie^{i(t-t')\overline{\mu}} \frac{\mathrm{Tr}\left[e^{\beta\overline{\mu}N}\mathcal{T}_{\mathcal{C}} e^{-i\int_{\mathcal{C}} \mathrm{d}t_1 (H(t_1)-\lambda N)} c(t) c^\dagger(t')\right]}{\mathrm{Tr}\left[e^{\beta\overline{\mu}N}\mathcal{T}_{\mathcal{C}} e^{-i\int_{\mathcal{C}} \mathrm{d}t_1 (H(t_1)-\lambda N)}\right]}. \tag{4.92}$$

By expanding the grand-canonical trace $\mathrm{Tr}[e^{\beta\overline{\mu}N}...]$ in powers of $\xi = e^{\beta\overline{\mu}}$, known as the fugacity, as $\sum_{n=0}^{\infty} \xi^n \mathrm{Tr}_{N=n}[...]$, we will be able to disassemble $N = n$ electronic contributions. In the one electron limit, dominant terms, in the above fugacity expansion of the trace, are $N = 0$, and $N = 1$. $N = 0$ corresponds to the case where $c^\dagger$ is located later than $c$ on the Keldysh contour $t' \succ t$, while $N = 1$ occurs when the location of $c$ is later than $c^\dagger$ on the contour. A similar fugacity expansion has been previously proposed for the non-crossing approximation in the strong electron-electron coupling limit [29].

Keeping only the relevant terms, we will write the impurity Green's function as

$$G_{\mathrm{imp}}(t, t') = -ie^{i(t-t')\overline{\mu}} \left[\Theta(t, t') + \xi\Theta(t', t)\right] \left[\widetilde{G}(t, t') + \mathcal{O}(\xi)\right], \tag{4.93}$$

where $\Theta$ is the Keldysh step-function, introduced in Eq. (2.19). Here, $\widetilde{G}$ is

$$\widetilde{G}(t, t') = -i\frac{1}{\mathcal{Z}_0} \mathrm{Tr}_{N=0}\left[\mathcal{T}_{\mathcal{C}} e^{-i\int_{\mathcal{C}} \mathrm{d}t_1 (H(t_1)-\lambda N)} c(t) c^\dagger(t')\right] \quad \text{for} \quad t \succ t', \tag{4.94}$$

$$\widetilde{G}(t, t') = -i\frac{1}{\mathcal{Z}_0} \mathrm{Tr}_{N=1}\left[\mathcal{T}_{\mathcal{C}} e^{-i\int_{\mathcal{C}} \mathrm{d}t_1 (H(t_1)-\lambda N)} c(t) c^\dagger(t')\right] \quad \text{for} \quad t' \prec t, \tag{4.95}$$

where zero-electron partition function is given by

$$\mathcal{Z}_0 = \mathrm{Tr}_{N=0}\left[\mathcal{T}_{\mathcal{C}} e^{-i\int_{\mathcal{C}} dt_1 (H(t_1)-\lambda N)}\right]. \tag{4.96}$$

$\widetilde{G}$ is represented in a micro-canonical ensemble with a fixed particle number of either one or zero. We thereby entitle $\widetilde{G}$ as a projected Green's function from the grand-canonical ensemble to zero- or one-particle sectors.

Before further going into details of the evaluation of $\widetilde{G}$, let us clarify the purpose and prerequisite of shifting the chemical potential by $\lambda$. To validate the possibility of shifting the chemical potential, we should prove that such a change will not drag any unphysical state into the physical quantities. To check that, we would have a look at the particle number, defined as $n = -iG^<(t,t)$, in the projected space,

$$n = -i\xi\widetilde{G}(t,t) + \mathcal{O}(\xi^2). \tag{4.97}$$

Slightly perturbing $\lambda$ to $\lambda \to \lambda + \delta\lambda$ will shift the projected Green's functions, Eqs. (4.94, 4.95), to

$$\widetilde{G}(t,t') \to e^{i(t-t')\delta\lambda}\widetilde{G}(t,t') \quad \text{for} \quad t \succ t', \tag{4.98}$$

$$\widetilde{G}(t,t') \to e^{\beta\delta\lambda}e^{i(t-t')\delta}\widetilde{G}(t,t') \quad \text{for} \quad t' \succ t, \tag{4.99}$$

and the fugacity will also be modified as $\xi \to \xi e^{-\beta\delta\lambda}$. Inserting all of these modifications back into Eq. (4.93), and evaluating the particle number, ascertain that, up to the first order in the fugacity, there would be no drawback from $\lambda$. We employ $\lambda$ to keep $\widetilde{G} = -i$ satisfied, which is precisely the purpose of its introduction. The importance of such a normalization lies on the numerical simulation of systems at large $\beta$, where the projected Green's function can reach exponentially large values, and therewith hard to numerically implement.

Since we have been convinced that, in the one-electron system, the evaluation of the Green's function is effectively mapped to the projected space with zero and one particles, we will map the DMFT scheme also onto this subspace. To seize this goal, we first cover the Green's function properties in the micro-canonical ensemble, and then carry out the discussion to the properties of the Dyson equation in this space.

For projected Green's functions, defined in Eqs. (4.94,4.95), the electronic anti-periodic boundary condition (c.f. Eqs. (2.26, 2.27)) is expressed as

$$\widetilde{G}(0^+,t) = -\widetilde{G}(-i\beta,t), \tag{4.100}$$

$$\widetilde{G}(t,0^+) = -\widetilde{G}(t,-i\beta), \tag{4.101}$$

where $0^+$ is the initial time on $\mathcal{C}^+$. The hermiticity (c.f. Eqs. (2.22, 2.23, 2.24)) also implies that

$$\widetilde{G}^<(t,t') = -\widetilde{G}^<(t',t)^*, \tag{4.102}$$

$$\widetilde{G}^>(t,t') = -\widetilde{G}^>(t',t)^*, \tag{4.103}$$

$$\widetilde{G}^{\rm tv}(t,\tau) = \widetilde{G}^{\rm vt}(\beta-\tau,t)^*. \tag{4.104}$$

As we pointed out in Chap. 2, it suffices to only compute four components of the Keldysh Green's function, namely the lesser, Greater, Matsubara, and left-mixing (tv) components. (Other components will be simply calculated using Eqs. (2.13-2.18).)

The convolution relation, introduced in Sec.2.3.1, of the form $C = A*B$ in the projected space can be approximated as

$$C(t,t') = \underbrace{-ie^{i(t-t')\overline{\mu}}\big[\Theta_{\mathcal{C}}(t,t') + \xi\Theta_{\mathcal{C}}(t',t)\big]}_{\mathcal{P}(t,t')}\big[\widetilde{C}(t,t') + \mathcal{O}(\xi)\big], \tag{4.105}$$

$$[A*B](t,t') \approx \mathcal{P}(t,t')[\widetilde{A}*\widetilde{B}](t,t'), \tag{4.106}$$

where $\mathcal{P}$ only includes terms of the order $\mathcal{O}(1)$ and $\mathcal{O}(\xi)$. Up to the leading order in the fugacity, we, by arranging the contributions of the integral, can write the convolution integral as

$$[\widetilde{A} \circlearrowleft \widetilde{B}](t,t') = \int_{\mathcal{C},t'}^{t} A(t,t_1)B(t_1,t')\mathrm{d}t_1. \tag{4.107}$$

For brevity, we denote the above "cyclic" convolution of the projected space by $\circlearrowleft$ as

$$[A \circlearrowleft B](t,t') = \begin{cases} \int_{\mathcal{C},t<t_t<t'} A(t,t_1)B(t_1,t')\mathrm{d}t_1 & \text{for } t' \succ t \\ \int_{\mathcal{C},t<t_t<-i\beta} A(t,t_1)B(t_1,t')\mathrm{d}t_1 + \int_{\mathcal{C},0^+<t_t<t'} A(t,t_1)B(t_1,t')\mathrm{d}t_1 & \text{for } t' \succ t \end{cases}. \tag{4.108}$$

Accordingly, we are able to project any Dyson equation for a generic local interaction $(h)$, from

$$\big[i\partial_t + \mu - h(t)\big]X(t,t') - \big[A*X\big](t,t') = \delta_{\mathcal{C}}(t,t'), \tag{4.109}$$

$$X(t,t') + \big[A*X\big](t,t') = B(t,t') \tag{4.110}$$

to the few-carrier subspace as

$$\big[i\partial_t + \lambda - h(t)\big]\widetilde{X}(t,t') - \big[\widetilde{A} \circlearrowleft \widetilde{X}\big](t,t') = \delta_{\mathcal{C}}(t,t'), \tag{4.111}$$

$$\widetilde{X}(t,t') + \big[\widetilde{A} \circlearrowleft \widetilde{X}\big](t,t') = \widetilde{B}(t,t'). \tag{4.112}$$

In the following, we will determine the lesser and greater components of the projected Green's function. Although we will only cover lesser and greater components explicitly, the equations would stand valid even after replacing a real time variable by the imaginary one.

### Greater component

In Eq. (4.94), we presented the greater component of the projected Green's function ($\widetilde{G}^{>}$). Exploiting the time-evolution operator ($\mathcal{U}$) will suggest that the Green's function have the explicit form of

$$\widetilde{G}^{>}(t,t') = -\frac{1}{\mathcal{Z}_0}\mathrm{Tr}_{N=0}\big[\mathcal{U}(-i\beta,t)c\mathcal{U}(t,t')c^{\dagger}\mathcal{U}(t',0)\big], \tag{4.113}$$

where the time-evolution operator along the contour $\mathcal{C}$ is given by

$$\mathcal{U}(t,t') = \mathcal{T}_{\mathcal{C}}\exp\Big[-i\int_{\mathcal{C},t'}^{t}\mathrm{d}t_1\big(H(t_1)-\lambda N\big)\Big], \tag{4.114}$$

with $H(t)$ defined in Eq. (4.91). Since $\widetilde{G}^{>}$ corresponds to the zero-electron sector, its Hilbert space is a product state of a zero-electronic and phononic Hilbert space, let's say containing $p$ phonons on the impurity site, with the explicit form of $|p\rangle = (b^{\dagger})^p/\sqrt{p!}|0\rangle_{\mathrm{ph}}|0\rangle_{\mathrm{el}}$. In this phononic space, we would have

$$\langle p|\mathcal{U}(t,t')|p'\rangle = \delta_{pp'}e^{-i(t-t')p\omega_0} \quad \text{for} \quad t \succ t'. \tag{4.115}$$

By introducing a propagator as

$$\mathcal{G}^{>}_{pp'}(t,t') = -i\langle p|c\mathcal{U}(t,t')c^{\dagger}|p'\rangle \quad \text{for} \quad t \succ t', \tag{4.116}$$

we can rewrite the greater component of the projected Green's function as

$$\widetilde{G}^{>}(t,t') = (1-e^{-\beta\omega_0})\sum_{p=0}^{\infty}e^{-\beta p\omega_0}e^{itp\omega_0}\mathcal{G}^{>}_{pp}(t,t')e^{-itp\omega_0}. \tag{4.117}$$

Here, we inserted the zero-electron partition function,

$$\mathcal{Z}_0 = \sum_{p=0}^{\infty}e^{-\beta p\omega_0} = \frac{1}{1-e^{-\beta\omega_0}}. \tag{4.118}$$

### Lesser component

The lesser component of the projected Green's function has been introduced in Eq. (4.95). Applying time ordering will offer

$$\widetilde{G}^{<}(t,t') = -i\frac{1}{\mathcal{Z}_0}\mathrm{Tr}_{N=1}\Big[\mathcal{U}(-i\beta,t')c^{\dagger}\mathcal{U}(t',t)c\mathcal{U}(t,0)\Big], \tag{4.119}$$

where $\mathcal{U}$ has been defined in Eq. (4.114). To employ a similar approach followed for $\widetilde{G}^{>}$, we first should reorder the trace of $N=1$ by inserting a complete set with zero-electron after $c$ on the contour and thereby bring the trace to $N=0$ sector as

$$\widetilde{G}^{<}(t,t') = -i\frac{1}{\mathcal{Z}_0}\mathrm{Tr}_{N=0}\big[c\mathcal{U}(t,0)\mathcal{U}(-i\beta,t')c^{\dagger}\mathcal{U}(t',t)\big], \tag{4.120}$$

where

$$\langle p|\mathcal{U}(t,t')|p'\rangle = \delta_{pp'}e^{-i(t-t')p\omega_0}\times\begin{cases}1 & \text{for} \quad t\succ t'\\ e^{-\beta p\omega_0} & \text{for} \quad t'\succ t\end{cases}. \tag{4.121}$$

At last, the lesser component of the projected Green's function will become

$$\widetilde{G}^{<}(t,t') = (1-e^{-\beta\omega_0})\sum_{p=0}^{\infty}e^{itp\omega_0}\mathcal{G}^{<}_{pp}(t,t')e^{-it'p\omega_0}. \tag{4.122}$$

### Projected Green's function

Bringing Eqs. (4.117, 4.122) to a general form will give us

$$\widetilde{G}(t,t') = (1-e^{-\beta\omega_0})\sum_{p=0}^{\infty}\langle p|\mathcal{U}(t',t)|p\rangle\mathcal{G}_{pp}(t,t'), \tag{4.123}$$

where $\mathcal{U}$ satisfies Eqs. (4.114, 4.121). Eq. (4.123) is also valid when either one, related to the tv component, or both, related to the Matsubara component, of time arguments are on $\mathcal{C}^{|}$. Eq. (4.123) implies that evaluating the propagator $\mathcal{G}_{pp}$ is the only requirement for obtaining the projected Green's function. In the following, we will derive the Dyson equation of this propagator.

### Recursive Dyson equations for $\mathcal{G}$

To determine the propagator of $\mathcal{G}$, we expand $\mathcal{U}$ in terms of $H_{\mathrm{el-ph}}$ as

$$\begin{aligned}\mathcal{G}_{pp'}(t,t') = \sum_{n=0}^{\infty}(-i)^{n+1}\int_{\mathcal{C},t'}^{t}\mathrm{d}t_1\int_{\mathcal{C},t'}^{t_1}\mathrm{d}t_2\ldots\int_{\mathcal{C},t'}^{t_{n-1}}\mathrm{d}t_n\times\\ \langle p|\mathcal{T}_{\mathcal{C}}e^{-i\int_{\mathcal{C}}\mathrm{d}s(H_{\mathrm{ph}}(s)-\lambda N)}cH_{\mathrm{el-ph}}(t_1)\ldots H_{\mathrm{el-ph}}(t_n)c^{\dagger}|p'\rangle,\end{aligned} \tag{4.124}$$

where $H_{\rm ph} = \omega_0 b^\dagger b$, $H_{\rm el-ph} = g c^\dagger c(b + b^\dagger)$, and the cyclic time-ordering is set within the integral sequence as $t \succ t_1 \succ \ldots \succ t'$. By defining the noninteracting time-evolution operator as

$$\mathcal{U}_0(t, t') \equiv \mathcal{T}_\mathcal{C} \exp\big( - i \int_{\mathcal{C},t'}^{t} \mathrm{d}t_1 (H_{\rm ph}(t_1) - \lambda N)\big), \tag{4.125}$$

we can rewrite the expectation value in the integrand of Eq. (4.124) as

$$\langle p|c\mathcal{U}_0(t, t_1) H_{\rm el-ph}(t_1)\mathcal{U}_0(t_1, t_2)\ldots H_{\rm el-ph}(t_n)\mathcal{U}_0(t_n, t')c^\dagger|p'\rangle. \tag{4.126}$$

To express Eq. (4.126) in phononic states, we represent $H_{\rm el-ph}$ in the phonon basis. Since the electron-phonon interaction is nonzero in the one electron sector, we can write

$$\begin{aligned} H_{\rm el-ph}(t) &= g(t) c^\dagger c(b + b^\dagger), &(4.127)\\ &= \sum_{mm'} g(t) c^\dagger|m\rangle\langle m|(b + b^\dagger)|m'\rangle\langle m'|c, &(4.128)\\ &= \sum_{mm'} c^\dagger|m\rangle X_{mm'}(t)\langle m'|c, &(4.129)\end{aligned}$$

where

$$\begin{aligned} X_{mm'}(t) &= g(t)\langle m|(b + b^\dagger)|m'\rangle, &(4.130)\\ &= g(t)\sqrt{m + 1}\delta_{m',m+1} + g(t)\sqrt{m}\delta_{m',m-1}. &(4.131)\end{aligned}$$

Substituting Eqs. (4.126, 4.129) in Eq. (4.124) will provide

$$\begin{aligned} \mathcal{G}_{pp'}(t, t') = \sum_{n=0}^{\infty}(-i)^{n+1} \int_{\mathcal{C},t'}^{t} \mathrm{d}t_1 \int_{\mathcal{C},t'}^{t_1} \mathrm{d}t_2 \ldots \int_{\mathcal{C},t'}^{t_{n-1}} \mathrm{d}t_n \sum_{m_1,m_1',\ldots,m_n,m_n'} \times \\ \mathcal{G}_{0,pm_1}(t, t_1) X_{m_1,m_1'}(t_1)\mathcal{G}_{0,m_1'm_2}(t_1, t_2)\ldots X_{m_n,m_n'}(t_n)\mathcal{G}_{0,m_n'p'}(t_n, t'), \end{aligned} \tag{4.132}$$

where the noninteracting propagator is given by

$$\mathcal{G}_{0,pp'}(t, t') = \delta_{pp'}\widetilde{G}_0(t, t')\langle p|\mathcal{U}(t, t')|p\rangle. \tag{4.133}$$

In the above equation, $\widetilde{G}_0(t, t')$ is the noninteracting projected Green's function which satisfies the Dyson equation of the form

$$(i\partial_t + \lambda)\widetilde{G}_0(t, t') - [\widetilde{\Delta} \circlearrowleft \widetilde{G}_0](t, t') = \delta_\mathcal{C}(t, t'), \tag{4.134}$$

where $\widetilde{\Delta}$ is the projected hybridization function. Subsequently, the Dyson equation of the noninteracting propagator will become

$$(i\partial_t + \lambda - p\omega_0)\mathcal{G}_{0,pp'}(t,t') - [\widetilde{\Delta}_p \circlearrowleft \mathcal{G}_{0,pp'}](t,t') = -i\delta_{\mathcal{C}}(t,t')\delta_{pp'}, \tag{4.135}$$

where

$$\widetilde{\Delta}_p(t,t') = \widetilde{\Delta}(t,t')\langle p|\mathcal{U}(t,t')|p\rangle. \tag{4.136}$$

One should note that $\mathcal{G}_0$, $\mathcal{G}$, and $X$ are matrices, where rows and columns indicate various phonon numbers. Theoretically, the size of these matrices are infinite, since there is no upper bound for the on-site number of phonons (bosons). However, numerically, we should define a finite, but rather large, number as the maximum number of involved phonons. This number ($N_{\rm pn}^{\rm cut}$) is larger in adiabatic and strong-coupling regimes than the nonadiabatic and weak-coupling regimes.

Eq. (4.132) will finally get a Dyson-like form as

$$\begin{aligned}\mathcal{G} &= \mathcal{G}_0 + \mathcal{G}_0 \circlearrowleft X \circlearrowleft \mathcal{G}_0 + \mathcal{G}_0 \circlearrowleft X \circlearrowleft \mathcal{G}_0 \circlearrowleft X \circlearrowleft \mathcal{G}_0 + \dots \\ &= \mathcal{G}_0 + \mathcal{G}_0 \circlearrowleft X \circlearrowleft \mathcal{G}.\end{aligned} \tag{4.137}$$

Eqs. (4.137,4.135) will help us to yield the Dyson equation for the interacting propagator as

$$\big[i\partial_t + \lambda - p\omega_0\big]\mathcal{G}_{pp'}(t,t') - [\widetilde{\Delta}_p \circlearrowleft \mathcal{G}_{pp'}](t,t') - \sum_{\alpha=\pm1} X_{p,p+a}(t)\mathcal{G}_{p+a,p'}(t,t') = -i\delta_{\mathcal{C}}(t,t')\delta_{pp'}, \tag{4.138}$$

with the matrix representation of

$$\begin{pmatrix} \widetilde{G}_{0,0}^{-1} & -g & 0 & 0 & \dots \\ -g & \widetilde{G}_{0,1}^{-1} & -g\sqrt{2} & 0 & \dots \\ 0 & -g\sqrt{2} & \widetilde{G}_{0,2}^{-1} & -g\sqrt{3} & \dots \\ \vdots & \vdots & \vdots & \ddots & \end{pmatrix} \begin{pmatrix} \mathcal{G}_{00} & \mathcal{G}_{01} & \mathcal{G}_{02} & \dots \\ \mathcal{G}_{10} & \mathcal{G}_{11} & \mathcal{G}_{12} & \dots \\ \mathcal{G}_{20} & \mathcal{G}_{21} & \mathcal{G}_{22} & \dots \\ \vdots & \vdots & \vdots & \ddots \end{pmatrix} = -i\delta_{\mathcal{C}}(t,t')\mathbb{I}. \tag{4.139}$$

Here, $\mathbb{I}$ is the identity matrix, and the time-dependent part of the left-hand side has the explicit form of

$$\widetilde{G}_{0,p}^{-1}\mathcal{G}(t,t') = \big[i\partial_t + \lambda - p\omega_0\big]\mathcal{G}(t,t') - [\widetilde{\Delta} \circlearrowleft \mathcal{G}](t,t'). \tag{4.140}$$

**Equilibrium approach for evaluating $\mathcal{G}$**

In equilibrium, the two time Green's function, as a consequence of the time-translational symmetry, would be a function of time-differences. Furthermore, the computation of various components of the two-time Green's function will shrink only to the evaluation of the retarded Green's function with the help of the fluctuation dissipation theorem, captured using Eq. (2.38). Employing the retarded Green's function, the spectral function would be $A(\omega) = (-i/\pi)\Im G^{\rm ret}(\omega + i0^+)$, occupied density of states will simply obtained by $G^<(\omega) = 2\pi i f(\omega)A(\omega)$, and unoccupied density of state by $G^> = -2\pi i[1 - f(\omega)]A(\omega)$. It is now clear that having the spectral function, in equilibrium, will disclose the physics of the problem. In the remaining of this section, we will pursue the goal of finding the spectral function for a dilute system.

For a generic Hamiltonian, the Lehmann representation of the spectral function in the Hamiltonian's eigenstate ($|n\rangle$), with energy levels of $E_n$ and particle number of $N_n$ is given by

$$A(\omega) = \sum_{n,m} \frac{e^{-\beta(E_n+\mu N_n)} + e^{-\beta(E_m+\mu N_m)}}{\mathcal{Z}} |\langle n|c|m\rangle|^2 \delta(\omega + \mu + E_n - E_m), \tag{4.141}$$

where $\mathcal{Z}$ is the partition function, and $H = H_{\rm local} + \mu N$. The fugacity expansion of $A(\omega)$ in the low density limit suggests that

$$A(\omega - \mu) = A_0(\omega + \lambda) + \mathcal{O}(\xi), \tag{4.142}$$

where the zero-electron spectral function is defined as

$$A_0 = \sum_{n:N_n=0,m} \frac{e^{-\beta E_n}}{\mathcal{Z}_0} |\langle n|c|m\rangle|^2 \delta(\omega + E_n - E_m). \tag{4.143}$$

By exploiting Eq. (4.142), we are able to write the projected Green's function in terms of the zero-electron spectral function as

$$\widetilde{G}(t,t') = -i \int \mathrm{d}\omega A_0(\omega + \lambda) e^{i\omega(t-t')} \quad \text{for} \quad t \succ t', \tag{4.144}$$

$$\widetilde{G}(t,t') = i \int \mathrm{d}\omega A_0(\omega + \lambda) e^{-\beta\omega} e^{i\omega(t'-t)} \quad \text{for} \quad t' \succ t. \tag{4.145}$$

$A_0(\omega)$ can be evaluated by a Laplace transform of Eq. (4.144),

$$A_0(z) = -\frac{1}{\pi} \Im \int_0^\infty \mathrm{d}s \widetilde{G}^>(s,0) e^{izs} \quad \text{for} \quad z = \omega + i0^+, \tag{4.146}$$

which would be sufficient to calculate other components of Green's functions. This means that we must only obtain the greater component of the projected Green's function.

The Laplace transform of Eq. (4.123) for the greater projected Green's function is

$$\widetilde{G}(z) = (1 - e^{-\beta\omega_0}) \sum_{p=0}^{\infty} e^{-\beta p\omega_0} \mathcal{G}_{pp}(z + p\omega_0), \tag{4.147}$$

where the matrix representation of the propagator is shown as

$$\begin{pmatrix} \mathcal{G}_{00}(z) & \mathcal{G}_{01}(z) & \dots \\ \mathcal{G}_{10}(z) & \mathcal{G}_{11}(z) & \dots \\ \vdots & \vdots & \ddots \end{pmatrix} = \begin{pmatrix} \widetilde{G}_0^{-1}(z) & -g & 0 & \dots \\ -g & \widetilde{G}_0^{-1}(z-\omega_0) & -g\sqrt{2} & \dots \\ 0 & -g\sqrt{2} & \widetilde{G}_0^{-1}(z-2\omega_0) & \dots \\ \vdots & \vdots & \vdots & \ddots \end{pmatrix}^{-1}. \tag{4.148}$$

The projected noninteracting Green's function and the hybridization function are

$$\widetilde{G}_0(z) = \frac{1}{z + \lambda - \widetilde{\Delta}(z)}, \tag{4.149}$$

$$\widetilde{\Delta}_p(z) = \widetilde{\Delta}(z - p\omega_0). \tag{4.150}$$

Eq. (4.147) implies that the diagonal element of $\mathcal{G}$ would suffice to produce $\widetilde{G}^{>}$. To find the diagonal elements of the inverse of a tri-diagonal matrix, in Eq. (4.148), we will employ two auxiliary functions ($A$, $B$) in which

$$\mathcal{G}_{pp}(z + p\omega_0) = \frac{1}{\widetilde{G}(z)^{-1} - A_p(z) - B_p(z)}, \tag{4.151}$$

where each of these auxiliary functions are obtained using recursive relations as

$$A_p(z) = \cfrac{pg^2}{\widetilde{G}_0(z+\omega_0)^{-1} - \cfrac{(p-1)g^2}{\widetilde{G}_0(z+2\omega_0)^{-1} - \cfrac{(p-2)g^3}{\ddots - \cfrac{g^2}{\widetilde{G}_0(z+p\omega_0)^{-1}}}}}, \tag{4.152}$$

and

$$B_p(z) = \cfrac{(p+1)g^2}{\widetilde{G}_0(z-\omega_0)^{-1} - \cfrac{(p+2)g^2}{\widetilde{G}_0(z-2\omega_0)^{-1} - \cfrac{(p+3)g^3}{\widetilde{G}_0(z-3p\omega_0)^{-1} - \ddots}}}. \tag{4.153}$$

Achieving $\widetilde{G}^{>}$ would be the closure of solving the impurity problem. Using the self-energy as $\Sigma = A + B$, we are prepared for starting the DMFT self-consistency introduced in Sec. 3.1.2.

Equilibrium results on the Bethe lattice has been extensively discussed in [17, 19]. For the completeness purpose, we will also briefly discuss some of the outcomes in Sec. 4.3.

#### Nonequilibrium approach for evaluating $\mathcal{G}$

To track the electron evolution under a time-dependent electron-phonon coupling, we should achieve the diagonal element of $\mathcal{G}$. This goal can be done by solving a coupled set of equations as

$$[i\partial_t + \lambda - p\omega_0]\mathcal{G}_{pp}(t,t') - [(\widetilde{\Delta}_p + \widetilde{A}_p + \widetilde{B}_p) \circlearrowright \mathcal{G}_{pp}](t,t') = -i\delta_{\mathcal{C}}(t,t'). \tag{4.154}$$

Here, $A$ and $B$ are two auxiliary functions governed by

$$\widetilde{A}_p(t,t') = pg(t)\widetilde{G}^{[p]}_{p-1}(t,t')g(t'), \tag{4.155}$$

$$[i\partial_t + \lambda - (p-1)\omega_0]\widetilde{G}^{[p]}_{p-1}(t,t') - [(\widetilde{\Delta}_{p-1} + \widetilde{A}_{p-1}) \circlearrowright \widetilde{G}^{[p]}_{p-1}](t,t') = -i\delta_{\mathcal{C}}(t,t'), \tag{4.156}$$

and

$$\widetilde{B}_p(t,t') = (p+1)g(t)\widetilde{G}^{[p]}_{p+1}(t,t')g(t'), \tag{4.157}$$

$$[i\partial_t + \lambda - (p+1)\omega_0]\widetilde{G}^{[p]}_{p+1}(t,t') - [(\widetilde{\Delta}_{p+1} + \widetilde{B}_{p+1}) \circlearrowright \widetilde{G}^{[p]}_{p+1}](t,t') = -i\delta_{\mathcal{C}}(t,t'). \tag{4.158}$$

Numerically, we first determine all $G^{[p]}_{p\pm1}$ functions for $p \in [0, N^{\text{cut}}_{\text{ph}}]$ using Eqs. (4.155, 4.156, 4.157, 4.158). After computing auxiliary Green's functions, we will solve the Dyson equation in Eq. (4.154) to compute the propagator ($\mathcal{G}$). This propagator will be then employed in calculating the projected Green's function using Eq. (4.123).

### 4.2.2 Observables

Using the above formalism, we will analyze our data using some time-dependent observables as follows.

#### Pure Electronic observables

***Electron density***

In every Green's function formalism, the particle density in obtained by

$$n(t) = \langle c_i^\dagger(t) c_i(t) \rangle \tag{4.159}$$
$$= -iG(t,t)^<. \tag{4.160}$$

In low density limit, the above Green's function should be swapped with the projected Green's function as

$$n(t) = -i\xi \widetilde{G}^<(t,t), \tag{4.161}$$

where $\xi$ is the fugacity. In our numerical simulation, we will enforce $-i\widetilde{G}^<(t,t) = 1$ and determine $\lambda$ to fulfill this demand.

***Kinetic energy***

The kinetic energy of the system can be achieved by

$$E_{\text{kin}}(t) = \sum_k \epsilon_k(t) n_k(t), \tag{4.162}$$
$$= \sum_k \epsilon_k(t) \langle c_k^\dagger(t) c_k(t) \rangle, \tag{4.163}$$
$$= -i \sum_k \epsilon_k(t) G_k^<(t,t'), \tag{4.164}$$

where $\sum_k = 1$, $G_k$ is the momentum-resolved Green's function, and $\epsilon_k$ is the dispersion relation. Here, we take the advantage of Eq. (4.160) to replace the momentum-dependent electron density by the corresponding lesser Green's function. In addition, the impurity and lattice Dyson equations are

$$(i\partial_t - \mu) G_{\text{imp}}(t,t') - [\Delta * G_{\text{imp}}](t,t') = \delta_{\mathcal{C}}(t,t'), \tag{4.165}$$
$$(i\partial_t - \mu) G_k(t,t') - [\epsilon_k * G_k](t,t') = \delta_{\mathcal{C}}(t,t')\delta_{k,0}. \tag{4.166}$$

Taking the momentum sum of the lattice Dyson equation for the lesser component will provide

$$(i\partial_t - \mu) \sum_k G_k(t,t') - \sum_k [\epsilon_k * G_k]^<(t,t') = \delta_{\mathcal{C}}(t,t'). \tag{4.167}$$

Substituting $\sum_k G_k = G_{\text{imp}}$ in the above equation, and comparing that with the impurity Green's function of Eq. (4.165) will allow us to evaluate the kinetic energy as

$$E_{\text{kin}}(t) = -i \sum_k \epsilon_k(t) G_k^<(t,t'), \tag{4.168}$$
$$= -i[\Delta * G_{\text{imp}}]^<(t,t'). \tag{4.169}$$

This evaluation of the kinetic energy is applicable for every system, studied within the DMFT framework. In the one-electron system, the kinetic energy will be computed by

$$E_{\mathrm{kin}}(t) = -i\xi[\widetilde{\Delta} \circlearrowleft \widetilde{G}_{\mathrm{imp}}]^{<}(t,t'). \tag{4.170}$$

***Time/Momentum resolved photoemission spectrum***

To monitor the evolution of the occupied transient state, we will compute the photoemission spectrum [43]. This spectrum is experimentally measurable within pump-probe experiments, where the system is excited by a short and intense pump pulse and will be measured by a probe pulse with the delay time of $t$. Ignoring the induced excitation by the probe pulse on the sample, and considering the situation where the pump and probe pulses have no overlap, we can write the photoemission spectrum as

$$I(\omega,t) = -i\int \mathrm{dt}_1\mathrm{dt}_2 S(t_1)S(t_2)e^{i\omega(t-t')}G^{<}(t+t_1,t+t_2), \tag{4.171}$$

where $t$ is the probe time, $\omega$ is the energy, and $S(t)$ is the probe shape which we usually set to a Gaussian form. (One should note that when the system is exposed by pump and probe pulses, some multi-phonon excitations, which were not accessible when either the pump or the probe pulse is active, can be occupied. Thereby, studying such situations requires that both pump and probe pulses included into the model, which is not the case in our presented results.) $I(\omega,t)$ is the time-resolved photoemission spectrum, which in equilibrium can be written as

$$I(\omega) = \int \mathrm{d}\omega' A(\omega-\omega')f(\omega-\omega')|\widetilde{S}(\omega')|^2, \tag{4.172}$$

where $\widetilde{S}(\omega) = \int \mathrm{dt}e^{i\omega t}S(t)$, $A$ is the electron spectral function, and $f(\omega)$ is the Fermi distribution function.

Changing the Green's function in Eq. (4.171) by a momentum-resolved Green's function will let us yield the momentum-resolved photoemission spectrum,

$$I_k(\omega,t) = -i\int \mathrm{dt}_1\mathrm{dt}_2 S(t_1)S(t_2)e^{i\omega(t_1-t_2)}G_k^{<}(t+t_1,t+t_2). \tag{4.173}$$

In the low-density limit, the Green's function in Eqs. (4.171, 4.173) will be replaced by $\widetilde{G}$ and $\widetilde{G}_k$, respectively.

***Electron-phonon correlation functions***

We can define a generic mixed observable of the form

$$\mathcal{O}_{\rm imp}(t) = \langle n(t)\mathcal{F}[b, b^\dagger](t)\rangle, \tag{4.174}$$

where $\mathcal{F}$ is a function of the impurity phononic operators. Following similar approach introduced in Sec. 4.2.1, we would have

$$\langle n(t)\mathcal{F}[b, b^\dagger](t)\rangle = -i\xi(1-\beta\omega_0)\sum_{p,p'}\langle p|\mathcal{F}[b, b^\dagger](t)|p'\rangle\mathcal{G}^<_{p,p'}(t,t). \tag{4.175}$$

***Phonon number distribution function***

The phonon number distribution function on the impurity site is defined as

$$P_{\rm ph}(n,t) = \langle n_{\rm imp}(t)\delta_{b^\dagger_{\rm imp}(t)b_{\rm imp}(t)=n}\rangle, \tag{4.176}$$

where $\delta$ is the Kronecker delta function.

This observable can be simply evaluated by the diagonal propagator, using Eq. (4.175), as

$$P_{\rm ph}(n,t) = -i\xi(1-e^{\beta\omega_0})\delta_{p,n}\mathcal{G}^<_{p,p}(t,t). \tag{4.177}$$

***Average of the phonon number***

The average of the phonon number on the impurity is given by

$$N_{\rm ph} = \langle n_{\rm imp}(t)b^\dagger_{\rm imp}(t)b_{\rm imp}(t)\rangle, \tag{4.178}$$

where $\mathcal{F}[b, b^\dagger]$ is replaced by $b^\dagger b$. Using Eq. (4.175) will lead us to

$$N_{\rm ph}(t) = -i\xi(1-e^{\beta\omega_0})\langle p|b^\dagger(t)b(t)|p\rangle\mathcal{G}^<_{p,p}(t,t). \tag{4.179}$$

***Electron-displacement correlation function***

The electron-displacement correlation function on the impurity site is defined as

$$C(t) = \langle n_{\rm imp}(t)(b_{\rm imp}(t) + b^\dagger_{\rm imp}(t))\rangle. \tag{4.180}$$

Using Eq. (4.175) suggests that

$$C(t) = -i\xi(1-\beta\omega_0)\Big[(\sqrt{p+1})\mathcal{G}^<_{p,p+1}(t,t) + (\sqrt{p-1})\mathcal{G}^<_{p,p-1}(t,t)\Big]. \tag{4.181}$$

It is apparent that either we should compute two off-diagonal elements of the propagator, which is accompanied by further numerical costs, or we need to make an alternative strategy which takes an advantage of already computed Green's functions.

To acquire a relation for $C(t)$, we would again have a look at the impurity Dyson equation,

$$(i\partial_t - \mu)G_{\rm imp}(t,t') - [\Delta * G_{\rm imp}](t,t') - [\Sigma * G_{\rm imp}](t,t') = \delta_{\mathcal{C}}(t,t'). \tag{4.182}$$

This equation can be simply derived, using the Heisenberg equation of the electron annihilation operator as

$$\partial_t c_{\rm j}(t) = i[H(t), c_{\rm j}(t)], \tag{4.183}$$

where j is a site index. The corresponding lattice Green's function would be

$$\begin{aligned} i\partial_t G_{\rm ii}(t,t') =& iJ \sum_{\rm j\ nn\ i} \Big( \langle c_{\rm j}^\dagger(t') c_{\rm i}(t) \rangle \Big) \\ & - i\mu \langle c_{\rm i}^\dagger(t') c_i(t) \rangle + ig(t) \langle c_{\rm i}^\dagger(t') c_{\rm i}(t) (b_{\rm i}(t) + b_{\rm i}^\dagger(t)) \rangle. \end{aligned} \tag{4.184}$$

Rearranging different terms of above equation yields

$$(i\partial_t - \mu)G_{\rm ii}(t,t') - J[G_{\rm ij} + G_{\rm ji}](t,t') - ig(t)\langle c_{\rm i}^\dagger(t) c(t) (b_{\rm i} + b_{\rm i}^\dagger) \rangle = 0, \tag{4.185}$$

where by considering the impurity site on site $i$, the nonlocal term, consisting of the Green functions ($G_{\rm ij}$), can be represented as

$$-J \sum_{\rm j\ nn\ i} G_{\rm ij}(t,t') = \big[\Delta * G_{\rm imp}\big](t,t'). \tag{4.186}$$

Comparing Eq. (4.185) with Eq. (4.182), and summing over momentum space would finally suggests that

$$C(t) = -i[\Sigma * G]^<(t,t'), \tag{4.187}$$

$$= -i\xi(1 - e^{-\beta\omega_0}) \sum_p [(\widetilde{A}_p + \widetilde{B}_p) \circlearrowleft \mathcal{G}_{pp}]^<(t,t). \tag{4.188}$$

Here, in the last equation, we brought the convolution to the one electron limit and substitute the self-energy by the summation of $A$ and $B$ Green's functions.

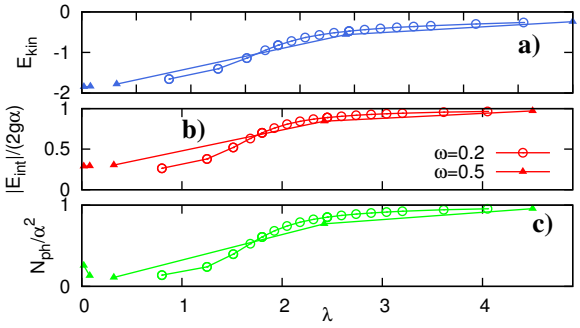


Figure 4.3: The kinetic energy, interaction energy, and phonon number correlation function as a function of $\lambda$ for systems with $\omega_0 = 0.2$ and $\omega_0 = 0.5$ at $\beta = 10$.

## 4.3 Results and discussion

In Sec.4.2.1, we proposed an accurate DMFT scheme for studying the low-density limit of carriers in the Holstein model. Here, we will investigate the properties of the Holstein model in and out of equilibrium on the Bethe lattice. We will investigate the relaxation properties of a hot initial carrier which is suddenly coupled to the phonons. Such an initial state is an effective modeling for experiments in which a low density of carries is transfered to the valance band, well-separated from the conduction band, by a short and ultrafast laser pump pulse to address the dynamical formation of polarons [46, 49, 50, 1]. Succeeding this ultra-fast particle transfer, a natural question would be the relevant relaxation, or thermalization, mechanism of such promoted carries.

In the following, we first explain the equilibrium physics of the Holstein model in the low-density limit of carriers, and will continue the discussion by presenting the nonequilibrium results. Regarding the nonequilibrium results, after explaining the preparation of the initial state, we will inquire its time-evolution after a sudden interaction-quench, and we will present the response of several observables under a sudden time-dependent change of the electron-phonon coupling.

### 4.3.1 Equilibrium results

Fig. 4.3 shows the equilibrium kinetic energy, interaction energy, and average number of phonons for two sets of systems with $\omega_0 \in \{0.2, 0.5\}$. Results in Fig. 4.3 a), for both phonon frequencies, exhibit that in the strong coupling limit the kinetic energy of the system is

decreasing. In addition, the curvature of the kinetic energy is also changing from weak to strong coupling limit. This change is taking place for $\lambda > 1$ which is an imprint of the presence of a polaron in the system. In the extreme strong coupling limit, where the polaron is formed, it can be straightforwardly shown that

$$J_{\mathrm{r}} = Je^{-\alpha^2}, \tag{4.189}$$

where $J_{\mathrm{r}}$ is the renormalized hopping amplitude in the shifted oscillator basis. Although this renormalization has a $\omega_0$ dependence, at very large couplings the limits of renormalized hopping amplitude would go to zero, and thereby the kinetic energy will not express a significant differences for $\omega = 0.2$ and $\omega = 0.5$. To study such a response more systematically, we also have a look at the average number of phonons. Fig. 4.3 c) presents the renormalized average number of phonons ($N_{\mathrm{ph}}$). The renormalization is obtained in the atomic limit as

$$N_{\mathrm{ph}} = \lim_{\lambda\to\infty} \langle a^\dagger a\rangle = \langle \widetilde{X}^2 + \widetilde{P}^2\rangle, \tag{4.190}$$

$$= \frac{1}{2}\langle (X - X_0)^2 + P^2\rangle = \alpha^2 = \frac{\lambda}{\gamma}, \tag{4.191}$$

where we have used Eq. (4.7, 4.8) in the first line of the above equality. On should note that the renormalization factor for a fixed $\lambda$ has a phonon-dependancy, via $\gamma$, and thus the averaged number of phonons is larger when $\omega_0$ is smaller.

Fig. 4.3 b) displays the renormalized interaction energy, by the factor of $2g\alpha = 2g^2/\omega_0$. This renormalization factor is obtained in the extreme strong coupling limit as

$$E_{\mathrm{int}} = g\langle c^\dagger c(a^\dagger + a)\rangle = g\langle c^\dagger c\widetilde{X}\rangle, \tag{4.192}$$

$$= g\langle c^\dagger c(X - X_0)\rangle, \tag{4.193}$$

$$= -2g\alpha. \tag{4.194}$$

The renormalization factor is known as the polaron energy. A small deviation from this energy in Fig. 4.3 b) indicates that the lattice solution is a mixture of a localized and a delocalized state, where its nonlocal nature is responsible for the deviation from the atomic picture. This delocalized state in the strong coupling limit can be fully realized in the adiabatic picture where the effective adiabatic potential has two minima, see Fig. 4.2 b). Moreover, since the interaction energy is a representative of the electron-phonon correlation in distorted potential, either adiabatic or the local one, its larger values indicates severe deformation of the lattice. Such a deformation traps the electron, and consequently the kinetic energy will reduces considerably. To collect more information about the number of

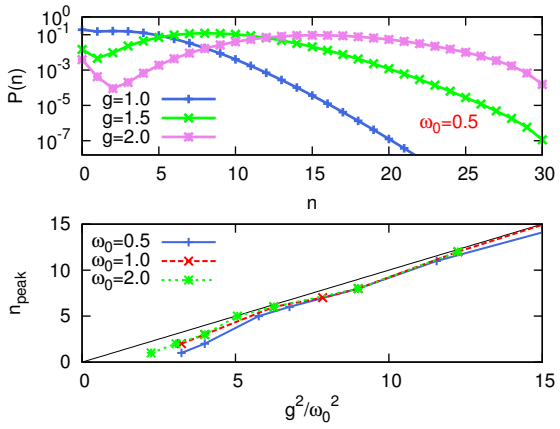


Figure 4.4: The equilibrium phonon distribution function at $\beta = 10$ in the strong coupling regime. a) $P_{\rm ph}(n)$ for systems at $\omega_0 = 0.5$ and $g \in \{1.0, 1.5, 2.0\}$. b) The nonzero location of $\max[P_{\rm ph}(n)]$ as a function of $g^2/\omega_0^2$ for phonon frequencies $\omega_0 \in \{0.5, 1.0, 2.0\}$.

accompanied phonons in the phonon cloud of a polaron, we plot the phonon distribution function in Fig. 4.4.

Fig. 4.4 a) plots the phonon distribution function as a function of phonon number for $\omega_0 = 0.5$ in the strong coupling regimes. As we discussed in Sec. 4.1.1, in the local picture, the strong coupling regimes, $P(n)$ is a shifted Poisson distortion at very small temperatures. For a system at finite temperature, $P(n)$ presents a sharp peak at nonzero phonon number. This number of phonons is related to the most probable phononic state in averaging the phonon distribution operator. When the full density of the electron is accumulated on one site, in the local picture, we would have

$$\langle c_i^\dagger c_i a_i^\dagger a_i \rangle \approx \langle a_i^\dagger a_i \rangle, \tag{4.195}$$

$$\approx \frac{g^2}{\omega_0^2}. \tag{4.196}$$

To investigate this relation in our results, we plot the location of the maximum in $P(n)$, namely $n_{\rm peak}$, as a function of $g^2/\omega_0^2$ for three different phonon frequencies in Fig. 4.4 b). Results are in good agreement with the expected Lang-Firsov correspondence. Slight deviations in smaller $\alpha^2$ values, from the expected black line, is connected to the violation of the local picture, where part of the electron density is spread to other sites of the lattice.

Apart from the local observables, the described equilibrium physics of the Holstein model can be also studied by spectral functions. Spectral functions at various phonon

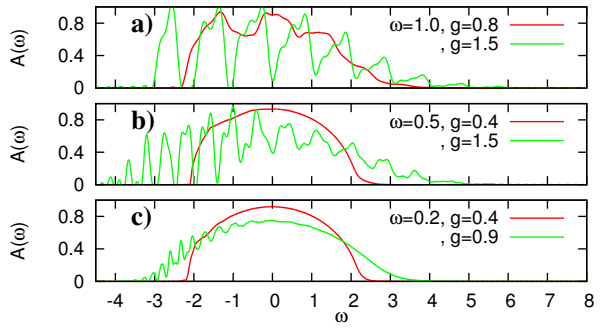


Figure 4.5: The equilibrium spectral function for three phonon frequencies $\omega_0 = 1, 0.5, 0.2$ in weak and strong coupling regime at $\beta = 10$.

frequencies are plotted in Fig. 4.5 for both the weak and strong coupling limits. The semi-elliptical density of state for the uncoupled system with the bandwidth from -2 to 2, is modified when the electron-phonon coupling is nonzero. These modifications strongly depend on coupling strength. In the weak coupling limit, we would see an slight deformation of the density of state. In contrast to that, in the strong coupling regime, the deformation drastically changes the spectral function and brings it into some separated phononic sidebands in addition to a connected part at higher energies. The distance between these side bands is close to $\omega_0$, slightly renormalized by the real part of the self-energy in equilibrium.

The lowest well-separated sidebands, with bandwidths much smaller than $J$, are related to the coherent state satisfying the condition that $\Im\Sigma(\omega_*) \ll J$, where $\omega = \omega_*$ is the location of the coherent sideband [19].

### 4.3.2 Nonequilibrium results

In the remaining of this chapter, we will explore the physics of the Holstein model out of equilibrium. As we have mentioned, we will simulate the properties of a single photoexcited carrier. We will first elaborate the preparation of the initial state, and then explore the relaxation dynamics of such an initial state by presenting the local observables as well as spectral properties of different systems, for various electron-phonon coupling.

### Preparation of the initial state

As we mentioned before, we are willing to provide a description for the photoexcited carriers, created within the photoemission experiments. We are interested to those experiments where the density of promoted particles are very small, and thereby our proposed theory would be applicable. To be more precise, we are determined to understand the relaxation dynamics of the conduction electron which has been excited to the valance band, well-separated from the conduction band. As these carriers absorb energy, during their excitation process, the effective temperature of these carriers would be larger than the temperature of unexcited electrons as well as the lattice. Hence, to describe the injection of energy to the excited electrons on a one-band system, we will prepare a system where the initial temperature of the lattice is lower than the associated electronic temperature. Considering the lattice in smaller temperature is also rooted in the fact that, experimentally, the transferring duration of the electron carrier is ultra-short, the lattice will not be affected in the electron-promotion mechanism, and thereby we are allowed to keep its phonon frequency as well as its temperature fixed before and after the incidence of the pump-pulse. In addition, as has been mentioned before, we will try to investigate a system under the quench of $g$, as the electron and phonons are decoupled during the promotion process of the electron to the valance band. Such a preparation will enable us to, instead of exciting the carrier in a multi-band system, adjust the initial distribution function in a one-band model, and as a result reduce the computational costs.

To perform such an adjustment, we will employ an effective temperature which satisfies the condition

$$\omega_0^{\mathrm{ini}}\beta^{\mathrm{ini}} = \omega_0\beta_{\mathrm{latt}}, \tag{4.197}$$

where $\omega_0^{\mathrm{ini}}$ is the frequency of the auxiliary bath with the temperature $1/\beta^{\mathrm{ini}}$ at $t = 0$. Besides, as initially the electron and phonons are decoupled ($g = 0$), we would consider our initial electronic density in a phononic bath with a higher temperature to manipulate the initial electronic distribution function. Later on ($t > 0$), by switching the electron-phonon coupling to a nonzero value ($g > 0$), we would set the lattice temperature to $\beta_{\mathrm{latt}}$ with the frequency of $\omega_0$. In addition, initially at ($t = 0$), any thermal expectation values of the impurity Hamiltonian, introduced in Eq. (4.88), have only the Boltzmann like ($e^{-\omega_0^{\mathrm{ini}}\beta^{\mathrm{ini}}}$) contribution. Immediately after quenching el-ph coupling, we would still expect the same thermal expectation value since, despite the nonzero coupling, the number of excited phonons is still the same as uncoupled thermal value.

Exploiting such a preparation, we will now demonstrate the electron relaxation under various parameter regimes of the Holstein model. In the following, we will present results

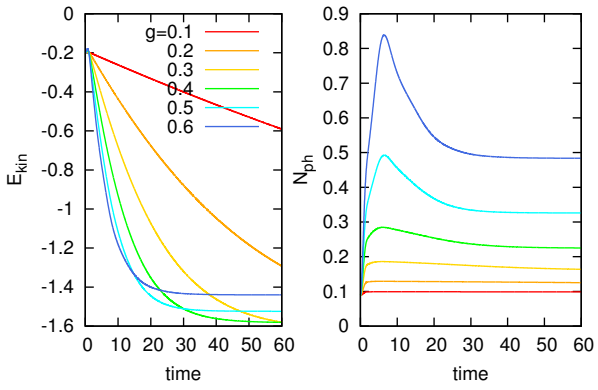


Figure 4.6: The out of equilibrium kinetic energy, and average phonon number at $\omega_0 = 0.5$, and $\beta_{\rm latt} = 5$, initially prepared at $\beta^{\rm ini} = 0.2$.

in the weak and strong coupling regimes. Within these regimes, we will also explore the adiabatic and nonadiabatic physics of the model.

### Local observables in weak coupling limit

In this section, we will present the properties of a transient state created after a sudden ramp of the el-ph coupling. Figs. (4.6, 4.7, 4.8) plot the evolution of the local observables out of equilibrium. Weak coupling results, e.g. $(\omega_0 = 0.5, g \in \{0.1, 0.2, 0.3, 0.4\})$, $(\omega_0 = 1.0, g \in \{0.3, 0.6\})$,and $(\omega_0 = 0.2, g = 0.4)$, show that the kinetic energy is monotonously relaxing, after a fast transient response, headed to the bottom of the band. This relaxation depends on $g$, and is faster in stronger couplings. The phonon number $N_{\rm ph}$ exhibits a rapid transient increase of the involved phonons, followed by a subsequent slower decrease.

This behavior can be easily understood within the perturbation theory, where only one phonon contributions are included in the self-energy of the system. Using Eqs. (4.155, 4.157), we can write the one-phonon self-energy as

$$\widetilde{\Sigma}_{p=0}(t,t') = \widetilde{A}_{p=0}(t,t') + \widetilde{B}_{p=0}(t,t'), \tag{4.198}$$

$$= 0 + g(t)\widetilde{G}_1^{[1]}(t,t')g(t'), \tag{4.199}$$

where $\widetilde{G}_1^{[1]}$ is determined by the initial hot electron distribution.

Eq. (4.199) implies that, in the weak-coupling limit, the electron energy will be dissipated as a result of inelastic scattering of the electron with phonons. The assigned

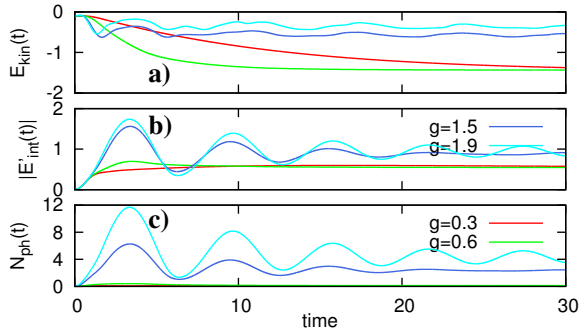


Figure 4.7: The out of equilibrium kinetic energy, interaction energy, and average phonon number at $\omega_0 = 1.0$, and $\beta = 10$, initially prepared at $\beta^{\rm ini} = 0.1$.

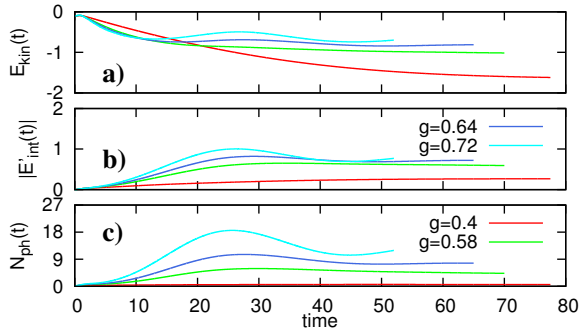


Figure 4.8: The out of equilibrium kinetic energy, interaction energy, and average phonon number at $\omega_0 = 0.2$ and $\beta = 10$, initially prepared at $\beta^{\rm ini} = 0.1$.

time-scale for this type of scattering, at large $\beta_{\rm latt}$, can be obtained from the Fermi golden rule, since the time variation of the corresponding state is slow,

$$\frac{1}{\tau(\epsilon)} = g^2 G(\epsilon - \omega_0), \tag{4.200}$$

where $G(\epsilon - \omega_0)$ is the energy-representation of the one-phonon screened Green's function, obtained from $\widetilde{G}_1^{[1]}$. In addition, $G(\epsilon - \omega_0)$ describes the rearrangement of the initial uncoupled density, obtained by $G(\epsilon)$. In the weak coupling limit, this rearrangement is mainly a shift of the semi-elliptical density of state by $\omega_0$, see also Fig. 4.5 c) at $\omega_0 = 0.2$, and $g = 0.4$.

In the following, we will show that how the transfer rate ($\tau$) governs the long-time response of the kinetic energy. Generally speaking, for densities of state with van Hove

singularities at their edges, with the general form of $D(\epsilon) = \sqrt{\epsilon}$, we can write the transfered density as

$$N_{\rm d}(t) = -i \sum_k \epsilon_k G_k^<(t,t'), \tag{4.201}$$

$$= -i \int_0^{\omega_0} {\rm d}\epsilon \quad G_\epsilon^<(t,t), \tag{4.202}$$

$$= \int_0^{\omega_0} {\rm d}\epsilon \quad n_\epsilon(t), \tag{4.203}$$

$$= \int_0^{\omega_0} {\rm d}\epsilon \quad n_0 e^{-t/\tau(\epsilon)}, \tag{4.204}$$

where in the second line we replaced the momentum sum by the energy integration, and in the last line we substitute $n_\epsilon(t)$ by

$$n_\epsilon(t) = n_0 e^{-t/\tau}. \tag{4.205}$$

Here, we employed the exponential relaxation rate of the electron density, which we will affirm in Sec. 4.3.2. To evaluate the integration of Eq. (4.204), we first introduce a new variable

$$x = \frac{t}{\tau} = t\sqrt{\epsilon}, \tag{4.206}$$

where we set $g = 1$ for simplicity, later we will assess its impact on the response of the system. Changing the $\epsilon$ variable by $x$ will bring the long-time limit of Eq. (4.204) to the form

$$N_{\rm d}(t) \propto \lim_{x\to\infty} \int_0^{t\sqrt{\omega_0}} {\rm dx} \frac{2x}{t^2} e^{-x}, \tag{4.207}$$

$$\propto \frac{1}{t^2}. \tag{4.208}$$

$N_{\rm d}$ is the amount of electron density which has been excited to the deformed part of the density of state. These electrons are playing the major role in the asymptotic behavior of the kinetic energy. We thus will obtain

$$\frac{dE_{\rm kin}}{dt} \propto \frac{dN_d}{dt}, \tag{4.209}$$

$$\propto \frac{1}{t^3}. \tag{4.210}$$

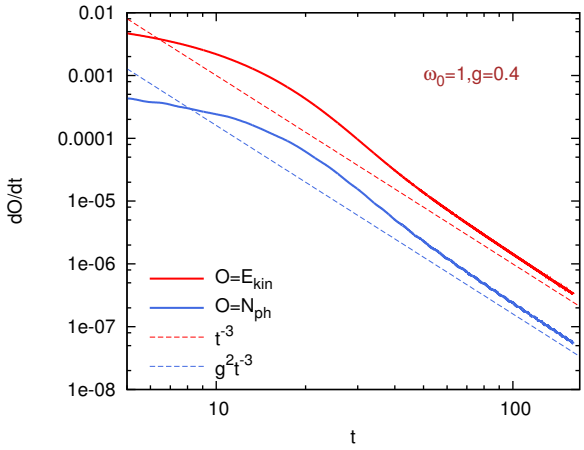


Figure 4.9: The time-derivative of the kinetic energy and the average phonon number as a function of time for a system at $(\omega_0 = 1.0, g = 0.4, \beta_{\rm latt} = 10, \beta^{\rm ini} = 0.1)$(Solid lines) is compared with its long-time behavior (dashed line), obtained from Eqs. (4.210, 4.213).

As the dimensionality has been entered $N_{\rm d}$ by the depicted density of state, in our case with the van Hove singularity, one should expect different asymptotic behavior of the kinetic energy in various dimensions. For instance, it has been shown that in one-dimension the kinetic energy decays exponentially [55].

In addition, the large-time response of the average of phonon numbers is also related to $N_{\rm d}$. This can be easily realized by Eq. (4.179). Since the el-ph coupling is so small, one can assume that the phonon number-operator is the constant of motion, and thereby the time evolution of $\langle p|b^\dagger b|p\rangle$ do not play significant role in determining the time-evolution of the system. Moreover, small $g$ will result in the activation of few phonons, as has been employed also in Eq. (4.200), thereby the only long-time contribution should originate from $\mathcal{G}_{00}$.

The equation of motion of this propagator, which is obtained by Eq. (4.154), is

$$i\partial_t \mathcal{G}_{00}(t,t') - \left[\widetilde{\Delta}_0 + \Sigma_0\right] \circlearrowright \mathcal{G}_{00}(t,t') = \delta_{\mathcal{C}}(t,t'), \tag{4.211}$$

where $\Sigma_0$ is defined in Eq. (4.199). Transforming the above equation to its lattice counterpart first, replacing the momentum sum by the energy integration (explained above) second, and finally evaluating the energy integral at the edge of the density of state, similar to Eq. (4.204), will suggest that the time-derivative of the $\mathcal{G}_{00}$ is proportional to

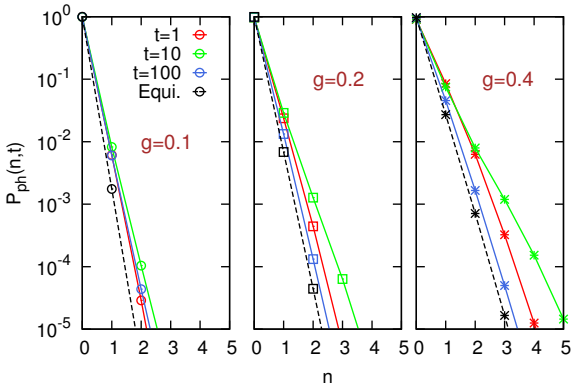


Figure 4.10: Phonon distribution function in the weak coupling regime for a system at $(\omega_0 = 1, \omega^{\text{ini}} = 100, \beta^{\text{ini}} = 0.1, \beta_{\text{latt}} = 10)$.

time-derivative of $\Sigma_0$, which by itself is related to $g^2 dN_d/dt$. We hence can conclude that

$$\frac{dN_{\text{ph}}}{dt} \propto g^2 \frac{dN_d}{dt}, \tag{4.212}$$

$$\propto \frac{g^2}{t^3}. \tag{4.213}$$

In Fig. 4.9, we present the agreement between the asymptotic expressions in Eqs. (4.210, 4.213), and our DMFT result for a system at $(\omega_0 = 1.0, g = 0.4, \beta_{\text{latt}} = 10, \beta^{\text{ini}} = 0.1)$.

The renormalized interaction energy ($E'_{\text{int}} = E_{\text{int}}/(2g\alpha)$) of the system is plotted in Fig. 4.7 b) and Fig. 4.8 b). Results show that, in the weak coupling regime, the interaction energy is very small and the electron is a mobile and inconsiderably, dressed particle. The larger the electron-phonon coupling is, the larger is the transient response, which is followed by a quicker relaxation in stronger coupling values. We strengthen this statement by presenting the phonon distribution function in Fig. 4.10. The phonon distribution functions are all zero centered, confirming that the electronic state is delocalized. The transient response is larger than the equilibrium values, emphasizing on the activation of more phonon in the process of electron relaxation. This activation is due to the absorption and emission of phonons by the hot carrier to reduce its energy. Furthermore, the thermalization timescale is longer for smaller electron-phonon couplings. This can be clearly observed by comparing $t = 100$ (blue line) from the equilibrium value (black line) in Fig. 4.10.

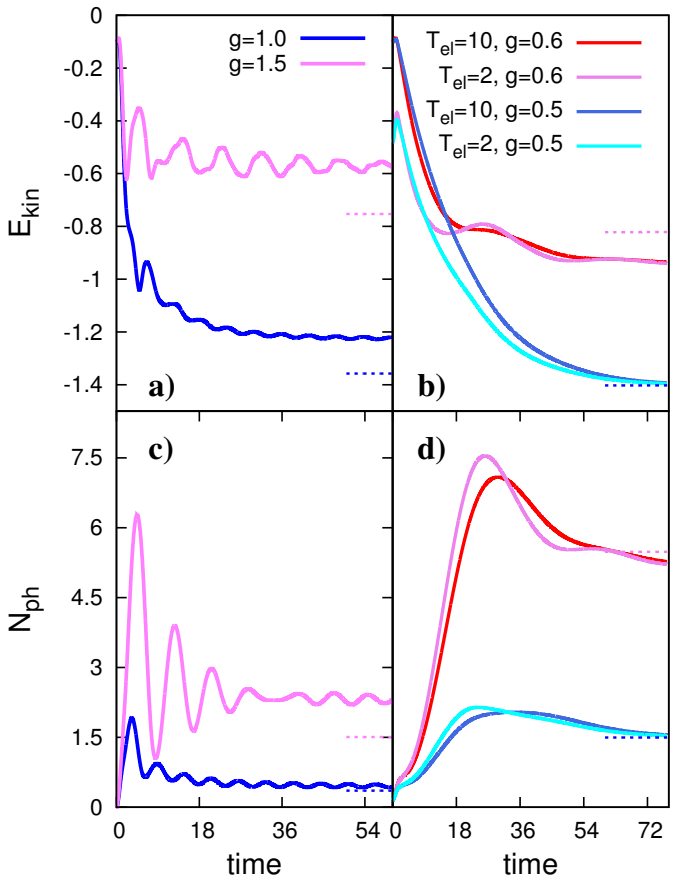


Figure 4.11: The kinetic energy and average phonon number. a), c) Strong coupling nonadiabatic results at ($\omega_0 = 1.0, \beta_{\rm latt} = 10, \beta^{\rm ini} = 1$). b), d) Strong coupling adiabatic results at ($\omega_0 = 0.2, \beta_{\rm latt} = 10, \beta^{\rm ini} = 1/T_{\rm el}$). Taken from Ref. [128].

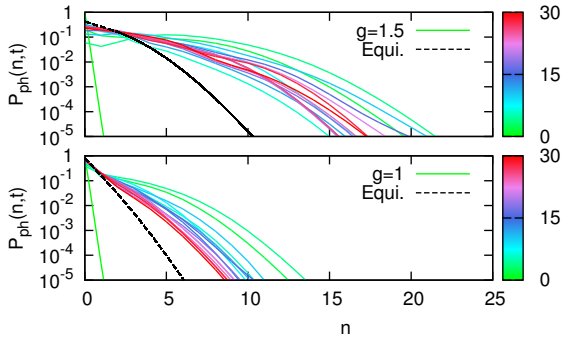


Figure 4.12: Phonon distribution function in nonadiabatic strong coupling regime for a system at ($\omega_0 = 1.0, \beta^{\rm ini} = 0.1, \beta_{\rm latt} = 10$). The color coding indicates different times. Black lines are equilibrium results at $\beta = 10$.

### Local observables in the strong coupling limit

In the strong coupling limit, local observables, plotted in Figs. 4.7-4.8, show a coherent oscillation with the frequency of $\omega_0$. The amplitude of this oscillation is smaller in the adiabatic regime, i.e. at $\omega_0 = 0.2$, than in the non-adiabatic regime. The damping of this amplitude is connected to the number of excited phonons, as the relaxation mechanism. Eq. (4.191) shows that in the strong coupling limit the average number of phonons, for a fixed $\lambda$ and $J$, is proportional to $1/\omega_0$. Thus, the smaller phonon frequency leads to a larger number of phonons, which reduce the kinetic response of the system by renormalizing its hopping amplitude as mentioned in Eq. (4.189). In the nonadiabatic regime, apart from the coherent oscillating response, the kinetic energy also exhibits multi-phonon coherent oscillations, for instance $2\omega_0$, see also Fig. 4.11 a).

Furthermore, the long-time nonequilibrium response does not lead to the thermalization in the strong coupling regime. The reason behind this response is as follows. As phonons are the only decaying mechanism in the one-electron system, the reduced energy would be multiple of the phonon frequency. Thereby, larger $\omega_0$ can not bring the system to the equilibrium and thus the system would be trapped. Such a response is sometimes called as the phonon-window effect. Moreover, due to the nonequilibrium preparation of the system, the nonequilibrium dressed particle is dragging more number of phonons with itself, indicating that the electron is not experiencing the ground state Holstein physics.

We also assess the influence of the initial decoupled state in the adiabatic regime on the long-time response in Fig. 4.11 b) and d). It is shown that despite the distinguishable correlation between the short-time dynamics and the initial state, this correlation will

vanish at later times, and results are approaching the same final state. In strong-coupling adiabatic regime, the kinetic energy, plotted in Fig. 4.11 b), exhibits a slight larger absolute values for $g = 0.6$ cases than in equilibrium. This is due to the coexistence of a delocalized and localized state in this parameter regimes, which we will discuss that in more details in the upcoming section.

The presence of a delocalized state is also visible when we study the time-evolution of $P_{\rm ph}(n,t)$, see Fig. 4.13-4.12. Fig. 4.12 presents $P_{\rm ph}(n,t)$ for systems in the nonadiabatic regime. All nonequilibrium results display larger distribution function at a fixed number of phonons in comparison to the equilibrium curves (black lines). This support the finding that the nature of the formed polaron which is clearly distinguishable from the the ground-state polaron in $P_{\rm ph}$. Fig. 4.12 also shows that as a function of time a zero-centered Poisson-like distribution function will be evolved into a broadened, but still zero-centered, Poisson distribution at smaller el-ph couplings, i.e. $g = 1$, and its center will be shifted to a nonzero value in stronger coupling regimes, i.e. $g = 1.5$.

In adiabatic regime, phonon distributions are, both in and out of equilibrium, non-zero centered Poisson-like distribution functions, where the position of their centers determines the number of phonons in polarons. In Fig. 4.13, we plot $P_{\rm ph}$ for two systems with $\omega_0 = 0.2$. As a result of initial hot carrier, the short time response of the system exhibit a delocalized nature which is strongly suppressed, although it is still larger than the equilibrium counterpart, in long-times. Hence, the system is still have a metallic tendency, even in very strong coupling regime, in this limit.

In Fig. 4.14, we make a comparison between nonequilibrium $n_{\rm peak}$ at $t = 40$ and its equilibrium counterpart. It is evident that the nonequilibrium polaron is accompanied by large phonon numbers. Moreover, $n_{\rm peak}$ is varying as a function of time. This variation also presents a coherent oscillation of phonons in larger phonon frequencies, see Fig. 4.12, which can be interpreted as a breathing mode of the lattice. When $\omega_0$ is in the adiabatic regime, we only can see the reduction of $n_{\rm max}$ as a function of time, which corroborates the relaxation of an excited transient polaron.

To obtain the exact phononic state of the polaron, we will now try to use the relation that we have provided in Sec. 4.1.1. There, we have derived the atomic limit phonon distribution function in Eq. (4.42), as

$$P_m(n+m) = P_0(n)\frac{n!m!}{(n+m)!}|L_m^{(n)}(\gamma^2)|^2, \tag{4.214}$$

where $\gamma = g/\omega_0$ and $P_0(n) = e^{-\gamma^2}\gamma^{2n}$. In Fig. 4.14, we plot the position of maximum, $n_{\rm max}$, for $P_m$ with $m \in \{0,1,2,3\}$. Results reveal that unsurprisingly equilibrium physics

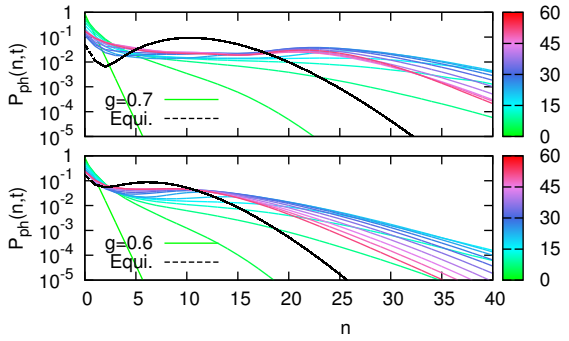


Figure 4.13: Phonon distribution function in the strong coupling regime for a system at $(\omega_0 = 0.2, \beta^{\text{ini}} = 0.1, \beta_{\text{latt}} = 10)$. Different line color corresponds to different times. Black lines are equilibrium results at $\beta = 10$.

can be understood from the ground state ($m = 0$) atomic limit. One should note that small deviations between equilibrium and $m = 0$ values of $n_{\max}$ are the consequence of not being at extreme strong coupling limit, results in observing nonlocal contributions. Nonequilibrium $n_{\max}$ crosses $m \neq 0$ lines of the atomic limit, which supports the presence of an excited polaron in these systems.

### Spectral functions and photoemission spectrum

In this section, we will continue the discussion by presenting results which are obtained from the Green's function. The presented results are spectral functions and photoemission spectrums, whose measurements are more accessible experimentally. Employing these results, we will consolidate our above mentioned conclusions.

We now study the evolution of the occupied state, related to the lesser Green's function out of equilibrium. We will present the evolution of the occupied state using the time/momentum resolved photoemission spectrum (PES), derived in Eqs. (4.171, 4.173), in several parameter regimes. We employed a Gaussian probe pulse of width $\delta$, see Fig. 4.15. (For technical reasons, the tail is cut off at times larger than $2\delta$.)

The time-resolved photoemission spectrum in the weak-coupling regime exhibits the exponential relaxation of the initial broad distribution function, see Fig. 4.17 a). The stronger the el-ph coupling is, the faster the broad initial distribution is relaxed, approaching the bottom of the band. Fig. 4.16 manifests that even for a relaxed spectral weight, the equilibration was not possible. This is due to the emission and absorption of opti-

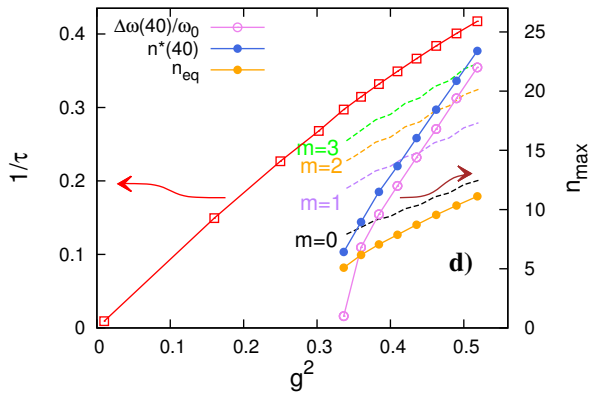


Figure 4.14: Left axis: The red curve with empty square points is the inverse of the relaxation time as a function of $g^2$ for a set of system at $(\omega_0 = 1.0, \beta_{\text{latt}} = 10, \beta_{\text{el}} = 0.1)$. Right axis: Orange solid line with filled circle in th maximum of $P_{\text{ph}}$ at $(\omega_0 = 0.2, \beta_{\text{latt}} = 10)$. Blue solid line with filled circle in nonequilibrium $n_{\max}$ for $(\omega_0 = 0.2, \beta_{\text{latt}} = 10, \beta^{\text{ini}} = 0.1)$ at $t = 40$. Dashed lines are related to the atomic limit $n_{\max}$ for $m \in \{0, 1, 2, 3\}$ obtained from Eq. (4.214). Magenta solid line with empty circles presented the band splitting of the PES at $t = 40$, which has been divided to $\omega_0$. Taken from Ref. [128].

cal phonons, which are dispersion-less quanta, as the only relaxation mechanism of these systems, known as the phonon-window effect.

To check the relaxation of the high energy PES, at $\omega \in [2 : 6]$, we would fit our data to an exponential function as

$$F(t) = Ae^{-t/\tau} + C, \tag{4.215}$$

where $\tau$ is the relaxation time which we have expressed in Eq. (4.200), see also Fig. 4.14. Results fulfill our expectation on the linear dependancy of $\tau$ on $g^2$ in weak coupling regime.

In the nonadiabatic strong coupling regime, the nonequilibrium PES, displays a coherent oscillation, after the relaxation of high-energy densities, see Fig. 4.17 c-d). These oscillations reflect the excited polaron and can be understood already in the atomic limit. To show this, we computed the photoemission spectrum using the lesser Green's function defined in Eq. (4.59). The comparison, plotted in Fig. 4.18 b), indicates that the nonadiabatic polaron is almost the ground-state polaron.

Fig. 4.17 a-b) shows the photoemission spectrum in the adiabatic strong coupling regime. The initial exponential relaxation is slower than the nonadiabatic relaxation, as a result of smaller phonon frequency and slower activation of phonons, c.f. Fig. 4.11 c-d).

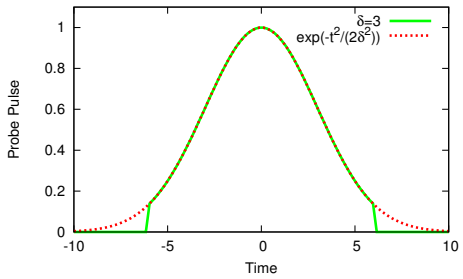


Figure 4.15: The Gaussian probe pulse cut at $t \pm 2\delta$ (solid line) and a Gaussian function $F(t) = \exp(-t^2/2\delta^2)$ (dashed line).

This response is followed by the emergence of two bands in the spectrum, where the density of the band close to $\omega = 0$ is larger. In Fig.4.14, we plot the band splitting of these with bands, divided by $\omega_0$, at $t = 80$ as a function of $g^2$. Results reveal that the plotted curve is almost parallel to the curve, which has been captured by the non-zero maximums of the phonon distribution functions. We thereby can conclude that the multi-peak structure of the PES is rooted in the same presented physics, related to the coexistence of the localized and delocalized states in the system. It is worthwhile noting that the small deviation between these two curves are originating from the frequency resolution of the probe pulse which is around $1/\delta = 0.33$. To unfold the nature of the two-peak structure in the PES even further, we first compare the spectrum with the atomic limit photoemission spectrum in Fig. 4.18 a). The multi-peak structure is also achievable in the atomic limit, related to the excited state of the shifted oscillator. The height of these peaks in the spectrum of the isolated atom are almost the same. This indicates that the system in the adiabatic regime should be explained in the adiabatic picture where apart from the polaronic state, which is an excited band out of equilibrium, a delocalized state at $\omega = 0$ is living in these systems.

To obtain further intuition about such a mixed state, we plot the energy-resolved photoemission spectrum in Fig. 4.19 a). One should recall that in the energy-resolved spectrums, the linear dispersions corresponds to the delocalized state, while dispersion-less bands are representing a delocalized state. We thereby can notice that the linear dispersion at $t = 6$ is indeed the delocalized state, which its density is relaxing to the edge of the bare bandwidth. Along with the relaxation of the delocalized state, two dispersion-less bands appear in the spectrum, which are assigned to the excited polaron formation. By passing the time, the delocalized state keeps concentrating at $\epsilon = -2$, and the density of the exited polaron is enhancing.

To elucidate the absence of a delocalized state in the nonadiabatic regime, we present

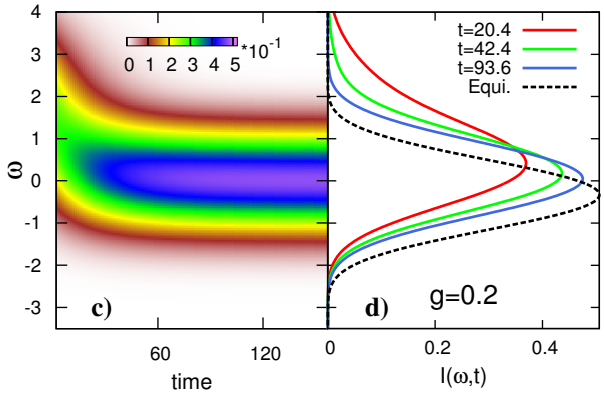


Figure 4.16: The photoemission spectrum in the nonadiabatic weak coupling regime for a system at $(\omega_0 = 1, \beta^{\text{ini}} = 0.1, \beta_{\text{latt}} = 10, g = 0.2)$ under a Gaussian pulse with $\delta = 3$. Taken from Ref. [128].

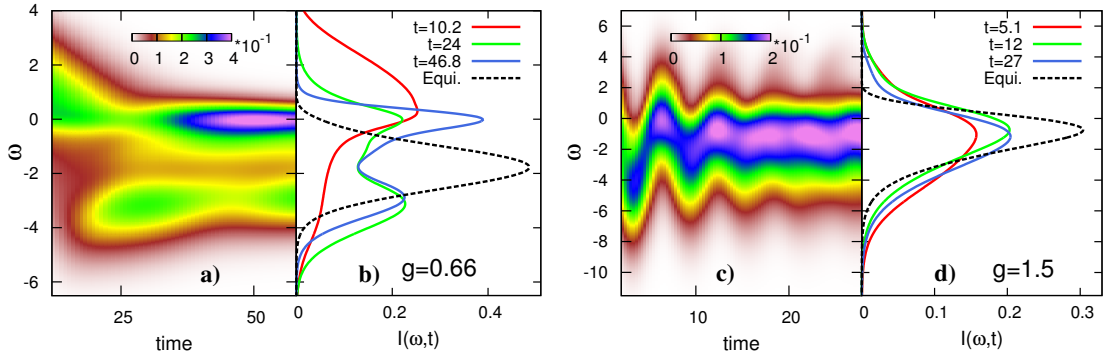


Figure 4.17: a-b) The photoemission spectrum in the adiabatic strong coupling regime for systems at $(\omega_0 = 0.2, \beta^{\text{ini}} = 0.1, \beta_{\text{latt}} = 10, g = 0.66)$ under a Gaussian pulse with $\delta = 1$. c-d) The photoemission spectrum in the nonadiabatic strong coupling regime for a system at $(\omega_0 = 1, \beta^{\text{ini}} = 0.1, \beta_{\text{latt}} = 10, g = 1.5)$ under a Gaussian pulse with $\delta = 1$. Taken from Ref. [128].

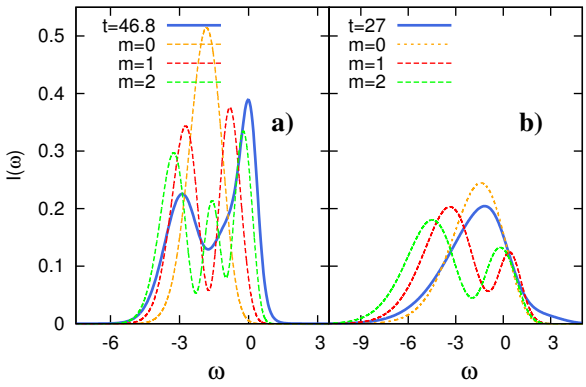


Figure 4.18: The photoemission spectrum in the atomic limit is compared with a) adiabatic results plotted in Fig. 4.17, b) nonadiabatic results plotted in Fig. 4.17. The temporal resolution of the pulse is the same as the DMFT results. Taken from Ref. [128].

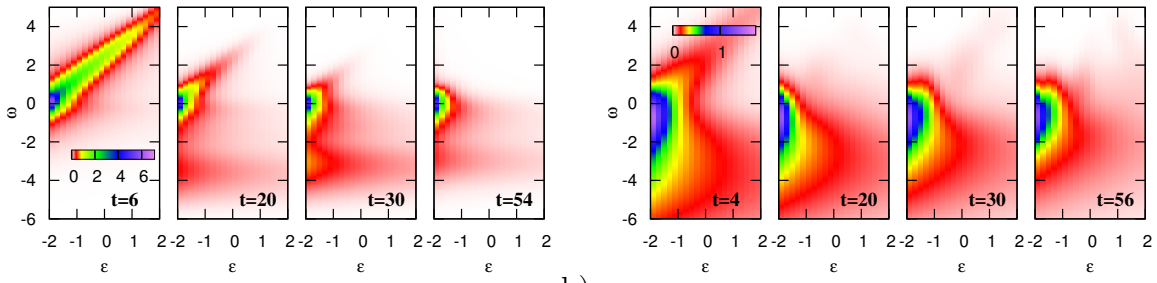


a) b)

Figure 4.19: The energy resolved photoemission spectrum for a system at ($\omega_0 = 0.2, g = 0.66, \beta_{\text{latt}} = 10, \beta^{\text{ini}} = 0.1$) at different times as indicated on the plots. The energy resolved photoemission spectrum for a system at ($\omega_0 = 1.0, g = 1.5, \beta_{\text{latt}} = 10, \beta^{\text{ini}} = 0.1$) at different times as indicated on the plots.

the energy-resolved photoemission spectrum, at $\omega_0 = 1.0$, in Fig. 4.19. Results show that after the rapid suppression of the density of the delocalized state, there is only one connected spectrum, related to the dressed electron, which is evolving in time.

## 4.4 Conclusion and outlook

As an extension of our work, it is interesting to study the inhomogeneous system under the similar preparation approach to investigate the properties of the formed nonequilibrium polaron. Another intriguing problem is solving a Holstein-t-J model with one hole carrier [12], which is interacting with its anti-ferromagnet background, and the lattice. The reported equilibrium results exhibit the formation of the magnetic polaron in weak electron-phonon coupling, and the suppression of the spin defects of the background in strong electron-phonon coupling regimes. It is tantalizing to tackle such a problem out of equilibrium to characterize the formation of such a polaron.

# Chapter 5

# Nonequilibrium DMFT study of the Hubbard Model

In the preceding chapter, we have studied the one-electron system under the influence of electron-phonon coupling. We have explored the physics of this system under various parameter regimes in and out of equilibrium. We have also presented that in the adiabatic strong-coupling regime, a sudden quench of the coupling parameter for an initial state with broad distribution function leads to the emergence of an excited polaronic band which coexists with a delocalized metallic state. We also have pointed out that in the weak-coupling regime, we would observe a relaxation in local observables which is due to the transfer of energy to the phononic bath.

The interesting question that we have investigated in the previous chapter is one of the examples in the class of photo-induced phase transitions in many body systems [119]. As the observed phase transitions, and their associated timescales, depend on interactions between particles, it is essential to understand the behavior of these systems in the presence of many electrons. We thus would put our effort on demonstrating the physics of many interacting electrons. We would explore systems which are close to the phase transition from a metallic to a Mott-insulating phase. We will characterize the underlying physics both in the metallic and insulating part of the phase diagram, and will also analyze the applicability of the adiabatic theorem near the Mott transition.

To be more precise, we will investigate the properties of the Hubbard model out of equilibrium. We will first explain the model and we will then extend the discussion by generalizing a particular method to solve DMFT equations, known as the slave-rotor technique [38].

## 5.1 Model and method

Unveiling the involved physics of an interacting electronic system is accompanied by many difficulties. This physics is therefore often discussed in terms of simple models. In this context, the Hubbard model is one of the prosperous approximations that discloses some of the properties of correlated electronic systems. In this section, we will elaborate this model Hamiltonian as well as its well-known properties.

### 5.1.1 Model Hamiltonian

The one-band Hubbard model in the second-quantization is given by

$$H = -\sum_{\langle ij\rangle,\sigma} J_{ij}(c^{\dagger}_{i\sigma}c_{j\sigma} + h.c.) - \mu\sum_{i} c^{\dagger}_{i}c_{i} + U\sum_{i} n_{i\uparrow}n_{i\downarrow}, \tag{5.1}$$

where $c^{\dagger}_{\sigma}$ ($c_{\sigma}$) creates (annihilates) an electron with spin $\sigma$, $J_{ij}$ is the hopping matrix element from site $i$ to the next nearest site $j$, $U$ is the on-site Coulomb repulsion, and $\mu$ is the chemical potential. Despite the incomplex form of the Hamiltonian, capturing its solution is a big deal due to the presence of both nonlocal (hopping) and a local (Hubbard interaction) terms in the Hamiltonian. In one-dimension these difficulties have been overcome by an exact solution based on the Bethe-ansatz [90], while in higher dimensions no exact solution is known.

The schematic phase diagram, shown in Fig. 5.1 [81], incorporates three main phases which are metallic, Mott insulating, and ordered phases. The metallic phase can be well described within the Fermi liquid picture, where electrons are mobile. This phase of matter exhibit a three-peak structure on its density of state (DOS), shown in Fig. 5.2 a), with two peaks at $\approx \pm U/2$, known as upper and lower Hubbard bands, and a central coherent quasiparticle peak at zero frequency. At a fixed Hubbard interaction, the height of the quasiparticle peak depends very much on the temperature. Increasing the temperature, brings the three-peak DOS to a two connected peaks where the quasiparticle peak is not well-defined.

On the $U$-dominant part of the phase diagram, we would have a Mott-insulator with a well-separated two-peak DOS located at $\approx \pm U/2$, see also Fig. 5.2 c). In the bad-insulating phase, presented in Fig. 5.1, the Hubbard gap, at large temperatures, is closed by a small spectral density at low frequencies.

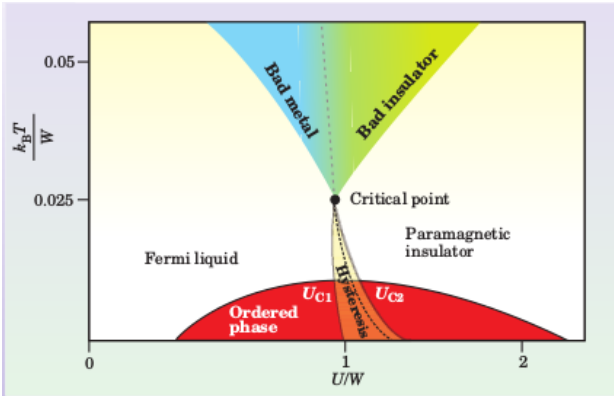


Figure 5.1: The phase diagram of the Hubbard model consisting of a Fermi liquid, insulating, crossover (bad metal and bad insulator), coexistence (hysteresis) regions. Taken from [81].

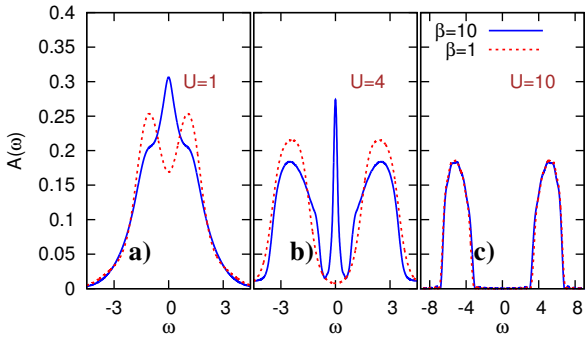


Figure 5.2: Density of states for systems in metallic a), near phase transition b), and insulating phase c) at $\beta \in \{1, 10\}$.

When $U$ is comparable to the bandwidth ($W$), the system undergoes a first-order phase transition by lowering the temperature. The endpoint of the transition-line is a second-order critical point located at $(U_c, T_c)$. Around the phase transition line, showed by a dashed line in yellow region of Fig. 5.1, there is a hysteresis region, also called the co-existence region, where the system can be either a metal or an insulator. The curves of the coexistence regime are defined by $U_{c1}(T)$ and $U_{c2}(T)$, where the former is a line connecting the zero-temperature metallic phase to the critical point and the latter continuously joins the zero-temperature insulating phase to the same point, where we have $U_{c1}(T_c) = U_{c2}(T_c)$ [51].

At very low temperature, the system will become magnetically ordered to an antiferromagnetic state. The transition temperature from a paramagnetic to an antiferromagnetic phase strongly depends on the lattice properties and hopping parameters. More precisely, the antiferromagnetic phase of systems with only a weak next-neighbor hopping ($t_2$) term in the Hamiltonian, which leads to a partial magnetic frustration, can cover full or part of the metal-insulator paramagnetic phase transition [157]. In case of complete magnetic frustration, the antiferromagnetic phase will be suppressed, and the metal-insulator transition line will be visible [51].

Due to the lack of exact solutions, the Hubbard model is studied with various computational methods, which are either fully numeric, for instance the density matrix renormalization group (DMRG) [33], quantum Monte-Carlo (QMC) [142], and exact diagonalization (ED) [139], or a mixture of analytical and numerical solutions such as slave-boson [10], slave-spin [23], and slave-rotor [38] techniques. In this thesis, we will tackle the problem using a DMFT scheme, introduced in Sec. 3.1.2, with a slave-rotor Anderson impurity-solver.

### 5.1.2 Slave-rotor representation

The slave-rotor technique was introduced as an efficient, computationally inexpensive, impurity solver for the DMFT by Florens and Georges [38]. In the following, we will explain the basics of this method using th Hubbard model. For the first step, we will consider the atomic limit of the Hubbard model, and will try to elaborate the idea behind the slave-rotor method by that.

**Hubbard model: Atomic limit**

In the atomic limit, Eq. (5.1) will become a $SU(N)$-symmetric model as

$$H_{\rm at} = \epsilon_{\rm at} \sum_{\sigma} c^{\dagger}_{\sigma} c_{\sigma} + \frac{U}{2} \Big[ \sum_{\sigma} c^{\dagger}_{\sigma} c_{\sigma} - \frac{N}{2} \Big]^2, \tag{5.2}$$

where $\sigma$ stands for the spin and orbital degrees freedom runs from one to $N$ ($N = 2$ corresponds to the up and down spin in a one-band system.). Here, $\epsilon_{\rm at}$ is the on-site energy set as $\epsilon_{\rm at} = \mu + \frac{U}{2}$ which will be set to zero at half-filling due to the particle-hole symmetry. The energy of the atomic Hamiltonian, in Eq. (5.2), only depends on the electron number, $\sum_{\sigma} c^{\dagger}_{\sigma} c_{\sigma} = Q$. This implies that separating the spin and charge degrees of freedom is a reasonable choice as it preserves the electron number.

The slave-rotor decomposition is based on fractionalizing a creation operator of an electron as

$$c^{\dagger}_{\sigma} = f^{\dagger}_{\sigma} e^{i\theta}, \tag{5.3}$$

where $\theta$ is an angular variable defined in $[0, 2\pi)$ for a quantum rotor, and $f^{\dagger}_{\sigma}$ is the creation operator of a fermionic particle with spin ($\sigma$), known as the spinon, which carries the information of spin and Fermi-statistics of the electron. In this representation, the quantum number of an angular momentum will determine the charge, and $e^{i\theta}$ will be the rising operator of the angular momentum. The Fermi statistics of an electron is fulfilled by satisfying

$$\begin{cases} \{f_{\sigma}, f^{\dagger}_{\sigma'}\} = \delta_{\sigma\sigma'}, \\ [L, \theta] = -i. \end{cases} \tag{5.4}$$

Here, $L$ is the associated angular momentum of $\theta$, defined as $L = -i\frac{\partial}{\partial\theta}$. This angular momentum will introduce the Hilbert space of the quantum rotor by

$$L|l\rangle_{\theta} = l|l\rangle_{\theta}. \tag{5.5}$$

As $e^{i\theta}$ is the charge raising operator, $l$ is connected to $Q$. As a result, we can express the eigenvector of an electron on the $SU(N)$ atomic model by a product state of spinon and rotor as

$$|\psi^{Q}_{\sigma}\rangle_{\rm el} = |\psi_{\sigma}\rangle_{f} |l\rangle_{\theta} = |\psi_{\sigma}\rangle_{f} |Q - \frac{N}{2}\rangle_{\theta}, \tag{5.6}$$

where $|\psi^{Q}_{\sigma}\rangle_{\rm el}$ is the electronic eigenstate of the atomic model with spin $\sigma$, and the total charge of $Q$. Here, $N$ is an integer, which is attributed to the total number of $\sigma$, spin or orbital specious.

As an example, the physical states of the one-band atomic model ($N = 2$), with the representation introduced in Eq. (5.3) and constraint of Eq. (5.11), are

$$|0\rangle_{\rm el} = |0\rangle_f|-1\rangle_\theta, \tag{5.7}$$
$$|\uparrow\rangle_{\rm el} = |\uparrow\rangle_f|0\rangle_\theta, \tag{5.8}$$
$$|\downarrow\rangle_{\rm el} = |\downarrow\rangle_f|0\rangle_\theta, \tag{5.9}$$
$$|\uparrow\downarrow\rangle_{\rm el} = |\uparrow\downarrow\rangle_f|+1\rangle_\theta. \tag{5.10}$$

One should note that the background charge in set to $-1$. Moreover, apart from the physical states defined in Eqs. (5.7-5.10), there are some unphysical states, for instance $|\uparrow\rangle_f|-1\rangle_\theta$. These states can be eliminated by the constraint of

$$L = \Big[\sum_\sigma f_\sigma^\dagger f_\sigma - \frac{N}{2}\Big]. \tag{5.11}$$

This constraint imposes the charge-conservation by connecting the spin and charge degrees of freedom. It would also suggest that eigenvalues of $L$, with the total charge of $Q$, are $l = Q - \frac{N}{2} = -\frac{N}{2}, -\frac{N}{2}+1, ..., \frac{N}{2}+1, \frac{N}{2}$. We thus can represent Eq. (5.2) within the slave-rotor decomposition as

$$H_{\rm at} = \sum_\sigma \epsilon_{\rm at} f_\sigma^\dagger f_\sigma + \frac{U}{2}L^2. \tag{5.12}$$

**Slave-rotor representation of the Hubbard model**

Substituting every electron operator in Eq. (5.1) by spinon and rotor, with the help of Eq. (5.3), will bring the Hubbard model into the form

$$H = -\sum_{ij} J_{ij}(f_i^\dagger e^{i\theta_i} f_j e^{-i\theta_j} + H.c.) - \mu\sum_i f_i^\dagger f_i + \frac{U}{2}\sum_i L_i^2. \tag{5.13}$$

Using Eq. (5.13), one can obtain the partition function, the action, and the Lagrangian of the system as

$$\mathcal{Z} = \int \mathcal{D}[f, f^\dagger]\mathcal{D}[L, \theta] e^{i\mathcal{S}[f, f^\dagger, L, \theta]}, \tag{5.14}$$
$$\mathcal{S} = -\int_{\mathcal{C}} {\rm d}t \mathcal{L}(t), \tag{5.15}$$

$$\mathcal{L} = -\sum_i L_i \partial_t \theta_i - i \sum_i \sum_\sigma f^\dagger_{i\sigma} \partial_t f_{i\sigma} + H, \tag{5.16}$$

$$= \sum_\sigma \sum_i f^\dagger_{i\sigma} \big( -i\partial_t - \mu \big) f_{i\sigma} - \sum_{\langle ij \rangle} \sum_\sigma J_{ij} \big( f^\dagger_{i\sigma} e^{i\theta_i} e^{-i\theta_j} f_{j\sigma} + \text{H.c.} \big)$$

$$- \sum_i L_i \partial_t \theta_i + \frac{U}{2} \sum_i L_i^2 - \lambda_i \big( L_i - \sum_i \sum_\sigma f^\dagger_{i\sigma} f_{i\sigma} + \frac{N}{2} \big). \tag{5.17}$$

Here $\lambda_i$ is the Lagrange multiplier which softly, on average, imposes the constraint of Eq. (5.11) at site $i$.

To obtain a $L$-free action, we will employ the Hubbard-Stratonovich identity on the Keldysh contour as

$$\exp\Big(-\frac{i}{2}\iint_{\mathcal{C}} \mathrm{dtdt}' b(t) A(t,t') b(t')\Big) \propto \exp\Big(\frac{i}{2}\big[\iint_{\mathcal{C}} \mathrm{dtdt}' x(t) A^{-1}(t,t') x(t') - x(t) b(t) \delta_{\mathcal{C}}(t,t')\big]\Big). \tag{5.18}$$

This relation yields

$$\int \mathcal{D}[L_j] \exp\Big( -i \int_{\mathcal{C}} \mathrm{dt} \Big[ \frac{U(t)}{2} \sum_j L_j^2(t) + \sum_j L_j(-\partial_t \theta_j - \lambda_j) \Big] \Big) \tag{5.19}$$

$$\approx \exp\Big( \frac{-i}{2} \sum_i \int_{\mathcal{C}} \mathrm{dt} \frac{1}{U(t)} (-\partial_t \theta_i - \lambda_i)(-\partial_t \theta_i - \lambda_i) \Big). \tag{5.20}$$

At last, we will replace the rotor by a $U(1)$ boson as

$$X^\dagger = e^{i\theta}, \text{ with the constraint } X^\dagger X = 1. \tag{5.21}$$

We finally cast a $L$-free Lagrangian in terms of $X$ and $f$ fields,

$$\mathcal{L} = \sum_\sigma \sum_i f^*_{i\sigma} \big( -i\partial_t - \mu + \lambda_i \big) f_{i\sigma} - \sum_{\langle ij \rangle} \sum_\sigma J_{ij} \big( f^*_{i\sigma} X^*_i X_j f_{j\sigma} + \text{h.c.} \big)$$

$$+ \frac{1}{2U} \sum_i \Big[ X^*_i (-i\partial_t + \lambda_i)(i\partial_t + \lambda_i) X_i \Big] + \sum_i \delta_i (X^*_i X_i - 1), \tag{5.22}$$

where $\delta_i$ imposes the $U(1)$ constraint introduced in Eq. (5.21).

### 5.1.3 Anderson Impurity model of the Hubbard model: slave-rotor representation

After representing our original Lagrangian in the slave-rotor language, the Hubbard term can be expressed by a quadratic form, while the complexity will flow to the hopping term with four nonlocal fields in its new representation. To tackle this inconvenience, we will map the lattice problem onto an Anderson impurity site embedded in a self-consistent bath. By this mapping, we will get

$$\begin{aligned}\mathcal{S} = &\int_{\mathcal{C}} \mathrm{dt} \sum_{\sigma} f^*_{\sigma}(t)\big(-i\partial_t - \mu + \lambda(t)\big) f_{\sigma}(t) - \iint_{\mathcal{C}} \mathrm{dtdt}' \sum_{\sigma} f^*_{\sigma}(t) X^*(t) \Delta(t,t') X(t') f_{\sigma}(t') \\ &+ \int_{\mathcal{C}} \mathrm{dt} \frac{1}{2U} \sum_{i} \Big[ X^*(t)\big(-i\partial_t + \lambda(t)\big)\big(i\partial_t + \lambda(t)\big) X(t) \Big] + \int_{\mathcal{C}} \mathrm{dt} \delta\big(X^*(t)X(t) - 1\big),\end{aligned} \tag{5.23}$$

where $\Delta(t,t')$ is the DMFT hybridization function.

For the later argument, it will be useful to generalize the action to a $M$-component rotoric field with the constraint $\sum_{\alpha} |X_{\alpha}|^2 = M$, and thereby have an action of the form

$$\begin{aligned}\mathcal{S} = &\int_{\mathcal{C}} \mathrm{dt} \sum_{\sigma} f^*_{\sigma}(t)\big(-i\partial_t - \mu + \lambda(t)\big) f_{\sigma}(t) - \iint_{\mathcal{C}} \mathrm{dtdt}' \frac{1}{M} \sum_{\sigma} \sum_{\alpha} f^*_{\sigma}(t) X^*_{\alpha}(t) \Delta(t,t') X_{\alpha}(t') f_{\sigma}(t') \\ &+ \int_{\mathcal{C}} \mathrm{dt} \frac{1}{2U} \sum_{i} \sum_{\alpha} \Big[ X^*_{\alpha}(t)\big(-i\partial_t + \lambda(t)\big)\big(i\partial_t + \lambda(t)\big) X_{\alpha}(t) \Big] + \int_{\mathcal{C}} \mathrm{dt} \sum_{\alpha} \delta\big(X^*_{\alpha}(t)X_{\alpha}(t) - M\big).\end{aligned} \tag{5.24}$$

We finally are ready to derive the Dyson equations, associated with the spinon and the rotor, using Euler-Lagrange equation of the form

$$\langle q(t) \frac{\partial \mathcal{L}}{\partial q(t')} \rangle - \langle q(t) \frac{\partial \mathcal{L}}{\partial t} \Big( \frac{\partial \mathcal{L}}{\partial \dot{q}(t')} \Big) \rangle = i\delta_{\mathcal{C}}(t,t'), \tag{5.25}$$

where $q$ is the canonical variable corresponding to $f$ or $X$ fields. We restricted the solution to a time-independent Hubbard interaction, decomposed any generated four-point Green's functions from Eq. (5.25) to two-point Green's functions by a mean-field theory, and thereby yield

$$(i\partial_t - \mu - \lambda) G_f(t,t') - \int_{\mathcal{C}} \mathrm{d\bar{t}} \quad \Sigma_X(t,\bar{t}) G_f(\bar{t},t') = \delta_{\mathcal{C}}(t,t'), \tag{5.26}$$

$$\Big(\frac{-1}{2U}\partial_t^2 + \frac{-1}{2U} 2i\lambda\partial_t + \delta\Big) G_X(t,t') - \int_{\mathcal{C}} \mathrm{d\bar{t}} \quad \Sigma_f(t,\bar{t}) G_X(\bar{t},t') = \delta_{\mathcal{C}}(t,t'), \tag{5.27}$$

where spinon and rotor Green's functions are defined as

$$G_X(t,t') = -i\langle T_{\mathcal{C}} X_\alpha(t) X_\alpha^*(t')\rangle, \tag{5.28}$$
$$G_f(t,t') = -i\langle T_{\mathcal{C}} f_\sigma(t) f_\sigma^*(t')\rangle. \tag{5.29}$$

with self-energies of the form

$$\Sigma_X(t,t') = i\frac{N}{M}\Delta(t,t')G_X(t',t), \tag{5.30}$$
$$\Sigma_f(t,t') = i\Delta(t,t')G_f(t',t). \tag{5.31}$$

These Green's functions, which are satisfying Eqs. (5.26, 5.27), would be exact in the limit of large $N$ and $M$, keeping their ratio fixed $\mathcal{N} = N/M$. However, when $N = 2$ and $M = 1$ in a one-band system, it has been shown that $\mathcal{N} = 3$ gives better results for the phase diagram, and a quantitatively more accurate description of the quasiparticle peak [38]. At last the electronic impurity Green's function will be

$$G_{\text{imp}}(t,t') = iG_f(t,t')G_{\text{X}}(t',t). \tag{5.32}$$

### Constraints and Lagrange multipliers

As we have mentioned, we will softly constrain the slave-rotor method by satisfying Eqs. (5.11, 5.21). For the rotor contribution, we should ascertain the relation

$$G_X^<(t,t) = 1, \tag{5.33}$$

and for the spinon constraint, we should enforce

$$\langle L\rangle = -\langle\sum_\sigma f_\sigma^\dagger f_\sigma\rangle + 1, \tag{5.34}$$
$$\langle L\rangle = -2iG_f^<(t,t) + 1, \tag{5.35}$$
$$iG_f^<(t,t) = \frac{1}{2} - \frac{1}{2}\langle L\rangle. \tag{5.36}$$

This relation connects the spinon Green's function to the rotor angular momentum. As we are computing the spinon and rotor Green's function in the slave-rotor impurity problem, we will now try to acquire a relation between $\langle L\rangle$ and the rotor Green's function. To achieve this goal, we will employ the Heisenberg equation for the the rotor Hamiltonian,

$H_\theta = UL^2/2 - \lambda L$, and the rotor phase ($\theta$) as

$$[\frac{U}{2}L^2 - \lambda L, \theta] = -iLU + i\lambda, \tag{5.37}$$

$$[H, \theta] = -i\frac{d\theta}{dt}, \tag{5.38}$$

$$L = \frac{1}{U}\frac{d\theta}{dt} + \frac{\lambda}{U}, \tag{5.39}$$

$$\langle L\rangle = \frac{1}{U}\langle\frac{d\theta}{dt}\rangle + \frac{\lambda}{U}. \tag{5.40}$$

It is worthwhile noting that, due to $[H_\theta, L] = 0$, the rotor angular momentum is the conserved quantity of the system. Inserting Eq. (5.40) in Eq. (5.36) yields

$$iG_f^<(t,t) = \frac{1}{2} - \frac{\lambda}{2U} - \frac{1}{2U}\langle\frac{d\theta(t)}{dt}\rangle. \tag{5.41}$$

In the last step, we will find a substitution for the $\langle\frac{d\theta(t)}{dt}\rangle$ in terms of the boson $X$. This can be fulfilled by using the definitions

$$G_X^<(t,t') = \langle X^\dagger(t')X(t)\rangle = -i\langle e^{-i\theta(t')+i\theta(t)}\rangle, \tag{5.42}$$

$$G_X^>(t,t') = \langle X(t)X^\dagger(t')\rangle = -i\langle e^{i\theta(t)-i\theta(t')}\rangle, \tag{5.43}$$

where,

$$G_X^<(t,t') = G_X^{>*}(t',t) = G_X^>(t,t'), \tag{5.44}$$

$$\frac{dG_X^<(t,t')}{dt} = \frac{dG_X^{>*}(t',t)}{dt} = \frac{dG_X^>(t,t')}{dt}. \tag{5.45}$$

The time derivative of the lesser and the greater rotor Green's function are

$$\frac{dG_X^<(t,t')}{dt} = -i\langle\frac{d\theta(t)}{dt}e^{-i\theta(t')+i\theta(t)}\rangle, \tag{5.46}$$

$$\frac{dG_X^>(t,t')}{dt} = -i\langle\frac{d\theta(t)}{dt}e^{i\theta(t)-i\theta(t')}\rangle, \tag{5.47}$$

Summing the last two equations yields

$$\Big(\frac{dG_X^<(t,t')}{dt} + \frac{dG_X^>(t,t')}{dt}\Big) = \langle\frac{d\theta}{dt}\Big(e^{-i\theta(t')+i\theta(t)} + e^{i\theta(t)-i\theta(t')}\Big)\rangle. \tag{5.48}$$

Taking the advantage of the limit $t' \to t$, and using $G^<(t,t) = G^>(t,t) = 1$ will suggest that

$$\Big(\frac{dG_X^<(t,t')}{dt}\Big|_{t=t'} + \frac{dG_X^>(t,t')}{dt}\Big|_{t=t'}\Big) = 2\langle\frac{d\theta}{dt}\rangle, \tag{5.49}$$

Finally, substituting Eq. (5.49) in Eq. (5.41) will provide a boundary condition for the spinon, connected to the rotor Green's function, which is

$$iG_f^<(t,t) = \frac{1}{2} - \frac{i\lambda G_X(t,t)}{2U} + \frac{1}{4U}\Big(\frac{dG_X^<(t,t')}{dt}\Big|_{t=t'} + \frac{dG_X^>(t,t')}{dt}\Big|_{t=t'}\Big). \tag{5.50}$$

At last, the boundary conditions can be summarized as

$$iG_f^<(t,t) = \frac{1}{2} - \frac{\lambda}{2U(t)} + \frac{1}{4U(t)}\Big(\frac{dG_X^<(t,t')}{dt}\Big|_{t=t'} + \frac{dG_X^>(t,t')}{dt}\Big|_{t=t'}\Big), \tag{5.51}$$

$$G_X^<(t,t) = -i. \tag{5.52}$$

## 5.2 Numerical evaluation

In this section, we will summarize the equations, which have been derived in previous sections. We will explain the DMFT self-consistency loop, and will elaborate the enforcement of the constraints.

### 5.2.1 DMFT self-consistency loop

To solve of the half-filled one-band Hubbard model, we now incorporate the DMFT self-consistency loop by the slave-rotor impurity solver. In Sec. 3.1.2, we introduced the general DMFT recipe, where its second step was the impurity-solver dependent. In the following, we will explain this step based on the slave-rotor impurity-solver.

1. We determine two uncoupled solutions for the spinon and the rotor subsystems. The spinon Green's function satisfies Eq. (5.26) with a zero spinon self-energy. The uncoupled rotor Green's function is obtained by Eq. (5.54) for a fixed nonzero $\delta_0$.

2. The spinon self-energy will be determined by Eq. (5.31), and the rotor self-energy will be computed by Eq. (5.30) with $\mathcal{N} = 3$.

3. We acquire the spinon and rotor Green's functions by solving Eqs. (5.26, 5.27) for a trial $\eta(t)$, with, usually, the first guess of $\eta(t) = 2\delta_0$. These Dyson equations are standard equations that we have explicitly explained in Chap. 2.

4. We enforce the constraints. For the half-filled case, Eqs. (5.51) will be satisfied by setting $\lambda = 0$. To obtain $\eta(t)$, we will go through the steps which will be explained in Sec. 5.2.2.

5. The new Green's functions and self-energies for the rotor and spinon are computed using Eqs. (5.26, 5.27, 5.31, 5.30).

6. We calculate new electronic Green's function using Eq. (5.32).

### 5.2.2 Lagrange multipliers

To close the DMFT self-consistency loop, we will now illustrate how we will impose Eqs. (5.51, 5.52). In Sec. 5.1.3, we have shown that $L$ is preserved in the rotor subsystem, while $\theta$ is not a conserved quantity of the system. This immediately implies that the associated Lagrange multiplier of the rotor angular momentum, known as $\lambda$, is time-independent. In contrast, $\delta$, which imposes the $U(1)$ constraint, has a time dependence. At a fixed filling, we thus can set $\lambda = c$, where $c$ is a constant.

To determine $\delta$, we first rearrange the rotor Dyson equation to the form

$$G_X(t,t') = g_X(t,t') + \Big[g_X * \big(\eta + \Sigma_X\big) * G_X\Big](t,t'), \tag{5.53}$$

where $\delta(t) = \delta_0 + \eta(t)$, and $g_X$ is the uncoupled rotor Green's function governed by

$$\Big(\frac{-1}{2U}\partial_t^2 + \delta_0\Big) g_X(t,t') = \delta_{\mathcal{C}}(t,t'). \tag{5.54}$$

The above equation induces, that $g_X$ is a harmonic oscillator with the mass of $2U$, and the oscillating frequency $\frac{\delta_0}{U}$.

After inserting $\delta_0$ in the uncoupled rotor Green's function, satisfaction of Eq. (5.52) is reduced to evaluating $\eta(t)$. As we are imposing the constraint of Eq. (5.21), there will be multiple solutions, $\eta$, to the Eq. (5.52). Most of these roots carry unphysical states, which should be rejected by the $\eta$-finder. In the following, we will elaborate how such a finder is implemented, based on a modified Newton's root-finder.

The Newton's method is a one-dimensional root-finder routine, where the root of the function $f(x)$, located at $x_0$, is determined by employing the Taylor expansion of the function near a trial point, let's say at $x = x_0 + \epsilon$, as

$$f(x_0 + \epsilon) \approx f(x_0) + \frac{df}{dx}(x_0)\epsilon + \frac{1}{2}\frac{d^2 f}{dx^2}(x_0)\epsilon^2 + .... \tag{5.55}$$

In Newton's root-finder, it is assumed that (i) the trial point $(x)$ is close enough to $x_0$, (ii) the function is well-behaved, so that the higher orders of $\epsilon$, in the Taylor expansion, are not important. Considering these assumptions suggest that, for a trial point of $x_{\rm old}$,

$$\epsilon_{\rm old} = -\frac{f(x_{\rm old})}{\frac{df}{dx}(x)\Big|_{x=x_{\rm old}}}. \tag{5.56}$$

As the trial point is, usually, away from $x_0$, after each step of obtaining new $\epsilon_{\rm old}$ using Eq. (5.56), new trial point $x_{\rm new} = x_{\rm old} + \epsilon_{\rm old}$ will be used to calculate $f(x_{\rm new})$. After replacing $x_{\rm old} = x_{\rm new}$, one should again evaluate the next $\epsilon_{\rm old}$, and this routine must be continued till we find $x_0$.

In the slave-rotor $\eta$-finder, as a result of the integral equation, introduced in Eq. (5.53), capturing the derivative of the rotor Green's function is a true challenge. To overcome such a difficulty, we will approximate the derivative of $G_X$ as

$$\begin{cases} \frac{dG_X(\tau=0)}{d\eta(\tau=0)} = \big[g_X(\tau)G_X(-\tau)\big]_{\tau=0} & \tau \in \mathcal{C}^{|}, \\ \frac{dG_X(t,t)}{d\eta(t')} = g_X(t,t')G_X(t',t) & (t,t') \in \mathcal{C}^{\pm}. \end{cases} \tag{5.57}$$

For the Matsubara component of $G_X$, we start from a trial $\eta$, usually setting that to a large value is the best choice. One should note that some of the choices of $\eta$ can lead to unphysical solutions, indicated by positive value of $G_X(\tau)$. Such solutions basically correspond to an inversion of the harmonic potential of the rotor, and must be avoided by the $\eta$-finder.

To avoid the penetration of any unphysical state in the parameter space of the chosen $\eta$, we first compute the new $G_X$, using Eq. (5.53), and verify the absolute negativeness of $\Re G_X^{\rm mat}(\tau)$, which is the time-dependent equivalence of the positive spectral weight in equilibrium.

If $\eta$ pass the previous verifications successfully, we will update that by

$$\Delta\eta = \frac{1 + |\Re G_X^{\rm mat}(0)|}{\frac{dG_X^{\rm mat}(0)}{d\eta}}, \tag{5.58}$$

where selecting $\tau = 0$ is due to the imaginary-time independency of $\eta$, and $\eta_{\text{new}} = \eta + \Delta\eta$. Exploiting $\eta_{\text{new}}$ would be the starting point of the next iteration, which will be continued till the time that we capture an accurate Lagrange multiplier where $G_X^{\text{mat}}(0) = -1$.

For the real-time components, in each steps of iteration, let's say at time $t$, $\eta$ is, initially set to its previous time ($\eta(t-h)$) with the time-interval of $h$, computed by Eq. (5.57) as

$$\mathcal{G}_{\text{conv}}(t, t-h) = \frac{dG_X^{\text{ret}}(t,t)}{d\eta(t-h)} \approx g_X^{\text{ret}}(t, t-h) G_X^{\text{ret}}(t-h, t). \tag{5.59}$$

Exploiting the above relation, we would have

$$\Delta\eta = \frac{\Im G_X^{<} + 1}{\mathcal{G}_{\text{conv}}(t, t-h) w_t h}, \tag{5.60}$$

where $w_{\text{t}}$ is the integration numerical weight. In the next step, $\Delta\eta$ will be used to update $\eta$ and, correspondingly, the Green's function at time $t$ and $t-h$. Such a indirect approach of updating the Green's function at times $t-h$ and $t$ is because of $G_X^{\text{ret}}(t,t) = 0$, and thereby $\Delta\eta$ can not be updated using $\mathcal{G}_{\text{conv}}(t,t)$. We thus determine the $\eta(t)$ by the rotor Green's function at $\widetilde{t} = t + h$. Such an approach implies that at any steps of iteration, we not only should calculate the Green's functions, spinon and rotor, at $\widetilde{t} = t$, but also we should update the Green's function at $\widetilde{t} = t - h$ as well.

**Assessing the $\eta$-finder**

Before going into the application of the proposed method, it would be crucial to assess the functionality of our employed $\eta$-finder. Checking the Matsubara component is straight forward since at half-filling we would have the symmetry of $G^{\text{mat}}(0) = G^{\text{mat}}(\beta)$. Thereby, we only should check for $\eta$ values which satisfy $G^{\text{mat}}(\beta) = -1$. In equilibrium, as a result of time-independence of the Hamiltonian, $\eta$ is also time-independent. We thus can evaluate the efficiency of the proposed $\eta$-finder by

$$\mathcal{R}(t) = \eta(t) - \eta^{\text{mat}}, \tag{5.61}$$

where $\eta^{\text{mat}}$ is obtained from the satisfaction of the rotor constraint on the Matsubara axis.

Results, in Fig. 5.3, indicate that the largest error is occurring at small times. Moreover, it can be easily shown that larger number of grid points on the Matsubara axis will reduce the error of this method. We illustrate this behavior in Fig. 5.3. Results indicate that few Matsubara grid points, as it was expected, can be a source of inaccuracy of $\eta(t)$. Although even in that case, the solution is still stable. Moreover, for the total grid points which are more than an "optimal" grid numbers, i.e. $n_\tau > 300$ for the results plotted in Fig. 5.3, $\eta(t)$ is almost independent of the initial simulation conditions.

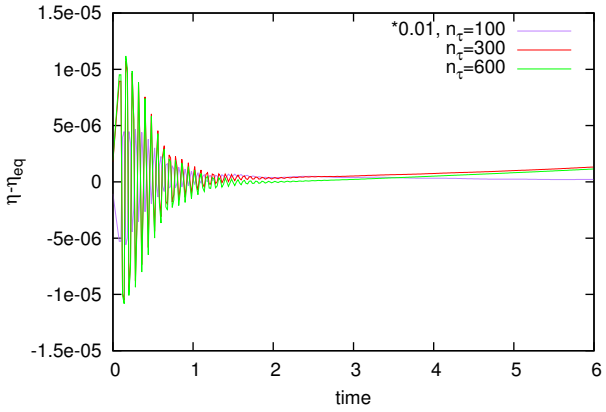


Figure 5.3: The difference between time-dependent $\eta$ is compared with $\eta_{\text{eq}}$ for a system at $U = 4$, and $\beta = 10$. $n_\tau$ is the total number of points for an equidistant mesh of the Matsubara branch. Results with $n_\tau = 100$ has been multiplied by 0.01.

### 5.2.3 Observables

Employing the slave-rotor impurity solver within the DMFT formalism will enable us to explore the physics of the Hubbard model in and out of equilibrium. Here, we will provide a list of observables, which will be measured in the rest of this chapter.

***Kinetic energy***

The derivation of the kinetic energy is precisely the same as what we have presented in Eq. (4.169).

***Spectral function***

The spectral function is obtained using Eq. (2.40). Acquiring the spinon and rotor spectral functions can be straightforwardly done by substituting the spinon and rotor Green's functions as $G$ in Eq. (2.40). We also have access to the occupied spectral functions of the electron, rotor, and spinon after replacing the retarded Green's function by the lesser Green's function in Eq. (2.40).

***Double occupancy***

Employing Eq. (5.39) will enable us to write the density-density correlation function as

$$\chi(t,t') = \langle n_\uparrow(t) n_\downarrow(t')\rangle = \langle L(t)L(t')\rangle, \tag{5.62}$$

$$= \frac{1}{U^2}\langle \frac{d\theta(t)}{dt}\frac{d\theta(t')}{dt'}\rangle + \frac{\lambda}{U^2}\langle \frac{d\theta}{dt} + \frac{d\theta}{dt'}\rangle + \frac{\lambda^2}{U^2}, \tag{5.63}$$

At half-filling, we will set $\lambda = 0$, and thereby the above equation will be simplified to

$$\chi(t,t') = \frac{1}{U^2}\langle \frac{d\theta(t)}{dt}\frac{d\theta(t')}{dt'}\rangle. \tag{5.64}$$

Using the definition of the rotor, provided in Eq. (5.21), we would have

$$X(t) = e^{i\theta(t)} \rightsquigarrow \partial_t\theta(t) = -iX^\dagger(t)\partial_t X(t), \tag{5.65}$$

$$X(t') = e^{i\theta(t')} \rightsquigarrow \partial_{t'}\theta(t') = iX(t')\partial_{t'}X^\dagger(t'). \tag{5.66}$$

We thus can represent $\langle \frac{d\theta(t)}{dt}\frac{d\theta(t')}{dt'}\rangle$ as

$$\langle \frac{d\theta(t)}{dt}\frac{d\theta(t')}{dt'}\rangle = \langle X^\dagger(t)\partial_t X(t)X(t')\partial_{t'}X^\dagger(t')\rangle, \tag{5.67}$$

$$\begin{aligned}=&\langle X^\dagger(t)\partial_t X(t)\rangle\langle X(t')\partial_{t'}X^\dagger(t')\rangle + \langle X^\dagger(t)X(t')\rangle\langle \partial_t X(t)\partial_{t'}X^\dagger(t')\rangle \\ &+ \langle X^\dagger(t)\partial_{t'}X^\dagger(t')\rangle\langle X(t')\partial_t X(t)\rangle + \langle X^\dagger(t')X(t')\rangle\langle \partial_t X(t)\partial_{t'}X^\dagger(t')\rangle, \qquad (5.68)\\ &+ \langle X^\dagger(t)X(t)\rangle\langle X(t')\partial_t\partial_{t'}X(t')\rangle, \qquad (5.69)\\ =&-2\partial_t G_X(t,t'')\mid_{t''=t}\partial_{t'}G_X(t'',t')\mid_{t''=t'} + 2G_X(t,t')\partial_t\partial_{t'}G_X(t,t') + 2U\delta_{\mathcal{C}}(t,t'). \qquad (5.70)\end{aligned}$$

Finally, the density-density correlation function at half-filling will get the form of

$$\chi(t,t') = \frac{2}{U^2}\Big[-\partial_t G(t,t'')\mid_{t''=t}\partial_{t'}G(t'',t')\mid_{t''=t'} + G(t,t')\partial_t\partial_{t'}G(t,t') + U\delta_{\mathcal{C}}(t,t')\Big]. \tag{5.71}$$

Exploiting this correlation function enables us to derive the double occupancy of the system as

$$d(t) = \frac{1}{2}\chi(t,t). \tag{5.72}$$

## 5.3 Results and discussion

In Sec. 5.2.1, we have presented the DMFT self-consistency loop using the slave-rotor impurity solver. In the following, we will employ this approach to investigate the paramagnetic phase of the Hubbard model at half-filling near the paramagnetic metal-insulator transition (PMIT). Since we are concerned about the near phase-transition physics, we will put our effort on exploring this part of the phase diagram. We will investigate the response of the system both in the metallic and insulating part of the phase diagram in and out of equilibrium. The out of equilibrium preparation, with parameters which are set to be near the PMIT, is done by

- applying a quick quench protocol of the hopping amplitude to bring a metal (insulator) to the bad-metallic (-insulating) phase of the system.
- comparing the phase which is obtained after a quick quench of the hopping amplitude with a state obtained after excitation with a short laser pulse, which "heats" the system so that it is transfered to the bad-metallic phase.
- trying to determine the nonadiabatic window of the phase diagram, within which the evolution can not be described by the adiabatic theorem.

The above mentioned nonequilibrium preparations will transfer some energy to the system. As we mainly would like to explore the physics below the bad-insulating (-metallic) regime of the phase diagram, we will couple a dissipative bosonic bath to the system. This will allow us to study how, and whether, the excited state returns to the low temperature equilibrium phase. In a real solid, such a dissipative environment is always present, in the form of coupling to the lattice. Such a coupling will be performed by exploiting the self-energy of the form

$$\Sigma_{\text{bath}} = \lambda D(t,t')G(t,t'), \tag{5.73}$$

where $\lambda$ is the square of the electron-boson coupling, $D$ is the bare bosonic Green's function with the frequency of $\omega_0 = 1$, and $G$ is the local Green's function of the system. As the bath is bosonic, there is no particle-transfer between the bath and the fermionic system. Thereby, the introduced statistical bath will be the canonical heat-bath, which can exchange energy with the system. To keep the influence of the bath negligible, we will opt for small couplings satisfying $\lambda < \frac{\omega_0 W}{2}$, where $W$ is the bandwidth of the system. (The case of stronger electron lattice coupling, when the phonons have a profound influence on the electronic density of states, will be studied in Chap. 6.) We will mainly present our results on the Bethe lattice with the bandwidth of $W = 4$, and at half-filling. We will present our results in the energy (time) unit of the hopping amplitude (inverse of the hopping amplitude), where we set $\hbar = 1$.

In the following, we will first explain the equilibrium physics of the model, and will continue the discussion by elaborating the nonequilibrium properties of the system under above mentioned preparations.

### 5.3.1 Equilibrium physics

To characterize the equilibrium physics of the model within the slave-rotor method, we will plot the spectral function of the system in the metallic and insulating phase of the diagram.

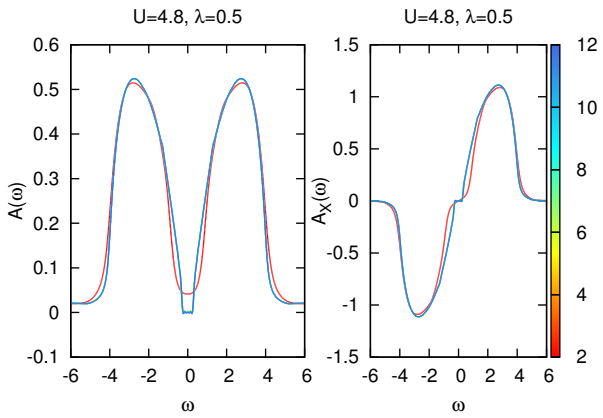


Figure 5.4: The electron and rotor spectral functions in equilibrium at $U = 4.8$, and $\lambda = 0.5$. Color coding indicates the value of $\beta$.

The spectral function of an insulating phase, known as a "Mott" insulator, is characterized by the presence of two-peak structure in the spectral function, which are approximately separated by $U$ with the bandwidth of $D$. There is also a well-defined gap with the width of $U - D$. Fig. 5.4 displays the electronic and rotoric spectral function at $U = 4.8$. Varying $\beta$ from a small to a large value, brings the system from a bad-insulator, where the gap is slightly filled, to a Mott-insulator which has no spectral weight inside the gap. The rotor, representative of the charge excitations, also exhibits similar response in its spectral density. At higher temperatures, we can observe very small density near $\omega = 0$, while at lower temperatures, the accumulation of the rotor density is pushed to frequencies which are $|\omega| > (U - D)/2$.

Fig. 5.5 presents the spectral function of a metallic system, $U = 4$, at three different temperatures. The plot shows that in the bad metallic state, the spectral function have two peaks which are related to very small density at $\omega = 0$. The two bands located at, roughly, $\pm U/2$, related to empty or double occupied sites, are the particle-like excitation of the system, related to the high-energy charge excitations. Going further down in temperature is accompanied by the accumulation of the density around small frequencies. This quasiparticle peak can be understood in the wave-like picture of the particle as a coherent excitation of the system.

The height of the spectral density at zero frequency ($A(\omega = 0)$) is not only controlled by the temperature, but is also connected to the Hubbard interaction. Fig. 5.6 shows a dramatic enhancement of $A(\omega = 0)$ by cooling down the system. In addition, the Hubbard interactions which are closer to the PMIT ($U_c$) are exhibiting smaller height of

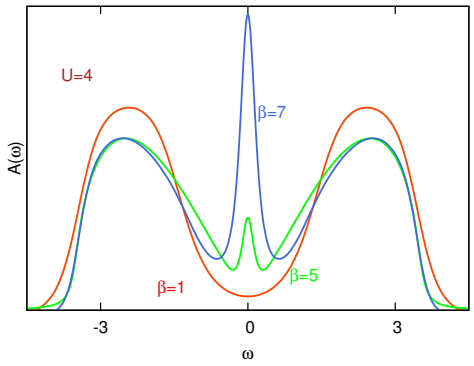


Figure 5.5: The equilibrium spectral function for a system with $U = 4$ at $\beta \in \{1, 5, 7\}$ and $\lambda = 0$.

the quasiparticle peak at the same $\beta$. Within the slave-rotor impurity methods, the phase transition is occurring at $U_{c1} = 4.6$ [38]. Due to the coupling of our systems to the bosonic bath, the system will experience the PMIT at slightly larger $U_c = 4.69$. Such a response is a consequence of the boson-mediated renormalization of the Hubbard interaction, which strengthen the metallic tendency of the system. We will extensively explain this behavior in Chap. 6.

We now take the advantage of the slave-rotor method and explore the height-enhancement of the quasiparticle peak in the language of the rotor and spinon. In Fig. 5.7, we surveil the spinon and rotor spectral functions for systems which have the same parameters as Fig. 5.5. Fig. 5.7 a) displays that at small $\beta$ the rotor has two peaks, separated by $U$, with very small density at small frequency, almost like a gap. Besides, the spinon shows a broad mono peak spectral function, centered around $\omega = 0$ with a bandwidth which is almost inside the gap of the rotor density. This collection of spinon and rotor spectral behavior is attainable in the bad metallic regime of the Hubbard model, see also the red spectral function at $\beta = 1$ in Fig. 5.6. Enhancing $\beta$ will enlarge the height of the quasiparticle peak. At $\beta = 5$ when the quasiparticle starts developing, the slope of the spectral density around $\omega = 0$ will become steeper. At the same time, the width of the spinon spectral function will become narrower indicating that the interaction between the spinon and rotor becomes weaker. At smaller temperatures, when the quasiparticle is intensified, the deformation of the rotor density near small frequencies is amplified, and the spinon bandwidth becomes wider.

These data show a nonmonotonous response of the spinon, which we will become important in Sec. 5.3.3. We can elucidate the nonmonotonous spinon response by considering

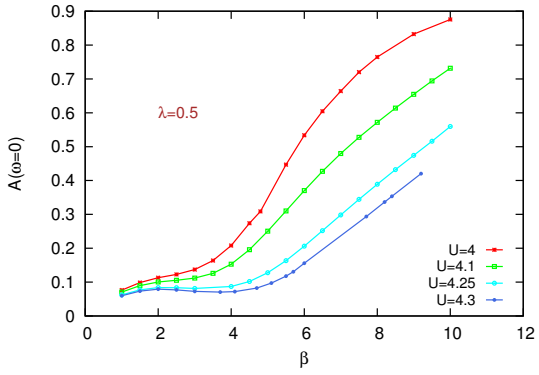


Figure 5.6: The height of the spectral function as a function of $\beta$ at $U \in \{4, 4.1, 4.25, 4.3\}$ and $\lambda = 0.5$.

the mutual interaction between the spinon and rotor as the spinon bandwidth, determined by its self-energy which is computed using the rotor Green's function, see also Eq. (5.31). At high temperatures, i.e. $\beta \in \{1, 5\}$ in Fig. 5.6, the thermal-induced charge density at small frequencies is responsible for the bandwidth of the spinon spectral peak. Thereby, the bandwidth will be reduced by cooling the system. However, after the emergence of the quasiparticle peak, and the resulting amassment of the rotor low-energy density, the coupling between spinon and rotor will be stronger, and the spinon bandwidth will start broadening.

To analyze spinon bandwidth as a function of $\beta$ for various Hubbard interactions, we will define the lifetime of the spinon as

$$\tau_{\text{eq}}^{-1}(\frac{1}{\beta}) = \Gamma(\frac{1}{\beta}), \tag{5.74}$$

where $\Gamma$ is the bandwidth of the Lorentzian spinon spectral density. Employing this definition, we have plotted the spinon lifetime as a function of $\beta$ in Fig. 5.8. Results emphasize that for each Hubbard interaction, there would be one temperature in which the spinon bandwidth (lifetime) acquires its smallest (largest) value. This maximum lifetime ($\tau^*$), defines a crossover temperature $T^* = 1/\beta^*$. It is worthwhile noting that the lifetime of spinon is not symmetric around $\beta = \beta^*$. This supports the influence of the rotor low-frequency spectral density on the broadening of the spinon bandwidth, and different broadening mechanism before and after $\beta^*$. In addition, the larger electron-bath coupling ($\lambda$) corresponds to the smaller $\tau^*$. This is transpired as a result of the slight broadening of the spinon bandwidth with respect to the electron-bath self-energy, introduced in Eq. (5.73).

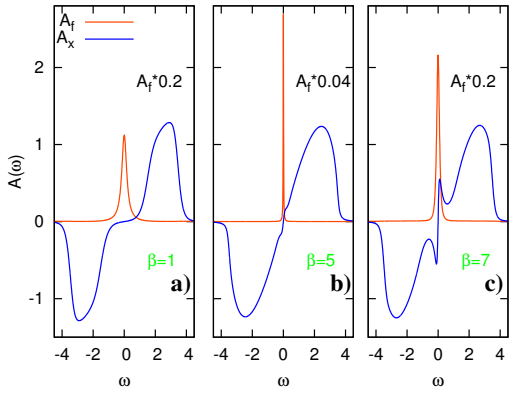


Figure 5.7: The rotor and spinon spectral function for $U = 4$ at a) $\beta = 1$, b) $\beta = 5$, and c) $\beta = 7$.

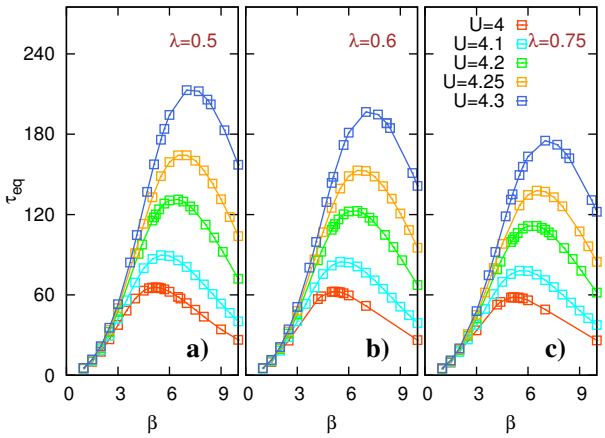


Figure 5.8: Equilibrium spinon lifetimes for $U \in \{4, 4.1, 4.2, 4.25, 4.3\}$, $\beta = 10$, and $\lambda \in \{0.5, 0.6, 0.75\}$.

One should note that despite the presence of the nonmonotonous spinon response, no evidence of such a behavior can be detected in the spectral function, see Fig. 5.6. It is also noticeable that for $T > T^*$, the spectral function of the system mainly depends on the charge response, c.f. also Fig. 5.5, as the spinon and rotor are almost decoupled and the spinon density is accumulated inside the quasi-gap of the rotor spectral function. To strengthen this statement, we will try to find a relation between the electronic spectral density and the spinon nonmonotonous bandwidth. In equilibrium, a two-time electronic Green's function can be easily represented in the real-frequency, using the analytical continuation for the convolution, see Eq. (B3) in Ref. [38], one obtains

$$G_{\rm el}(\omega) = -\int \frac{d\epsilon}{\pi} \Im G_X(\epsilon) n_B(\epsilon) G_f(\omega+\epsilon) - \int \frac{\mathrm{d}\epsilon}{\pi} \Im G_f(\epsilon) n_F(\epsilon) G_X(\omega-\epsilon), \tag{5.75}$$

where $n_{F(B)}$ is the Fermi-Dirac (Bose-Einstein) distribution function. Considering an extremely weak coupling between spinon and rotor at $T = T^*$, and the presence of the spinon bandwidth between the rotor bands, would suggest that approximating the spinon spectral weight as a delta function ($A_{\rm f}(\omega) = \delta(\omega)$) is reasonable. This approximation would give us

$$A(\omega) = \frac{1}{2} \Im G_X(\omega) \coth(\frac{\beta\omega}{2}). \tag{5.76}$$

In addition, we can also present an analytically continued form of the spinon self-energy, see Eq. (B4) in Ref. [38], as

$$\Sigma_{\rm f}(\omega) = -\int \frac{d\epsilon}{\pi} \Im G_X(\epsilon) n_B(\epsilon) \Delta(\omega+\epsilon) - \int \frac{\mathrm{d}\epsilon}{\pi} \Im \Delta(\epsilon) n_F(\epsilon) G_X(\omega-\epsilon). \tag{5.77}$$

This representation after substituting the fermionic and bosonic distribution functions at very small frequencies can be rewritten as

$$\Sigma_{\rm f}(\omega=0) \approx \int \mathrm{d}\epsilon \frac{\Im G_{\rm X}(\epsilon) \Im \Delta(\epsilon)}{\sinh(\beta\epsilon)}. \tag{5.78}$$

Finally, substituting Eq. (5.76) in Eq. (5.78) will suggests that

$$\begin{aligned} \Im\Sigma_{\rm f}(\omega=0) &\approx \int \mathrm{d}\omega \frac{\Im\Delta(\omega) A(\omega)}{\cosh(\omega\beta/2)^2}, \\ &\approx \int \mathrm{d}\omega \frac{-\pi J^2 A(\omega) A(\omega)}{\cosh(\omega\beta/2)^2}, \end{aligned} \tag{5.79}$$

where in the last line, we substituted the imaginary part of the hybridization function of the Bethe lattice, given by Eq. (3.25). This approximated self-energy evaluates the

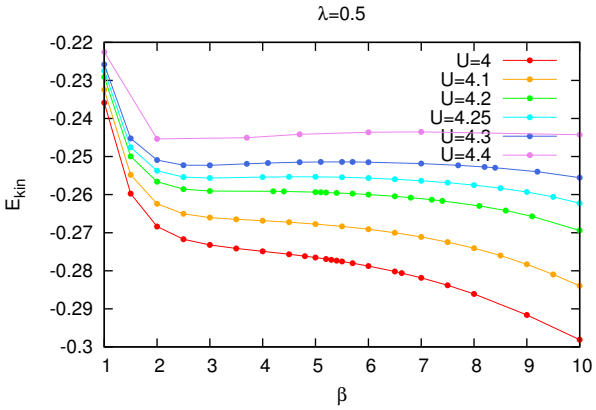


Figure 5.9: The equilibrium kinetic energy as a function of inverse temperature for $U \in \{4, 4.1, 4.2, 4.25, 4.3, 4.4\}$ at $\beta = 10$, and $\lambda = 0.5$.

spinon bandwidth in the regime where the rotor spectral function has very small density at low frequencies. In Fig. (5.16), we plot the spinon lifetime, using $\tau_{\text{eq}}^{-1} = -\Im\Sigma_f(\omega = 0)$, as triangular points. The comparison between the equilibrium and approximated spinon lifetime will show good agreement at $T > T^*$. It is shown that around $\tau_*$, the above approximation, as it was mentioned before, is not valid any more as the spinon and rotor will be strongly coupled.

Furthermore, Fig. 5.9 displays that the kinetic energy of the system preforms differently before and after $\beta^*$. Because going to the Fermi-liquid from a high-temperature metal is accompanied by the enhancement of the electron mobility, at $\beta > \beta^*$ the gradual enhancement of the kinetic energy speeds up in this parameter regime.

The collected observations of this section confirm that when the system makes a passage from high to low temperatures, its spin-related response will exhibit a distinguishable non-monotonic behavior. We also demonstrate that this response is connected to the stronger spin-charge correlations in the Fermi-liquid phase, which was also traceable in local observables like the kinetic energy of the system.

### 5.3.2 Nonequilibrium physics: Approaching the Mott transition from the insulating region

In the previous chapter, we have discussed the equilibrium physics of the Hubbard model on the Bethe lattice both in metallic and insulating regions of the phase diagram. In

the following, we will investigate the relaxation behavior in systems with an insulating nature which is weakly coupled to a dissipative bosonic bath. We will first perform a time-dependent quick ramp of the hopping amplitude, which promotes the spectral density to a higher effective temperature, and then we will let the system evolve on its own. We will explore the thermalization behavior of this system, will characterize the dependence of its relaxation response on the electron-bath coupling.

To bring the system out of equilibrium, we preform a hopping quench according to the protocol of

$$J(t) = \begin{cases} \frac{J_0}{2}(1 - \cos(\frac{\pi t}{t_{\text{cut}}})) & \text{for } t < t_{\text{cut}} \\ J_0 & \text{Otherwise.} \end{cases}, \tag{5.80}$$

where $J_0$ is the hopping amplitude for $t > t_{\text{cut}} = 2.5$. This ramping of the hopping amplitude will bring the system from the atomic limit ($J = 0$) to a bad-insulator, where the spectral function has nonzero, but very small, weight at $\omega = 0$. The system at $t = t_{\text{cut}}$ represents a hot-carrier distribution which can be experimentally produced by a few-cycle pump-pulse. Due to the coupling to the heat-bath, the absorbed energy of this hot carrier can be dissipated by the bath and the system can effectively cool down. Without the bosonic bath, the only available cooling mechanism was due to the electron-electron scattering. In this case, when the system is its own bath, the transition from the bad-insulator to a good Mott-insulator is not possible as the total energy of the system can not be sufficiently reduced. However, in our proposed approach, the presence of the heat bath feasiblize the above mentioned transition in our setup.

Fig. 5.10 presents the kinetic energy and the double occupancy of some insulating systems. Results indicate two distinguishable relaxation mechanism for these local observables. The first one, is the exponential decay of the kinetic energy and double occupancy for smaller Hubbard interactions. To evaluate the exponential relaxation rate of these observables, we fit our data at $U \leq 5$ to $f(x) = f_{\text{eq}} + a\exp(-t/\tau)$, where $f$ is either the kinetic energy or the double occupancy. Fig. 5.11 shows the determined $\tau$ for the functions which have been plotted in Figs. 5.10 b) and d) for $10 < t \leq 80$.

Results reveal that the relaxation rate has a $U$ dependency, which is in agreement with previous reported results [134],[132]. It has been shown that in a pure electronic system the relaxation rate of the Mott-insulator is given by

$$\tau \propto \exp\left(\alpha \frac{U}{W} log(\frac{U}{W})\right), \tag{5.81}$$

where $\alpha$ is a constant. Such a $U$-dependent scaling can be understand easily. Conceivable relaxation channels in an insulating electronic system are related to the recombination of

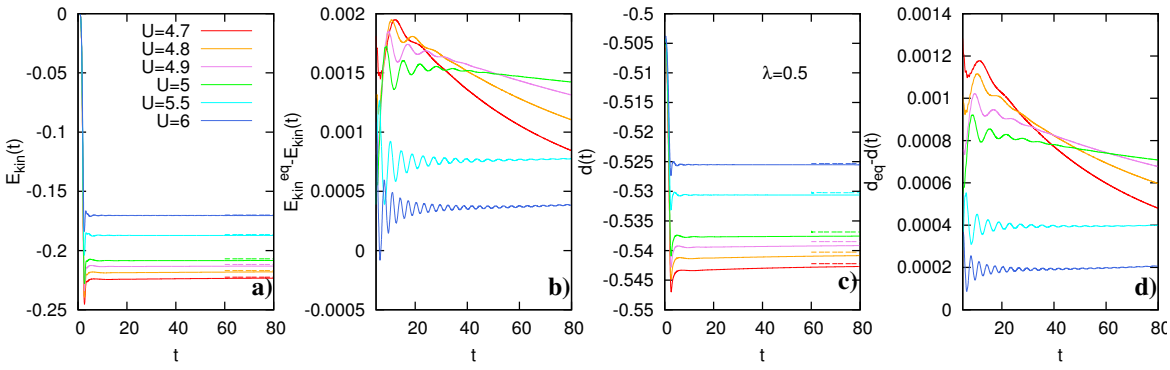


Figure 5.10: The kinetic energy and double occupancy for $U \in \{4.7, 4.8, 4.9, 5, 5.5, 6\}$ and $\lambda = 0.5$ at $\beta = 10$. a) The kinetic energy as a function of time. b) The difference between the thermal and the time-dependent kinetic energy. c) The double occupancy of the system as a function of time. d) The difference between the thermal and the time-dependent double occupancy. Dashed lines are thermal values.

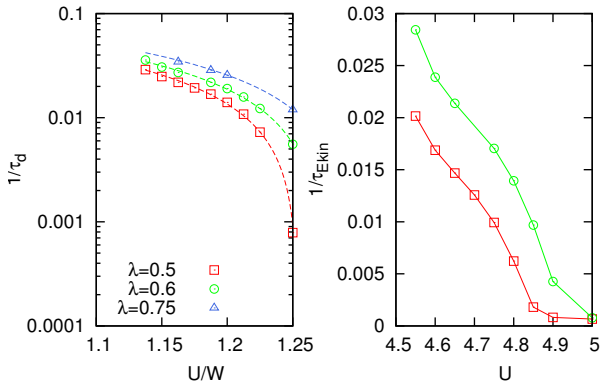


Figure 5.11: The relaxation rate of the kinetic energy, on the right, as a function of $U$ for systems at $\beta = 10$ and $\lambda \in \{0.5, 0.6\}$. On the left, the relaxation rate of the double occupancy as a function of $U/W$ for systems at $\beta = 10$ and $\lambda \in \{0.5, 0.6\}$. Dashed lines obtained using $\tau_{\mathrm{d}} \propto \frac{U}{W} log(\frac{U}{W})$.

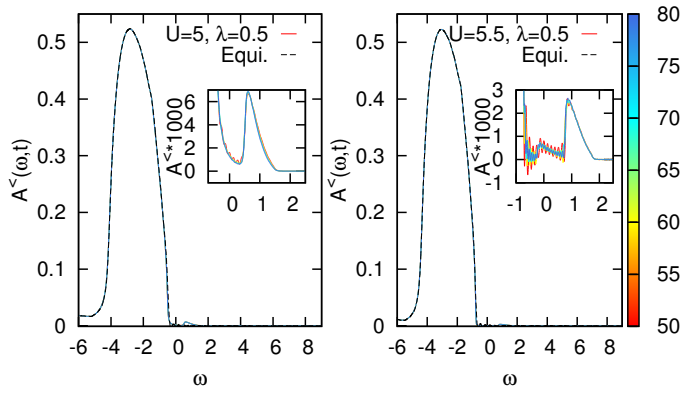


Figure 5.12: The occupied density of state for system at $U \in \{5, 5.5\}$, $\beta = 10$, $\lambda = 0.5$ as a function of time. The insets magnify the upper band spectral density, where the data is multiplied to $10^3$. Color coding represents the time. Dashed black lines are equilibrium counterparts.

the higher energy quasiparticles of the system with the lower energy quasiparticles. In the Hubbard model, these quasiparticles are doublons, located at the upper Hubbard band, and holons, placed in the lower Hubbard band. The recombination energy of these two quasiparticles is related to the Hubbard interaction $U$. When $U$ is large, the recombination of the doublon-hole would be larger than the kinetic energy of an individual doublon and holon, and thereby the system would rather to undergo into a multi-particle relaxation mechanism [154]. In our case where the electronic system is coupled to a heat-bath, the double occupancy relaxation time ($\tau_{\mathrm{d}}$), unsurprisingly, depends also on the bath-coupling, where the stronger the coupling to the bosonic bath is, the faster its transient state is relaxing. This is due to the opening of a new relaxation channel by bosons, as the doublon-holon recombination speeds up by the emission and absorption of bosons. However, the exponential relaxation is still governed by Eq. (5.81), where $\alpha$ depends on $\lambda$.

The exponential relaxation time of the kinetic energy ($\tau_{\mathrm{Ekin}}$) is plotted in Fig. 5.11. Comparing the relaxation behavior of the double occupancy and the kinetic energy is showing that $\tau_{\mathrm{d}} > \tau_{\mathrm{Ekin}}$. This relation would reveal that there must be another relaxation mechanism, which is absent for the relaxation of the double occupancy. This mechanism which is related to the intraband relaxation of the kinetic energy will not play any role when $U$ is large.

In Fig. 5.12, we plot the occupied density of state as a function of time. Results present that the exponential decay is taking place in systems, i.e. at $U = 5$, where the occupied

density is nonzero and the gap is still closed. In this case the outer edge of the high-energy densities are relaxing to the low energy states, heading to reach a thermal occupation, which is known as the impact ionization. However, when the gap is large, for instance at $U = 5.5$, the spectral density on the upper Hubbard band is almost trapped, and the density is mainly occupied the lower edge of the the high-energy band as a function of time. The wiggly lines at frequencies near $\omega = 0$, around the gap, are numerical Fourier artifacts. The very small accumulated density is the boson-mediated in-gap spectral weight, which its density is lesser at smaller $\lambda$. This density is responsible for the extremely gradual enlargement of $d - d_{\mathrm{eq}}$, in Fig. 5.10 b) and d) at $U \in \{5.5, 6\}$. In Chap. 6, we will elaborate such a boson-mediate relaxation mechanism in more details.

### 5.3.3 Nonequilibrium physics: Approaching the Mott transition from the metallic region

After covering the physics of the Hubbard model in the insulating part, it is tantalizing to investigate the metallic phase near PMIT under the same nonequilibrium initial excitation. On the metallic side of the phase diagram, the quick ramp of the hopping amplitude will destroy the quasiparticle peak of the phase diagram and will bring the system to a bad-metallic state. In Sec. 5.3.4, we will show that this bad-metallic state is a good representation of the photoexcited state. The natural question regarding the relaxation dynamics of the this excited state would then be how long it would take for such a system, which is weakly coupled to a dissipative bosonic bath, to equilibrate or thermalize. We devote this section to demonstrate an answer to such a question.

Here, we will perform a similar quench protocol, which we have been employed in the Sec. 5.3.2, given by Eq. (5.80). We will set the ramp-duration to $t_{\mathrm{c}} = 2.5$. This time-manipulation will form a high-temperature bad metallic state.

We now focus on exploring the formation of the quasiparticle band under the above mentioned quench of the hopping amplitude. We would like to elaborate the temporal evolution of the system during the relaxation from the bad-metallic state to the Fermi-liquid phase.

In Figs. 5.13, we compare the nonequilibrium spectral functions (solid lines at times indicated in plots), with their equilibrium correspondences (dashed lines). Plots show that at high temperature, i.e. at $\beta = 3$, corresponding to the bad metallic phase in equilibrium, the out of equilibrium spectral density at time ($t \approx 20$) retrieved the equilibrium density of state. At lower temperatures, i.e. at $\beta = 10$, the Hubbard bands are well built up while the quasiparticle peak is still away from its equilibrium counterpart. We also track this

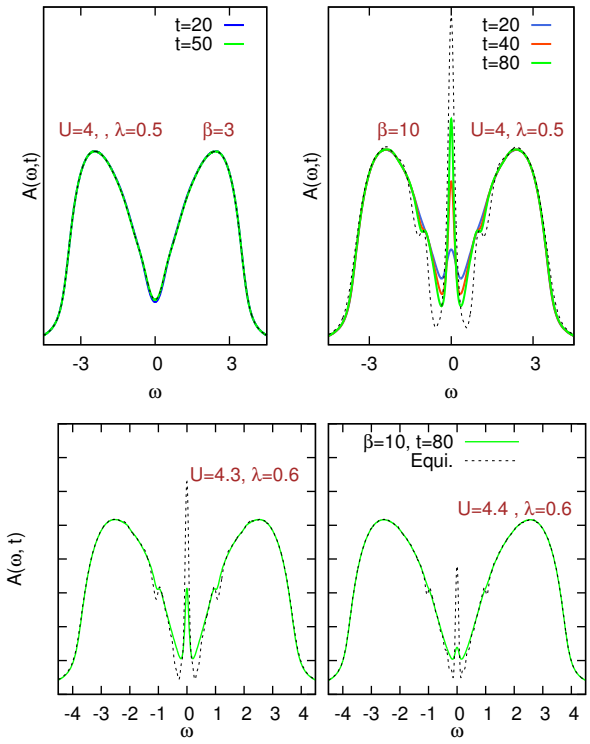


Figure 5.13: The spectral functions of four systems with parameter given by $(U, \beta, \lambda) \in \{(4, 3, 0.5), (4, 10, 0.5), (4.3, 10, 0.6), (4.4, 10, 0.6)\}$, in and out of equilibrium. Dashed lines indicate the equilibrium spectral functions for indicated parameters of each plot.

behavior in various systems with different Hubbard interactions, namely at $U \in \{4.3, 4.4\}$, see Fig. 5.13. Presented results at $\beta = 10$, similarly, show that apart from the large-frequency spectral weight, the low-energy density of state does not recover even at long times like $t = 80$. Besides, comparing the spectral weights at the same temperature, i.e. $\beta = 10$, displays that the bandwidth and the height of the quasiparticle peak is smaller in systems, which are closer to the PMIT.

These observations arouse our curiosity to systematically study the formation of the quasiparticle peak, specifically the height of the quasiparticle peak at $\omega = 0$ in the spectral function. In Fig. 5.14 a), we show that at high temperatures, i.e. at $\beta = 5$, the height of the quasiparticle attains its equilibrium value. However, $A(t, \omega = 0)$ at lower temperature deviates from its thermal value, and this difference would be larger in colder systems. In addition, the nonequilibrium evolution of the quasiparticle formation is almost

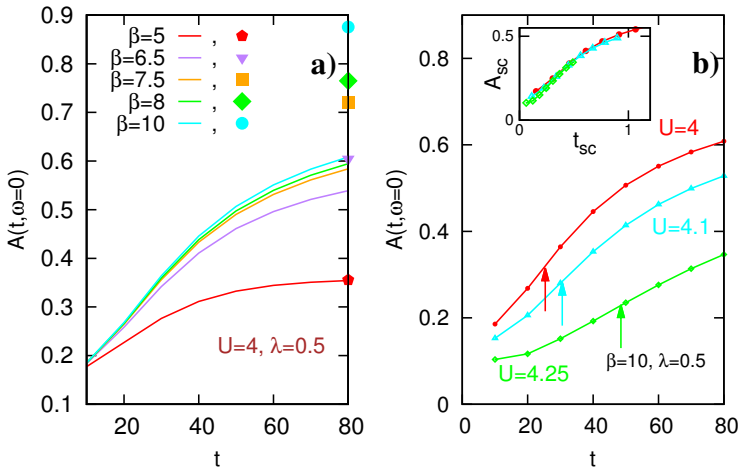


Figure 5.14: a) The nonequilibrium height of the spectral function at $\omega = 0$ for $U = 4$, $\lambda = 0.5$, and $\beta \in \{5, 6.5, 7.5, 8, 10\}$, solid lines. Points at $t = 80$ indicate to the thermal values. b) The height of the quasiparticle peak at $\beta = 10$, $\lambda = 0.5$, and $U \in \{4, 4.1, 4.25\}$. Arrows point to the height value at $t_{\max}$. Inset of b) Renormalized spectral functions, with an arbitrary factor, as a function of $t_{\rm sc} = t/\tau*$ (see main text for more details).

temperature-independent, which conveys that we are facing a regime where dynamics has a bottleneck. We also present the transient response of the quasiparticle peak for various Hubbard interactions at the same temperatures in Fig. 5.14 b). The results confirm that in systems which are closer to the PMIT, the quasiparticle peak is smaller and the associated evolution is slower.

Analyzing the recovery time of the Hubbard bands reveals that their build-up is reached within few multiples of the bandwidth-related timescale $[1/W]$. In contrast, neither the hopping time, nor the timescale related to the inverse width of the quasiparticle peak in equilibrium is found to explain the slow buildup of spectral weight at low frequencies. (For instance, the equilibrium bandwidth for $U = 4$ and $\lambda = 0.5$ at $\beta = 10$ is around 0.8. Its assigned timescale, which is $[1/0.8]$, is much smaller than $t = 80$, when even then the thermalization has not been attained.) In Sec. 5.3.4, we will show that despite the lattice-relate results, presented here, the bandwidth of the quasiparticle in the impurity model, known as the Kondo peak, will assign the relaxation timescale of the system.

The collected pieces of information, so far, expose the presence of a salient timescale in the system. In the following, we will characterize such a timescale using the spinon and rotor Green's function.

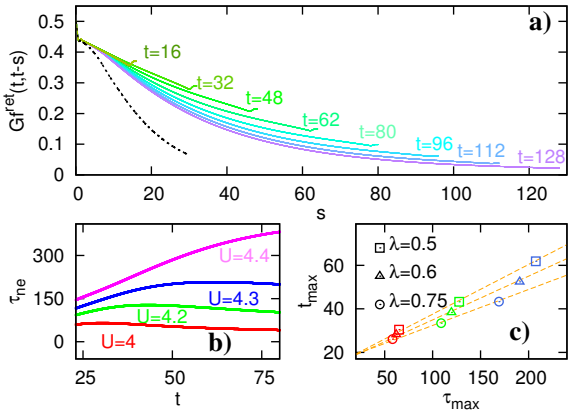


Figure 5.15: a) The retarded component of the spinon Green's function as a function of relative time ($s$) at various times $t$. Black dashed lines represent the retarded component of the equilibrium Green's function. b) The spinon lifetime ($\tau_{\rm ne}$) as a function time corresponding to the $s_0 = 16$. c) The maximum of spinon lifetime ($\tau_{\rm ne}$) as a function of its corresponding time ($t_{\rm max}$) for $\lambda \in \{0.5, 0.6, 0.75\}$. Figure is taken from Ref. [129].

We start the analysis by presenting the spinon Green's function in Fig. 5.15. Here, we plot the two-time spinon retarded Green's function ($G_f^{\rm ret}(t, t-s)$) as a function of the relative time for a sequence of first time-arguments ($t$). The time-evolution of $G_f^{\rm ret}(t, t-s)$ discloses the presence of a "$\bigcap$" turn, where the slope of the curve first goes up and then starts going down, taking place at $t = t_{\rm max}$, in the evolution of the spinon. As the evolution of the system starts heading back to the equilibrium (dashed line) after $t > t_{\rm max}$, one can immediately realize that this time is related to the bottleneck of the dynamics.

To elucidate this connection, we will define the nonequilibrium spinon lifetime as

$$\tau_{\rm ne}^{-1}(t) = \frac{\frac{\partial G_{\rm f}^{\rm ret}(t,t-s)}{\partial s}}{G_{\rm f}^{\rm ret}(t, t-s)}\Big|_{s=s_0}. \tag{5.82}$$

This relaxation is originated from considering the spinon Green's function as a Lorentzian function, where for a generic zero-centered Lorentzian function of the form

$$L(\omega) = \frac{1}{\pi}\frac{\Gamma}{\omega^2 + \Gamma^2}, \tag{5.83}$$

with the Fourier transform

$$FT\left[\frac{1}{\pi}\frac{\Gamma}{\omega^2 + \Gamma^2}\right] = e^{-\Gamma t}, \tag{5.84}$$

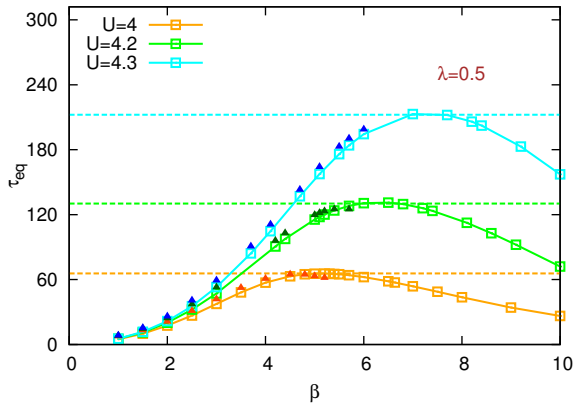


Figure 5.16: The spinon equilibrium lifetime as a function of $\beta$ for $U \in \{4, 4.2, 4.3\}$ and $\lambda = 0.5$. Dashed lines represent $\tau_{\max}$. Triangular points are obtained Using Eq. (5.79). Taken from Ref. [129].

the relation Eq. (5.82) would yield

$$\frac{\frac{\mathrm{d}e^{-\Gamma t}}{\mathrm{d}t}}{e^{-\Gamma t}} = \Gamma. \tag{5.85}$$

Thereby, Eq. (5.82) is the relation which captures the inverse lifetime, bandwidth, of the spinon Green's function. Fig. 5.15 b) displays $\tau_{\mathrm{ne}}(t)$ for various $U$ values. Results exhibit an initial increase of $\tau_{\mathrm{ne}}$ as a function of time and its reduction after passing a maximum. This maximum ($\tau_{\max}$) appears at $t_{\max}$. $t_{\max}$ is larger when the Hubbard interaction is closer to the PMIT. To understand the influence of the dissipative bath on the spinon "$\bigcap$" turn, we plot the $t_{\max}$ as a function of $\tau_{\max}$ for various electron-bath couplings in Fig. 5.15 c). Results shows that for larger couplings, i.e. $\lambda = 0.75$, $t_{\max}$ and $\tau_{\max}$ are smaller. This behavior can be easily understood by recalling that the introduced bath is a statistical canonical bath which exchange energy with the system. The energy exchange will cool down the system, and thereby speed up the process of passing through the "$\bigcap$" turn.

Transpiring of this nonmonotonous response in the evolution of the nonequilibrium spinon Green's function will immediately arouse the question about its connection to the nonmonotonous spinon response in the presented equilibrium physics, see Sec. 5.3.1. To answer this intriguing question, we plot Fig. 5.16 by drawing dashed lines at $\tau_{\max}$ for various Hubbard interactions. The plot clearly shows that $\tau_{\mathrm{eq}}$ coincides with $\tau_{\max}$. We hence can comprehend the nature of the "$\bigcap$" turn in the spinon response as an analog of the nonmonotonous bandwidth evolution in equilibrium.

It is also possible to present a functional form for the zero-frequency of the electron

spectral function using $\tau_*$ as

$$A_{\rm sc}(t,\omega=0) = a_{\rm U} f(\frac{t}{\tau_*}), \tag{5.86}$$

where $a_{\rm U}$ is an arbitrary $U$-dependent factor, and $f(t)$ is plotted in Fig. 5.14 e). In the inset of Fig. 5.14 e), we show the $A_{\rm sc}$ of systems with various Hubbard interactions are almost lie on top of each other. Such an overlap implies that the only relevant parameter which determines the response of the system is the spinon maximum lifetime as we were able to present the system as a functional of $t/\tau_*$. Capturing better agreement of the presented functional form of $A_{\rm sc}$ requires longer simulation times, which are currently out of reach due to the large computational cost.

After disclosing the nature of the bottleneck of dynamics, in the remaining, we will put our attention on the rotor Green's function to examine the presence of the thermalization as well as the footprint of $t_{\rm max}$ in its dynamics. Assessing the thermalization in the charge-related subspace can be easily done by checking the fluctuation dissipation theorem, described in Sec. 2.38. This theorem implies that if the subsystem is thermalized one can assign an effective temperature ($\beta_{\rm eff}$) to that which satisfies

$$e^{\beta_{\rm eff}\omega} = \frac{G^{>}_X(\omega,t)}{G^{<}_X(\omega,t)}, \tag{5.87}$$

where $G^{>,<}(\omega,t)$ is obtained using Eq. (2.41) after replacing the retarded function by $G^{>,<}$. Fig. 5.17 a) presents the absence of such a thermalization in the rotor Green's function as the low-energy part of the $G^{>}/G^{<}$ at $t = 80$ behaves differently from the height energy sector. This evidence is the consequence of the retrieval of the Hubbard bands as well as the on-going evolution of the quasiparticle density in small frequencies.

Due to the spinon and rotor interaction, one would expect that the spinon nonmonotonous evolution would also be imprinted on the rotor Green's function. In Fig. 5.17 b), we plot the partial integrated rotor Green's function as

$$I(t) = \int_0^{0.5} {\rm d}\omega \quad A_X(t,\omega), \tag{5.88}$$

where the integration energy window is set such that the small bath-related sub-bands in the rotor Green's function will not be included in $I(t)$. Results present that till $t_{\rm max}$ the density will be accumulated in the above mentioned energy window, while after passing this time the concentration of the rotor density starts decreasing. This can be understand by recalling that at $t_{\rm max}$ the spinon bandwidth is in its lowest value, and after passing $t_{\rm max}$ its bandwidth starts enlarging, which results in the broadening of the rotor spectral weight.

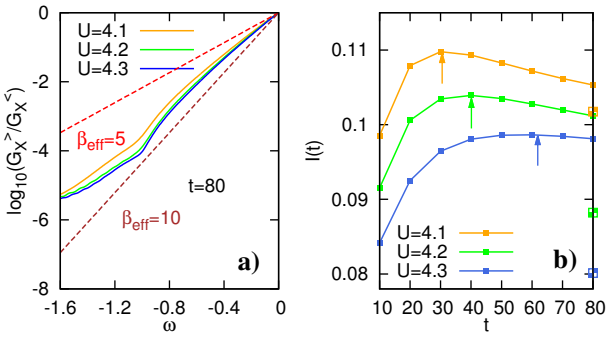


Figure 5.17: a) The ratio between the unoccupied ($G^{>}$) over occupied ($G^{<}$) density of state as a function of energy at $t = 80$ for $U \in \{4.1, 4.2, 4.3\}$ at $\beta = 10$. Dashed lines are $f(\omega) = \beta_{\text{eff}}\omega$ with $\beta_{\text{eff}}$ as indicated in the plots. b) Integrated spectral density in the low-energy window of $\omega \in [0, 0.5]$ at $t = 80$ for $U \in \{4.1, 4.2, 4.3\}$ at $\beta = 10$. Arrows points to $I(t_{\max})$. Half-filled square points corresponds to the equilibrium values.

### 5.3.4 Nonequilibrium physics: Equilibration of the slave-rotor impurity solver

This section is aimed to strengthen two statements which have been mentioned in the previous section. To be more precise, we would like to demonstrate the relaxation timescale as well as the thermalization process in the system which has one site. In the preceding section, we have pointed out that the relaxation timescale of an impurity site is determined by the bandwidth of the Kondo peak, and within this timescale the system is able to reach its thermal state. We also have concluded that the very slow relaxation dynamics of the excited state is a clear lattice effect and completely distinctive from the physics of the impurity problem. In this section, we will investigate the nonequilibrium Kondo physics using the Anderson impurity model. We would like to explore the relaxation dynamics of an excited state under the hopping quench protocol, which has been employed in previous sections.

To achieve these goals, we studied a one-site system at $U = 2$ under the ramp of the hopping amplitude as

$$J(t) = \begin{cases} \frac{J_0}{2}(1 - \cos(\frac{\pi t}{t_c})) & \text{for} t < t_c \\ J_0 & \text{Otherwise.} \end{cases}, \tag{5.89}$$

where $t_c = 0.25$, and $J_0 = 0.4$. We solved this problem using the slave-rotor impurity solver with the hybridization function of the form $\Delta(t, t') = J(t)G_0(t, t')J(t')$, where $G_0$ is

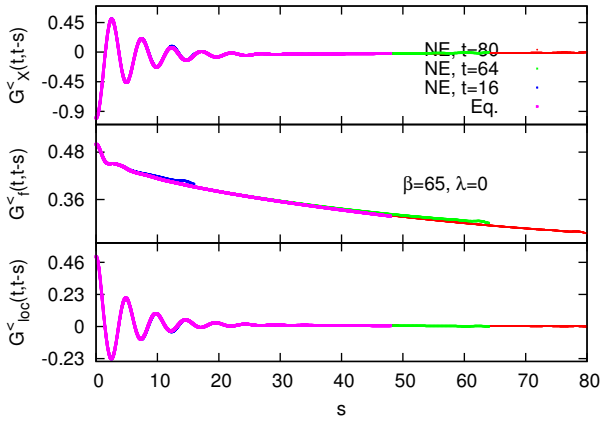


Figure 5.18: Lesser components of the rotor a), spinon b), and electron c) Green's functions as a function of time difference ($s$) for $t \in \{16, 64, 80\}$ at $\beta = 65$ in and out of equilibrium.

the noninteracting Bethe Green's function with the half bandwidth of $2J_0$. This parameter regime is characterized by a three well-separated peaks in the density of state. The bandwidth of Kondo peak (centered at $\omega = 0$) is 0.25.

In Fig. 5.18, we plot lesser components of the rotor, spinon, and electron Green's function as a function of time-difference $s = t - t'$. We show that the nonequilibrium outcome is almost time-independent for $t > 16$. This implies that the system reached an steady state. Moreover, out of equilibrium results lie on top of equilibrium correspondences, indicating that the system is equilibrated. Using the equilibrium bandwidth ($W_{\text{kondo}}$), we can introduce a timescale due to the energy uncertainty as $1/W_{\text{kondo}}$. This timescale, is almost $t \approx 16$, manifests the nonequilibrium relaxation timescale [110]. Hence, the temporal evolution of the Kondo problem, which is governed by the equilibrium physics, is thermalizing in a short period of time.

### Nonequilibrium physics: Thermalization of the photoexcited electrons in the square lattice

In the preceding sections, we have exploited a particular time-dependent hopping amplitude which brings the system from an atomic limit to a bad-metallic (-insulating) regime. There, we have mentioned that such a quench protocol will lead to a state which is also attainable after exposing the system to a pump-pulse. In this section, we will focus on investigating the properties of a induced bad-metallic state under both the time-dependent hopping

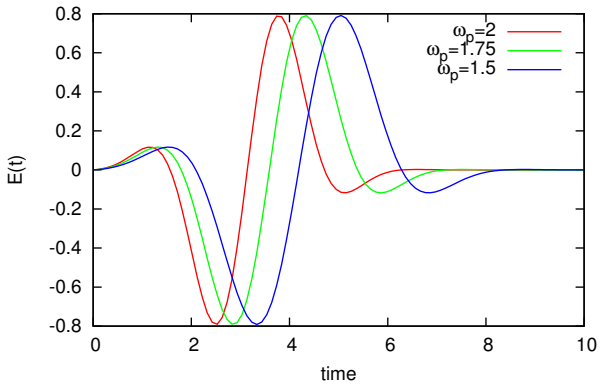


Figure 5.19: Electric field of the pulse with $\omega_p \in \{1.5, 1.75, 2\}$.

amplitude and the laser pulse. Other than in the previous sections, we will conduct a research on the two-dimension square lattice, and will study the influence of the initial preparation on the properties of the bad-metallic state. We would like to present the results which support our above-mentioned claim on the possibility of capturing similar physics with both applying a pump-pulse and a rapid quench of the hopping amplitude, to prepare the initial state.

Here, we will consider systems under the ramping of the hopping amplitude, introduced in Eq. (5.80), as well as the incident of a few-cycle pump pulse. We consider a pulse with the wavelength which is longer than the lattice spacing with the electric field given by

$$\overrightarrow{E} = E_0 \sin\big(\omega_p(t-t_0)\big) e^{-\frac{4.6(t-t_0)^2}{t_0^2}} \widehat{n}, \tag{5.90}$$

where $\widehat{n}$ is the polarization direction set on the body diagonal of the lattice, $\widehat{n} = (1,1)$, $E_0 = 1$, $t_0 = 2\pi/\omega_p$, $\omega_p$ is the pulse frequency, and the exponential Gaussian term determines the pulse envelope. Using Peierls substitution, we can write the Hubbard model as

$$H = \sum_{\mathbf{k},\sigma} \epsilon_{\mathbf{k}-\frac{e}{\hbar c}\mathbf{A}}(t) c^\dagger_{\mathbf{k}\sigma} c_{\mathbf{k}\sigma} + U \sum_i n_{i\uparrow} n_{i\downarrow}, \tag{5.91}$$

where $\mathbf{k}$ is the momentum in the Brillouin zone. Here, $\mathbf{A}$ is the vector potential obtained by $\overrightarrow{E}(t) = -\partial_t \mathbf{A}(t)/c$, $c$ is the speed of light, $h$ is the Planck constant, $e$ is the electron charge, and we will choose the unit in which $e/hc$ is one. $\epsilon_{\mathbf{k}}$ is the dispersion relation of the square lattice given by

$$\epsilon_{\mathbf{k}} = 2J_0\big(\cos(k_x a) + \cos(k_y a)\big), \tag{5.92}$$

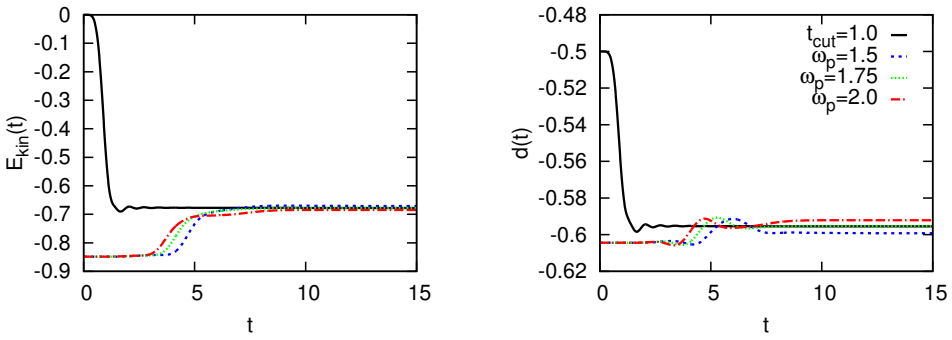


Figure 5.20: a) The kinetic energy and b) the double occupancy of a system at $U = 6.5$, $\beta = 10$, under hopping ramp with $t_{\rm cut} = 1.0$ (red solid line), and the pulse with $\omega_p \in \{1.5, 1.75, 2\}$ (dashed lines).

with the lattice constant $a = 1$, and $J_0 = 1$ is the hopping amplitude, which corresponds to the bandwidth of $W = 8$.

Since the pulse is included only in the nonlocal term of the Hamiltonian, the DMFT self-consistency, with the slave-rotor impurity solver, will be closed after computing the hybridization function introduced in Sec. 3.1.1.

It has been shown that the photo-excited state of the Hubbard model on the hypercubic lattice is rapidly thermalized [30]. Here, we will not only examine this conclusion on the square lattice, but also we will show that its final state is the same as a ramped hopping state. To reach this conclusion, we use $t_{\rm cut} = 1$ for the hopping quench protocol, given by Eq. (5.80). The frequency of the pump pulse will be set to $\omega_p \in \{1.5, 1.75, 2\}$, where the depicted pulses are plotted in Fig. 5.19. One should note that these pulse energies are strong enough to melt the quasiparticle peak of the Hubbard model, with frequencies which will tune the absorbed energy to the same value of the hopping quench. The absorbed energy of the pulse will bring the system to the bad-metallic state. Therefore, the presented results are distinct from the physics which has been discussed in Sec. 5.3.3.

In Fig. 5.20, we plot the kinetic energy and the double occupancy of systems under the two above mentioned preparation protocols. Results exhibit that the short-time responses of these systems dependents strongly on the initial memory of the system. By passing the time, this memory will be lost, and the system reaches a thermal state. It is remarkable to note that the thermalization is reached within few $1/J_0$, which has been previously reported also on the hypercubic lattice [30]. It is also shown that final values of the kinetic energy and double occupancy for a system under the pump pulse with the frequency of

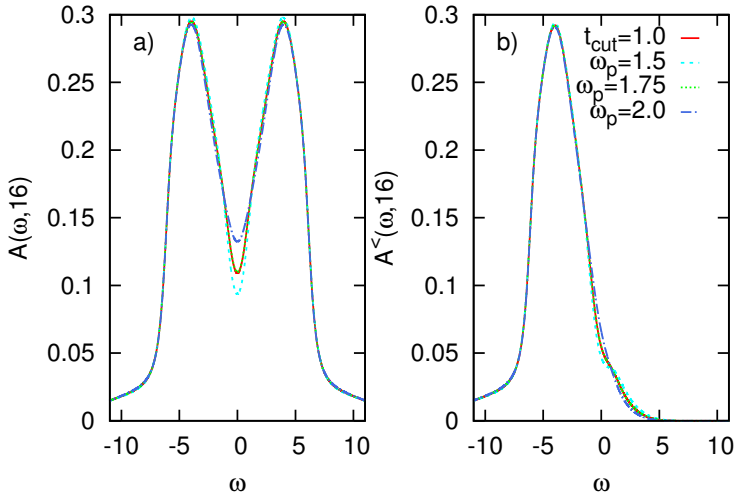


Figure 5.21: a) The occupied and b) unoccupied spectral functions of the system at $U = 6.5$, $\beta = 10$, under hopping ramp with $t_{\rm cut} = 1.0$ (red solid line), and the pulse with $\omega_p \in \{1.5, 1.75, 2\}$ (dashed lines).

$\omega = 1.75$ are the same as the values of local observables under the ramp of the hopping amplitude with $t_{\rm cut} = 1$. This matching of the final state was due to the same total energy of these systems, or equivalently, the same amount of the transfered energy during the nonequilibrium manipulation of the system.

Fig. 5.21 also confirms that $\omega_p = 1.75$ is relaxed to the same transient state as the hopping ramp-protocol with $t_c = 1$. Results reveal that at $t = 16$, not only the spectral function but also the occupied spectral density ($A^<$), obtained using Eq. (2.41), are presenting the same long-time features.

In addition, comparing total spectral densities as well as unoccupied ones for various pulse frequencies indicate that shorter pulse durations, larger $\omega_p$, excite less carriers to the upper Hubbard band, and thereby its double occupancy is lesser and electrons are more mobile, larger absolute values of the kinetic energies.

The presented observation manifests that the preparation of the bad metallic state via the hopping quench or pulse protocols can serve similar thermalized state in a short period of time. We thus can generalize our presented results in Secs. (5.3.2, 5.3.3), to any pulse-excited states, which have the same total energies as the quench excited states.

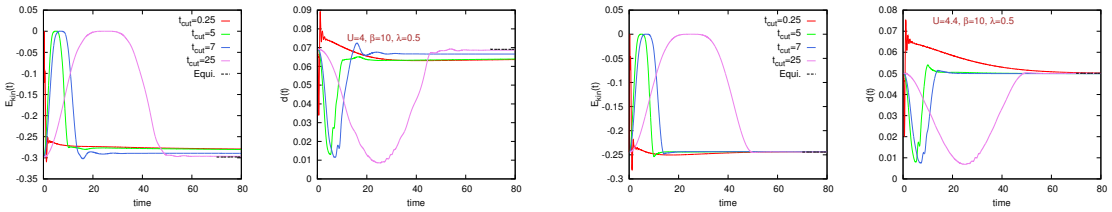


Figure 5.22: The right panel is the kinetic energy and double occupancy for systems with $U = 4$ at $\beta = 10$ for $t_c \in \{0.25, 5, 7, 25\}$. The left panel is the kinetic energy and double occupancy for systems with $U = 4.4$ at $\beta = 10$ for $t_c \in \{0.25, 5, 7, 25\}$. Dashed lines are thermal values of the local observables at parameter regimes indicated on the plots.

### 5.3.5 Nonequilibrium physics: Limit of adiabaticity near Mott transition

The adiabatic theorem states that if the time-evolution of the system is performed "very" slowly, the system will gradually go from the eigenstate of the initial Hamiltonian to the eigenstate of the final Hamiltonian. In this class of evolution the transient state corresponds to the instantaneous Hamiltonian. This theorem is no longer applicable near, either the first or the second kind, phase transitions where "very" slow evolutions will be no longer accessible. In general, the determination of the nonadiabatic window, where inside that the adiabatic theorem does not hold, is not clear and it depends on the model Hamiltonian.

We hence try to investigate such a window near PMIT. Here, we consider a time-dependent hopping amplitude with the form of

$$J(t) = \begin{cases} J_0 \cos\left(\frac{\pi t}{2t_c}\right) & \text{for } t \geq t_c \\ J_0 \cos\left(\pi + \frac{\pi t}{2t_c}\right) & \text{for } t_c < t \geq 2t_c \\ J_0 & \text{Otherwise} \end{cases}, \tag{5.93}$$

with $J_0 = 1$. We will vary $t_c$ and will analyze the response of the system with respect to different $t_c$. The idea behind this quench protocol is to find the time in which the destructed correlations at $t \leq t_c$ can be fully reconstructed in $t > t_c$.

In Fig. 5.22, we plot kinetic energies and double occupancies of two systems at $U \in \{4, 4.4\}$, and $\beta = 10$ for various $t_c$. Results exhibit that the time-evolution of local observables corresponding to larger $t_c$ are closer to their thermal counterparts.

To analyze such a behavior more systematically, we plot the kinetic energy and double occupancy at $t = 80$ in Fig. 5.23. For $U > 4$, adiabaticity is achieved only at the largest

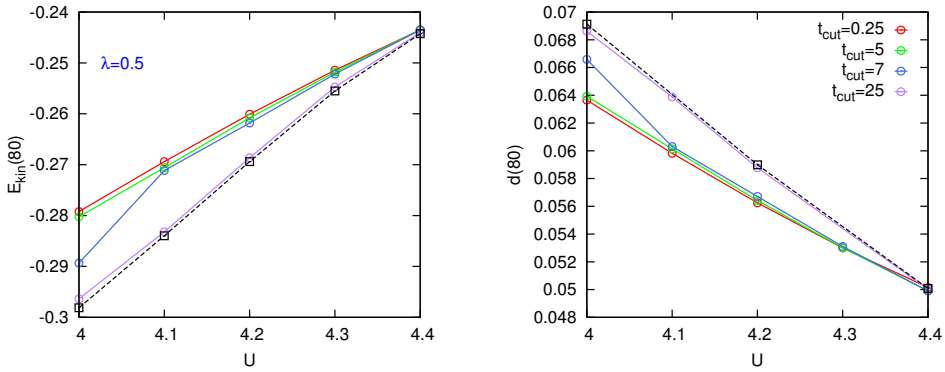


Figure 5.23: Left: The kinetic energy values at $t = 80$ as a function of Hubbard interaction. Right: The double occupancy values at $t = 80$ for various $t_c \in \{0.25, 5, 7, 25\}$. Dashed lines indicate the equilibrium values.

ramp time, while for $U = 4$ already a short ramp time $t_{cut} = 7$ leads to more adiabatic behavior. These observations indicate that the nonadiabatic window of the Hubbard model, on the metallic side, is in the window of $[4, U_c]$.

Spectral function of these systems will provide a clue for such a response. Fig. 5.24 displays the density of state ($A(\omega, t)$) of the system at $t = 80$. Results show that this slow retrieval is related to the build-up of the quasiparticle peak, and larger $A(\omega = 0, 80)$ is observed in systems with larger $t_c$. We thereby can conclude that the similar to the physics discussed in Sec. 5.3.3, spinon lifetime is the underlying physics of this nonadiabatic dynamics of the system, where the height enhancement of the quasiparticle peak present a slow retrieval.

## 5.4 Outlook

As a continuation of the presented work, it would be extremely interesting to study the optical conductivity of the system during the bad-metal-to-good-metal transition, as equilibrium measurements of this quantity exhibit the fingerprints of the non-Fermi-liquid responses [87, 80, 25], connected to the spin-spin correlation function [153]. A substantial extension of our work is related to the investigation of the doped case using the slave-rotor formalism. As by including such investigations, we can provide an extensive understanding of the Hubbard model. Particularly, it would be so interesting to figure out whether various amounts of doping can modify the slow retrieval of the quasiparticle peak close

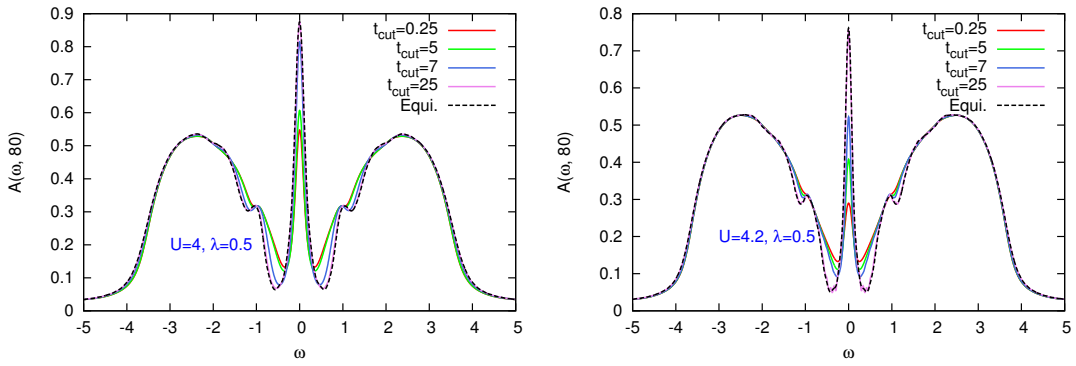


Figure 5.24: The spectral function of the system for $U = 4$ (the left panel) and $U = 4.2$ (the right panel) for systems at $\beta = 10$, $\lambda = 0.5$, and $t = 80$.

to PMIT, or not. In addition, the study of the antiferromagnetic phase of the system strongly arouses our curiosity. It would be interesting to conduct a research on systems with partial magnetic frustrations. Furthermore, surveilling the properties of the system in the coexistence regime out of equilibrium entices us to also perform a study on this region of the phase diagram in near future.

# Chapter 6

# Nonequilibrium DMFT study of the Hubbard-Holstein model

In the preceding chapter, we have extensively explored the enchanting physics of an interacting electronic system close to the transition from the Fermi-liquid to an insulating phase. We have presented that in the insulating phase the physics of the system is mainly dominated by the charge excitations, as spin and charge degrees of freedom become almost uncoupled. We have also illustrated the physics of the metallic phase, where the coupling of spin and charge is intensified at low temperatures, and therefore the slow dynamics of spinons in the crossover regime becomes relevant. We also have demonstrated a slow thermalization both in the metallic and insulating phases close to the Mott transition.

In the previous chapter, we have weakly coupled the system to a bosonic heat bath. In this chapter, we would like to develop a more systematic study on such a coupling by not only treating the bosons as a heat bath, but also self-consistently including the feedback from electrons into the bosonic bath. We would like to be able to understand how the delocalization tendency of electrons and the localization by the Coulomb interaction can be modified upon embedding the system in a polarizable medium. To achieve this goal and to investigate phonon-stimulated properties of the system in and out of equilibrium, we will employ the Hubbard-Holstein Hamiltonian, which incorporates both electron-electron and electron-phonon interactions. We will tackle this problem by introducing a generalized slave-rotor impurity solver within the DMFT formalism.

## 6.1 Model and methods

Investigating the interplay between the lattice and electrons degrees of freedom in an interacting system is considered an exceedingly difficult problem as the Hilbert space is too large for Hamiltonian-based numerical techniques, and analytical problems are scarce. Nevertheless, researchers proposed various methods to confront these challenges, which are mainly based on integrating part of degrees of freedom out, known as "downfolding" [155], or employing perturbative methods [16]. Various model Hamiltonians have been studied, which differ in the type of phonons and in the coupling. In this chapter, we will put our focus on studying the problem under the Hubbard-Holstein model.

This model Hamiltonian for a one-band system is defined as

$$H = -\sum_{\langle ij\rangle,\sigma} J_{ij}(c^{\dagger}_{i\sigma}c_{j\sigma}+H.c)-\mu\sum_{i} c^{\dagger}_{i}c_{i}+U\sum_{i} n_{i\uparrow}n_{i\downarrow}+\omega_0\sum_{i} b^{\dagger}_{i}b_{i}+g\sum_{i\sigma} n_{i\sigma}(b^{\dagger}_{i}+b_{i}), \quad (6.1)$$

where $c^{\dagger}_{\sigma}(c_{\sigma})$ is the electron creation (annihilation) operator with spin $\sigma$, $J_{ij}$ is the hopping amplitude from site $i$ to the next nearest site $j$, $U$ is the on-site Coulomb repulsion, and $\mu$ is the chemical potential. $\omega_0$ is the phonon frequency, and $g$ is the electron-phonon coupling, which determines the strength of the coupling between the density of electron ($n_i$) at site $i$ and the displacement of phonon ($X_i = (b_i + b^{\dagger}_i)/\sqrt{2}$) at the same site. The energy scales which characterize this model are related to the Holstein model, namely $\lambda$, $\gamma$, $E_{\mathrm{p}}$, and $\alpha$ which have been introduced in Sec.4.1, and the Hubbard model ($U/W$), where $W$ is the bandwidth of the system.

For a fixed phonon frequency, the schematic phase diagram of this model Hamiltonian at half-filling is composed of metallic, Mott insulating, and bipolaronic insulating phases [73], shown in Fig. 6.1. We pictorially draw the electron configuration within different parameter regimes of the Hubbard-Holstein model in Fig. 6.1. The phase transition from the metal to the Mott insulator is presented by the red line in Fig. 6.1. Due to the screening effect, induced by phonons for $\lambda \neq 0$, the strength of the repulsive interaction between electrons will be reduced, and thereby the transition line from metal to Mott insulator is curved towards larger Hubbard interactions. This reduction is given by $U_{\mathrm{eff}}(\omega) = U - \frac{2g^2\omega_0}{\omega_0^2-\omega^2}$ [149, 126, 11]. In the extreme adiabatic regime $\omega_0 \to \infty$, where the Lang-Firsov approximation is applicable, the dynamical Hubbard interaction ($U_{\mathrm{eff}}$) will become static as $U_{\mathrm{eff}} = U - 2g^2/\omega_0$ [64]. It has been also shown that when $\lambda$ is small, the system can be effectively described by the Hubbard model [126], while when $U$ is negligible, the system is exhibiting Holstein-like physics [64].

In Fig. 6.1, we also sketch generic real-space configurations of electrons on a square lattice in the metallic, Mott, and bipolaronic insulating phases. In the Mott insulating

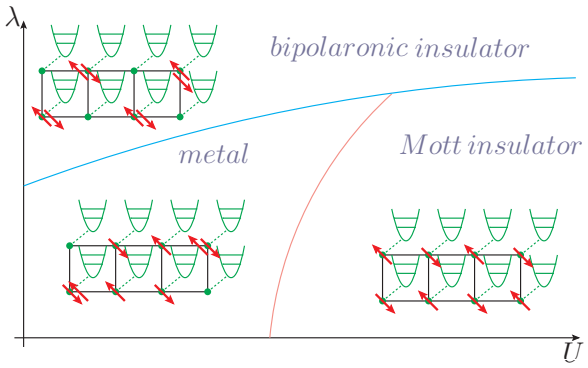


Figure 6.1: The zero-temperature phase diagram of the Hubbard Holstein model consisting of the metal, Mott insulating, and bipolaron insulating regions [73]. The red solid line indicates the phase transition from metallic to Mott insulating phase. The phase of the system at $U = 0$ and large $\lambda$ is corresponding to a phase known as the charge-density wave. The blue solid line is the phase boundary of the bipolaronic insulator from the metallic phase in small $U$ and Mott insulating phase in $U$-dominant regimes. The electron configuration (red arrows) on the square lattice, connected to Holstein phonons (harmonic potentials), is shown by the inset.

phase, the number of doublons is smaller than the metallic phase, as the large Coulomb interaction prohibits electrons, with opposite spins, from occupying one site of the lattice. When the electron-phonon coupling is very large, the screening effect will enhance the probability of forming doublons, and the bipolaronic insulator will occur when $U_{\text{eff}} < 0$. In the bipolaronic insulating phase, the effective attractive interaction ($U_{\text{eff}} < 0$) impels the formation of a bound state, known as a *bipolaron*, which is associated with the energy $E_{\text{bp}} = 2E_{\text{p}}$. The bipolaronic bound state is a two-electron singlet, in which the electrons are bounded together by a phonon-mediated attractive interaction taking place when both electrons with opposite spins are at the same site of the lattice.

In this chapter, we aim at the intriguing parameter regime in the vicinity of the phase transition from metallic to (bipolaronic / Mott) insulator. In the upcoming section, we will incorporate the slave-rotor technique, introduced in Chap. 5, with a perturbative treatment of the phonons to conduct a research on the above-mentioned regime of the system.

### 6.1.1 Methods for studying the Hubbard-Holstein model

In this section, we will introduce an approach to incorporate the electron-phonon interaction into the slave-rotor impurity-solver. Two possible approaches for achieving this goal are employing a retarded Hubbard interaction, and introducing an auxiliary boson within the framework of the extended DMFT. We will explain these two approaches in the following.

The action of the Hubbard-Holstein model can be written as

$$\begin{aligned}\mathcal{S}[c^*,c,b^*,b] = \Big\{ &\int_{\mathcal{C}} \mathrm{d}t \sum_{i,\sigma} c^*_{i\sigma}(t)\big(i\partial_t+\mu\big)c_{i\sigma}(t) + J\int_{\mathcal{C}}\mathrm{d}t\sum_{\langle ij\rangle,\sigma} c^*_{i\sigma}(t)c_{j\sigma}(t) \\ &- U\int_{\mathcal{C}}\mathrm{d}t\sum_i n_{\uparrow i}n_{\downarrow i} \\ &+ \int_{\mathcal{C}}\mathrm{d}t\sum_i b^*_i(t)\big(i\partial_t-\omega_0\big)b_i(t) - g\int_{\mathcal{C}}\mathrm{d}t n_i(t)(b_i(t)+b^*_i(t))\Big\}, \end{aligned} \tag{6.2}$$

where $J$ denotes the site-independent hopping amplitude, and the partition function is given by $\mathcal{Z}=\int\mathcal{D}[c,c^*]\mathcal{D}[b,b^*]e^{i\mathcal{S}}$. To bring the action into the slave-rotor treatable form, we will separate the action into two parts, as

$$\mathcal{S} = \mathcal{S}_{\mathrm{el}} + \mathcal{S}_{\mathrm{nb}}, \tag{6.3}$$

where

$$\mathcal{S}_{\mathrm{el}}[c^*,c] = \Big\{\int_{\mathcal{C}}\mathrm{d}t\sum_{i,\sigma} c^*_{i\sigma}(t)\big(i\partial_t+\mu\big)c_{i\sigma}(t) + J\int_{\mathcal{C}}\mathrm{d}t\sum_{\langle ij\rangle,\sigma} c^*_{i\sigma}(t)c_{j\sigma}(t) - \frac{U}{2}\int_{\mathcal{C}}\mathrm{d}t\sum_{i\sigma} n_{\sigma i}n_{\overline{\sigma}i}\Big\}, \tag{6.4}$$

$$\mathcal{S}_{\mathrm{nb}}[n,b^*,b] = \Big\{\int_{\mathcal{C}}\mathrm{d}t\sum_i b^*_i(t)\big(i\partial_t-\omega_0\big)b_i(t) - g\int_{\mathcal{C}}\mathrm{d}t\sum_i n_i(t)(b_i(t)+b^*_i(t))\Big\}, \tag{6.5}$$

where $\sigma$ is the spin indices, and $\overline{\sigma}=1-\sigma$. Here, $\mathcal{S}_{\mathrm{el}}$ is a pure electronic action, which we have studied in Chap.5. $\mathcal{S}_{\mathrm{nb}}$ is the remaining part of the action, containing the phononic terms of the model Hamiltonian.

Representing $\mathcal{S}_{\mathrm{nb}}$ in terms of the phonon displacement operator yields

$$\begin{aligned}\mathcal{S}_{\mathrm{nb}}[n,b^*,b] &= \Big\{\int_{\mathcal{C}}\mathrm{d}t\sum_i b^*_i(t)\big(i\partial_t-\omega_0\big)b_i(t) - g\int_{\mathcal{C}}\mathrm{d}t\sum_i n_i(t)(b_i(t)+b^*_i(t))\Big\} \\ &= \Big\{\int_{\mathcal{C}}\mathrm{d}t\sum_i X_{\mathrm{ph},i}(t)\mathcal{D}_0^{-1}X_{\mathrm{ph},i}(t) - \sqrt{2}g\int_{\mathcal{C}}\mathrm{d}t\sum_i n_i(t)X_{\mathrm{ph},i}(t)\Big\}. \end{aligned} \tag{6.6}$$

Here, the bare phonon Green's function defined as

$$\mathcal{D}_0(t,t') = -2i\langle \mathcal{T}_{\mathcal{C}} X_{\rm ph}(t) X_{\rm ph}(t')\rangle, \tag{6.7}$$

$$\mathcal{D}_0^{-1}(t,t') = \frac{-\partial_t^2 - \omega_0^2}{\omega_0}\delta_{\mathcal{C}}(t,t'), \tag{6.8}$$

where $\mathcal{T}_{\mathcal{C}}$ is the time-ordering operator along the Keldysh contour ($\mathcal{C}$). To have an interacting solution of the model, we should solve a coupled set of Dyson equations, which are obtained from $\mathcal{S}_{\rm nb}$ and $\mathcal{S}_{\rm el}$. We will present the DMFT scheme using this approach in Sec. 6.1.2.

But before going to details of this scheme, we would build the foundation of our second approach by deriving a retarded Hubbard interaction. To separate the bosonic from the fermionic degrees of freedom, we will integrate out the bosonic fields using a Hubbard-Stratonovich identity

$$\begin{aligned}
&\int \mathcal{D}[x]\mathcal{D}[c,c^*] e^{i\mathcal{S}_{\rm nb}[n,x]} = \\
&= \int \mathcal{D}[c,c^*]\mathcal{D}[x] \exp\Big(i\big[\int_{\mathcal{C}} {\rm d}t \sum_i X_{{\rm ph},i}(t)\mathcal{D}_0^{-1} X_{{\rm ph},i}(t) - \sqrt{2}\int_{\mathcal{C}} {\rm d}t g(t)\sum_i X_{{\rm ph},i}(t) n_i(t)\big]\Big), \\
&\propto \int \mathcal{D}[c,c^*] \exp\Big(i\iint_{\mathcal{C}} {\rm d}t'{\rm d}t \sum_i n_i(t)[ig(t)]2\mathcal{D}_0(t,t')[ig(t')]n_i(t')\Big),
\end{aligned} \tag{6.9}$$

where we performed the Keldysh path integral by noting that $-i\mathcal{D}_0^{-1}$ is positive definite. As a result, we will obtain a retarded Hubbard interaction as

$$\mathcal{U}(t,t') = -2g(t)\mathcal{D}_0(t,t')g(t'). \tag{6.10}$$

Subsequently, the total on site electron-electron interaction will be renormalized to the form of

$$\mathcal{U}_{\rm eff} = \frac{U}{2} - 2g(t)\mathcal{D}_0(t,t')g(t'). \tag{6.11}$$

Here, $\mathcal{U}_{\rm eff}$ is the phonon-mediated dynamical screening [149, 126, 11]. Using this effective Hubbard interaction ($\mathcal{U}_{\rm eff}$), we will propose a purely electronic generalized slave-rotor method to treat the Hubbard-Holstein model in Sec. 6.1.3.

### 6.1.2 Impurity solver using the Hartree-Fock/ Migdal prescription

We map the lattice action of $\mathcal{S}_{\rm el}$ onto the impurity-bath problem to be able to apply the DMFT formalism to the system. Such a mapping can be preformed by integrating the

bath degrees of freedom at the cost of introducing a hybridization function ($\Delta$), leading to the impurity action

$$\mathcal{S}_{\rm el}[c^*,c] = i\Big\{ \int_{\mathcal{C}} \mathrm{d}t \sum_\sigma c^*_\sigma(t)\big(i\partial_t+\mu\big)c_\sigma(t) - \frac{U}{2}\int_{\mathcal{C}} \mathrm{d}t \sum_\sigma n_\sigma(t) n_{\bar\sigma}(t) + \iint_{\mathcal{C}} \mathrm{d}t\mathrm{d}t' c^*_\sigma(t)c_\sigma(t)\Delta(t,t')c^*_\sigma(t')c_\sigma(t')\Big\}. \tag{6.12}$$

Exploiting this action in companion with electron-boson action of Eq. (6.5) will empower us to write down two Dyson equations for the electronic and phononic subsystems as

$$G_{\rm imp}(t,t') = G_0 + [G_0 * (\Sigma_{\rm ph}+\Sigma_{\rm el}+\Delta) * G_{\rm imp}](t,t'), \tag{6.13}$$

and

$$\mathcal{D}(t,t') = \mathcal{D}_0(t,t') + [\mathcal{D}_0 * \Pi_{\rm ph} * \mathcal{D}](t,t'), \tag{6.14}$$

respectively. Here,

$$G_{\rm imp}(t,t') = -i\langle \mathcal{T}_{\mathcal{C}} c(t) c^\dagger(t')\rangle, \tag{6.15}$$

and the bare electronic Green's function satisfies

$$(-i\partial_t - \mu)G_0(t,t') = \delta_{\mathcal{C}}(t,t'). \tag{6.16}$$

$\Sigma_{\rm ph}$, $\Sigma_{\rm el}$, and $\Pi_{\rm ph}$ are self-energies of the system. We prepare these functions using a Luttinger-Ward functional, after neglecting the vertex corrections, which consistent of two terms as

$$\Phi_{\rm total}[G,\mathcal{D}] = \Phi_{\rm ph}[G,\mathcal{D}] + \Phi_{\rm U}[G], \tag{6.17}$$

where $\Phi_{\rm ph}$ is the first-order electron-phonon Luttinger-Ward functional, drew in Fig. 6.2, and $\Phi_{\rm U}$ is the pure electronic Luttinger-Ward functional. By exploiting $\Phi_{\rm total}$, we will introduce the self energies as

$$\Sigma_{\rm ph}(t,t') = \frac{\partial \Phi_{\rm ph}}{\partial G} = i\mathcal{D}(t,t')G_{\rm imp}(t,t')g(t)g(t'), \tag{6.18}$$

$$\Sigma_{\rm el}(t,t') = \frac{\partial \Phi_{\rm U}}{\partial G}, \tag{6.19}$$

and

$$\Pi_{\rm ph}(t,t') = \frac{\partial \Phi_{\rm ph}}{\partial \mathcal{D}} = -2ig(t)g(t')G_{\rm imp}(t,t')G_{\rm imp}(t',t). \tag{6.20}$$

We draw $\Sigma_{\rm ph}$, and $\Pi_{\rm ph}$ in Fig. 6.2.

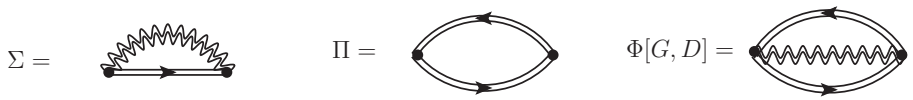


Figure 6.2: The first order Feynman diagrams, from left to right, are the electronic self-energy ($\Sigma_{\rm ph}$), phononic self-energy ($\Pi_{\rm ph}$) and the Luttinger-Ward functional ($\Phi_{\rm ph}$) for the proposed self-energies ($\Sigma_{\rm ph}$, $\Pi_{\rm ph}$). double lines represent the interacting electron Green's function and the double wiggly line denotes an interacting phonon Green's function.

To obtain $\Sigma_{\rm el}$, we will take the advantage of the slave-rotor technique, introduced in Chap. 5. As in the slave-rotor method the electronic problem is solved at the level of auxiliary particles, spinon and rotor, it would suffice if we only transfer the phonon-mediated self-energies to the slave-rotor impurity solver. To satisfy this demand, we will introduce a shifted hybridization function as

$$\Delta_{\rm eph}(t,t') = \Delta(t,t') + \Sigma_{\rm ph}(t,t'). \tag{6.21}$$

By employing $\Delta_{\rm eph}$, we can express the electronic Dyson equation, in Eq. (6.13), as

$$G_{\rm imp}(t,t') = G_0 + [G_0 * (\Sigma_{\rm el} + \Delta_{\rm eph}) * G_{\rm imp}](t,t'). \tag{6.22}$$

The above equation fulfill the general form of the fermionic Dyson equation, which we will solve using the slave-rotor method, explained in Sec. 5.1.2.

The proposed set of self-energies in Eqs. (6.18, 6.20), and the approximate separation in Eq. (6.17) of the Luttinger-Ward functional in electron and phonon contributions (which neglects el-ph vertex corrections), are known as the "**Migdal approximation**". In the Migdal approximation, the vibration of ions will dress electrons, and these dressed particles polarize the medium and modify the vibrational frequency of the ions in a self-consistent way. Thereby, the Migdal approximation can describe the problem of the self-localized carriers as the formation of polarons. This approximation will breakdown if $\lambda_{\rm eff} = g^2/\omega_0 > 1$, indicating that studying systems deep in the bipolaronic regime requires an improvement of this treatment.

It is apparent that when lattice sites are massive, the electron-mediated renormalization of the phononic system will be negligible, and thereby the Migdal approximation can be reduced to the "**Hartree-Fock approximation**". In this approximation the interacting phononic Green's functions will be replaced by their bare correspondence in the electronic self-energy as

$$\Sigma_{\rm ph}(t,t') = i\mathcal{D}_0(t,t')G_{\rm imp}(t,t')g(t)g(t'). \tag{6.23}$$

In this approximation, phonons play the role of heat bath [107]. In addition, since Eq. (6.23) can not be derived from any Luttinger-ward functional, the approximation is not conserving, and thereby, the total energy of the system will not be preserved. One should recall that, although it has not explicitly mentioned, we also employed the Hartree-Fock approximation in Chap. 5 to couple a dissipative bosonic bath to the Hubbard model.

### The DMFT self-consistency loop

The second step of the DMFT self-consistency loop, introduced in Sec. 3.1.2, using the above mentioned impurity solver will be as follows.

1. We compute the bare phonon Green's function using Eq. (6.8). This Green's function will be computed once and will be used in the rest of the DMFT loop.

2. We determine two uncoupled solutions for the spinon and the rotor subsystems. The spinon Green's function satisfies Eq. (5.26) with a zero spinon self-energy. The uncoupled rotor Green's function is obtained by Eq. (5.54) for a fixed nonzero $\delta_0$.

3. The spinon self-energy will be determined by Eq. (5.31), and the rotor self-energy will be computed by Eq. (5.30) with $\mathcal{N} = 3$. Depending on the approximation, we will either compute the phononic and electronic self-energies, in the Migdal approximation, with Eqs. (6.18, 6.20), or we will determine the electronic self-energy, in the Hartree-Fock method, by Eq. (6.23).

4. We compute the modified hybridization function ($\Delta_{\text{eph}}$) using Eq. (6.21).

5. We acquire the spinon and rotor Green's functions by solving Eqs. (5.26, 5.27) for a trial $\eta(t)$, with, usually, the first guess of $\eta(t) = 2\delta_0$.

6. We enforce the boundary conditions. For the half-filled case, Eqs. (5.51) will be satisfied by setting $\lambda = 0$. To find $\eta(t)$, we will go through the steps explained in Sec. 5.2.2.

7. The new Green's functions and self-energies for the rotor and spinon is computed using Eqs. (5.26, 5.27, 5.31, 5.30).

8. We calculate new electronic Green's function using Eq. (5.32). In the Migdal approximation, we also update the interacting phononic Green's function by Eq. (6.14).

### 6.1.3 Impurity solver with retarded Hubbard interaction

In the previous section, we regard the slave-rotor approximation as a "black box" to compute the electronic self-energy, in Eq. (6.19), for a static Hubbard interaction, and avoid any internal modification on the method. Here, we propose an alternative approach to tackle the problem of the retarded Hubbard interaction by the slave-rotor impurity solver.

In Chap. 5, we explicitly explained the slave-rotor method for solving the Hubbard model with a constant Hubbard interaction of $U$. In this chapter, after integrating the phononic degrees of freedom in Eq. (6.9), we are facing a Hubbard interaction which has instantaneous and retarded contributions. To treat this type of retarded density-density interactions within the framework of the slave-rotor impurity solver, we will modify the computation of the rotor Green's function.

We start the modification by writing the action as a combination of Eqs. (6.4 6.9) as

$$\begin{aligned}\mathcal{S}_{\mathrm{el}}[c^*,c] = i\Big\{ &\int_{\mathcal{C}} \mathrm{d}t \sum_\sigma c^*_\sigma(t)\big(i\partial_t+\mu\big)c_\sigma(t) \\ &- \frac{U}{2}\int_{\mathcal{C}} \mathrm{d}t \sum_\sigma n_\sigma(t) n_{\bar\sigma}(t) - \iint_{\mathcal{C}} \mathrm{d}t'\mathrm{d}t n(t)[ig(t)]2\mathcal{D}_0(t,t')[ig(t')]n(t') \\ &+ \iint_{\mathcal{C}} \mathrm{d}t\mathrm{d}t' c^*_\sigma(t)c_\sigma(t)\Delta(t,t')c^*_\sigma(t')c_\sigma(t')\Big\}. \end{aligned} \tag{6.24}$$

Transforming this action into the slave-rotor representation results in

$$\begin{aligned}\mathcal{S}_{\mathrm{el}}[f^*,f,X^*,X] = \Big\{ &\int_{\mathcal{C}} \mathrm{d}t \sum_\sigma f^*_\sigma(t)\big(i\partial_t+\mu\big)f_\sigma(t) \\ &- \iint_{\mathcal{C}} \mathrm{d}t'\mathrm{d}t X^*(t)\partial_t X(t)\mathcal{P}^{-1}(t,t')X(t')\partial_t X^*(t') \\ &+ \iint_{\mathcal{C}} \mathrm{d}t\mathrm{d}t' f^*_\sigma(t)X^*(t)\Delta(t,t')f_\sigma(t')X(t')\Big\}, \end{aligned} \tag{6.25}$$

where $\mathcal{P}^{-1}$, is the inverse of the full interaction given by

$$\mathcal{P}(t,t') = U\delta_{\mathcal{C}}(t,t') + \mathcal{U}(t,t'), \tag{6.26}$$

with the inverse which is given by

$$\mathcal{P}^{-1}(t,t') = \frac{1}{U}\delta_{\mathcal{C}}(t,t') - \mathcal{B}(t,t'), \tag{6.27}$$

where $\mathcal{U}$ has been introduced in Eq. (6.10), and $\mathcal{B}$ satisfies

$$\int_{\mathcal{C}} \mathrm{dt}_1 \Big[ g(t) 2\mathcal{D}_0(t,t') g(t') \Big] \mathcal{B}(t_1,t') = \delta_{\mathcal{C}}(t,t'). \tag{6.28}$$

Employing the relation between $\mathcal{P}$ and its inverse, which is $\mathcal{P} * \mathcal{P}^{-1} = \delta_{\mathcal{C}}(t,t')$, we will obtain

$$\Big[ \delta_{\mathcal{C}}(t,t_1) + \frac{1}{U}\mathcal{U}(t,t_1) \Big] * \mathcal{B}(t_1,t') = \frac{1}{U}\mathcal{U}(t,t')\frac{1}{U}, \tag{6.29}$$

which is the Voltera equation of the second type, see also Eq. (2.91) and its related discussion.

The spinon sector of the above action is the same as what we have encountered in Chap. 5. Hence, solving Eq. (5.29), with the self-energy introduced in Eq. (5.31), will provide the spinon Green's function.

For the rotoric subsystem, we will employ Eq. (6.25) to derive the rotor equation of motion as

$$\frac{-1}{U}\partial_t^2 G_X(t,t') + \big[\partial_t \mathcal{B} * \partial_t G_X\big](t,t') + \delta_0 G_X(t,t') - \Big[ \big(\eta + \Sigma_X\big) * G_X \Big](t,t') = \delta_{\mathcal{C}}(t,t'), \tag{6.30}$$

where we also employed the approximation that

$$\forall \quad t' \neq t \qquad\qquad \theta(t') \approx \theta(t), \tag{6.31}$$

which results in

$$X(t)X^*(t') = e^{i\theta(t) - i\theta(t')} \approx 1. \tag{6.32}$$

This approximation implicitly implies that the charge fluctuation of the system, with respect to the phononic timescale ($g^2/\omega_0$), is small, and thereby it will not be a trustable approximation near the Mott transition.

After obtaining $\mathcal{B}$ from Eq. (6.29), we should try to provide a numerically stable procedure to solve Eq. (6.30). In the following, we will first explain a general approach which is applicable for any time-dependent $\mathcal{B}$, and then we will present an analytical solution for a one-mode phononic system, which time-independently coupled to the electronic system.

**Computing the uncoupled rotor Green's function**

For a generic $\mathcal{B}$, we should first split Eq. (6.30) into a static and a dynamic subequations. This splitting enables us to enhance the accuracy of the numerical solution by solving two stable equations, which are as follows.

We first compute the uncoupled Green's function with the static Hubbard interaction by

$$-\frac{1}{U}\partial_t^2 g_{\mathrm{X}}(t,t') + \delta_0 g_{\mathrm{X}}(t,t') = \delta_{\mathcal{C}}(t,t'), \tag{6.33}$$

where $\delta_0$ is the Lagrange multiplier, that we have introduced in Sec. 5.2.2. This equation describes a renormalized harmonic oscillator with the frequency of $\sqrt{U\delta_0}$, and the renormalization factor of $0.5\sqrt{U/\delta_0}$. The full uncoupled Green's function ($G^0_{\mathrm{X}}$) is then captured by

$$-\frac{1}{U}\partial_t^2 G^0_{\mathrm{X}}(t,t') + \int_{\mathcal{C}} \mathrm{d}t_1 \partial_t \mathcal{B}(t,t_1)\partial_{t_1} G^0_{\mathrm{X}}(t_1,t') + \delta_0 G^0_{\mathrm{X}}(t,t') = \delta_{\mathcal{C}}(t,t'), \tag{6.34}$$

where $\mathcal{B}$ satisfies Eq. (6.29). The above equation can also be expressed as

$$G^0_{\mathrm{X}}(t,t') = g_{\mathrm{X}}(t,t') - \iint_{\mathcal{C}} \mathrm{d}t_1 \mathrm{d}t_2 g_{\mathrm{X}}(t,t_1)\overrightarrow{\partial}_{t_1}\mathcal{B}(t_1,t_2)\overrightarrow{\partial}_{t_2} G^0_{\mathrm{X}}(t_2,t'), \tag{6.35}$$

where $\overrightarrow{\partial}_t$ is the Keldysh derivative operator acting on the Green's function on its right hand side.

To have a, numerically stable, Voltera integral equation of the second type, we will apply two integrations by part over $t_1$ and $t_2$ in Eq. (6.35) to achieve

$$G^0_{\mathrm{X}}(t,t') = g_{\mathrm{X}}(t,t') - \iint_{\mathcal{C}} \mathrm{d}t_1 \mathrm{d}t_2 g_{\mathrm{X}}(t,t_1)\overleftarrow{\partial}_{t_1}\mathcal{B}(t_1,t_2)\overleftarrow{\partial}_{t_2} G^0_{\mathrm{X}}(t_2,t'). \tag{6.36}$$

By substituting $G^0_{\mathrm{X}}$ in Eq. (6.30), we will yield

$$G_X(t,t') = G^0_{\mathrm{X}}(t,t') + \Big[G^0_{\mathrm{X}} * \big(\eta + \Sigma_X\big) * G_X\Big](t,t'), \tag{6.37}$$

which is again another second-type Voltera equation. We thus fragmented the initial complex equation into three, numerically stable, equations as Eqs. (6.33, 6.36, 6.37).

Solving Eqs. (6.33, 6.36) is a general approach of finding the uncoupled rotor Green's function. For a particular case, where the electron-phonon coupling is time-independent, and only one phonon mode is present in the system, we can cast an analytical approach.

In this case, the uncoupled uncoupled rotor Green's function under the phonon-mediated retarded Hubbard interaction is given by (details of the calculation can be found in Appendix A.)

$$G^0_{\mathrm{X}}(z) = \frac{A}{z-\omega_1} + \frac{B}{z-\omega_2} - \frac{A}{z+\omega_1} - \frac{B}{z+\omega_2}, \tag{6.38}$$

where $z$ is the real frequency, and the poles of the Green's function are located at

$$\omega_1 = \sqrt{\frac{1}{2}(\delta_0 U + \omega_0^2) + \frac{1}{2}\sqrt{(\delta_0 U + \omega_0^2)^2 - 4(\delta_0 U \omega_0^2 - 4\delta_0 g^2 \omega_0)}}, \tag{6.39}$$

$$\omega_2 = \sqrt{\frac{1}{2}(\delta_0 U + \omega_0^2) - \frac{1}{2}\sqrt{(\delta_0 U + \omega_0^2)^2 - 4(\delta_0 U \omega_0^2 - 4\delta_0 g^2 \omega_0)}}. \tag{6.40}$$

Here the coefficients $(A, B)$ are given by

$$A = \frac{-\omega_1^2 U - (-U\omega_0^2 + 4g^2\omega_0)}{2\omega_1(\omega_2^2 - \omega_1^2)}, \tag{6.41}$$

$$B = \frac{\omega_2^2 U + (-U\omega_0^2 + 4g^2\omega_0)}{2\omega_2(\omega_2^2 - \omega_1^2)}, \tag{6.42}$$

where $U$, $g$, and $\omega_0$ are time-independent. Exploiting the analytical representation of the uncoupled rotor Green's function in Eq. (6.38) enables us to determine the full rotor Green's function only by solving Eq. (6.37).

#### The DMFT self-consistency loop

As the above mentioned impurity solver is similar to the conventional slave-rotor, we only need to modify the rotor-related step, in particular only the first step of Sec. 5.2.1. To be specific, we should compute the uncoupled Green's function either using Eqs. (6.33, 6.35) or employing Eq. (6.38).

### 6.1.4 Observables

The observables, which we will employ to analyze the underlying physics of the Hubbard-Holstein model, are as follows. The purely electronic observables are those which we have already introduced in Chap. 5.2.3. In addition, we would also compute the phonon momentum-momentum expectation value, renormalized phonon frequency, phonon density, and two-body phonon expectation value.

#### *Renormalized phonon frequency*

In the Migdal approximation, the phonon frequency ($\omega_\mathrm{r}$) will be softened by electrons. As this frequency is the pole of the phonon Green's function $\mathcal{D}(t, t')$, we thereby determine $\omega_\mathrm{r}$ from the location of the peak in the phonon spectral functions, obtained using Eq. (2.40).

***Phonon density***

The phonon density is defined as

$$\langle b^\dagger b\rangle = -id^<(t,t'), \tag{6.43}$$

where $d$ is the one-pole phononic Green's function ($d(t,t') = -i\langle \mathcal{T}_\mathcal{C} b(t)b^\dagger(t')\rangle$). To obtain the lesser part of the phononic Green's function, we will express its equation of motion in terms of charge-charge correlation function ($\chi(t,t') = -i\langle n(t)n(t')\rangle$).

The equation of motion for any two-point correlation function is given by

$$i\partial_t\langle \mathcal{T}_\mathcal{C} A(t)B(t')\rangle = \langle [A(t),B(t')]_\pm\rangle\delta_\mathcal{C}(t,t') + \langle \mathcal{T}_\mathcal{C}[A(t),H(t)],B(t')\rangle, \tag{6.44}$$

where the plus (minus) sign is taken for fermionic (bosonic) operators. Employing this relation for a phononic Green's function with $A = b$, and $B = b^\dagger$, results in

$$i\partial_t\langle \mathcal{T}_\mathcal{C} b(t)b^\dagger(t')\rangle = \langle [b(t),b^\dagger(t')]\rangle\delta_\mathcal{C}(t,t') + \langle \mathcal{T}_\mathcal{C}[b(t),H(t)]b^\dagger(t')\rangle, \tag{6.45}$$

$$i\partial_t\langle \mathcal{T}_\mathcal{C} b(t)b^\dagger(t')\rangle = \delta_\mathcal{C}(t,t') + g(t)\langle n(t)b^\dagger(t')\rangle + \omega_0(t)\langle \mathcal{T}_\mathcal{C} b(t)b^\dagger(t')\rangle, \tag{6.46}$$

where we have employed the Hubbard-Holstein Hamiltonian, introduced in Eq. (6.1). To bring Eq. (6.46) into a closed form, we should also determine the equation of motion for $\langle n(t)b^\dagger\rangle$, which is

$$i\langle \mathcal{T}_\mathcal{C} n(t)b^\dagger(t')\rangle\partial_{t'} = \langle \mathcal{T}_\mathcal{C} n(t)[b^\dagger(t'),H]\rangle, \tag{6.47}$$

$$i\langle \mathcal{T}_\mathcal{C} n(t)b^\dagger(t')\rangle\partial_{t'} = -g(t')\langle \mathcal{T}_\mathcal{C} n(t)n(t')\rangle - \omega_0\langle \mathcal{T}_\mathcal{C} n(t)b^\dagger(t')\rangle. \tag{6.48}$$

Rearranging Eqs. (6.46, 6.48) would give us

$$\big(i\partial_t - \omega_0\big)\langle \mathcal{T}_\mathcal{C} b(t)b^\dagger(t')\rangle = \delta_\mathcal{C}(t,t') + g(t)\langle \mathcal{T}_\mathcal{C} n(t)b^\dagger(t')\rangle, \tag{6.49}$$

$$\big(-i\partial_{t'} - \omega_0\big)\langle \mathcal{T}_\mathcal{C} n(t)b^\dagger(t')\rangle = \langle \mathcal{T}_\mathcal{C} n(t)n(t')\rangle g(t'), \tag{6.50}$$

which results in

$$d(t,t') = d_0(t,t') + g(t)d_0(t,t)\underbrace{\big(-i\langle \mathcal{T}_\mathcal{C} n(t)n(t')\rangle\big)}_{\chi(t,t')}g(t')d_0(t',t'), \tag{6.51}$$

where $d_0$ is the noninteracting bosonic Green's function

$$(i\partial_t - \omega_0)d_0(t,t') = \delta_\mathcal{C}(t,t'). \tag{6.52}$$

Eq. (6.51) is exact, but here we use the bubble diagram with only some phonon corrections as a first approximation to calculate $\chi$ as

$$\chi(t,t') = \Pi(t,t') + \Big[\Pi * \big(2g(t)\mathcal{D}(t,t')g(t')\big) * \chi\Big](t,t'), \tag{6.53}$$

where $\mathcal{D}$ is the solution of Eq. (6.14), and $\Pi$, in the first order approximation, can be obtained from the electronic Green's function as

$$\Pi(t,t') = 2g^2 G(t,t')G(t',t). \tag{6.54}$$

Further approximations regarding the computation of $\chi$, to be explored in future, are to get density-density correlation function from rotor Green's function.

Finally, substituting the solution of Eq. (6.53) in Eq. (6.51) would enable us to calculate the phonon density.

***Phonon momentum-momentum expectation value***

The phonon momentum-momentum expectation value is defined as

$$C^{ph}_{pp}(t) = \langle T_{\mathcal{C}} P_{\rm ph}(t) P_{\rm ph}(t)\rangle, \tag{6.55}$$

where $P_{\rm ph}$ is the phonon momentum operator.

To evaluate this observable, we use the fact that the expectation values of any pure phononic observables in the Hubbard-Holstein model is exactly the same as the Holstein model, as phonon-related terms are the same as the Holstein model. We thereby can exploit the relation that has been derived for the Holstein model [107], for the phonon momentum-momentum expectation value as

$$\overrightarrow{\partial}_t \mathcal{D} \overleftarrow{\partial}_{t'}(t,t') \equiv 2\omega_0 \delta_{\mathcal{C}}(t,t') - 2i\langle T_{\mathcal{C}} P(t)P(t')\rangle, \tag{6.56}$$

where $D$ is the phonon Green's function, and $\overrightarrow{\partial}\,(\overleftarrow{\partial}\,)$ is the Keldysh derivative operator acting from the left (right). The above equation shows that $\langle T_{\mathcal{C}} P(t)P(t')\rangle$ is related to the derivatives of the phononic Green's function. Numerical derivations induces inaccuracy into our results, where errors depends on the numerical method, and such errors would be enlarged when we are seeking a second derivative of a Green's function. To maintain this issue, instead of directly compute the numerical derivatives, we solve three second-order Voltera equations which are

$$\overrightarrow{\partial}_t \mathcal{D}(t,t') = \overrightarrow{\partial}_t \mathcal{D}_0(t,t') + \big[\overrightarrow{\partial}_t \mathcal{D}_0 * \Pi * \mathcal{D}\big](t,t'), \tag{6.57}$$

$$\mathcal{D}\overleftarrow{\partial}_{t'}(t,t') = \mathcal{D}_0 \overleftarrow{\partial}_{t'}(t,t') + \big[\mathcal{D} * \Pi * \mathcal{D}_0 \overleftarrow{\partial}_{t'}\big](t,t'), \tag{6.58}$$

$$\overrightarrow{\partial}_t \mathcal{D}\overleftarrow{\partial}_{t'}(t,t') = \overrightarrow{\partial}_t \mathcal{D}_0 \overleftarrow{\partial}_{t'}(t,t') + \big[\overrightarrow{\partial}_t \mathcal{D}_0(t,t') * \Pi * \mathcal{D}\overleftarrow{\partial}_{t'}(t,t')\big](t,t'). \tag{6.59}$$

These equation can be solved using the boundary conditions in Eqs. ( 2.22, 2.23, 2.24, 2.26, 2.27). We finally yield the second derivative of the phonon Green's function, and as a result obtain the phonon momentum-momentum expectation values using Eq. (6.56).

***Variance of the phonon displacement***

The variance of the phonon displacement is defined as

$$C_{XX}(t) = \langle T_{\mathcal{C}} X_{\mathrm{ph}}(t) X_{\mathrm{ph}}(t) \rangle. \tag{6.60}$$

This correlation function can be obtained by

$$\langle T_{\mathcal{C}} X_{\mathrm{ph}}(t) X_{\mathrm{ph}}(t) \rangle = 2\langle b^\dagger(t) b(t) \rangle + 1 - \langle T_{\mathcal{C}} P_{\mathrm{ph}}(t) P_{\mathrm{ph}}(t) \rangle, \tag{6.61}$$

where the involved terms in the right hand side of Eq. (6.61) has been introduced in Eqs. (6.43, 6.56).

***Two-body phonon expectation value***

The two-body phonon expectation value is defined as

$$C_{2ph}(t) = \langle b(t) b(t) + b^\dagger(t) b^\dagger(t) \rangle. \tag{6.62}$$

Exploiting the definition of the phonon momentum and displacement operators in terms of phonon creation and annihilation operators as

$$X_{\mathrm{ph}} = \frac{1}{\sqrt{2}}(b + b^\dagger), \tag{6.63}$$

$$P_{\mathrm{ph}} = \frac{i}{\sqrt{2}}(b^\dagger - b), \tag{6.64}$$

we can obtain $C_{2ph}$ by

$$C_{2ph}(t) = \langle b(t) b(t) + b^\dagger(t) b^\dagger(t) \rangle = 2\langle b^\dagger(t) b(t) \rangle + 1 - 2\langle T_{\mathcal{C}} P(t) P(t) \rangle. \tag{6.65}$$

Here, the involved terms in the right hand side of Eq. (6.65) are introduced in Eqs. (6.43, 6.56).

## 6.2 Results and discussion

In this section, we will discuss the physics of the Hubbard-Holstein model. Using the solutions introduced in Sec. 6.1.1, we will explore the equilibrium and nonequilibrium

physics of the system. We will compare the equilibrium properties of the system, obtained using different impurity solvers, and will also assess their efficiency. We then continue the discussion by presenting the nonequilibrium response of the systems to a sudden quench of the electron-phonon coupling. Concerning the range of the electron-phonon coupling, we will mainly investigate the intermediate regime, where $E_p = g^2/\omega_0 < 1$. We will present our results in the adiabatic as well as nonadiabatic regime, with special attention on the small phonon frequencies.

### 6.2.1 Failure of the impurity solver based on the retarded Hubbard interaction

Fig. 6.3 presents the spectral function of two metallic systems at $\beta = 10$, and $U \in \{4, 4.25\}$. The phonon frequency is set to $\omega_0 = 1$ with the electron-phonon (el-ph) coupling of $g \in \{0.3, 0.5, 0.8\}$, which corresponds to the polaron energy of $E_p \in \{0.09, 0.25, 0.64\}$. The spectral function has five major peaks. These structures consists of the three Hubbard-like peaks, and two phononic sidebands. The properties of the Hubbard bands are similar to what we have already presented in Chap. 5. The phononic sidebands at very small polaron energies are located at $\omega = \omega_0$, and will be posited closer to the quasiparticles peak at stronger el-ph couplings. It is apparent that the larger $E_p$ is associated with an enhancement of the spectral function at $\omega = 0$, and a displacement of the Hubbard bands to higher frequencies.

The height of the phonon-related peaks is unexpectedly large, even at $g = 0.3$, and the peaks become almost well-separated from the Hubbard bands when the Hubbard interaction is increased, i.e. $E_{\rm p} = 0.64$. In Fig. 6.4, we plot the spectral function of a system at $U = 4.5$, $\omega_0 = 1.0$, and $E_p = 0.64$ with three different impurity solvers, which are the combination of the slave-rotor with the retarded Hubbard interaction ($SR + \mathrm{ret}U$), Hartree-Fock, and Migdal approximations. Both spectral functions captured by Migdal and Hartree-Fock approximations are exhibiting broader Hubbard bands in comparison to the result of the $SR + \mathrm{ret}U$ impurity solver. The plot also clearly shows that the phononic sidebands as well as the quasiparticle peak are much more pronounced in the spectral function which has been obtained with $SR + \mathrm{ret}U$ impurity solver. We also can notice that the height of the quasiparticle peak within the Migdal approximation is larger than its counterpart within the Hartree-Fock approximation. This response is rooted in the softening of the effective phonon frequency ($\omega_{\rm r} = 0.9 < \omega_0$) associated with $E_p^{\rm r} = g^2/\omega_{\rm r} = 0.7 > E_p$, see also Sec. 6.2.2 for more details.

Equilibrium studies on the Hubbard-Holstein model at small el-ph couplings stated

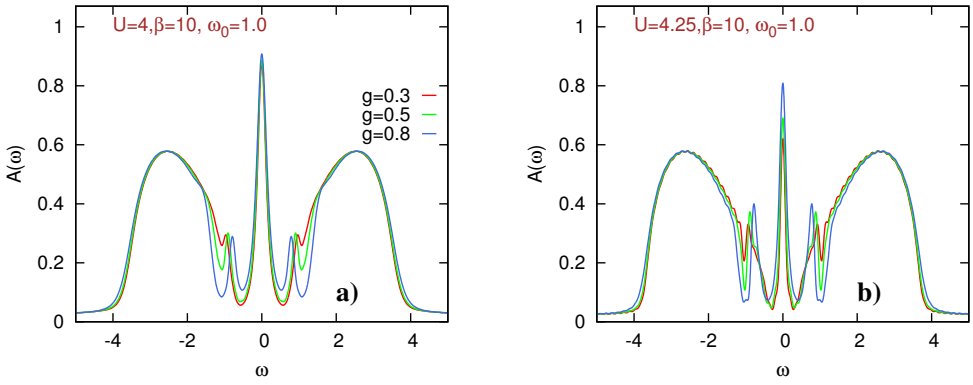


Figure 6.3: Spectral functions of two systems, obtained using the impurity solver based on the retarded Hubbard interaction, at $\beta = 10$ with $\omega_0 = 1$, $g \in \{0.3, 0.50.8\}$, and a) $U = 4$. b) $U = 4.25$.

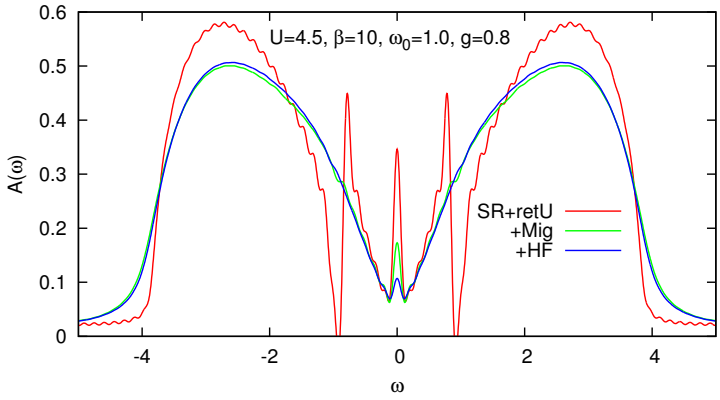


Figure 6.4: Spectral functions of a system at $\beta = 10$ with $\omega_0 = 1.0$, $g = 0.8$, and $U = 4.5$. The red solid line is obtained using the slave-rotor and retarded Hubbard interaction. The green (blue) spectral functions are computed using the Migdal (Hartree-Fock) approximation.

that the system effectively can be mapped to the Hubbard model whose strength is reduced [126]. This statement implies that in weak-coupling regime the phononic sidebands should not be prominent, in contrast to the reported results related to the $SR + \mathrm{ret}U$ impurity solver. The reason behind this inconsistency between the expected and presented ($SR + \mathrm{ret}U$) results rooted in the approximation, introduced in Eq. (6.32). To strengthen this reasoning, in the following, we will evaluate the equation of motion of $\langle\theta(t)\theta(t')\rangle$. Assuming Eq. (6.31) enforces that the time-derivative of the above correlation function must be negligible.

The equation of motion for any two-point correlation function is given by

$$i\partial_t\langle\mathcal{T}_\mathcal{C}A(t)B(t')\rangle = \langle[A(t),B(t')]_\pm\rangle\delta_\mathcal{C}(t,t') + \langle\mathcal{T}_\mathcal{C}[A(t),H(t)],B(t')\rangle, \tag{6.66}$$

where the plus (minus) sign is taken for fermionic (bosonic) operators. To derive the equation of motion for $\langle\theta(t)\theta(t')\rangle$, we would present the last three local terms of the Hamiltonian, introduced in Eq. (6.1), in the slave-rotor representation (Eq. (5.3)), as

$$H_{\mathrm{Lph}} = UL^2 + \sqrt{2}gLX_{\mathrm{ph}} + \frac{\omega_0}{2}\big(X_{\mathrm{ph}}^2 + P_{\mathrm{ph}}^2\big), \tag{6.67}$$

where we have dropped the summation over the site indices for simplicity. $X_{\mathrm{ph}}$ and $P_{\mathrm{ph}}$ are phonon displacement and momentum operator with the commutation relation of

$$[X_{\mathrm{ph}}(t),P_{\mathrm{ph}}(t')] = i\delta_\mathcal{C}(t,t'). \tag{6.68}$$

Employing $H_{\mathrm{Lph}}$, we will be able to derive the equation of motion for $\langle\theta(t)\theta(t')\rangle$ as

$$i\partial_t\langle\mathcal{T}_\mathcal{C}\theta(t)\theta(t')\rangle = 2U(t)i\langle\mathcal{T}_\mathcal{C}L(t)\theta(t')\rangle + \sqrt{2}g(t)i\langle\mathcal{T}_\mathcal{C}X_{\mathrm{ph}}(t)\theta(t')\rangle, \tag{6.69}$$

which is coupled to two correlation functions, satisfying

$$i\partial_t\langle\mathcal{T}_\mathcal{C}L(t)\theta(t')\rangle = 0, \tag{6.70}$$

$$\big(-\partial_t^2 - \omega_0^2\big)\langle\mathcal{T}_\mathcal{C}X_{\mathrm{ph}}(t)\theta(t')\rangle = -\sqrt{2}\omega_0 g(t)\langle\mathcal{T}_\mathcal{C}L(t)\theta(t')\rangle. \tag{6.71}$$

To fulfill the assumption of Eq. (6.31), the time-dependency, with respect to $t$, of the right-hand side of Eq. (6.69) must be insignificant. As $L$ is the constant of motion, $[L,H_{\mathrm{Lph}}] = 0$, Eq. (6.70) implies that $\langle L(t)\theta(t')\rangle$ is only function of $t'$, and thus this correlation function does not depend on $t$. However, Eq. (6.71) shows that $\langle X_{\mathrm{ph}}(t)\theta(t')\rangle$ is oscillating function of $t$, which is driven by the $t$-dependent force, proportional to $\omega_0 g(t)$. As the amplitude of this oscillating behavior, in equilibrium, is proportional to $2g^2|\langle L(t)\theta(t')\rangle|^2$, we will notice that

in stronger el-ph couplings, the validity of Eq. (6.31) will be under question. Furthermore, getting a second time-derivative from Eq. (6.69) results in

$$-\partial_t^2\langle\theta(t)\theta(t')\rangle = -\sqrt{2}g(t)\omega_0\langle P_{\rm ph}(t)\theta(t')\rangle. \tag{6.72}$$

As we know that in the adiabatic regime (static picture), the lattice response, e.g. $P_{\rm ph}$, is much slower than the electronic response, e.g. $\theta(t')$, we can conclude that in the nonadiabatic regime, as well as strong el-ph coupling regimes, the equality of Eq. (6.69) will be strongly violated, and restrict the applicability of the method. As a consequence of this short validity range of $SR+\mathrm{ret}U$, we will continue the discussion by presenting the results, which are obtained from the Migdal and Hartree-Fock approximations.

### 6.2.2 Equilibrium physics: Migdal and Hartree-Fock approximations

In the previous section, we have presented the equilibrium results which have been computed using the $SR+\mathrm{ret}U$ impurity solver. We have discussed some of the equilibrium properties of the system, and have assessed the validity of the involved assumption in the $SR+\mathrm{ret}U$ approach. As a result of our assessments, we have ended up with the conclusion that the $SR+\mathrm{ret}U$ approach restricts our investigations to very small area in the phase diagram.

In the following, we will investigate the equilibrium properties of the Hubbard-Holstein model using the diagrammatic approaches, introduced in Secs. (6.1.1, 6.1.2). We will manifest the equilibrium physics of the problem in various parameter regimes with particular attention on the properties of the system near the Mott transition. We will explain the properties of the system as a function of temperatures, electron-phonon couplings, and Hubbard interactions. We also will study the electron-induced (phonon-induced) renormalization of the phonon frequency (bandwidth) in various systems.

#### Influence of the temperature on the Mott transition within the Hartree-Fock approximation

Fig. 6.5 displays kinetic energies and double occupancies of systems within the HF approximation. Plots are drawn for various temperatures, indicated by colors, and various sets of phononic parameters, shown by point types, corresponding to the bare polaron energy of $E_{\rm p} = 0.968$. At high temperature ($\beta = 5$), the kinetic energies gradually reduce, when

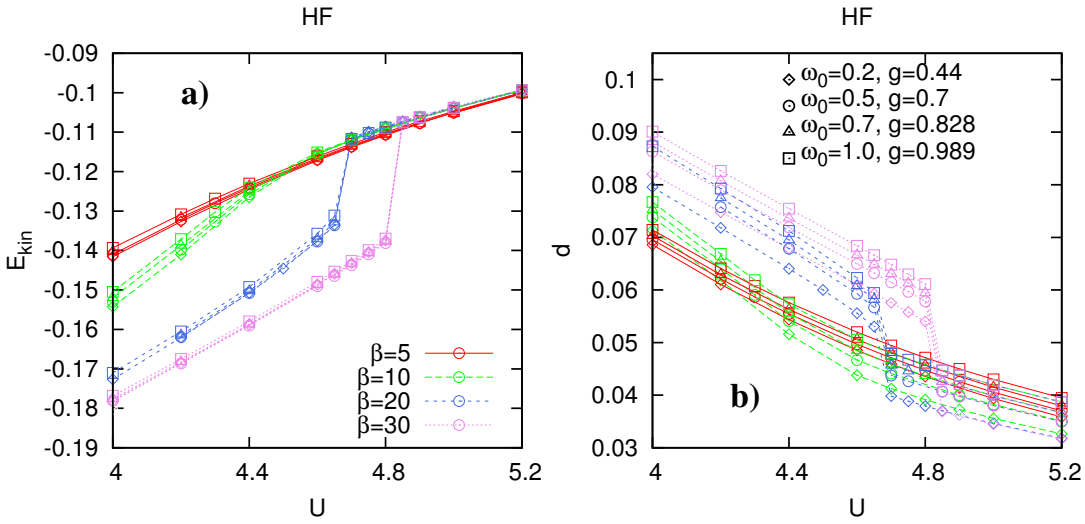


Figure 6.5: Equilibrium kinetic energies (a) and double occupancies (b) of systems obtained using the HF approximation, at $\beta \in \{5, 10, 20, 30\}$ with parameters associated with the bare polaron energies of $E_{\mathrm{p}} \approx 0.98$ as $(\omega_0, g) \in \{(0.2, 0.44), (0.5, 0.7), (0.7, 0.828), (1.0, 0.989)\}$.

the Hubbard interaction is enlarged. This behavior is simply due to the decrease of the metallic behavior at larger electron-electron (el-el) couplings, which has been extensively discussed in Chap. 5. In addition, the spectral functions, plotted in Fig. 6.6, clearly show that $\beta = 5$ is a bad-metallic state. Double occupancies at $\beta = 5$ also exhibit a mild suppression by increasing $U$. In contrast to the kinetic energy, the double occupancy depends on the phonon frequency. Smaller phonon frequencies are associated with lesser observed double occupancies. To understand this behavior, we plot the spectral densities at $U = 4.6$ for three sets of parameters with frequencies $\omega_0 \in \{0.2, 0.5, 1.2\}$ in Fig. 6.6. It is clear that, at $\beta = 5$, larger spectral densities around $\omega = 0$ are associated with smaller phonon frequencies. This is due to the lower energetic cost of exciting phonons in the nonadiabatic regime. Fig. 6.7 presents the phonon density at $\omega = 0.2$, red diamond points in b), is considerably larger than the phonon density at $\omega_0 = 1.0$, red diamond points in a).

Investigating systems with stronger metallic tendencies, at lower temperatures, reveals that both kinetic energies and double occupancies exhibit a prompt change at $\beta > 10$. This response is because of crossing the first-order Mott-transition, the dashed line in Fig. 5.1, by varying $U$ and temperatures. It is remarkable that at a fixed $E_p$ the critical Hubbard interaction, at which an abrupt jump takes place in both kinetic energies and double occupancies, only depends on the temperature. In addition, when the system passes

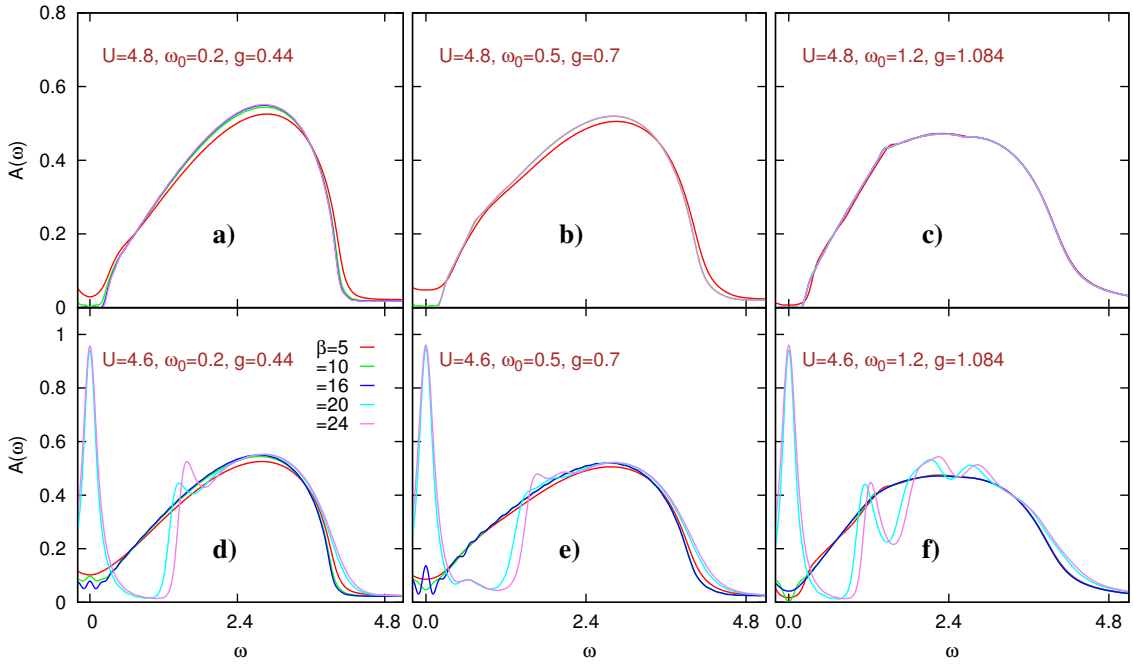


Figure 6.6: Spectral functions of systems within the HF approximation at $\beta \in \{5, 10, 16, 20, 24\}$ and $E_{\mathrm{p}} = 0.968$. The phononic parameters are a) $U = 4.8$, $\omega_0 = 0.2, g = 0.44$, b) $U = 4.8$, $\omega_0 = 0.5, g = 0.7$, c) $U = 4.8$, $\omega_0 = 1.2, g = 1.084$, d) $U = 4.6$, $\omega_0 = 0.2, g = 0.44$, e) $U = 4.6$, $\omega_0 = 0.5, g = 0.7$, f) $U = 4.6$, $\omega_0 = 1.2, g = 1.084$.

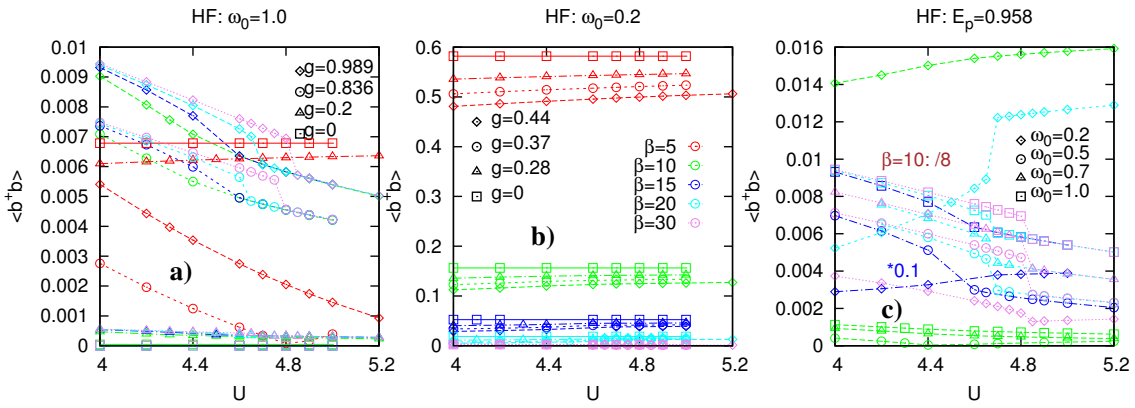


Figure 6.7: The phonon density of systems obtained using the Hartree-Fock approximation at a) $\omega_0 = 1.0$, $g \in \{0, 0.2, 0.836, 0.989\}$, and $\beta \in \{5, 10, 15, 20, 30\}$. b) $\omega_0 = 0.2$, $g \in \{0, 0.28, 0.37, 0.44\}$, and $\beta \in \{5, 10, 15, 20, 30\}$. c) $(\omega_0, g) \in \{(0.2, 0.44), (0.5, 0.7), (0.7, 0.828), (1.0, 0.989)\}$, and $\beta \in \{15, 20, 30\}$. Results at $\beta = 10$ is divided by 8. Parameters of panel c) correspond to $E_p = 0.968$.

the phase transition as a function of temperature, from a higher to a lower temperature, the kinetic energy of the system at a fixed Hubbard interaction will be enhanced, and the double occupancy will also present larger absolute values. It is apparent from the double occupancy results, plotted in Fig. 6.5, that the critical Hubbard interaction ($U_c$), where the phase transition is occurring, within the HF approximation, does not depend on $\omega_0$.

In the metallic regime ($U < U_c$), spectral functions, at low temperatures, exhibit multi-peak structures, where phonon-mediated sidebands are clearly visible, see Figs. 6.6 d-f). For larger phonon frequencies, i.e. $\omega_0 = 1.2$, the phonon-induced sidebands are more apparent. The position of these sidebands depend on temperature and $\omega_0$. The first sidebands, for $\omega_0 > 0.5$, is located at slightly above $\omega_0$, and the distance between this sideband and the quasiparticle peak would vary by changing the temperature. When the phonon frequency is smaller than the quasiparticle bandwidth, the first sidebands will be placed inside the bandwidth of the quasiparticle peak. It is important to note that the quasiparticle peak at low temperature, below the second-order point of the Mott-transition, is separated from the Hubbard bands by gap-like region in the spectral density. The accumulation of density inside these gap-like intervals is larger when the phonon frequency is about the frequency of these gaps, for instance at $\omega_0 = 0.5$ in Fig. 6.6 e). This is simply a consequence of the phononic sidebands which are placed inside the gap in these range of phonon frequencies.

Phonon densities in the nonadiabatic regime shows that by enlarging the Hubbard in-

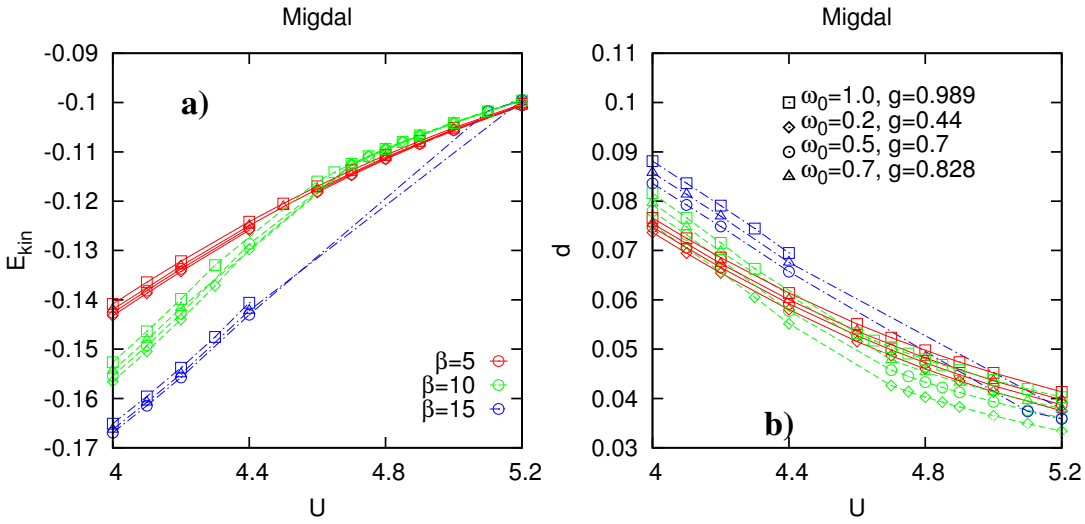


Figure 6.8: Equilibrium kinetic energies (a) and double occupancies (b) of systems obtained using the Migdal approximation, at $\beta \in \{5, 10, 15\}$ with parameters associated with the bare polaron energies of $E_{\rm p} \approx 0.98$ as $(\omega_0, g) \in \{(0.2, 0.44), (0.5, 0.7), (0.7, 0.828), (1.0, 0.989)\}$.

teraction, the phonon density will decrease and a prompt fall at $U = U_c$ is apparent at low temperatures, see Fig. 6.7 c). Both lessen and rapid jump of the phonon density as a function of $U$ reflects the behavior of the double occupancy. This is because the thermal excitations of phonons are negligible, see $g = 0$ results in Fig. 6.7 a), the charge-charge correlation function, whose time-local part is the double occupancy, would control the response of the system at large phonon frequencies, see also Eq. (6.51). At smaller phonon frequencies, the thermal and the electron-mediated phonon densities would compete. Results, plotted in Fig. 6.7 c), reveal that till $\beta < 30$ the thermal effect is dominant, and thereby the phonon density is enlarging by increasing $U$. However, at $\beta = 10$, the charge-charge correlation function prevails, and a gradual suppression of the phonon density is visible. It is also interesting to note that due to the above mentioned competition at $\beta = 10$, the associated change of the density at Mott transition is much lesser than its counterpart at $\beta = 20$.

At $U > U_{\rm c}$, systems with the same phonon frequency acquire almost the same amount of double occupancies when the temperature satisfies $\beta \leq 10$. This response is rooted in the shape of the spectral density which has an insulating two-peak structure, see Figs. 6.6 a-c). At small temperatures and $U > U_{\rm c}$, a well-defined gap is placed between these two spectral

peaks and the shape of these bands is altered very lightly as a function of temperature. Investigating the phonon density at $\beta > 5$, in the insulating regime, reveal a temperature-independent behavior in the nonadiabatic regime. At large phonon frequencies and $U > U_c$, the phonon density is reducing by decreasing the temperature. This is indeed the expected response of the "heat bath", where thermal excitations are playing a crucial roles. In the adiabatic regime, this thermal behavior of the system is also evident. However, reaching a temperature-independent response at $U > U_c$ is not visible at $\beta > 20$, which is due to the small excitation cost of these, small frequency, phonons. Moreover, in the contrary to the decreasing trend of the phonon density as a function of the Hubbard interaction in the nonadiabatic regime at $U > U_c$, this observable presents a gradual enhancement in the adiabatic regime, see also Fig. 6.7c). To explain this response, one can make a energy-based argument. As the total energy of the system is conserved, in our isolated system, and both kinetic energy and double occupancy of the system is decreasing, by enlarging $U$, the dissipated energy of the electronic subsystem must be absorbed in the phonon-related sectors. In the adiabatic regime, the lattice acts as classical phonons due to the slow dynamics of ions in this regime. As a consequence, one would expect that the el-ph correlation is smaller than its nonadiabatic counterparts. Thereby, the phononic energy, which is proportional to the phonon density, must enhance by increasing $U$.

**Influence of the temperature on the Mott transition within Migdal approximation**

Fig. 6.8 exhibits kinetic energies and double occupancies of systems which have been studied within the Migdal approximation. The high temperature response of these local observables are exposing similar behaviors as the HF approximation. A gradual decrease of both kinetic energies and double occupancies as a function of $U$ for systems at $\beta = 5$ is observed. Although the kinetic energies of these systems, obtained by HF or Migdal approximations, are exhibiting a quantitatively comparable values, the double occupancies in the Migdal approximation are larger than their HF counterparts. This response roots in the renormalization of the phonon frequency within the Migdal approximation as the electronic and phononic subsystems are interacting self-consistently, see also Sec. 6.2.2 for a detailed discussion.

Exploring the spectral functions of systems at $\omega_0 = 0.2$, $g = 0.4$, and $\beta = 5$ in Fig. 6.9 a-c) shows that at the smaller Hubbard interaction, the height of the quasiparticle peak is larger, and the phononic sidebands are barely visible. At lower temperatures, these sidebands are clearly noticeable, mainly in the metallic region of the phase diagram. Moreover, the position of these phononic sidebands are farther from the quasiparticle peak in colder

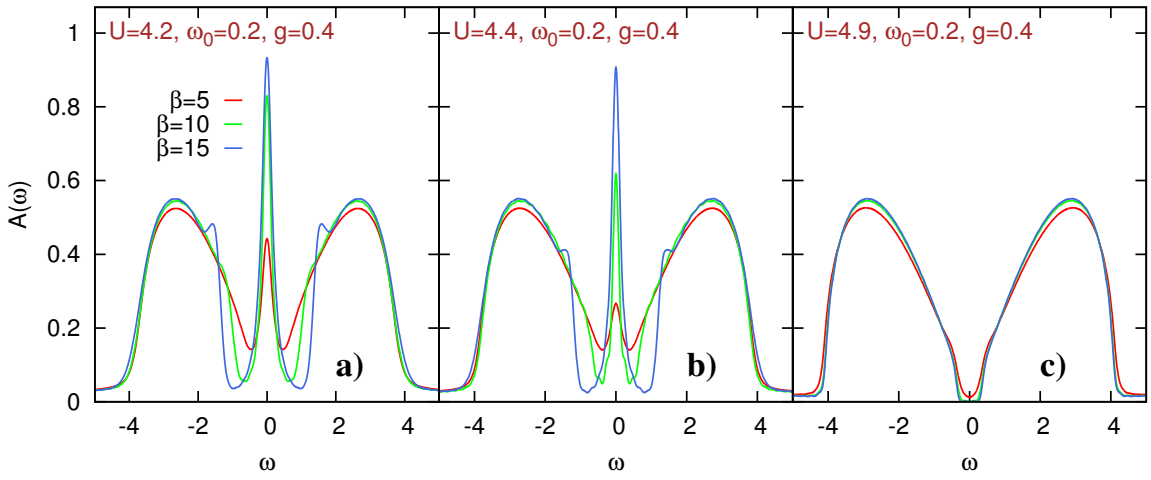


Figure 6.9: Spectral functions of systems at $\omega_0 = 0.2, g = 0.4$ within the Migdal approximation at $\beta \in \{5, 10, 15\}$ and $E_{\rm p} = 0.8$. The Hubbard interactions are a) $U = 4.2$, b) $U = 4.4$, and c) $U = 4.9$.

systems, where we can also observe higher peaks at $\omega = 0$.

Fig. 6.8 also displays the imprint of the phonon frequency on the kinetic energies and double occupancies of systems at a fixed $E_p = 0.968$. Results present that the kinetic energies (double occupancies) of systems at larger $\omega_0$ are less (more) than their counterparts at smaller phonon frequencies. This behavior can be easily understood by recalling that the phononic subsystem is almost static in the adiabatic regime with respect to the motion of electrons. Thereby, the phonon-mediated renormalization of the hopping amplitude would be very small. In addition, Figs. 6.10 b-c) show that the width of the quasiparticle peak is reduced more at larger phonon frequencies. Since the width of the quasiparticle peak is connected to the effective mass of carriers, we can conclude that dressing of electrons, by phonons, is performed more effectively in the nonadiabatic regime (larger phonon frequencies), where the kinetic energy is smaller. In the insulating regime, both the kinetic energies and double occupancies are small. A well-defined gap can be observed in the spectral function, see Fig. 6.10 a), and the phononic sidebands, shoulder-like features, are stronger at larger phonon frequencies. Investigating the phonon densities at various regimes, plotted in Fig. 6.11 a-c), exhibit that the larger phonon densities is in systems at higher temperatures, reflecting the thermal occupation of phonons. The smaller phonon frequency is associated with the larger phonon density in the system. At a fixed temperature ($\beta > 10$), the phonon

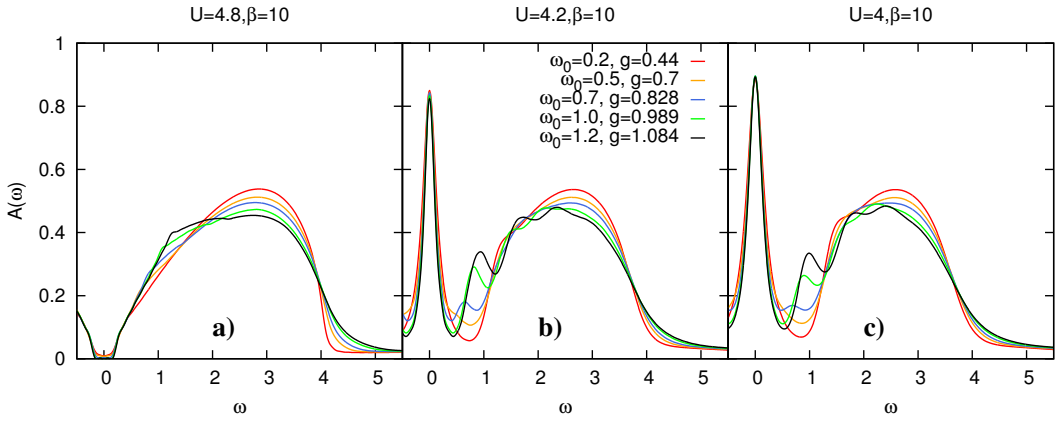


Figure 6.10: Spectral functions at $\beta = 10$ within the Migdal approximation with phononic parameters of $(\omega_0, g) = \{(0.2, 0.44), (0.5, 0.7), (0.7, 0.828), (1.0, 0.989), (1.2, 1.084)\}$, associated with $E_p = 0.968$, at a) $U = 4.8$, b) $U = 4.2$, and c) $U = 4$.

density at stronger el-ph coupling in the adiabatic (nonadiabatic) regime is less (more) than its uncoupled counterparts. This reflects that at large phonon frequencies, the phononic excited states are playing crucial role, via the el-ph correlations, in enhancing the phonon densities. However, in the adiabatic regime, the importance of the thermal occupation is undeniable, as systems at smaller el-ph couplings have larger phonon densities.

Unfortunately, investigating systems at lower temperatures in the Migdal approximation, we encounter technical difficulties which are as follows. The numerical cost of simulating these system is very large, as having a very fine mesh is necessary to correctly determine the thermal correlation, see also Sec. 5.2.2. Moreover, computing converged self-consistent results is considerably challenging, as imposing the $U(1)$ constraint is harder at lower temperatures. We thereby present mainly results at $\beta \leq 10$.

### Influence of the electron-phonon coupling on the Mott transition within Migdal and Hartree-Fock approximation

In previous sections, we have presented that the Mott transition, at a fixed $E_p$, solely depends on the temperature. We have shown that at colder systems $U_c$ is larger which were consistent with the curvature of the dashed line of the Hubbard model in Fig. 5.1. In this section, we would like to assess the dependency of $U_c$ to the el-ph coupling, which we have schematically drawn as a red line in Fig. 6.2.

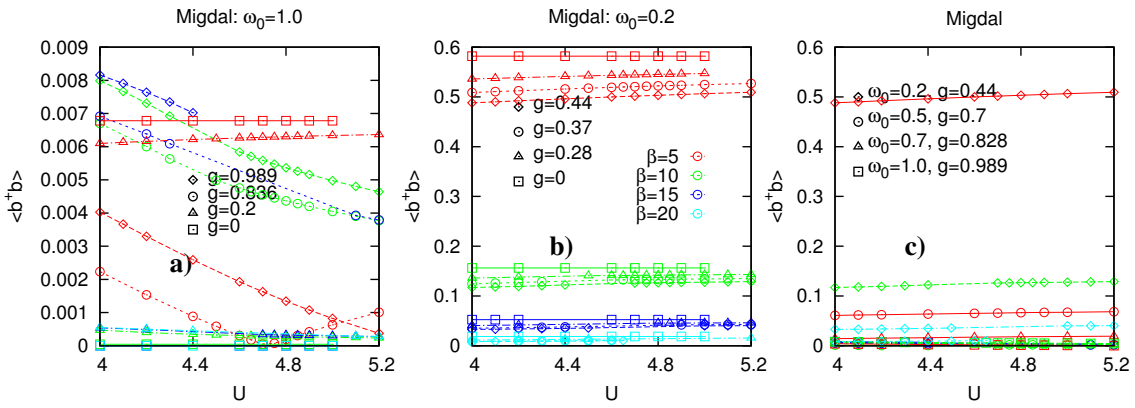


Figure 6.11: The phonon density of systems within the Migdal approximation at a) $\omega_0 = 1.0$, $g \in \{0, 0.2, 0.836, 0.989\}$, and $\beta \in \{5, 10, 15, 20\}$. b) $\omega_0 = 0.2$, $g \in \{0, 0.28, 0.37, 0.44\}$, and $\beta \in \{5, 10, 15, 20\}$. c) $(\omega_0, g) \in \{(0.2, 0.44), (0.5, 0.7), (0.7, 0.828), (1.0, 0.989)\}$, and $\beta \in \{5, 10, 15, 20\}$. Parameters of panel c) correspond to $E_p = 0.968$.

The kinetic energies and double occupancies of systems at $\omega_0 \in \{0.2, 1.0\}$ within HF and Migdal approximations are plotted in Figs. (6.12, 6.13, 6.14, 6.15), respectively. Results at $\beta > 10$ evidently show that $U_c$ depends on not only temperature, but also the el-ph coupling. At a fixed temperature, the larger $E_p$ is associated with larger $U_c$. This response reflects the phonon-mediated screening of the Hubbard repulsion, which we have expressed in Eq. (6.10). In addition, for the whole range of temperatures, the double occupancies of systems at weaker el-ph couplings are smaller. This response is observable both in the adiabatic and the nonadiabatic regimes, and indicates the reduction of the effective Hubbard repulsion. It is important to note that the simple picture of the static renormalized interaction is not valid if the phonon frequency is small, the LF transformation is not applicable, and also there is a bandwidth renormalization in the results which incorporates in the reduction of the above mentioned local observables. Similarly, the kinetic energy exhibit a larger absolute value in systems with stronger el-ph coupling, both in the Migdal and the HF approximations.

Exploring the phonon densities in the Migdal approximation, plotted in Fig. 6.11 a-b), reveal that the strength of coupling can not impose any change neither in the adiabatic nor in the nonadiabatic regime. This response is completely distinct from the "heat bath" nature of the phonons within HF approximation. Within the HF approximation, at $\omega = 0.2$ the more excitations of phonons is in systems with weaker el-ph coupling as the thermal effect controls this response. At $\omega_0 = 1.0$, where excitations of phonons is tamed by

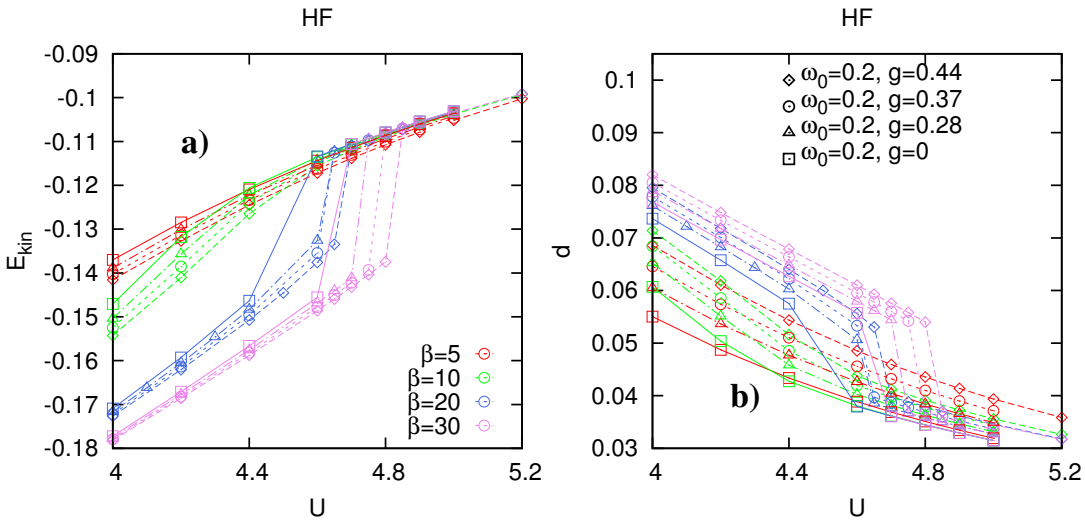


Figure 6.12: Equilibrium kinetic energies (a) and double occupancies (b) of systems within the HF approximation, at $\beta \in \{5, 10, 20, 30\}$, and $(\omega_0, g) \in \{(0.2, 0.44), (0.2, 0.37), (0.2, 0.28), (0.2, 0)\}$.

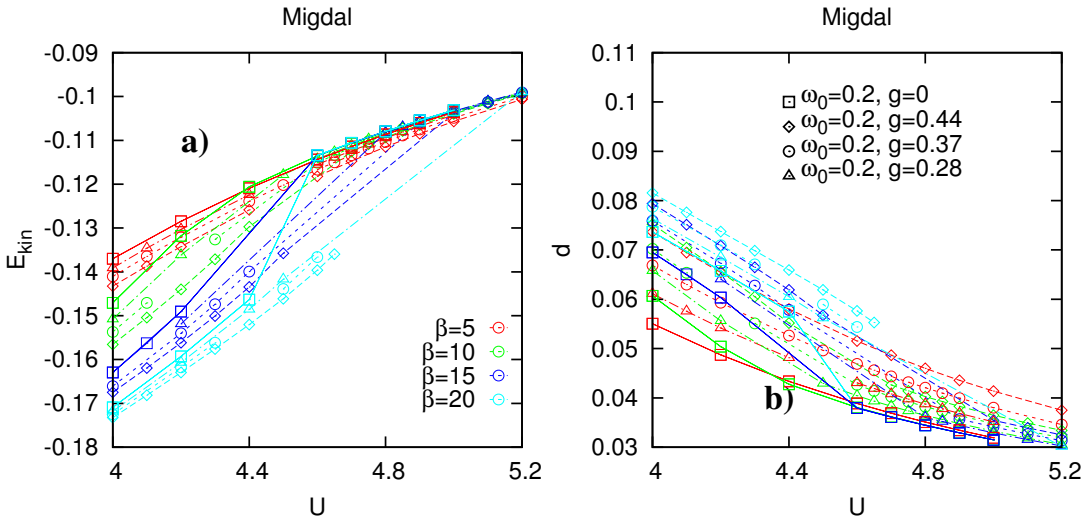


Figure 6.13: Equilibrium kinetic energies (a) and double occupancies (b) of systems within the Migdal approximation, at $\beta \in \{5, 10, 15, 20\}$, and $(\omega_0, g) \in \{(0.2, 0.44), (0.2, 0.37), (0.2, 0.28), (0.2, 0)\}$.

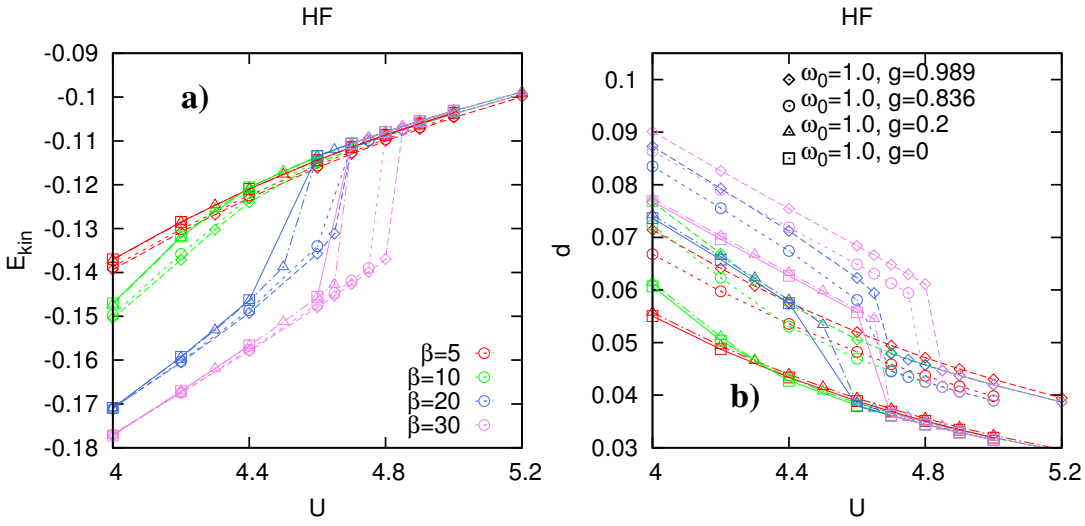


Figure 6.14: Equilibrium kinetic energies (a) and double occupancies (b) of systems within the HF approximation, at $\beta \in \{5, 10, 20, 30\}$, and $(\omega_0, g) \in \{(1.0, 0.989), (1.0, 0.836), (1.0, 0.2), (1.0, 0)\}$.

the charge-charge correlations, the larger phonon density is associated with systems with stronger couplings, see Fig. 6.11 a).

### Renormalization of the phonon frequency within the Migdal approximation

One of the significant effects of the Migdal approximation is the renormalization of the phonon frequency. To evaluate the dependency of $\omega_{\rm r}$ to the parameters of the Hubbard-Holstein model, we now perform a straightforward calculations using the space-local terms of the actions, in Eq. (6.5, 6.4), which consists of the electron-density and phononic fields, as

$$\mathcal{S}_{\rm nph} = \int_{\mathcal{C}} {\rm d}t \Big\{ X_{\rm ph}(t) \mathcal{D}_0^{-1} X_{\rm ph} - \sqrt{2} g(t) n(t) X_{\rm ph}(t) + \frac{U}{2} \sum_{\sigma} n_\sigma(t) n_{\bar{\sigma}}(t) \Big\}, \tag{6.73}$$

where $\sigma$ is the spin index. In the above action, we have omitted the site indices for simplicity. Presenting the above action in the slave-rotor language gives us

$$\mathcal{S}_{\rm nph} = \int_{\mathcal{C}} {\rm d}t \big\{ -\frac{U}{2} L(t)^2 + X_{\rm ph}(t) \mathcal{D}_0^{-1}(t,t) X_{\rm ph}(t) - \sqrt{2} g(t) X_{\rm ph}(t) L(t) + \lambda L(t) + L(t) \partial_t \theta \big\}, \tag{6.74}$$

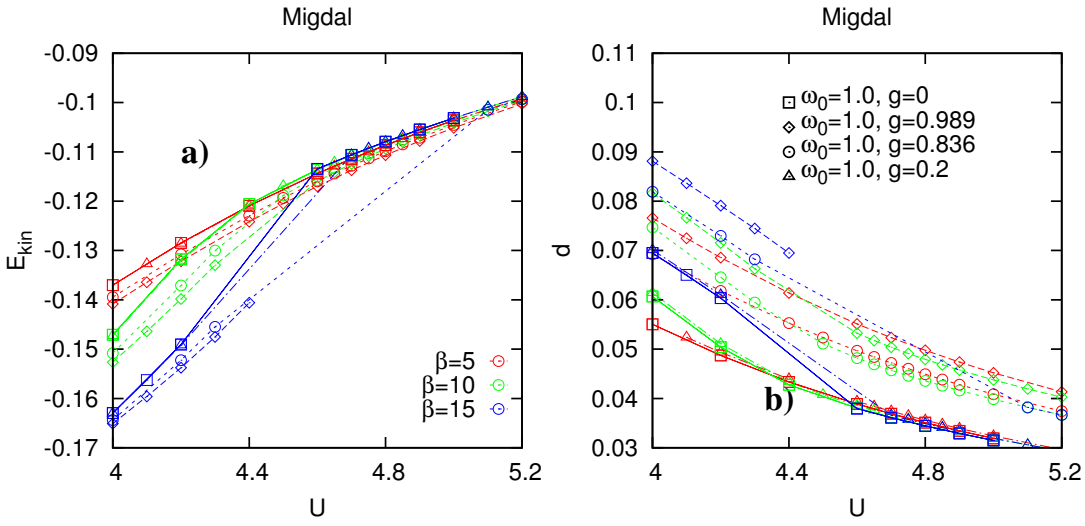


Figure 6.15: Equilibrium kinetic energies (a) and double occupancies (b) of systems within the Migdal approximation, at $\beta \in \{5, 10, 15\}$, and $(\omega_0, g) \in \{(1.0, 0.989), (1.0, 0.836), (1.0, 0.2), (1.0, 0)\}$.

where we replaced the phononic terms of the action by the representation introduced in Eq. (6.6). We now integrate out the the angular momentum fields and obtain

$$\mathcal{S}_{\theta\mathrm{ph}} = \int_{\mathcal{C}} \mathrm{d}t \Big\{ X_{\mathrm{ph}}(t)\mathcal{D}_0^{-1}(t,t)X_{\mathrm{ph}}(t) + \frac{1}{2}\big(\partial_t\theta + \lambda - \sqrt{2}g(t)X_{\mathrm{ph}}(t)\big)\frac{1}{U}\big(\partial_t\theta + \lambda - \sqrt{2}g(t)X_{\mathrm{ph}}(t)\big)\Big\}. \tag{6.75}$$

Expanding the last term of $\mathcal{S}_{\theta\mathrm{ph}}$ gives us

$$\begin{aligned}
&\frac{1}{2}\big(\partial_t\theta + \lambda - \sqrt{2}g(t)X_{\mathrm{ph}}(t)\big)\frac{1}{U}\big(\partial_t\theta + \lambda - \sqrt{2}g(t)X_{\mathrm{ph}}(t)\big) = \\
&\quad = \frac{1}{2}\big(\partial_t\theta + \lambda\big)\frac{1}{U}\big(\partial_t\theta + \lambda\big) \\
&\quad + \frac{1}{2}\big(\partial_t\theta + \lambda\big)\frac{1}{U}\big(-\sqrt{2}g(t)X_{\mathrm{ph}}(t)\big) + \frac{1}{2}\big(-\sqrt{2}g(t)X_{\mathrm{ph}}(t)\big)\frac{1}{U}\big(\partial_t\theta + \lambda\big) \\
&\quad + \frac{1}{2}\big(\frac{2g^2}{U}X_{\mathrm{ph}}(t)X_{\mathrm{ph}}(t)\big).
\end{aligned} \tag{6.76}$$

The last term of the above equation will soften the phonon frequency, as one can incorporate that in the first term of Eq. (6.75) by

$$\mathcal{D}_{\mathrm{r}} = \frac{-\partial_t^2}{2\omega_0} - \frac{\omega_0}{2} + \frac{1}{2}\frac{2g^2}{U}. \tag{6.77}$$

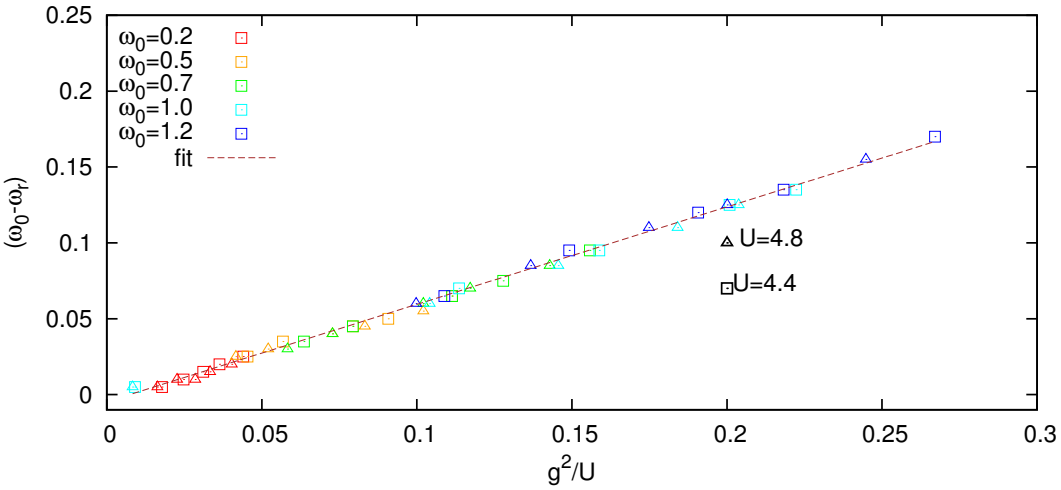


Figure 6.16: Deviations of the renormalized phonon frequencies as a function of $g^2/U$ at $\beta = 10$. Triangular (Square) points indicates $U = 4.4$ ($U = 4.8$). Various colors stands for different phonon frequencies.

We thereby can present the "bare" renormalized phonon frequency as

$$\omega_{\mathrm{r}}^0 = \omega_0 - \frac{2g^2}{U}. \tag{6.78}$$

In Fig. 6.16, we present the softening of the phonon frequency $(\omega_0 - \omega_{\mathrm{r}})$ as a function of $g^2/U$ for two Hubbard interactions. Results reveal that, as it was expected from Eq. (6.78), larger el-ph couplings correspond to stronger renormalization of phonon frequencies. Moreover, we fit the softening factor with

$$\omega_0 - \omega_{\mathrm{r}} \propto \alpha \frac{g^2}{U}, \tag{6.79}$$

where $\alpha$ is a constant which has been set to $\alpha \approx 0.6$ in Fig. 6.16. The value of the fitting parameter emphasis on the fact that the rotor-phonon coupling, in the third line of Eq. (6.76), will lead to an additional coupling shift of the frequency.

### 6.2.3 Nonequilibrium physics: a sudden quench of the electron-phonon coupling

In the preceding section, we have characterized the thermal properties of the system in Migdal and HF approximations. We have presented that, due to the el-ph coupling, both

the hopping amplitude and the Hubbard interaction will be renormalized in both approximations. We have also showed that in the Migdal approximation, the phonon frequency will be renormalized. In addition, investigations of the spectral functions for both approximations exhibit the phononic sidebands, which are more pronounced in the stronger el-ph couplings.

After characterizing the thermal properties of the system, we pursue our investigation by bringing the system out of equilibrium. As our first attempt, we would like to look for the emergence of a insulator-to-metal transitions. We would like to understand how out of equilibrium protocols can facilitate the formation of the metallic tendencies in systems, which are at the edge of insulating regimes.

To seize this goal, we will prepare the nonequilibrium initial state by a rapid quench of the el-ph coupling from $g(t = 0) = 0$ to $g(t > 0) > 0$. To understand the physics of the system out of equilibrium, we prepare a system in a state, governed by the Hubbard model, near paramagnetic metal-to-insulator transition (PMIT) in either the metallic or insulating phase. We then suddenly switch on the el-ph coupling, and set it to a value which is in the intermediate regime of the Holstein model $E_{\rm p} = g^2/\omega_0 \approx 1$. We will treat phonons either within the Migdal or HF approximation. In the following, we will discuss the physics of this system in more details.

**Nonequilibrium physics: Hartree-Fock approximation**

In Fig. 6.17, we plot the kinetic energy as well as the double occupancy of systems with $U \in \{4.4, 4.7\}$ at $\beta = 10$. We present results for three different phonon frequencies corresponding to the bare polaron energy of $E_{\rm p} \approx 0.8$. Results show that the kinetic energy ($E_{\rm kin}(t)$) of the system is more than its counterpart ($E_{\rm kin}(t = 0)$) in the uncoupled Hubbard-like system. This response is simply the consequence of the enhancement of the metallic tendency of system, see also Fig. 6.18. In addition, the variation of the kinetic energy, apart from the initial transient response, is almost converging to a value, which is independent of the phonon frequency. Despite the kinetic energy, the double occupancy depends on the phonon frequency. It is evident that at $\omega_0 = 0.2$ the induced double occupancy is smaller than results at $\omega \geq 0.7$. The responses of both kinetic energies and double occupancies are in agreement with the presented equilibrium results in Sec. 6.2.2. It is also apparent that the short-time transient responses are stronger in systems at larger phonon frequencies.

Fig. 6.18 compares the nonequilibrium as well as equilibrium spectral functions at $\beta = 10$. It is evident that the height of the quasiparticle peak at $\omega = 0$ is larger when the system is driven out of equilibrium. The phononic sidebands are also more pronounced in the nonequilibrium case. Moreover, the spectral density between the Hubbard bands and

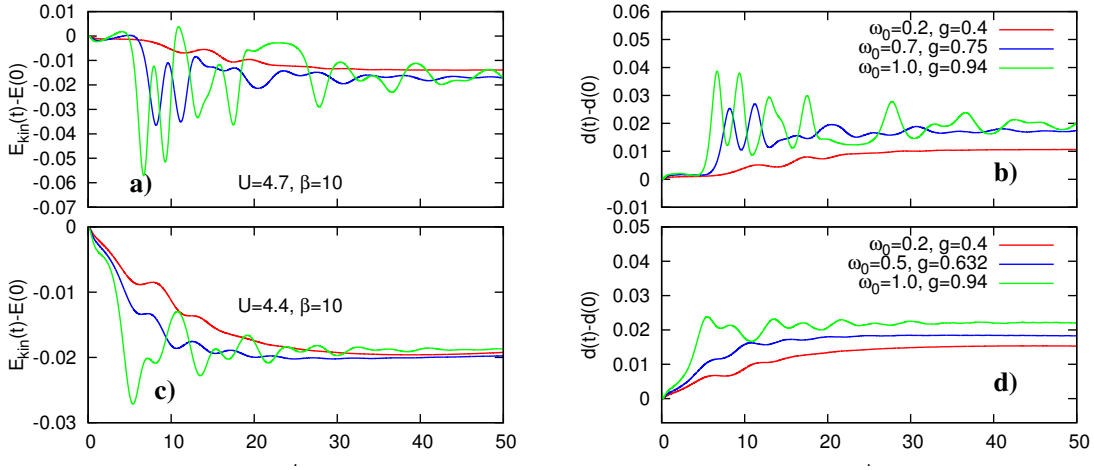


Figure 6.17: a) The Kinetic energies and b) double occupancies of systems at $U = 4.7$, $\beta = 10$, and $(\omega, g) \in \{(0.2, 0.4), (0.7, 0.75), (1.0, 0.94)\}$. c) The Kinetic energies and d) double occupancies of systems at $U = 4.4$, $\beta = 10$, and $(\omega, g) \in \{(0.2, 0.4), (0.5, 0.632), (1.0, 0.94)\}$. The values of the vertical axis is plotted with respect to their differences with their values at $t = 0$.

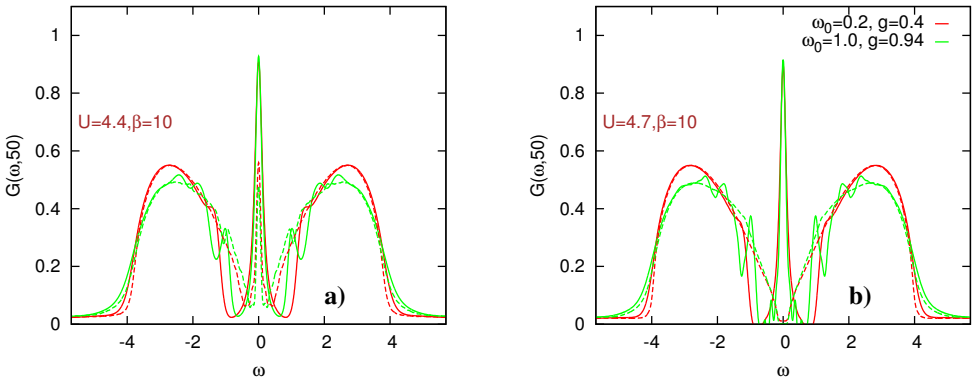


Figure 6.18: Spectral functions of systems at $\beta = 10$ within the HF approximation with the phononic parameters of $(\omega_0, g) = \{(0.2, 0.4), (1.0, 0.94)\}$, and a) $U = 4.4$, b) $U = 4.7$. Dashed lines are the equilibrium spectral functions computed at $\beta = 10$ and final coupling parameters.

the quasiparticle peak is suppressed at $t = 50$. Such a gap-like feature splits the spectral density into almost three separated sectors, consisting of two deformed Hubbard bands and a very large quasiparticle peak. The height of this peak at $t = 50$ is almost independent of the phonon frequency, but the gap-size as well as deformations of Hubbard bands will be modified by varying $\omega_0$, see Fig. 6.18 b). When the el-ph coupling is smaller, the redistributions of the spectral density is less drastic. These evidences are consistent with the equilibrium physics within HF approximation. To further explore the time-evolution of the spectral densities, we have plotted them at various times in Fig. 6.19. As we start from the phase diagram of the Hubbard model ($g(t = 0) = 0$), the initial spectral function at $U = 4.7$ has an insulating nature, and at $U = 4.4$, the associated density at $\omega = 0$ is small as the critical Hubbard interaction is almost at $U_c = 4.5$. Results at $t = 5$ in different panels of Fig. 6.19 present the formation of bad metallic states. By passing the time, more density will be accumulated around $\omega = 0$, and a gap-like features will appear in the spectral functions. As soon as these gap-like features emerge, the evolution of the spectral densities will become extremely slowed. Moreover, as we are plotting the nonequilibrium spectral functions, negative spectral functions should not be interpreted as the presence of unphysical states. At short simulation time, Fourier artifacts appear in the spectral function, mainly visible in Fig. 6.19 a).

We also analyze the height of the quasiparticle peak as a function of time in Fig. 6.20, as this quantity will inform us about the starting time of the slow evolution. Plots show that the time when the maximum of the quasiparticle peak occurs is mainly determined by the Hubbard interaction. It is also clear that at a fixed Hubbard interaction, a larger height of the quasiparticle peak is related to systems with larger phonon frequencies, although it is evident that the height of the quasiparticle peak has an oscillating behavior at larger phonon frequencies, which is more pronounced when the Hubbard interaction is larger, e.g. $U = 4.7$, and $\omega_0 = 0.7$.

In almost all of the reported results on the formation of the spectral functions, the formation of the gap-like density was clear, see Figs. 6.18, 6.19. These features in spectral densities in Fig. 6.6 at lower temperatures would hint that most likely the nonequilibrium dynamics is towards dissipating the injected energy, through the quench of the el-ph coupling, by interacting with lattice degrees of freedom, and relaxing to an effective colder temperature ($\beta > 10$). To investigate this scenario, we will explore the local responses of the lattice in Fig. 6.21.

In Fig. 6.21, we plot $\langle PP \rangle$, phonon densities, and $\langle XX \rangle$. $\langle PP \rangle$ presents an oscillating behavior with a $U$-independent frequency of $2\omega_0$. This vibrational behavior is centered around a time-dependent value. To explain this response, one should recall that when $g = 0$, the displacement and momentum of ions are oscillating functions with the frequency

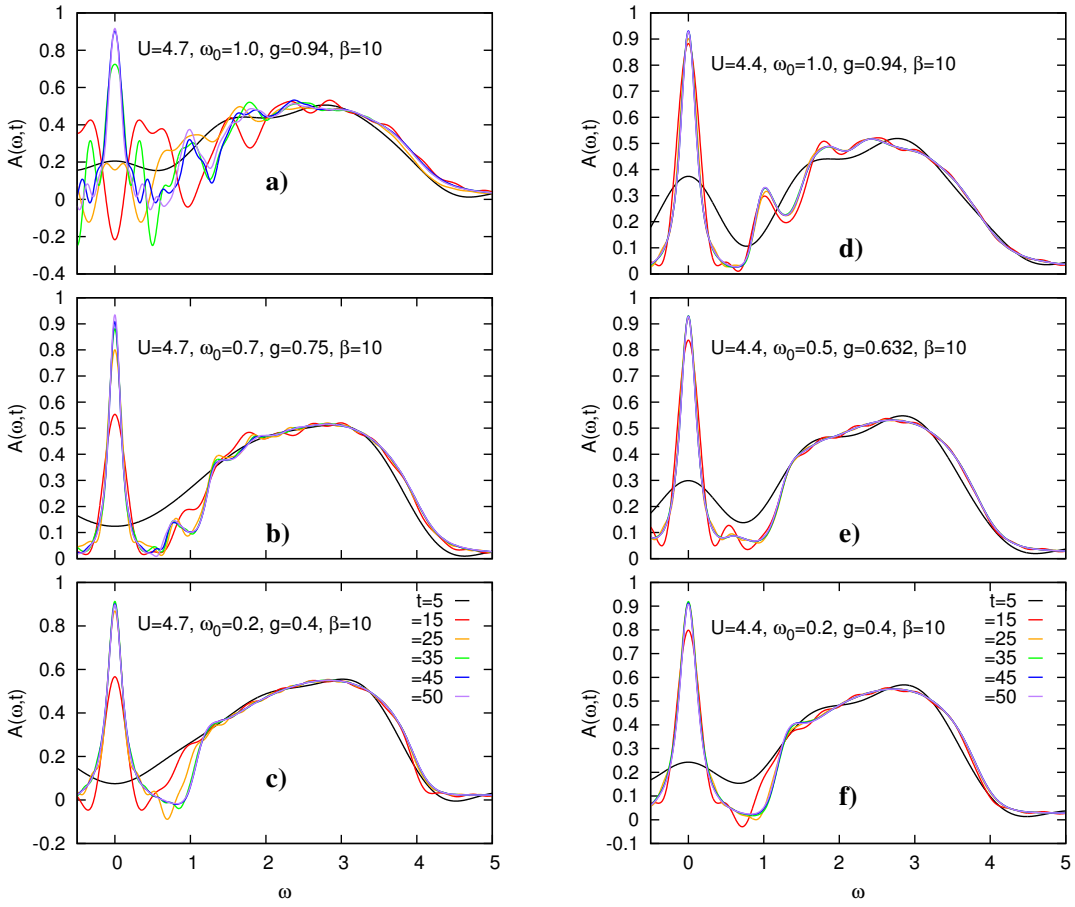


Figure 6.19: Time-evolution of spectral functions within the HF approximation at $\beta = 10$, a) $(\omega_0, g) \in \{(1.0, 0.94)\}$, and $U = 4.7$. b) $(\omega_0, g) \in \{(0.7, 0.75\}$, and $U = 4.7$. c) $(\omega_0, g) \in \{(0.2, 0.4\}$, and $U = 4.7$. d) $(\omega_0, g) \in \{(1.0, 0.94)\}$, and $U = 4.4$. e) $(\omega_0, g) \in \{(0.7, 0.75\}$, and $U = 4.4$. f) $(\omega_0, g) \in \{(0.2, 0.4\}$, and $U = 4.4$. plots are obtained at times $t \in \{5, 15, 25, 35, 45, 50\}$.

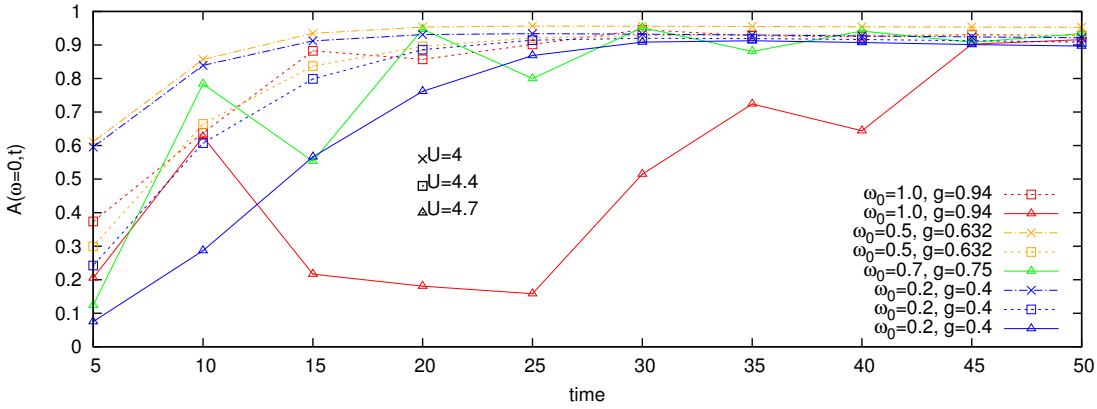


Figure 6.20: Temporal evolution of the spectral functions within the HF approximation at $\beta = 10$, $U \in \{4, 4.4, 4.7\}$, and various phononic parameters as indicated in the plot.

of $\omega_0$. Thereby, the correlation function of $\langle PP \rangle$ would have the oscillating frequency of $2\omega_0$. As the presented results are work in progress, we will postpone further discussion on the response of $\langle PP \rangle$ to future publications.

Figs. 6.21 b) and c) reveal that the enhancement of the oscillating amplitude in $\langle PP \rangle$ is associated with systems whose phonon density is larger. Results also exhibit larger phonon densities in systems which are deeper in the nonadiabatic regimes. This is because of the fact that the dynamics of the lattice and electrons would be almost decoupled in the adiabatic regime (in the static picture). In addition, the presence of an oscillating response with the frequency of $2\omega_0$ is also visible in Figs. 6.21 b) and c). Eq. (6.51) would also indicates that at $t = 0$, the phonon density is determined by the temperature which, at a fixed temperature, is larger when the phonon frequency is smaller. We thus can easily realize that, as it was expected, the enhancement of the phonon density is rooted in the electrons dynamics, by the density-density correlation function.

Exploring the variance of the phonon displacement ($\langle XX \rangle$) also reflects the influence of electrons on the phononic responses has not only oscillating behavior, with the frequency of $2\omega_0$, but also an ongoing grow of this correlation function is presented in Figs. 6.21 c) and f). Since $\langle XX \rangle$ can be obtained from the phonon Green's function ($\mathcal{D}$), the phonon Dyson equation would show that the phonon self-energy, computed by the electron Green's function, is responsible for the upward trend in the evolution of $\langle XX \rangle(t)$.

As our last attempt on understanding the phononic response of the system, we have plotted the two-body phononic correlation functions in Fig. 6.22. Results at $t = 0$ rep-

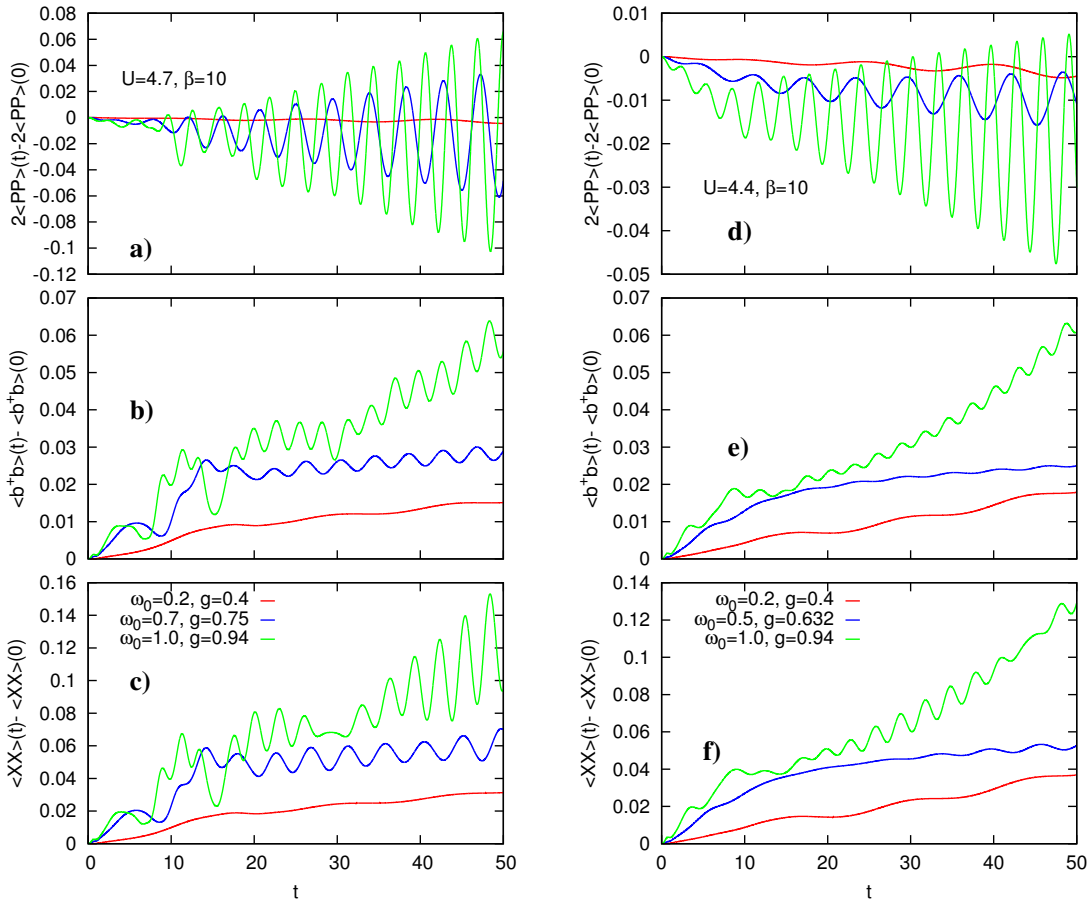


Figure 6.21: Time-evolution of $\langle PP \rangle$, phonon density, and $\langle XX \rangle$ within the HF approximation at $\beta = 10$, a-c) $(\omega_0, g) \in \{(0.2, 0.4), (0.7, 0.75), (1.0, 0.94)\}$, and $U = 4.7$, b-f) $(\omega_0, g) \in \{(0.2, 0.4), (0.5, 0.632), (1.0, 0.94)\}$, and $U = 4.4$. Panels a) and d) plot $\langle PP \rangle$. Panels b) and e) plot the phonon densities. Panels c) and f) plot $\langle XX \rangle$.

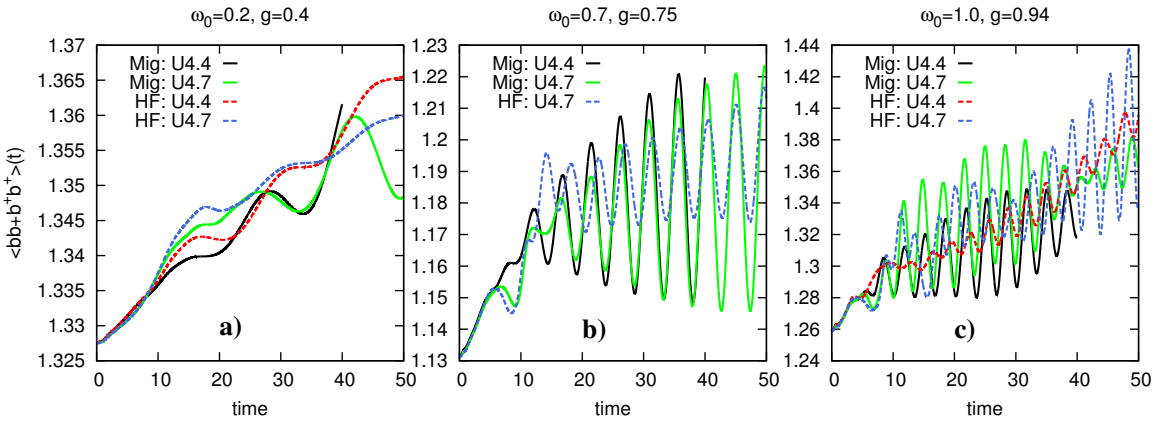


Figure 6.22: Temporal evolution of the two-body phonon correlation function within Migdal (solid lines) and HF (dashed lines) approximations at $\beta = 10$, $U \in \{4.4, 4.7\}$, and $E_{\rm p} = 0.8$. the phononic parameters are a) $\omega_0 = 0.2$, $g = 0.4$, b) $\omega_0 = 0.7$, $g = 0.75$, and c) $\omega_0 = 1.0$, $g = 0.94$.

resents the thermal values of the correlation function, which is larger when $\omega_0$ is smaller. This correlation function, similar to other phononic observables plotted in Fig. 6.21, is growing in time, and its value is oscillating with the frequency of $2\omega_0$. The amplitude of these oscillations is larger when the Hubbard interaction is closer to the insulating regime. The faster growth of the $\langle bb + b^\dagger b^\dagger \rangle$ at $\omega_0 = 1.0$ indicates that the occupation of the excited state is more probable in systems which are in the nonadiabatic regime. This can be grasped by recalling that the associated el-ph coupling, at a fixed $E_p$, is for the system whose phonon frequency is larger. This coupling parameter ($g$) controls the probability of creating an excited states, via the el-ph term of the Hubbard-Holstein Hamiltonian, and thus governs the rate of occupying multi-phonon states in the system.

In all of the above mentioned results, the dynamical responses of phononic correlation functions exhibit the transfer of energy to the phononic systems. We also showed that the spectral densities exhibit a gap-like features, which were only present in the spectral function at low temperature in equilibrium. Although we strongly emphasizes that the nonequilibrium state is purely non thermal, the collected evidences suggest that the slow evolution of the system is towards a thermal state which is colder than $\beta = 10$. To confirm this scenario, it is crucial to compute the total energy of the system and determine its corresponding effective temperature. This is the step which we would leave it for the future works.

**Nonequilibrium physics: the Migdal approximation**

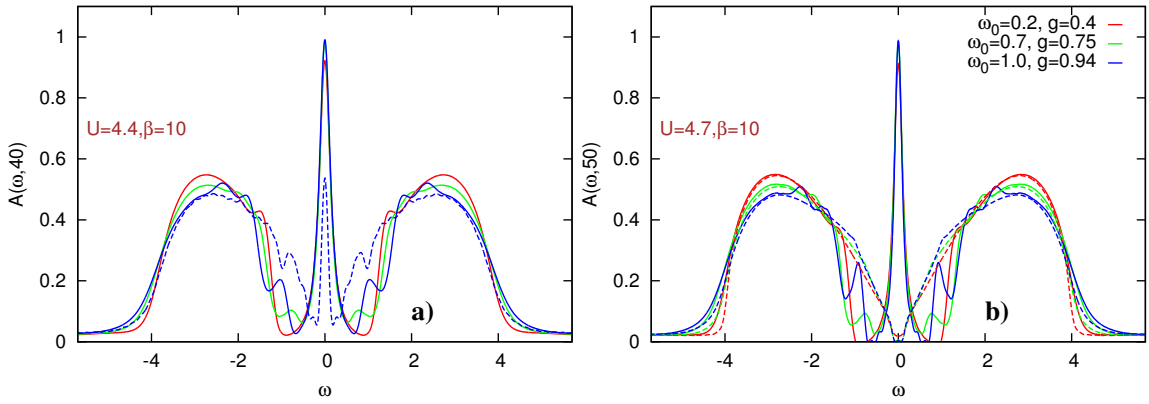


Figure 6.23: Spectral functions of systems within Migdal approximation at $\beta = 10$, $(\omega_0, g) \in \{(0.2, 0.4), (0.7, 0.75), (1.0, 0.94)\}$, and a) $U = 4.4$, b) $U = 4.7$. Dashed lines are the equilibrium spectral functions computed at $\beta = 10$ and final coupling parameters.

In the following, we will investigate the Hubbard-Holstein model within the Migdal approximation. We will also try to categorize the discrimination between the Migdal and HF approximations in this section.

Fig. 6.23 presents equilibrium and nonequilibrium spectral functions in metallic ($U = 4.4$), and insulating ($U = 4.7$) phases at $\beta = 10$. Plots exhibit that the height of the quasiparticle peaks in nonequilibrium results is significantly larger than the corresponding thermal state. The phononic sidebands are also present, and their height is more pronounced at larger phonon frequencies, at a fixed polaron energy. Moreover, similar to the results within the HF approximation, the gap-like features are clearly visible. In Fig. 6.24, we plotted the spectral function at various time for system with similar parameters as in Fig. 6.23. Short-time response of the system exhibit a bad metallic spectral function with small densities around $\omega = 0$. Within a short time-period, about $\Delta t \approx 20$, the system undergoes a rapid transition to a good metallic state with a very sharp peak in the density of states, at $\omega = 0$. This quasiparticle peak is almost separated from the Hubbard bands by a gap-like feature in between. After this period, we are observing a substantial suppression of the relaxation dynamics of the system.

To estimate a timescale for reaching an almost stable spectral density, we have plotted the height of the quasiparticle peak as a function of time in Fig. 6.25. Results show that, like the HF results, after a $U$-dependent time, e.g. $t \approx 35$ at $U = 4.7$, the height of the quasiparticle peak is very slowly descending. Moreover, the oscillating behavior of the quasiparticle peak is also present in results related to the nonadiabatic regime, c.f.

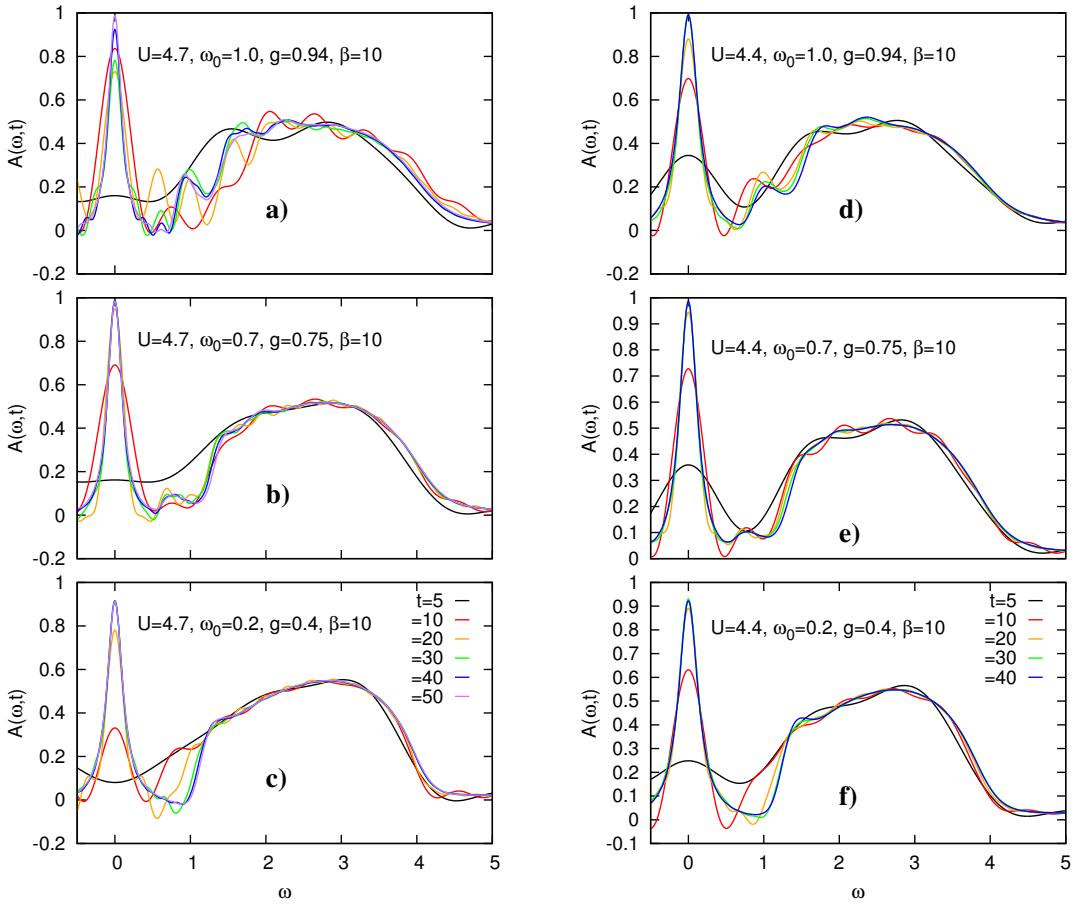


Figure 6.24: Time-evolution of spectral functions within the Migdal approximation at $\beta = 10$, a) $(\omega_0, g) \in \{(1.0, 0.94)\}$, and $U = 4.7$. b) $(\omega_0, g) \in \{(0.7, 0.75\}$, and $U = 4.7$. c) $(\omega_0, g) \in \{(0.2, 0.4\}$, and $U = 4.7$. d) $(\omega_0, g) \in \{(1.0, 0.94)\}$, and $U = 4.4$. e) $(\omega_0, g) \in \{(0.7, 0.75\}$, and $U = 4.4$. f) $(\omega_0, g) \in \{(0.2, 0.4\}$, and $U = 4.4$. plots are obtained at times $t \in \{5, 10, 20, 30, 40, 50\}$.

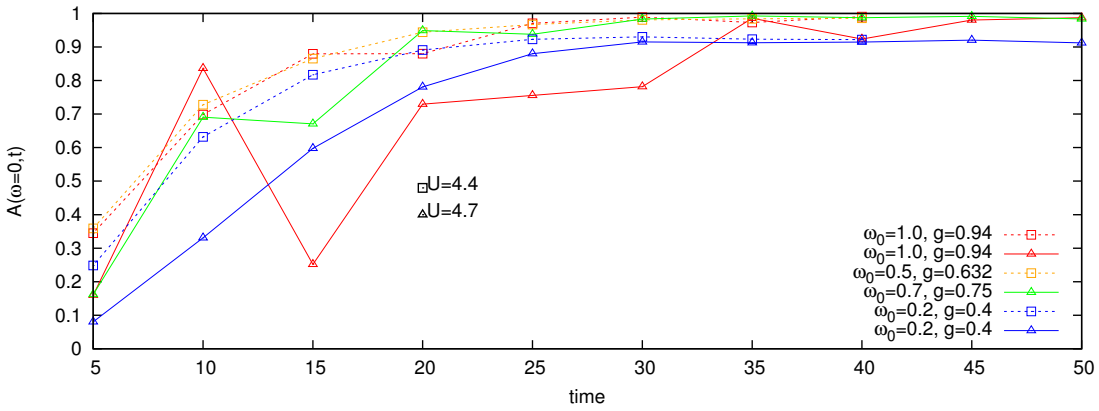


Figure 6.25: Temporal evolution of the spectral functions within the Migdal approximation at $\beta = 10$, $U \in \{4.4, 4.7\}$, and various phononic parameters as indicated in the plot.

Fig. 6.20.

Comparison between the spectral functions within HF and Migdal approximations, plotted in Fig. 6.26, shows that the height of the quasiparticle peak within Migdal approximation is larger than the associated results of the HF approximation. These differences are more visible at $\omega_0 = 1$ than $\omega_0 = 0.2$. Moreover, the location of phononic sidebands are also distinct within Migdal and HF approximations. These responses are linked to the softening of the phonon frequency within the Migdal approximation. As the effective phonon frequency within the Migdal approximation is less than its counterpart within the HF approximation, at a fixed $E_p$, and thus the system is in stronger coupling regime within the Migdal approximation. In the following we will analyze this renormalization of the phonon frequency.

In Fig. 6.27, we plot the softening of the phonon frequency, in panel a), and the renormalized polaron energy, in panel b), as a function of time. Results exhibit that the softening of the phonon frequency is stronger in the nonadiabatic regime than the regime, where the phonon frequency is small. This simply is because of the vigorous intertwined dynamics of the phononic and electronic subsystems in the nonadiabatic regime. It is important to note that the value of $\omega_{\rm r}$ exhibits a very small dependancy on the Hubbard interactions. Fig. 6.27 b) presents that $\omega_0 - \omega_{\rm r}$ at larger Hubbard interactions is smaller, which is in agreement with the equilibrium physics, in Eq. (6.79), within the Migdal approximation. In addition, there is also a visible oscillation, at $\omega_0 = 0.2$, in $\omega_{\rm r}$ with the frequency which is proportional to $g^2/U$, see also the discussion in Sec. 6.2.2. It is important to note that the normalized phonon frequency, will also reduce the effective renormalized Hubbard

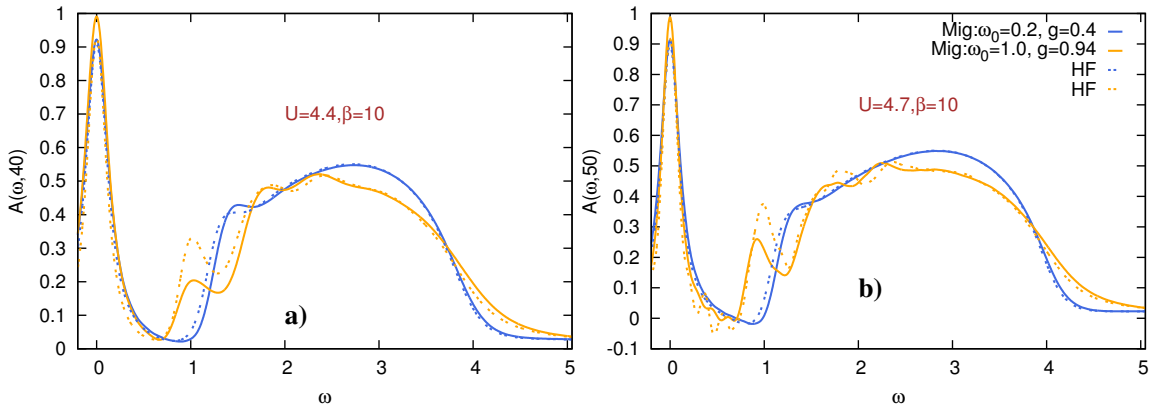


Figure 6.26: Spectral functions within the Migdal (solid lines) and HF (dashed lines) approximation at $\beta = 10$, a) $U = 4.4$, b) $U = 4.7$. Phononic parameters as $(\omega_0, g) \in \{(0.2, 0.4), (1.0, 0.94)\}$, corresponding to $E_p = 0.8$.

interaction as

$$U_{\text{eff}}^{\text{Mig}} \approx U - \frac{2g^2}{\omega_{\text{r}}}. \tag{6.80}$$

After collecting all pieces of evidences within the Migdal approximation, we can now realize the reason behind larger height of the quasiparticle peak within the Migdal than the HF approximation, which is as follows. At a fixed $U$, the effective phonon frequency in the Migdal (HF) approximation is $\omega_{\text{r}}$ ($\omega_0$), which renormalized the Hubbard interaction to $U_{\text{eff}}^{\text{Mig}} = U - \frac{2g^2}{\omega_{\text{r}}}$($U_{\text{eff}}^{\text{HF}} = U - \frac{2g^2}{\omega_0}$). As the smaller Hubbard interaction is associated with a more metallic tendency, and $U_{\text{eff}}^{\text{Mig}} < U_{\text{eff}}^{\text{HF}}$, the higher quasiparticle peak is for the Migdal approximation, see Fig. 6.26. Moreover, a very small oscillation is also realizable in results at $\omega_0 \in \{0.7, 1.0\}$, with the frequency of $\omega_0$, up to the resolution of the plot.

The renormalized polaron energy is plotted in Fig. 6.27 a). This quantity exhibits a short-lived transient response, which would be different for various phonon frequencies. At longer times, this transient response will be relaxed to an almost time-independent value.

This behaviour is consistent with the time-evolution of the spectral densities, see also Fig. 6.24. After applying the quench excitation, the deformation of the the spectral density is so large due to the dissipation of the gained energy to the heat bath, evolving from a bad-metallic densities to spectral function with a well-defined quasiparticle peak. Such a fast response results in the formation of the quasiparticle peak, phononic sidebands, and the gap-like spectral density between the quasiparticle peak and the Hubbard bands. When

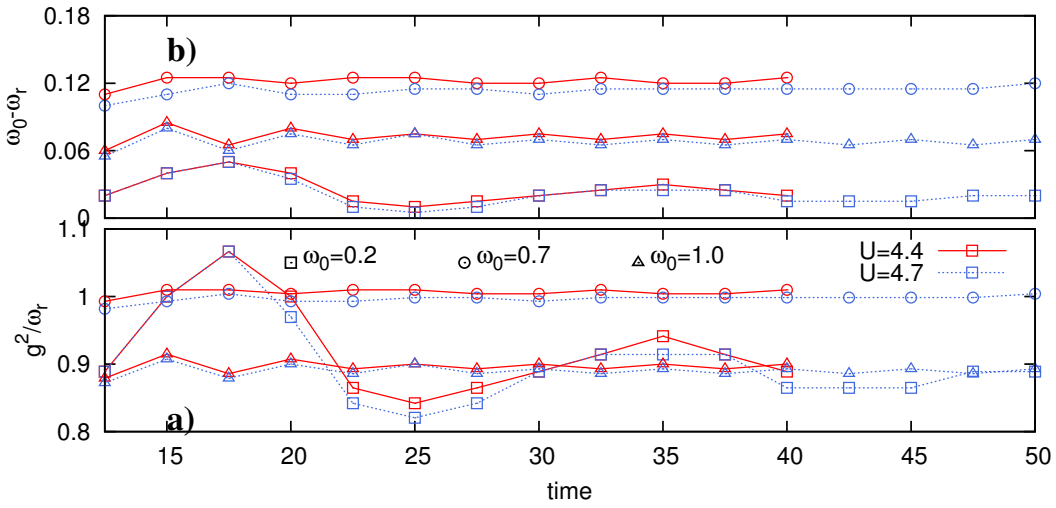


Figure 6.27: a)Renormalized polaron energy ($g^2/\omega_r$) as a function of time within Migdal approximation for systems at $U \in \{4.4, 4.7\}$ and $\beta = 10$ for system with the bare couplings of $(\omega_0, g) \in \{(0.2, 0.4), (0.7, 0.75), (1.0, 0.94)\}$. b) Renormalized phonon frequency as a function of time for parameters indicated in panel a). Line colors indicate the Hubbard interaction, point types stand for various phonon frequencies.

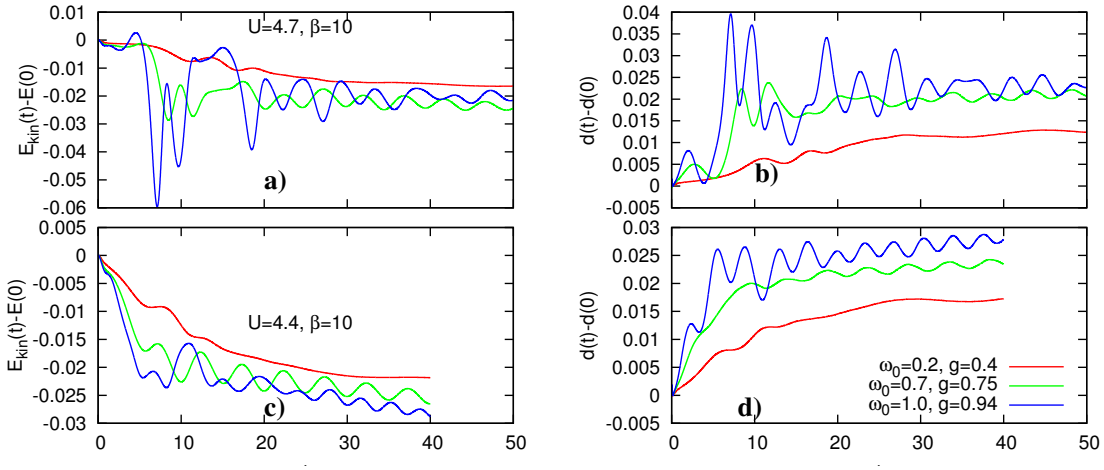


Figure 6.28: a) The Kinetic energies and b) double occupancies of systems at $U = 4.8$, $\beta = 10$, and $(\omega, g) \in \{(0.2, 0.37), (0.5, 0.7), (1.0, 0.836)\}$. c) The Kinetic energies and d) double occupancies of systems at $U = 4.4$, $\beta = 10$, and $(\omega, g) \in \{(0.2, 0.37), (0.5, 0.7), (1.0, 0.836)\}$. The values of the vertical axis is plotted with respect to their differences with their values at $t = 0$.

this gap is formed, the evolution of the system will be slowed down, and the bandwidth of the quasiparticle peak will become almost time-independent. Hence, the self-energy of the phononic subsystem, which contributes in the renormalization of $\omega_{\rm r}$, would loose its strong initial time-dependancy, and as a result, we would have an almost time-independent renormalized phonon frequencies after the formation of the quasiparticle.

To understand the dynamical response of these systems more deeply, we will now discuss the properties of various local observables. In our first attempt, we plot the kinetic energies and double occupancies at $U \in \{4.4, 4.8\}$, and $\beta = 10$ in Fig. 6.23. Results reveal that the long-time response of both the kinetic energy and double occupancy have a coherent oscillating response. Besides, the short-time transient response of systems at larger phonon frequencies is stronger than behavior of these observables at the adiabatic regime. This can be simply understand by recalling that screening of the Hubbard repulsion, induced by phonons, and controlled by the el-ph coupling, would enhance the effective mass of electrons as well as decrease the cost of creating doublons ($U_{\rm eff} < U$). Thereby, both the kinetic energy and double occupancy would be modified more in the stronger effective el-ph couplings.

In Fig. 6.29, we present $\langle PP \rangle$, phonon density, and $\langle XX \rangle$ at the same set of parameters as in Fig. 6.28. Presented results show that $\langle PP \rangle$ is oscillating with the frequency of $2\omega_{\rm r}$.

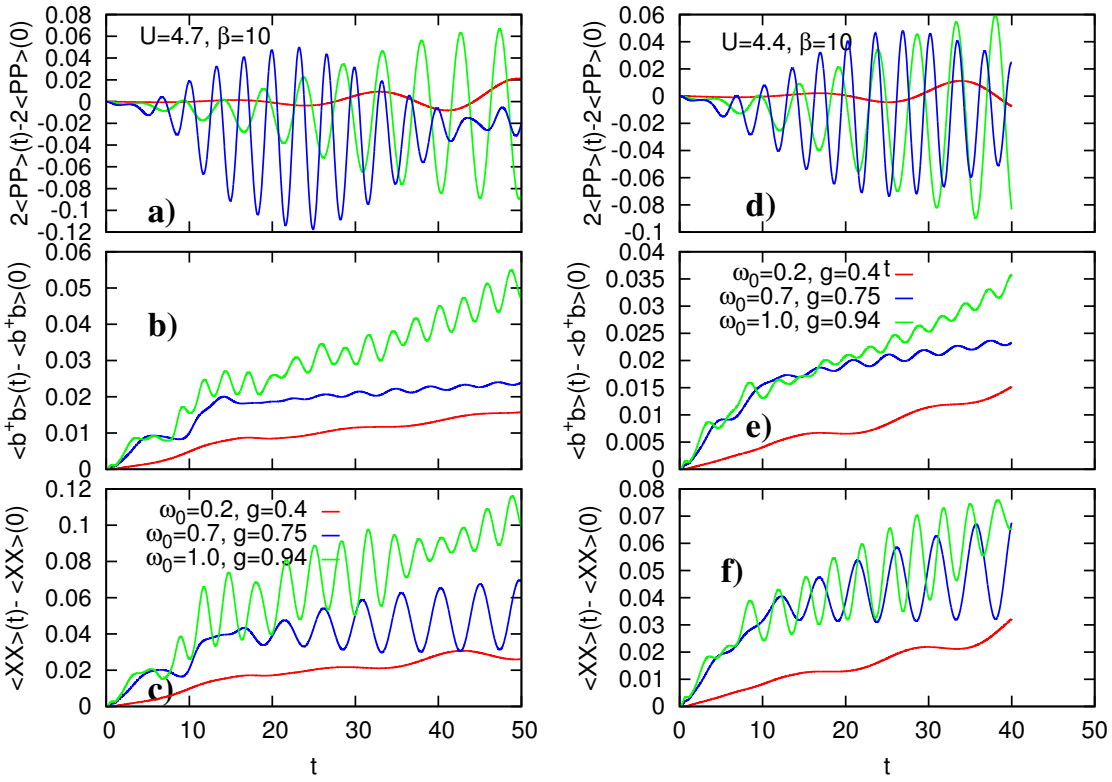


Figure 6.29: Time-evolution of $\langle PP \rangle$, phonon density, and $\langle XX \rangle$ within the Migdal approximation at $\beta = 10$, $(\omega_0, g) \in \{(0.2, 0.37), (0.5, 0.7), (1.0, 0.836)\}$, and a) $U = 4.8$, b) $U = 4.4$. The values of the vertical axis is plotted with respect to their differences with their values at $t = 0$.

Moreover, the momentum-momentum expectation values at $\omega_0 = 1.0$ exhibit an imprint of the Migdal self-consistent approximation. Results show that the oscillating amplitude of $\langle PP \rangle$ is increasing, and start decreasing after a while. On can easily see that the whole evolution is encapsulated in a small-frequency envelope. The time when $\langle PP \rangle$ acquires its maximum is determined by the Hubbard interaction, and is larger when $U$ is larger. This response is a result of electron feedback on the phononic observables, as phonons within the Migdal approximation are considered as a "self-consistent" bath. To capture more information regarding the timescale of the envelope, it is essential to have longer simulation times, which is not accessible at the moment.

Figs. 6.29 b), and e) present the phonon densities at $U \in \{4.4, 4.7\}$. It is clearly noticeable that, like the HF approximation, the creation rate of phonon densities is larger in

the nonadiabatic regime. One should note that the thermal phonon density ($\langle b^\dagger b\rangle(t=0)$) is larger at smaller phonon frequencies. Similar response can be also observed in the variance of the phonon displacement. Moreover, the oscillation in both phonon density, and $\langle XX\rangle$ has the frequency of $\omega_{\rm r}$.

Investigating the phonon squeezing in Fig. 6.25, shows that the time-dependent renormalized phonon frequency at $\omega_0 = 0.2$ is evidently reflected in the response of these correlation functions, in particular in the window of $t \in [10-35]$. In addition, the presence of the oscillating envelope, observed in $\langle PP\rangle$ in Fig. 6.29, hinted that the emergence of this envelope is indeed originated from the multi-phonon processes. We also can see the small oscillations with the frequency of $2\omega_{\rm r}$ in Figs. 6.25 b) and c). As it was plotted in Fig. 6.27 b), at $\omega_0 \in \{0.7, 1.0\}$, the renormalization of the phonon frequency is almost independent of time and Hubbard interaction, which is also presented in $\langle bb + b^\dagger b^\dagger\rangle$. Furthermore, comparing results within the HF and Migdal approximations, plotted in Fig. 6.25, exhibit distinguishable dynamics in the two-phonon correlation function. The absence of any oscillating envelope, the dependency on the Hubbard interaction, and the larger oscillating frequency ($\omega_0 > \omega_{\rm r}$) distinct the HF approximation from the Migdal approximation.

Nevertheless, both Migdal and HF approximations present the formation of a slow-evolving state. The associated spectral functions, in both approximations, were consisting of a well-separated quasiparticle peak close to $\omega = 0$, Hubbard bands which have been pushed to larger frequencies, and a very small, gap-like, spectral densities in between. To further disclosure of this nonequilibrium behavior of the system, we should compute more observables such as the total energy and the el-ph energy, related to $\langle c^\dagger cX\rangle$. The analysis of these quantities will then enable us to confirm, or reject, the proposed scenario of the dynamics which is related to the evolution of the system towards thermal states at $\beta > 10$. As both in the Migdal and HF approximation, thermal density of states at small temperatures ($\beta > 15$) exhibit similar features as the nonequilibrium reported spectral functions.

## 6.3 Outlook

As a continuation of the presented results, it is extremely important to understand the emergence of a stable metallic phase out of equilibrium in parameter regimes which are associated with insulators in equilibrium. It is also important to investigate the formation of the gap-like spectral densities in various regimes. Exploring the location of phononic

sidebands both in the adiabatic and nonadiabatic regimes can also unveil the underlying physics of the presented results. In addition, analyzing the quasiparticle weight as a function of time at different parameter regimes can be illustrative.

# Chapter 7

# Conclusion and outlook

The ongoing investigations of exotic material properties under extreme experimental conditions, such as low temperature, large pressure, and very short preparation timescales, are leading us to the conclusion that the equilibrium physics is an idealized concept. The observation of genuine nonequilibrium phenomenon [111], such as the light-induced superconductivity [97], and the dynamical stabilization of various unstable phases, for instance in the Kapitza Pendulum [18], evidence the fundamentality of the nonequilibrium physics. The opening of this perspective has initiated rapid progress of the field both in theoretical and experimental explorations of various problems. Despite an enchanting physics of these systems, exploring this field is accompanied by difficulties which have not been fully overcame yet. In the presented thesis, we discussed our contribution on tackling some of these challenges, which were originated from the time-dependent interaction between the lattice and electrons.

In one of our works, presented in Chap. 4, we have addressed the physics of a system in which a low density of carriers has been transfered to the conduction band, and a self-trapped delocalized state in the strong electron-lattice coupling regime has been observed [1, 46, 49, 50]. We have also presented that this localized state coexist with a delocalized state. The coexistence of such states has been also observed experimentally [1, 46, 49, 50].

Regarding the intriguing proposal on enhancing the metallic tendency of systems, we conducted some extensive exploration of the properties of many-body systems near the Mott transition, in Chaps. 5, and 6. We have shown that exciting a Mott insulator by a laser pulse will result in the closure of its gap in a very short timescale (few inverse of hopping), which is in agreement with experimental measurements [119]. Regarding the

relaxation of the induced bad-metallic state, we have shown that a rapid thermalization can be achieved in this phase, while its relaxation to the insulating phase is controlled by the electron-lattice interaction. The novelty of our results concerns the disclosure of the slow relaxation dynamics from the bad-metal to a good-metal. We have shown that the slowdown of the dynamics is rooted in the presence of a spin-related bottleneck in the evolution from a non-Fermi-liquid to the Fermi-liquid phase. Despite the very interesting physics of these systems, no experiment has been conducted so far. We propose that optical measurements on $LiV_2O_4$ would be a potential candidate for observing the long-lived relaxation dynamics in experiments [129].

Furthermore, we have presented in Chap. 6 some preliminary results that show the formation of stable nonequilibrium metallic phases in correlated materials with strong electron-lattice couplings. Although we would like to view these results as a work-in-progress, we have analyzed the properties of these systems, after a sudden quench of the electron-lattice coupling, and have shown that a very pronounced quasiparticle peak emerges, which is separated from the Hubbard bands by gap-like regions in the density of states. We also observed a slow dynamics in these systems, and attributed that to the formation of the quasiparticle peak. To achieve better understanding of the system, we would like to take steps towards detangling the underlying physics of this induced metallic phase.

Apart from the model-based investigations, we have proposed two novel impurity solvers for the dynamical mean field theory (DMFT). The first one, employed in Chap. 4, which has been introduced at the low-density limit of carriers and a linear electron-phonon interaction, is an analytical impurity solver, which generalized the continued fraction approach [19]. This impurity solver empowers us to demonstrate studies on various parameter regimes of the electron-phonon systems, see Chap. 4. Our second proposed impurity solver, exploited in Chaps. 5, and 6, concerns the generalization of the $U(1)$ slave-rotor impurity solver [38]. This impurity solver enables us to study the dynamics near the Mott-transition, which is the most challenging regime of the phase diagram.

The tremendous number of nontrivial observations in the field of nonequilibrium physics put a voracious demand on new numerical methods to push the boundaries of our knowledge further. Regarding this request, there is undoubtedly a room for proposing new impurity-solvers for DMFT. In this category, we would like to improve our generalized $U(1)$ slave-rotor, as its current version can not handle the pairing excitations [77], and the pseudospin symmetry [63]. We thereby are determined to extend the group symmetry of the current slave-rotor method to the $SU(2)$ gauge-theory. In addition, we are also planning to generalize the equilibrium slave-spin impurity solver to out of equilibrium [125, 23]. As this impurity solver would help us to surpass challenges of describing the multi-orbital

systems by using the representation of the Ising spins as auxiliary particles. One should note that the slave-rotor would also be a good candidate when the orbital symmetry is unbroken. Having these impurity solvers would lead us to understand the physics of various exotic phenomenon which did not fully described yet, for instance photo-induced high $T_c$ superconductivity [97, 40, 41].

It is also crucial to note that the underlying approximation of DMFT, related to its shortcoming on describing the non-local properties of the system, has to be overcome. The first steps on achieving this goal is to take the advantage of the cluster extension of DMFT, known as the dynamical cluster approximation (DCA) [141, 32]. By employing the DCA, we would like to incorporate the short-range correlations, still neglecting long-range correlations, into account, and explore phases of matter where non-local order parameters play a significant role in controlling the response of materials, for instance in d-wave superconductors [141]. Finally, the extremely enticing research plan is connected to the promotion of the $U(1)$, or $SU(2)$, slave-rotor impurity solver to the cluster-solvers, to be embedded in the DCA.

Nonequilibrium physics is a rapidly growing and intriguing field due to the magnificence of its underlying physics, but still major challenges persist to get the control over material properties. We hope that our contribution to overcome some of the challenges in this field, and to unveil tantalizing physics of electron-lattice problems were able to present the tip of this iceberg, and we are looking forward to being amazed by the further development of this young research field.

# APPENDICES

# Appendix A

# Analytical solution of the dynamical U with the phononic source

In Chap.5, we have shown that initiating a study on the Hubbard model within the slave-rotor language requires the determination of an uncoupled rotor Green's function, introduced in Eq. (5.54). This uncoupled rotor Green's function for a generic two-time Hubbard interaction satisfies Eqs. (6.33, 6.36). In this appendix, we will show that an analytical function can be obtained for the uncoupled rotor Green's function in the Hubbard-Holstein model. One should note that the upcoming derivation scheme is applicable when the electron-phonon coupling is time-independent, and only one phononic mode is present.

Rewriting the uncoupled rotor Green's function in real frequency have the form of

$$g_X(z) = \frac{1}{\frac{z^2}{2U} - \delta_0}, \tag{A.1}$$

which is a typical bosonic Green's function with two poles at $\omega = \pm\sqrt{2\delta_0 U}$, renormalized by a factor of $2U$.

Within Hubbard-Holstein model, the phonon-mediated Hubbard-like interaction results in defining an effective retarded interaction corresponding to an uncoupled [1]rotor Green's function of the form

$$G_X(z) = \frac{1}{\frac{z^2}{2\mathcal{U}(z)} - \delta_0}, \tag{A.2}$$

[1] "Uncoupled" refers to the case where there is no coupling between spinon and rotor Green's function.

where $\mathcal{U}$ for a electron-phonon coupling of $g$ was introduced as

$$\mathcal{U}(z) = U + 2g^2 D(z). \tag{A.3}$$

Substituting Eq. (A.3) into Eq. (A.2) and inserting the explicit form of $D(z)$ as

$$D(z) = \frac{1}{z-\omega_0} - \frac{1}{z+\omega_0}, \tag{A.4}$$

with the phonon frequency of $\omega_0$, will give us

$$G_X(z) = \frac{2U + 4g^2 D(z)}{z^2 - 2\delta_0 U - 4\delta_0 g^2 D(z)}, \tag{A.5}$$

$$= \frac{2U + \frac{4g^2}{z-\omega_0} - \frac{4g^2}{z+\omega_0}}{z^2 - 2\delta_0 U - \frac{4\delta_0 g^2}{z-\omega_0} + \frac{4\delta_0 g^2}{z+\omega_0}}, \tag{A.6}$$

$$= \frac{2U(z^2-\omega_0^2) + 8g^2\omega_0}{(z^2 - 2\delta_0 U)(z^2-\omega_0^2) - 8\delta_0 g^2 \omega_0}. \tag{A.7}$$

To get an intuition about the poles of Eq. (A.7), we try to bring Eq. (A.7) in to a general form as

$$G_X(z) = \frac{A}{z-\omega_1} + \frac{B}{z-\omega_2} - \frac{A}{z+\omega_1} - \frac{B}{z+\omega_2}, \tag{A.8}$$

$$= \frac{(z^2-\omega_2^2)(2A\omega_1) + (z^2-\omega_1^2)(2B\omega_2)}{(z^2-\omega_1^2)(z^2-\omega_2^2)}. \tag{A.9}$$

where $A$ and $B$ are renormalization factors, and $\omega_1$ and $\omega_2$ denotes poles of $G_X$. Finding $\omega_1$ and $\omega_2$ is straightforward calculation, since they are roots of

$$z^4 - (2\delta_0 U + \omega_0^2) z^2 + 2\delta_0 U \omega_0^2 - 8\delta_0 g^2 \omega_0 = 0, \tag{A.10}$$

with the explicit form of

$$\omega_1 = \sqrt{\frac{1}{2}(2\delta_0 U + \omega_0^2) + \frac{1}{2}\sqrt{(2\delta_0 U + \omega_0^2)^2 - 4(2\delta_0 U\omega_0^2 - 8\delta_0 g^2\omega_0)}}, \tag{A.11}$$

$$\omega_2 = \sqrt{\frac{1}{2}(2\delta_0 U + \omega_0^2) - \frac{1}{2}\sqrt{(2\delta_0 U + \omega_0^2)^2 - 4(2\delta_0 U\omega_0^2 - 8\delta_0 g^2\omega_0)}}. \tag{A.12}$$

In practice, we will choose $\delta_0$ such that the $\omega_1$ and $\omega_2$ have a positive real values. $A$ and $B$ can simply be found by comparing Eq. (A.7) to Eq. (A.9)

$$\begin{cases} 2A\omega_1 + 2B\omega_2 = 2U \\ -2\omega_1\omega_2(A\omega_2 + B\omega_1) = -2U\omega_0^2 + 8g^2\omega_0, \end{cases} \tag{A.13}$$

which is equivalent to a

$$\begin{pmatrix} 2\omega_1 & 2\omega_2 \\ -2\omega_1\omega_2^2 & -2\omega_1^2\omega_2 \end{pmatrix} \begin{pmatrix} A \\ B \end{pmatrix} = \begin{pmatrix} 2U \\ -2U\omega_0^2 + 8g^2\omega_0 \end{pmatrix}. \tag{A.14}$$

Inverting the matrix of the left hand-side, and multiplying that to both sides of the equation, will let us to express the renormalization parameters as

$$\begin{pmatrix} A \\ B \end{pmatrix} = \begin{pmatrix} \frac{-\omega_1}{2(-\omega_1^2+\omega_2^2)} & \frac{-1}{2\omega_1(-\omega_1^2+\omega_2^2)} \\ \frac{\omega_2}{2(-\omega_1^2+\omega_2^2)} & \frac{1}{2\omega_2(-\omega_1^2+\omega_2^2)} \end{pmatrix} \begin{pmatrix} 2U \\ -2U\omega_0^2 + 8g^2\omega_0 \end{pmatrix}. \tag{A.15}$$

Hence, we can write the phonon-mediated uncoupled rotor Green's function with poles at Eqs. (A.11, A.12) as

$$G_X(z) = \frac{A}{z-\omega_1} + \frac{B}{z-\omega_2} - \frac{A}{z+\omega_1} - \frac{B}{z+\omega_2}, \tag{A.16}$$

where these parameters are given by

$$A = \frac{-2\omega_1^2 U - (-2U\omega_0^2 + 8g^2\omega_0)}{2\omega_1(\omega_2^2 - \omega_1^2)}, \tag{A.17}$$

$$B = \frac{2\omega_2^2 U + (-2U\omega_0^2 + 8g^2\omega_0)}{2\omega_2(\omega_2^2 - \omega_1^2)}. \tag{A.18}$$

As a quick check, we set $g = 0$, and we get

$$B = 0, \quad A = \sqrt{\frac{U}{2\delta_0}}, \quad \omega_1 = \sqrt{2\delta_0 U}, \quad \omega_2 = \sqrt{\omega_0^2}. \tag{A.19}$$

ending up with the conventional uncoupled rotor Green's function in the Hubbard model, see Eq. (A.1).

# References


[1] K. J. Gaffney A. D. Miller, I. Bezel, S. H. Liu S. Garrett-Roe, and C. B. Harris P. Szymanski. Electron solvation in two dimensions. *Science*, 297:1163–1166, 2002.

[2] A. S. Alexandrov and J. T. Devreese. *Advances in Polaron Physics*. Springer Series in Solid-State Sciences. Springer Berlin Heidelberg, 2009.

[3] P. L. Alireza, Y. T. C. Ko, J. Gillett, C. M. Petrone, J. M. Cole, G. G. Lonzarich, and S. E. Sebastian. Superconductivity up to 29 K in $SrFe_2As_2$ and $BaFe_2As_2$ at high pressures. *Journal of Physics: Condensed Matter*, 21(1):12208, 2009.

[4] H. Aoki, N. Tsuji, M. Eckstein, M. Kollar, T. Oka, and Ph. Werner. Nonequilibrium dynamical mean-field theory and its applications. *Rev. Mod. Phys.*, 86(2):779–837, 2014.

[5] Th. Ayral, S. Biermann, and Ph. Werner. Screening and nonlocal correlations in the extended Hubbard model from self-consistent combined GW and dynamical mean field theory. *Phys. Rev. B*, 87(12):125149, 2013.

[6] G. Baym. Self-Consistent Approximations in Many-Body Systems. *Phys. Rev.*, 127(4):1391–1401, 1962.

[7] G. Baym and L. P. Kadanoff. Conservation Laws and Correlation Functions. *Phys. Rev.*, 124(2):287–299, 1961.

[8] M. Born and R. Oppenheimer. Zur Quantentheorie der Molekeln. *Annalen der Physik*, 389(20):457–484, 1927.

[9] R. Bulla. Dynamical mean-field theory: from quantum impurity physics to lattice problems. *Philosophical Magazine*, 86(13-14):1877–1889, 2006.

[10] M. Capone, L. Capriotti, F. Becca, and S. Caprara. Mott metal-insulator transition in the half-filled Hubbard model on the triangular lattice. *Phys. Rev. B*, 63(8):85104, 2001.

[11] M. Capone, P. Carta, and S. Ciuchi. Dynamical mean field theory of polarons and bipolarons in the half-filled Holstein model. *Phys. Rev. B*, 74(4):45106, 2006.

[12] E. Cappelluti and S. Ciuchi. Magnetic and lattice polaron in the Holstein t-J model. *Phys. Rev. B*, 66(16):165102, 2002.

[13] A. Cavalleri, Th. Dekorsy, H. H. W. Chong, J. C. Kieffer, and R. W. Schoenlein. Evidence for a structurally-driven insulator-to-metal transition in $VO_2$: A view from the ultrafast timescale. *Phys. Rev. B*, 70(16):161102, 2004.

[14] A. Cavalleri, M. Rini, H. H. W. Chong, S. Fourmaux, T. E. Glover, P. A. Heimann, J. C. Kieffer, and R. W. Schoenlein. Band-Selective Measurements of Electron Dynamics in $VO_{2}$ Using Femtosecond Near-Edge X-Ray Absorption. *Phys. Rev. Lett.*, 95(6):67405, aug 2005.

[15] A. D. Caviglia, R. Scherwitzl, P. Popovich, W. Hu, H. Bromberger, R. Singla, M. Mitrano, M. C. Hoffmann, S. Kaiser, P. Zubko, S. Gariglio, J.-M. Triscone, M. Först, and A. Cavalleri. Ultrafast Strain Engineering in Complex Oxide Heterostructures. *Phys. Rev. Lett.*, 108(13):136801, 2012.

[16] J. Chatterjee and A. N. Das. Two-site two-electron generalized HubbardHolstein model: a perturbation study. *Solid State Communications*, 129(4):273–278, 2004.

[17] M. Cini and A. D'Andrea. Exactly solved electron-boson models in condensed matter and molecular physics by a generalised recursion method. *Journal of Physics C: Solid State Physics*, 21(2):193, 1988.

[18] R. Citro, E. G. D. Torre, L. D'Alessio, A. Polkovnikov, M. Babadi, T. Oka, and E. Demler. Dynamical stability of a many-body Kapitza pendulum. *Annals of Physics*, 360:694–710, 2015.

[19] S. Ciuchi, F. de Pasquale, S. Fratini, and D. Feinberg. Dynamical mean-field theory of the small polaron. *Phys. Rev. B*, 56(8):4494–4512, 1997.

[20] P. Danielewicz. Quantum theory of nonequilibrium processes, I. *Annals of Physics*, 152(2):239–304, 1984.

[21] G. De Filippis, V. Cataudella, E. A. Nowadnick, T. P. Devereaux, A. S. Mishchenko, and N. Nagaosa. Quantum Dynamics of the Hubbard-Holstein Model in Equilibrium and Nonequilibrium: Application to Pump-Probe Phenomena. *Physical Review Letters*, 109(17):176402, 2012.

[22] T. Dekorsy, H. Auer, H. J. Bakker, H. G. Roskos, and H. Kurz. THz electromagnetic emission by coherent infrared-active phonons. *Phys. Rev. B*, 53(7):4005–4014, 1996.

[23] L. De'Medici, A. Georges, and S. Biermann. Orbital-selective Mott transition in multiband systems: Slave-spin representation and dynamical mean-field theory. *Phys. Rev. B*, 72(20):205124, 2005.

[24] J. Demsar, R. D. Averitt, K. H. Ahn, M. J. Graf, S. A. Trugman, V. V. Kabanov, J L Sarrao, and A J Taylor. Quasiparticle Relaxation Dynamics in Heavy Fermion Compounds. *Phys. Rev. Lett.*, 91(2):27401, 2003.

[25] J. S. Dodge, C. P. Weber, J. Corson, J. Orenstein, Z. Schlesinger, J. W. Reiner, and M. R. Beasley. Low-Frequency Crossover of the Fractional Power-Law Conductivity in $SrRuO_3$. *Phys. Rev. Lett.*, 85(23):4932–4935, 2000.

[26] F. Dorfner, L. Vidmar, C. Brockt, E. Jeckelmann, and F. Heidrich-Meisner. Real-time decay of a highly excited charge carrier in the one-dimensional Holstein model. *Phys. Rev. B*, 91(10):104302, 2015.

[27] F. J. Dyson. The S Matrix in Quantum Electrodynamics. *Physical Review*, 75(11):1736–1755, 1949.

[28] M. Eckstein, M. Kollar, and Ph. Werner. Thermalization after an Interaction Quench in the Hubbard Model. *Phys. Rev. Lett.*, 103(5):56403, 2009.

[29] M. Eckstein and Ph. Werner. Nonequilibrium dynamical mean-field calculations based on the noncrossing approximation and its generalizations. *Phys. Rev. B*, 82(11):115115, 2010.

[30] M. Eckstein and Ph. Werner. Damping of Bloch Oscillations in the Hubbard Model. *Physical Review Letters*, 107(18):186406, 2011.

[31] M. Eckstein and Ph. Werner. Dielectric breakdown of Mott insulators doublon production and doublon heating. *Journal of Physics: Conference Series*, 427(1):12005, 2013.

[32] M. Eckstein and Ph. Werner. Ultra-fast photo-carrier relaxation in Mott insulators with short-range spin correlations. *Scientific Reports*, 6:21235, 2016.

[33] G. Ehlers, J. Sólyom, Ö. Legeza, and R. M. Noack. Entanglement structure of the Hubbard model in momentum space. *Phys. Rev. B*, 92(23):235116, 2015.

[34] H. Ehrke, R. .I Tobey, S. Wall, S. A. Cavill, M. Först, V. Khanna, Th. Garl, N. Stojanovic, D. Prabhakaran, A. T. Boothroyd, M. Gensch, A. Mirone, P. Reutler, A. Revcolevschi, S. S. Dhesi, and A. Cavalleri. Photoinduced Melting of Antiferromagnetic Order in $La_{0.5}S_{1.5}MnO_4$ Measured Using Ultrafast Resonant Soft X-Ray Diffraction. *Phys. Rev. Lett.*, 106(21):217401, 2011.

[35] D. Fausti, R. I. Tobey, N. Dean, S. Kaiser, A. Dienst, M. C. Hoffmann, S. Pyon, T. Takayama, H. Takagi, and A. Cavalleri. Light-Induced Superconductivity in a Stripe-Ordered Cuprate. *Science*, 331(6014):189–191, 2011.

[36] A. L. Fetter and J. D. Walecka. *Quantum Theory of Many-particle Systems*. Dover Books on Physics. Dover Publications, 2003.

[37] R. P. Feynman. Forces in Molecules. *Phys. Rev.*, 56(4):340–343, 1939.

[38] S. Florens and A. Georges. Slave-rotor mean-field theories of strongly correlated systems and the Mott transition in finite dimensions. *Phys. Rev. B*, 70(3):35114, 2004.

[39] M. Först, R. Mankowsky, and A. Cavalleri. Mode-Selective Control of the Crystal Lattice. *Accounts of Chemical Research*, 48(2):380–387, 2015.

[40] M. Först, R. I. Tobey, H. Bromberger, S. B. Wilkins, V. Khanna, A. D. Caviglia, Y. D. Chuang, W. S. Lee, W. F. Schlotter, J. J. Turner, M. P. Minitti, O. Krupin, Z. J. Xu, J. S. Wen, G. D. Gu, S. S. Dhesi, A. Cavalleri, and J. P. Hill. Melting of Charge Stripes in Vibrationally Driven $La_{1.875} Ba_{0.125} CuO_{4}$: Assessing the Respective Roles of Electronic and Lattice Order in Frustrated Superconductors. *Phys. Rev. Lett.*, 112(15):157002, 2014.

[41] M. Först, R. I. Tobey, S. Wall, H. Bromberger, V. Khanna, A. L. Cavalieri, Y.-D. Chuang, W. S. Lee, R. Moore, W. F. Schlotter, J. J. Turner, O. Krupin, M. Trigo, H. Zheng, J. F. Mitchell, S. S. Dhesi, J. P. Hill, and A. Cavalleri. Driving magnetic order in a manganite by ultrafast lattice excitation. *Phys. Rev. B*, 84(24):241104, 2011.

[42] H. Fotso, K. Mikelsons, and J. K. Freericks. Thermalization of field driven quantum systems. *Scientific Reports*, 4:4699, 2014.

[43] J. K. Freericks, H. R. Krishnamurthy, and Th. Pruschke. Theoretical Description of Time-Resolved Photoemission Spectroscopy: Application to Pump-Probe Experiments. *Phys. Rev. Lett.*, 102(13):136401, 2009.

[44] H. Fröhlich. Electrons in lattice fields. *Advances in Physics*, 3(11):325–361, 1954.

[45] J. Fröhlich. Existence of Dressed One Electron States in a Class of Persistent Models. *Fortschritte der Physik*, 22(3):159–198, 1974.

[46] C. Gahl, U. Bovensiepen, C. Frischkorn, and M. Wolf. Ultrafast Dynamics of Electron Localization and Solvation in Ice Layers on Cu(111). *Phys. Rev. Lett.*, 89(10):107402, 2002.

[47] V. M. Galitskii and A. B. Migdal. Application of quantum field theory methods to the many body problem. *Soviet Physics JETP*, 34(34):139–150, 1958.

[48] M. Garny and M. M. Müller. Kadanoff-Baym equations with non-Gaussian initial conditions: The equilibrium limit. *Phys. Rev. D*, 80(8):85011, 2009.

[49] N. H Ge, C. M. Wong, and C. B. Harris. Femtosecond Studies of Electron Dynamics at Interfaces. *Accounts of Chemical Research*, 33(2):111–118, 2000.

[50] N. H. Ge, C. M. Wong, R. L. Lingle, J. D. McNeill, K. J. Gaffney, and C. B. Harris. Femtosecond Dynamics of Electron Localization at Interfaces. *Science*, 279(5348):202–205, 1998.

[51] A. Georges, G. Kotliar, W. Krauth, and M. J. Rozenberg. Dynamical mean-field theory of strongly correlated fermion systems and the limit of infinite dimensions. *Rev. Mod. Phys.*, 68(1):13–125, 1996.

[52] I. Gierz, M. Chávez-Cervantes, M. Mitrano, R. Tomar, H. Bromberger, H. Liu, S. Kaiser, M. A. Sentef, A. Stöhr, S. Link, U. Starke, C. Cacho, R. Chapman, E. Springate, F. Frasetto, L. Poletto, and A. Cavalleri. Enhanced electron-phonon coupling in a periodically distorted graphene lattice. *arXiv:1607.02314*, page 13, jul 2016.

[53] I. Gierz, J. C. Petersen, M. Mitrano, C. Cacho, I. C. E. Turcu, E. Springate, A. Stöhr, A. Köhler, U. Starke, and A. Cavalleri. Snapshots of non-equilibrium Dirac carrier distributions in graphene. *Nat Mater*, 12(12):1119–1124, 2013.

[54] F. Giustino. Electron-phonon interactions from first principles. *arXiv:1603.06965*, page 64, 2016.

[55] D. Golež, J. Bonča, L. Vidmar, and S. A. Trugman. Relaxation Dynamics of the Holstein Polaron. *Phys. Rev. Lett.*, 109(23):236402, 2012.

[56] D. Golež, M. Eckstein, and Ph. Werner. Dynamics of screening in photodoped Mott insulators. *Phys. Rev. B*, 92(19):195123, 2015.

[57] C. Gramsch, K. Balzer, M. Eckstein, and M. Kollar. Hamiltonian-based impurity solver for nonequilibrium dynamical mean-field theory. *Phys. Rev. B*, 88(23):235106, 2013.

[58] S. Guénon, S. Scharinger, S. Wang, J. G. Ramírez, D. Koelle, R. Kleiner, and I. K. Schuller. Electrical breakdown in a $V_2O_3$ device at the insulator-to-metal transition. *EPL (Europhysics Letters)*, 101(5):57003, 2013.

[59] M. C. Gutzwiller. Effect of Correlation on the Ferromagnetism of Transition Metals. *Physical Review*, 134(4A):159–162, 1964.

[60] A. K. Haghi, S. Thomas, and M. M. P. MirMahaleh. *Foundations of Nanotechnology, Volume One: Pore Size in Carbon-Based Nano-Adsorbents*. AAP Research Notes on Nanoscience and Nanotechnology. Apple Academic Press, 2014.

[61] D. R. Hamann and S. B. Fahy. Long-range interactions in auxiliary-field many-electron calculations. *Phys. Rev. B*, 47(4):1717–1725, 1993.

[62] H. Hellmann. *Einführung in die Quantenchemie*. Franz Deuticke, 1937.

[63] M. Hermele. $SU(2)$ gauge theory of the Hubbard model and application to the honeycomb lattice. *Phys. Rev. B*, 76(3):35125, 2007.

[64] A. C. Hewson and D. Meyer. Numerical renormalization group study of the Anderson-Holstein impurity model. *Journal of Physics: Condensed Matter*, 14(3):427, 2002.

[65] T. Holstein. Studies of polaron motion: Part I. The molecular-crystal model. *Annals of Physics*, 8(3):325–342, 1959.

[66] T. Holstein. Studies of polaron motion: Part I. The molecular-crystal model. *Annals of Physics*, 8(3):325–342, 1959.

[67] T. Holstein. Studies of polaron motion: Part II. The small polaron. *Annals of Physics*, 8(3):343–389, 1959.

[68] W. Hu, S. Catalano, M. Gibert, J. M. Triscone, and A. Cavalleri. Broadband terahertz spectroscopy of the insulator-metal transition driven by coherent lattice deformation at the $SmNiO_3/LaAlO_3$ interface. *Phys. Rev. B*, 93(16):161107, 2016.

[69] J. Hubbard. Electron Correlations in Narrow Energy Bands. *Proceedings of the Royal Society of London A: Mathematical, Physical and Engineering Sciences*, 276(1365):238–257, 1963.

[70] K. Inagaki, I. Terasaki, H. Mori, and T. Mori. Large Dielectric Constant and Giant Nonlinear Conduction in the Organic Conductor $\theta$-$(BEDT-TTF)_2CsZn(SCN)_4$. *Journal of the Physical Society of Japan*, 73(12):3364–3369, 2004.

[71] S. Iwai, M. Ono, A. Maeda, H. Matsuzaki, H. Kishida, H. Okamoto, and Y. Tokura. Ultrafast Optical Switching to a Metallic State by Photoinduced Mott Transition in a Halogen-Bridged Nickel-Chain Compound. *Phys. Rev. Lett.*, 91(5):57401, 2003.

[72] Sh. Iwai and H. Okamoto. Ultrafast Phase Control in One-Dimensional Correlated Electron Systems. *Journal of the Physical Society of Japan*, 75(011007), 2006.

[73] G. S. Jeon, T. H. Park, J. H. Han, H. C. Lee, and H. Y. Choi. Dynamical mean-field theory of the Hubbard-Holstein model at half filling: Zero temperature metal-insulator and insulator-insulator transitions. *Phys. Rev. B*, 70(12):125114, 2004.

[74] L. P. Kadanoff, G. Baym, and D. Pines. *Quantum Statistical Mechanics*. Advanced Books Classics Series. Perseus Books, 1994.

[75] J. Kanamori. Electron Correlation and Ferromagnetism of Transition Metals. *Progress of Theoretical Physics*, 30(3):275–289, 1963.

[76] L. V. Keldysh. Diagram Technique for Nonequilibrium Processes. *J. Exptl. Theoret. Phys.*, 47(1515), 1964.

[77] K. S. Kim. How to control pairing fluctuations: $SU(2)$ slave-rotor gauge theory of the Hubbard model. *Phys. Rev. B*, 75(24):245105, 2007.

[78] T. Kita. Introduction to Nonequilibrium Statistical Mechanics with Quantum Field Theory. *Progress of Theoretical Physics*, 123(4):581–658, apr 2010.

[79] A. Klein and R. Prange. Perturbation Theory for an Infinite Medium of Fermions. *Physical Review*, 5(112), 1957.

[80] P. Kostic, Y. Okada, N. C. Collins, Z. Schlesinger, J. W. Reiner, L. Klein, A. Kapitulnik, T. H. Geballe, and M. R. Beasley. Non-Fermi-Liquid Behavior of $SrRuO_3$: Evidence from Infrared Conductivity. *Phys. Rev. Lett.*, 81(12):2498–2501, 1998.

[81] G. Kotliar and D. Vollhardt. Strongly correlated materials: Insights from dynamical mean-field theory. *Physics Today*, 57(3):53–59, 2004.

[82] L. C. Ku and S. A. Trugman. Quantum dynamics of polaron formation. *Phys. Rev. B*, 75(1):14307, 2007.

[83] R. Kubo. Statistical-Mechanical Theory of Irreversible Processes. I. General Theory and Simple Applications to Magnetic and Conduction Problems. *Journal of the Physical Society of Japan*, 12(6):570–586, 1957.

[84] L. D. Landau. Über die Bewegung der Elektronen im Kristallgitter. *Physikalische Zeitschrift der Sowjetunion*, 3:644–645, 1933.

[85] L. D. Landau and S. I. Pekar. Effective mass of a polaron. *Eksp. Teor. Fiz*, 18(5):419–423, 1948.

[86] I. G. Lang and Y. A. Firsov. Kinetic theory of semiconductors with low mobility. *Sov. Phys. JETP*, 16(5):443450, 1963.

[87] Y. S. Lee, J. Yu, J. S. Lee, T. W. Noh, T. H. Gimm, H. Y. Choi, and C. B. Eom. Non-Fermi liquid behavior and scaling of the low-frequency suppression in the optical conductivity spectra of $CaRuO_3$. *Phys. Rev. B*, 66(4):41104, 2002.

[88] Z. Lenarcic and P. Prelovšek. Dielectric Breakdown in Spin-Polarized Mott Insulator. *Phys. Rev. Lett.*, 108(19):196401, may 2012.

[89] Z. Lenarčič and P. Prelovšiek. Ultrafast Charge Recombination in a Photoexcited Mott-Hubbard Insulator. *Phys. Rev. Lett.*, 111(1):16401, 2013.

[90] E. H. Lieb and F. Y. Wu. Absence of Mott Transition in an Exact Solution of the Short-Range, One-Band Model in One Dimension. *Phys. Rev. Lett.*, 20(25):1445–1448, 1968.

[91] H. Lu, C. Shao, J. Bonča, D. Manske, and T. Tohyama. Photoinduced in-gap excitations in the one-dimensional extended Hubbard model. *Physical Review B*, 91(24):245117, 2015.

[92] H. Lu, Sh. Sota, H. Matsueda, J. Bonča, and T. Tohyama. Enhanced Charge Order in a Photoexcited One-Dimensional Strongly Correlated System. *Physical Review Letters*, 109(19):197401, 2012.

[93] H. Lu, Sh. Sota, H. Matsueda, J. Bonča, and T. Tohyama. Photoinduced spin-order destructions in one-dimensional extended Hubbard model. *Journal of Physics: Conference Series*, 454:012079, 2013.

[94] J. M. Luttinger and J. C. Ward. Ground-State Energy of a Many-Fermion System. II. *Phys. Rev.*, 118(5):1417–1427, 1960.

[95] J. Maciejko. An Introduction to Nonequilibrium Many-Body Theory. Technical report, 2007.

[96] G. D. Mahan. *Many-Particle Physics*. Physics of Solids and Liquids. Springer US, 2013.

[97] R. Mankowsky, M. Först, and A. Cavalleri. Non-equilibrium control of complex solids by nonlinear phononics. *Reports on Progress in Physics*, 79(6):64503, 2016.

[98] P. C. Martin and J. Schwinger. Theory of Many-Particle Systems. I. *Phys. Rev.*, 115(6):1342–1373, 1959.

[99] H. Matsueda, Sh. Sota, T. Tohyama, and S. Maekawa. Relaxation Dynamics of Photocarriers in One-Dimensional Mott Insulators Coupled to Phonons. *Journal of the Physical Society of Japan*, 81(1):13701, 2012.

[100] R. Matsunaga and R. Shimano. Nonequilibrium BCS State Dynamics Induced by Intense Terahertz Pulses in a Superconducting NbN Film. *Phys. Rev. Lett.*, 109(18):187002, 2012.

[101] D. P. S. McCutcheon, N. S. Dattani, E. M. Gauger, B. W. Lovett, and A. Nazir. A general approach to quantum dynamics using a variational master equation: Application to phonon-damped Rabi rotations in quantum dots. *Phys. Rev. B*, 84(8):81305, 2011.

[102] R. Merlin. Generating coherent THz phonons with light pulses. *Solid State Communications*, 102(2):207–220, 1997.

[103] W. Metzner and D. Vollhardt. Correlated Lattice Fermions in $d = \infty$ Dimensions. *Phys. Rev. Lett.*, 62(3):324–327, 1989.

[104] M. Moeckel and S. Kehrein. Interaction Quench in the Hubbard Model. *Phys. Rev. Lett.*, 100(17):175702, 2008.

[105] E. Muller-Hartmann. Correlated fermions on a lattice in high dimensions. *Z. Phys. B -Condensed Matter*, 74:507–512, 1989.

[106] E. Muller-Hartmann. The Hubbard model at high dimensions: some exact results and weak coupling theory. *Z. Phys. B -Condensed Matter*, 76:211–217, 1989.

[107] Y. Murakami, Ph. Werner, N. Tsuji, and H. Aoki. Interaction quench in the Holstein model: Thermalization crossover from electron- to phonon-dominated relaxation. *Phys. Rev. B*, 91(4):45128, 2015.

[108] J. W. Negele and H. Orland. *Quantum Many-particle Systems*. Advanced Books Classics. Westview Press, 2008.

[109] D. Nicoletti and A. Cavalleri. Nonlinear light–matter interaction at terahertz frequencies. *Adv. Opt. Photon.*, 8(3):401–464, 2016.

[110] P. Nordlander, M. Pustilnik, Y. Meir, N. S. Wingreen, and D. C. Langreth. How Long Does It Take for the Kondo Effect to Develop? *Phys. Rev. Lett.*, 83(4):808–811, 1999.

[111] G. Ódor. Universality classes in nonequilibrium lattice systems. *Rev. Mod. Phys.*, 76(3):663–724, 2004.

[112] T. Oka. Nonlinear doublon production in a Mott insulator: Landau-Dykhne method applied to an integrable model. *Physical Review B*, 86(7):075148, 2012.

[113] T. Oka and H. Aoki. Ground-State Decay Rate for the Zener Breakdown in Band and Mott Insulators. *Physical Review Letters*, 95(13):137601, 2005.

[114] T. Oka and H. Aoki. Dielectric breakdown in a Mott insulator: Many-body Schwinger-Landau-Zener mechanism studied with a generalized Bethe ansatz. *Physical Review B*, 81(3):033103, 2010.

[115] T. Oka, R. Arita, and H. Aoki. Breakdown of a Mott Insulator: A Nonadiabatic Tunneling Mechanism. *Physical Review Letters*, 91(6):066406, 2003.

[116] H. Okamoto, H. Matsuzaki, T. Wakabayashi, Y. Takahashi, and T. Hasegawa. Photoinduced Metallic State Mediated by Spin-Charge Separation in a One-Dimensional Organic Mott Insulator. *Phys. Rev. Lett.*, 98(3):37401, 2007.

[117] H. Okamoto, T. Miyagoe, K. Kobayashi, H. Uemura, H. Nishioka, H. Matsuzaki, A. Sawa, and Y. Tokura. Photoinduced transition from Mott insulator to metal in the undoped cuprates $Nd_2CuO_4$ and $La_2CuO_4$. *Phys. Rev. B*, 83(12):125102, 2011.

[118] R. Peierls. Zur Theorie des Diamagnetismus von Leitungselektronen. *Zeitschrift für Physik*, 80(11):763–791, 1933.

[119] L. Perfetti, P. A. Loukakos, M. Lisowski, U. Bovensiepen, H. Berger, S. Biermann, P. S. Cornaglia, A. Georges, and M. Wolf. Time Evolution of the Electronic Structure of $1T - TaS_2$ through the Insulator-Metal Transition. *Phys. Rev. Lett.*, 97(6):67402, aug 2006.

[120] M. Potthoff. Non-perturbative construction of the Luttinger-Ward functional. *Condens. Mat. Phys.*, 9(557), 2006.

[121] J. Rammer. *Quantum Field Theory of Non-equilibrium States*. Cambridge University Press, 2011.

[122] M. Rini, R. Tobey, N. Dean, J. Itatani, Y. Tomioka, Y. Tokura, R. W. Schoenlein, and A. Cavalleri. Control of the electronic phase of a manganite by mode-selective vibrational excitation. *Nature*, 449(7158):72–74, 2007.

[123] J. M. Robin. *Dynamical Mean Field Theory*. LULU Press, 2010.

[124] M. J. Rozenberg, R. Chitra, and G. Kotliar. Finite Temperature Mott Transition in the Hubbard Model in Infinite Dimensions. *Phys. Rev. Lett.*, 83(17):3498–3501, 1999.

[125] A. Rüegg, S. D. Huber, and M. Sigrist. $Z_2$-slave-spin theory for strongly correlated fermions. *Phys. Rev. B*, 81(15):155118, 2010.

[126] G. Sangiovanni, M. Capone, C. Castellani, and M. Grilli. Electron-Phonon Interaction Close to a Mott Transition. *Phys. Rev. Lett.*, 94(2):26401, 2005.

[127] F. Sawano, I. Terasaki, H. Mori, T. Mori, M. Watanabe, N. Ikeda, Y. Nogami, and Y. Noda. An organic thyristor. *Nature*, 437(7058):522–524, 2005.

[128] Sh. Sayyad and M. Eckstein. Coexistence of excited polarons and metastable delocalized states in photoinduced metals. *Phys. Rev. B*, 91(10):104301, 2015.

[129] Sharareh Sayyad and Martin Eckstein. Slowdown of the Electronic Relaxation Close to the Mott Transition. *Phys. Rev. Lett.*, 117(9):96403, 2016.

[130] J. Schwinger. Brownian Motion of a Quantum Oscillator. *J. Math. Phys.*, 2:407–432, 1961.

[131] S. E. Sebastian, N. Harrison, C. D. Batista, S. A. Trugman, V. Fanelli, M. Jaime, T. P. Murphy, E. C. Palm, H. Harima, and T. Ebihara. Heavy holes as a precursor to superconductivity in antiferromagnetic $CeIn_3$. *Proceedings of the National Academy of Sciences*, 106(19):7741–7744, 2009.

[132] R. Sensarma, D. Pekker, E. Altman, E. Demler, N. Strohmaier, D. Greif, R. Jördens, L. Tarruell, H. Moritz, and T. Esslinger. Lifetime of double occupancies in the Fermi-Hubbard model. *Physical Review B*, 82(22):224302, 2010.

[133] G. Stefanucci and R. van Leeuwen. *Nonequilibrium Many-Body Theory of Quantum Systems: A Modern Introduction*. Cambridge University Press, 2013.

[134] N. Strohmaier, D. Greif, R. Jördens, L. Tarruell, H. Moritz, T. Esslinger, R. Sensarma, D. Pekker, E. Altman, and E. Demler. Observation of Elastic Doublon Decay in the Fermi-Hubbard Model. *Physical Review Letters*, 104(8):080401, 2010.

[135] N. Strohmaier, D. Greif, R. Jördens, L. Tarruell, H. Moritz, T. Esslinger, R. Sensarma, D. Pekker, E. Altman, and E. Demler. Observation of Elastic Doublon Decay in the Fermi-Hubbard Model. *Phys. Rev. Lett.*, 104(8):80401, 2010.

[136] P. Sun and G. Kotliar. Extended dynamical mean-field theory and GW method. *Phys. Rev. B*, 66(8):85120, 2002.

[137] H. Tasaki. The Hubbard model - an introduction and selected rigorous results. *Journal of Physics: Condensed Matter*, 10(20):4353, 1998.

[138] T. Tohyama. Nonequilibrium photo dynamics of low- dimensional strongly correlated electron systems. *Eur. Phys. J. Special Topics*, 222:1065–1075, 2013.

[139] T. Tohyama, Y. Inoue, K. Tsutsui, and S. Maekawa. Exact diagonalization study of optical conductivity in the two-dimensional Hubbard model. *Phys. Rev. B*, 72(4):45113, 2005.

[140] Y. Tokura, H. Okamoto, T. Koda, T. Mitani, and G. Saito. Nonlinear electric transport and switching phenomenon in the mixed-stack charge-transfer crystal tetrathiafulvalene-*p*-chloranil. *Phys. Rev. B*, 38(3):2215–2218, jul 1988.

[141] N. Tsuji, P. Barmettler, H. Aoki, and Ph. Werner. Nonequilibrium dynamical cluster theory. *Phys. Rev. B*, 90(7):75117, 2014.

[142] J. Vucicevic, D. Tanaskovic, M. Rozenberg, and V. Dobrosavljevic. Bad-Metal Behavior Reveals Mott Quantum Criticality in Doped Hubbard Models. *Phys. Rev. Lett.*, 114(24):246402, 2015.

[143] M. Wagner. Expansions of nonequilibrium Green's functions. *Phys. Rev. B*, 44(12):6104–6117, 1991.

[144] S. Wall, D. Brida, S. R. Clark, H. P. Ehrke, D. Jaksch, A. Ardavan, S. Bonora, H. Uemura, Y. Takahashi, T. Hasegawa, H. Okamoto, G. Cerullo, and A. Cavalleri. Quantum interference between charge excitation paths in a solid-state Mott insulator. *Nat Phys*, 7(2):114–118, 2011.

[145] Y. H. Wang, H. Steinberg, P. Jarillo-Herrero, and N. Gedik. Observation of Floquet-Bloch States on the Surface of a Topological Insulator. *Science*, 342(6157):453–457, 2013.

[146] Z. Wang, M. Pietz, J. Walowski, A. Förster, M. Lepsa, and M. Münzenberg. Spin dynamics triggered by subterahertz magnetic field pulses. *Journal of Applied Physics*, 103(12), 2008.

[147] D. Wegkamp, M. Herzog, L. Xian, M. Gatti, P. Cudazzo, C. L. McGahan, R. E. Marvel, R. F. Haglund, A. Rubio, M. Wolf, and J. Stähler. Instantaneous Band Gap Collapse in Photoexcited Monoclinic $VO_2$ due to Photocarrier Doping. *Phys. Rev. Lett.*, 113(21):216401, 2014.

[148] P. Weiss. L'hypothèse du champ moléculaire et la propriété ferromagnétique. *Journal de Physique Théorique et Appliquée*, 6(1):661–690, 1907.

[149] P. Werner and A. J. Millis. Efficient Dynamical Mean Field Simulation of the Holstein-Hubbard Model. *Phys. Rev. Lett.*, 99(14):146404, 2007.

[150] Ph. Werner and M. Eckstein. Phonon-enhanced relaxation and excitation in the Holstein-Hubbard model. *Phys. Rev. B*, 88(16):165108, 2013.

[151] Ph. Werner and M. Eckstein. Phonon-enhanced relaxation and excitation in the Holstein-Hubbard model. *Physical Review B*, 88(16):165108, 2013.

[152] Ph. Werner and M. Eckstein. Field-induced polaron formation in the Holstein-Hubbard model. *Europhysics Letters*, 109(3):37002, 2015.

[153] Ph. Werner, E. Gull, M. Troyer, and A. J Millis. Spin Freezing Transition and Non-Fermi-Liquid Self-Energy in a Three-Orbital Model. *Phys. Rev. Lett.*, 101(16):166405, 2008.

[154] Ph. Werner, K. Held, and M. Eckstein. Role of impact ionization in the thermalization of photoexcited Mott insulators. *Physical Review B*, 90(23):235102, 2014.

[155] Ph. Werner and A. J. Millis. Dynamical Screening in Correlated Electron Materials. *Phys. Rev. Lett.*, 104(14):146401, 2010.

[156] F. A. Wolf, I. P. McCulloch, and U. Schollwöck. Solving nonequilibrium dynamical mean-field theory using matrix product states. *Phys. Rev. B*, 90(23):235131, 2014.

[157] R. Zitzler, N.H. Tong, Th. Pruschke, and R. Bulla. Phase Diagram of the Frustrated Hubbard Model. *Phys. Rev. Lett.*, 93(1):16406, 2004.